THE FAINTEST STARS

Thesis by

Christopher G. Tinney

In Partial Fulfillment of the Requirements

for the Degree of

Doctor of Philosophy

California Institute of Technology

Pasadena, California

1993

(Defended 29 October, 1992)

ACKNOWLEDGEMENTS

I write this with some trepidation – I have this enormous fear that in the process of trying to express some of the gratitude I feel to the many people who have helped make this thesis possible, I will forget someone. I will make a sincere attempt not to do that, but just in case I want to say that I feel truly indebted to all the friends I have made and worked with during my time at Caltech. If anyone does get left out, its only because I screwed up.

Basically, I *really* got very lucky. First, I managed to come across a fascinating proposal for a thesis topic – one in which I remained interested right up to the end. But more importantly, I have had the experience of working with two great scientists. Throughout the course of this thesis Jeremy Mould and Neill Reid have been sources of support, advice and encouragement (a rare commodity at Caltech. I cannot think of two better role models for a young scientist to attempt to emulate. Jeremy has a truly amazing ability to look at a scientific problem and estimate what a given set of observations will, and – even more importantly – will not, tell us about what is going on. I can only hope to develop a fraction of the judgement he brings to the planning and execution of an astronomical project.

Despite his carefully cultivated image as the second oldest graduate student in the world, Neill is a truly fine scientist who never failed to use his expertise to set me on the right track when I came to him for help. Both were always available whenever I needed help (both scientific and personal) for which I will be eternally grateful. I cannot overstate the debt of gratitude I feel towards them.

Over the years many of the faculty and post-docs at Caltech have had an influence on me – usually for the better. I'd like to thank the members of my committe (Judy Cohen, Dave Stevenson, Nick "The Oldest Graduate Student in the World" Scoville, Jeremy and Neill) for actually plowing through all 200-odd pages of my thesis, and spotting typos that even the Caltech proofreader missed. Marshall Cohen gave me my first 'job' at Caltech doing VLBI, and Toni Zensus guided me through my first months at Caltech (as well as giving me sound advice – which I ignored – on how to pass my driving test – which I failed). I'm not sure whether it was VLBI, or my first exposure to Caltech which traumatised me so, but ever since I 've tended to give the VLBI group rather a hard time, for which I apologise. Nick Scoville not only put up with my not doing any work for two years, but

also put up with my following the bad example set for me by Steve and Shri and ragging on him terribly – I can only hope that if I ever reach a similair point in my career that I still enjoy life as much as Nick does.

On June 15, 1987, a lot of uniquely new things happened to me – I flew out of Australia for the first time and in doing so discovered that Continental is the worst airline in the world; I rode the 'FUNBUS' from LAX to Pasadena (which I seem to remember was only marginally more 'fun' than the aformentioned Continental flight); I arrived at Caltech and checked in the the Graduate Dorms (even drearier than the first two); and I had my first 'taste' of Caltech at Burger Continental (I've never been there since). The following day I came to Robinson and was 'inducted' into the graduate school lifestyle and given my first set of VLBI tapes to reduce. As one might guess I was soon feeling pretty damn sorry for myself. If it hadn't been for the older graduate students I met that week, I really don't know if I'd have survived over the weekend, let alone five years. Through the following years the support and friendship of Rich, Neill, Chris W., Julie and Steve (who not only put up with living with me, but also refrained from murder when I ruined his pans by frying chips in them) kept me going. My fellow classmate, Josh Roth, arrived at the end of the summer and has been a good friend since. The younger students (among them Angela, Todd, Kim, Nick, Jose, Will, Rachel and Peter) managed to keep some life in the department after the departure of the old guard, and were kind enough to humour me in my role as the crusty "Minister of Culture". I made a lot of other friends at Caltech whose company has meant much to me; the various members of the Astronomy softball, volleyball and soccer teams, especially Paolo Coppi, John the Greek, Hal Petrie, Bill Douglas, and Petra de la Paz; the staff of the Palomar and Owens Valley observatories who do such a marvelous job keeping those places running, especiallyDave Tennant, Mike Doyle, John Henning, Cindy Brewer, Jean Mueller, Dave Mendenhall, Juan Carrasco, and the two long-suffering night assistants who had to put up with me most, Will "Pigourney Weaver" M^{c}Kinley and Skip "Toys 'R' Us" Staples; the post-docs who didn't look down on me as a mere grad-student, especially John "D.A." Conway, Sponger Haniff, Claire Chandler and then post-doc, but now professor, John Carlstrom; and two lovely women who fall into none of the above categories, but who befriended me nonetheless, Helen Knudsen and Ann Palfreyman.

I would never have survived my time here at Caltech without the social support and emotional release provided by the musical activities I took part in. I most especially want to express my gratitude to Don and Wendy Caldwell. I joined the Glee Clubs (which I still think is an appalling name for a choir) mainly as a way of meeting people (OK -

I'll be honest, as a way of meeting women). In that respect alone they were a valuable resource, as I made many freinds there who enriched my time at Caltech, among them Joel, Bryan, Roger, Beth, Donnie, Suzanne, Dana and Jamie. But I also found that, above all else, I truly loved choral music – both performing it and listening to it. For that Don and Wendy are directly resonsible. Together they managed every year to turn a bunch of science geeks of highly variable talent into a functional (and very occasionally, inspiriational) choir. Despite our widely ranging skills, Don always chose music which taxed our abilities and drew out our best. I simply cannot thank him enough.

In 1989 a group of graduate students from the Glee Clubs who had been musically bereft by the summer break, formed an informal Renaisance music group, which eventually became the *Cantores Atri Mortis.* Somehow it managed to survive for three years (though my attendance was at best spotty) and its various members (Joel, Roger, Matt, Donnie, Bryan, Neill, Cathy, Jamie, Beth, Rachel, Helen and Chris W.) were a source of good company and fine music.

I wish to offer profound thanks to all the staff at the Caltech Counselling Centre. I've had call to meet several of the workers there, and have found them to be uniformly wonderful people. It amazes me that they are able to do the job they do under the load they have. I particularly wish to thank John, Dorit and Kevin. I'd also like to thank the members of what (for want of a better name) I'll call 'Kevin's group'. You're support has meant a great deal to me.

I don't think my family has ever quite understood why it is that I do what I do. But they have always supported me in my career regardless, and only occasionally ask me "So who is it that actually pays astronomers?" Mum and Dad, I know that the last five years have been a difficult time for you, but I appreciate your allowing me to always seek my own path. One day I will come to know my brother and sister far better than I do know – I know that they are wonderful people, but it saddens me to have known so little of what they have become.

Lastly, I wish to thank two people without whom I would not have lasted more than a year at Caltech. The first picked me up when I really needed it four years ago, and has been a support I could not have survived without ever since. Jackie, I cannot thank you enough. I have not lived closer than 5000 miles from the second in the last five years, but through it all she has been with me and closer to me than anyone else. This work is dedicated to her.

for Elizabeth

ABSTRACT

We construct a 270 square degree photometric catalogue from plate material of the UKSRC and POSSII surveys. The procedures used and quality checks applied are described in detail, and should be considered as illustrative for those planning scientific programmes with the forthcoming scans of these surveys.

Infrared JHKLL′ photometry and low resolution infrared spectra ($\lambda \approx 1.0-2.5\mu$m) for a selection of the latest stars known are presented. The combined photometric and spectral data are used to evaluate bolometric corrections and bolometric magnitudes for late type M-dwarfs almost 2-magnitudes fainter than the faintest previously measured objects. We examine some of the current problems associated with the effective temperature scale for very low mass stars.

First results are presented from a CCD trigonometric parallax programme at the Palomar 60″ telescope. We double the number of extremely late M-dwarfs ($M_{bol} > 13$) with directly measured distances. Structure in the main sequences so constructed suggest that the faintest known stars may not be stably supported by nuclear burning. We show that $\sigma(\pi) \leq 0.004''$ can be obtained in a few years using standard CCDs on a common-user telescope.

We present infrared K-band photometry of complete samples of VLM candidates selected by our photographic catalogues, and construct a bolometric luminosity function which extends to $M_{Bol} = 13.75$. We find significant evidence for a luminosity function decreasing towards these luminosities. We also find that our data are consistent with the results of studies based on the Nearby Star sample. We convert our observed LF into the form of a mass function which extends with reasonable statistics to $0.08M_{\odot}$ – the H-burning minimum mass. The mass function 'turns over' at $\approx 0.25M_{\odot}$, goes through a local minimum at $\approx 0.15M_{\odot}$, and seems to increase again below $0.1M_{\odot}$ – none of these features are predicted by any of the current theories of star formation. Lastly, the mass density we observe just above the H-burning minimum mass makes it difficult to envisage brown dwarfs contributing significant quantities of missing mass without invoking either a mass function in this region significantly steeper than that seen for main sequence stars, or an extremely low cut-off mass to the mass function.

CONTENTS

Chapter 1 - Foreword.

The biggest, the smallest, the furthest, the brightest – despite its musty old ethics of "hypothesis and testing" science is still galvanised on an emotional level (for most scientists at least) by the spirit of the hunt; the chase for knowledge at the limits of what can be seen. And, the role of discovery in astronomy is probably stronger than in any other field of scientific endeavour. If a physicist turns over a rock and finds something interesting, she can sit down and see how it works – in particular, she can poke it with a stick and see what happens. An astronomer, however, has no sticks which are long enough. When we see something interesting we can't *make* it happen again – all we can do is go and turn over a lot more rocks and see if we can find it one more time, in the hope that our understanding will be thus further illuminated. We are fundamentally limited to watching the universe in action, and as a result we usually have to do a *lot* of watching before we can understand what is going on.

As astronomers, therefore, we must attempt to observe as much of the universe as we can. Usually this translates to seeing as far away as we can. And since observing deeper into the universe also allows us to see backwards in time, it is not surprising that studying the universe outside our Galaxy become *the* hot astronomical field. The opposite extreme to looking for very bright, very large things a long way away, is looking for very faint, very small things nearby – and it is these objects, widely considered to be uninteresting, which I wish to examine in this thesis. Why? Well, it happens that there are a lot of very valid 'scientific' reasons; because stars at, or below, the bottom of the main sequence may make up the local 'hidden' mass; because the mass function is a fundamental parameter for everything from understanding star formation to modelling the integrated emission from external galaxies; and because the end of the main sequence shows evidence for changes in the slope of the mass function which is seen to be fairly smooth at all other masses. But the *real* reason is that these very small stars are poorly understood, and that this is largely because so few of them are known. And the objects *beyond* the bottom of the main sequence are a complete *terra incognita*. Who could resist?

Very small stars are *very* faint. Much like quasars at the edge of the observable universe, stars at the very bottom of the main sequence are at the limits of what can be observationally detected. To study them, such large areas of the sky must covered, to such

large depths that surveys for them must push the limits of the available technology. The advent of large format (greater than 4096×4096) Charge Coupled Devices (CCDs) and large format infrared arrays will revolutionise this field in about 10 years time. At present, however, CCD and infrared array detectors are just too small to survey sufficiently large areas of the sky to place meaningful limits of the space density of very faint stars.

In this thesis results are presented from a large (270 degree^2), deep ($I_C < 18$) photographic survey for Very Low Mass ($m \lesssim 0.2 M_\odot$, hereafter VLM) stars. Because these very faint stars emit most of their flux in the near-infrared ($\lambda = 1 - 4\mu$m) the optical fluxes measured by photographic techniques – while sufficient to identify candidate objects – are not sufficiently precise estimators of the fundamental properties of these stars to carry out a detailed study. Infrared K-band photometry has therefore been obtained for ≈ 400 VLM candidates identified by our photographic work. We have used this data (both photographic data for $M_{Bol} < 12$ and infrared data for $M_{Bol} > 12$) to construct luminosity and mass functions with considerably more precision than previous studies have been able to achieve.

An important part of obtaining that precision has been calibrating the fundamental properties of VLM stars. In particular; it was found that work needed to be done in better defining the colour-magnitude relations from which distance to candidate stars are estimated; and that complete spectra for these stars needed to be obtained in the infrared so that bolometric corrections could be accurately estimated.

The results of these studies are presented in the following chapters. Chapter 2 describes in detail the construction of our photographic catalogues and presents a discussion of the procedures used to estimate luminosity functions. Chapter 5 presents the infrared photometry obtained for the complete samples of VLM stars so identified, as well as the luminosity and mass function constructed from our data. Chapter 3 presents infrared photometry and spectra for a sample of VLM stars, which is used to construct bolometric corrections suitable for use with these very late stars. Chapter 4 presents results from a trigonometric parallax programme carried out on the Palomar 60″ telescope, the results of which are used to construct new colour magnitude diagrams for VLM stars.

Each of these chapters has been prepared as a paper suitable for separate publication. Throughout the text, therefore, the various chapters refer to each other, not by their chapter number, but by the 'Paper' number. Chapter 2 is designated as 'Paper I', chapter 3 as 'Paper II', chapter 4 as 'Paper III' and chapter 5 as 'Paper IV'. Chapters 3 and 4 have been accepted for publication, and should appear in the March 1993 issue of

The Astronomical Journal. Chapters 2 and 5 have been submitted (respectively) to *The Astrophysical Journal (Supplements)* and *The Astrophysical Journal.*

Chapter 2 - A 270 Square Degree Catalogue of Photographic Schmidt Data. [1,2]

Abstract

We construct a 270 square degree photometric catalogue from scans of IIIaF and IVN plate material from the UKSRC and POSSII surveys. The procedures used and quality checks applied are described in detail, and should be considered as illustrative for those planning scientific programmes with the forthcoming scans of these surveys. We find our plate material is complete to I $\approx$ 18 and R $\approx$ 20.5 with photometric uncertainties of $\pm$0.20 and $\pm$0.25 magnitudes (respectively) at those limits. These data are used to construct luminosity functions for stars within 150pc of the sun in four distinct directions. We find no significant evidence for variations in the form of the luminosity function in different locations within the Galactic disk. Approximately 10-20% variations are seen in the normalisation of the luminosity function. We find that we reproduce the steeply increasing luminosity function seen by previous studies for $M_{Bol} > 13$, however we show that this increase is completely spurious and is an artifact introduced by; the small number of *real* stars detected in our survey at these luminosities combined with the number of spurious sources which we are unable to reject without further observation, and the fact that optical colours are an extremely poor luminosity estimator for very faint stars. In light of this we show how our catalogues can be used to contruct samples of Very Low Mass (M $\lesssim 0.2M_{\odot}$) stars for further observation in the infrared.

---

[1] Observations were made partially on the 60-inch telescope at Palomar Mountain which is jointly owned by the California Institute of Technology and the Carnegie Institution of Washington. Observations were also made at the Las Campanas Observatory which is operated by the Carnegie Instituition of Washington.

[2] This work is partially based on photographic plates obtained at the Palomar Observatory 48-inch Oschin Telescope for the Second Palomar Observatory Sky Survey which was funded by the Eastman Kodak Company, the National Geographic Society, the Samuel Oschin Foundation, the Alfred Sloan Foundation, the National Science Foundation grants AST 84-08225 and AST 87-19465, and the National Aeronautics and Space Administration grants NGL 05002140 and NAGW 1710.

Section 2.1 - Introduction

The first recorded use of photographic techniques in astronomy is believed to be due to J. W. Draper (1840), who used the daguerrotype process to photograph the Moon. The development of the 'dry-gelatin' process in the 1880's (essentially the same system as is used today) made astronomical photography possible for objects at, or below, the limit of what could be seen by eye (Common 1883). Throughout the 100 years since, astronomical photography has been the premier tool for studies of the heavens. Only within the last 10 to 15 years have photoelectric and solid-state detectors become prevalent. Unfortunately since their introduction, there has been a tendency by the majority of astronomers to regard astro-photography as an 'ante-diluvian' technique, with as much relevance to modern astronomy as the hand-held sextant.

In reality astronomical photography can *still* carry out studies of which users of Charge-Coupled Devices (CCDs) can only dream. No semiconductor detector can be made in sizes even approaching those of commonly used photographic plates (even when their sizes are normalised by the relative sensitivities of the materials), making them uniquely suited to carrying out large-scale surveys. This is especially true for faint astronomical objects associated with the Galactic disk (i.e., low mass stars or brown dwarfs), where survey area is much more important than survey depth. Moreover, a vast quantity of photographic material is already in hand at epochs of up to 60 years prior to our own – a database of dynamical information which could not be duplicated by non-photographic processes in timescales of less than decades.

In this paper we describe the procedures and techniques used in the construction of a photometric catalogue covering 269.79 square degrees down to limiting magnitudes of $I_C \approx 18.0$ and $R_C \approx 20.5$[3] with photometric uncertainties of $\sim \pm 0.21$ and ± 0.25 magnitudes at the respective limits. The catalogue is based on IIIaF and IVN plates from 11 fields acquired with either the 48″ Oschin Telescope (as part of the Palomar Observatory Second Sky Survey, or POSS II), or the 48″ United Kingdom Schmidt Telescope (as part of the UK Science Research Council's Southern Sky Survey, or UKSRC). It was constructed with the aim of detecting *all* M dwarf stars present in the catalogue's surveyed area above a

[3] Throughout this work R and I magnitudes with the subscript 'C' refer to magnitudes on the Kron-Cousins photometric system (Cousins 1976, or see §2.2.2). When an R- or I-band without an identifying subscript is used we refer to the 'generic' photometric passbands at $\sim$ 6500Å and 8000Å rather than to any specific system.

limit of $I_C \approx 18$. In all our final catalogues contain over 593,000 objects, from which we photometrically select (by their red R–I colours) nearby M-dwarfs in order to study the luminosity and mass functions for low mass stars. We also target the class known as 'Very Low Mass' (VLM) stars – these are stars with $M_{Bol} > 12$ and have typical $(R–I)_C \sim 2.2 – 2.7$. We use our large photographic catalogue to identify a sample of VLM candidates for further study in the infrared.

The photographic plates of the 48″-class Schmidt telescopes are particularly suited to a study of such intrinsically faint objects, because they cover enormous areas of the sky ($\approx$ 25 usable square degrees per plate), down to significant limiting magnitudes. Even the advent of large format Charge Coupled Devices (CCDs) has not made it feasible to carry out a survey over such a volume in any other way. However, the use of photographic material introduces its own unique problems; first, the plates have to be converted into a digital format – in this study we used the COSMOS scanning machine of the Royal Observatory Edinburgh; second, as photographic materials are inherently non-linear all our photographic plates have to be calibrated with photometry obtained with a linear device – in this case a CCD; lastly, the acquiring of quality photographic materials is essentially a complicated art-form. Unlike CCD exposures which for given seeing and transparency are highly repeatable, the quality of photographic plates acquired can vary considerably – it is necessary to carefully examine each plate, the quality of its calibration and its completeness limit before including it in our catalogue.

In the sections that follow we describe how we have dealt with these, and other, difficulties. In Section 2.2 the CCD calibration photometry acquired for this study is described, along with some comments on photometric colour systems, which have historically been a bugbear of this field. In Section 2.3 we describe the photographic plate material used, its scanning with the COSMOS measuring machine and the calibration of the resulting photographic measures onto a uniform photometric system. In Section 2.4 we evaluate the quality of the data included in our catalogue – i.e., its completeness, its photometric uncertainties and the effects of colour terms on the selection of very red stars. Lastly, in Sections 2.5 and 2.6 we examine some of scientific questions which such a data set can address – specifically an examination of the luminosity function for early M-dwarfs, and the selection of a sample of VLM star candidates for study in the infrared. This paper is the first of a series presenting final results from our VLM survey at Palomar. Some preliminary results of this programme have been presented in Tinney, Mould & Reid (1992a). A second paper (Tinney 1992b, hereafter Paper IV) will present infrared photometry of a

complete sample of VLM candidates and use that data (together with the photographic data from this paper) to examine the mass and luminosity functions at the bottom of the main sequence. Other papers will present new determinations of VLM colour-magnitude relations (Tinney 1992a, hereafter Paper III) and VLM bolometric magnitudes (Tinney, Mould & Reid 1992b, hereafter Paper II).

Section 2.2 - CCD Calibration Photometry

2.2.1 - Observations

CCD observations were carried out over the period April 1990 to January 1992 in order to calibrate our photographic plate material. All observations were made with a 1024×1024 24μm-pixel Tektronix un-thinned CCD (denoted CCD11) at the Cassegrain focus of the Palomar 60-inch Telescope. CCD11 is configured to have a gain of $\approx 2.5e^-$/ADU and has a read noise of only $5e^-$. In direct imaging mode CCD11 gives a pixel scale of 0.372″/pixel which corresponds to a field of view of 6.35′×6.35′. The object of this observing programme was to acquire a database of CCD photometry with photometric uncertainties of $\approx 5\%$ down to the photographic plate limits mentioned above, which is more than sufficient for the purpose of calibrating our photographic material.

Table 2.1 lists the nights on which observations were carried out, and the quality of the data obtained. In all observations were attempted on 50 nights for which time was allocated to this project. On 18% (9) of these nights no observations were made. 50% (25) of the nights were non-photometric, and these nights were either used for carrying out CCD parallax observations of VLM stars (cf. Paper III), or for taking long exposures at positions subsequently calibrated on photometric nights.

2.2.2 - Photometric Systems

Three things define a photometric system; a detector, a set of filters, and a set of measurements of magnitudes and colours made with that detector and filter combination (i.e., a set of standard stars). For example, the commonly used Kron-Cousins ($R_C I_I$) photometric system is defined by observations made with a RCA 31034 GaAs photocathode through an OG570+KG3 filter combination for R_C and a RGN9 filter for I_C (Bessell 1979) of numerous stars in the southern E-regions (Cousins 1976). Northern hemisphere observers commonly make use of the standards of Landolt (1983) which, as they were observed using an identical detector and filter combination and calibrated with the Cousins standards, can be regarded as being also on the Kron-Cousins system. Both the Landolt and Cousins standards span a large range in colour and apparent magnitude and are extremely precise – they are an excellent resource for calibrating photometric observations.

Unfortunately, though it has an excellently determined set of standards the Kron-Cousins system does have its problems. In particular the Kron-Cousins R_C passband has an extremely long 'tail' to the red of its peak, owing to the fact that sufficiently sharp

glass cut-off filters were not then available (see Figure 2.1). This tail has its most serious effect on very red stars – the effective wavelength (λ_{eff}) of the R_C bandpass varies from $\lambda_{eff} \approx 6400$Å for an F0 star to $\lambda_{eff} \approx 7400$Å for an M6.5 star (Bessell 1986)! (The I_C passband is much more rectangular, its red cutoff being due to the sensitivity drop-off of the GaAs detector. Fortuitously this makes it a good match to the natural system of the IVN emulsion (see Figure 2.1) – in fact colour terms between almost all "I" passbands are extremely small). The R_C system is therefore a particularly poor match to the natural system of the IIIaF photographic emulsion which cuts-off sharply at $\sim$ 7000Å. A very strong colour term is required to place IIIaF photographic photometry on the R_C system and, moreover, this term is largest for the very reddest stars. But it is these stars that we are most interested in – they are the reason we are trying to construct a photometric catalogue from photographic material. It clearly does not make sense to attempt to place our catalogue on the Kron-Cousins system.

Thuan & Gunn (1976) have developed a photometric system which obviates some of these difficulties. Specifically they use an OG610+Balzers B1 short pass interference filter to define a "R" passband (hereafter denoted Gunn r) which is a good match to the IIIaF emulsion (see Figure 2.1). Later a Gunn i passband was defined which is essentially the same as the Kron-Cousins I_C. Unfortunately while the Gunn filters solve one very important problem, they raise another, which is that the Gunn standards are few, rather bright and none are very red.

Given both the colour-term problem of the Kron-Cousins system and the paucity of precise Gunn standards we have chosen to adopt a hybrid system for our photometric catalogue. CCD observations were carried out through r- and i-band filters normally employed for Gunn-system photometry - allowing us to calibrate our photographic photometry onto our CCD photometry using a simple colour term (as will be seen later, for extremely red stars a colour term is still required even with two well matched systems like the Gunn ri and IIIaF/IVN systems). The zero point for each nights observations was derived using Kron-Cousins standards over a small colour range; $(R-I)_C \approx 0.50 \pm 0.15$. We define the following nomenclature for our hybrid system; r^C_{Pal}, i^C_{Pal} and $(r-i)^C_{Pal}$ refer to observations made in the manner described above (the superscript 'C' denotes that they are CCD magnitudes – a superscipt 'P' will be used to photographic magnitudes in this system), and it is onto this natural system that we calibrate our photographic plates.

Observations were made of a large number of Landolt standards over a wide range of colours. The combined transformations – based on five nights of photometry – for

i^C_{Pal}–I_C and $(r-i)^C_{Pal}$–$(R\text{-}I)_C$ are shown in Figure 2.2. Within the limits we are able to measure no colour term is present in the transformation from i^C_{Pal} to I_C – this result agrees with that of Bessell (1986) who finds no colour term over a smaller range of colours in the transformation from Gunn i (there is only a zero point difference between i^C_{Pal} and Gunn i) to Cousins I_C. However, a colour-dependent transformation ($\sim$ 0.15 magnitudes total excursion) is required to place the $(r-i)^C_{Pal}$ photometry on the Cousins $(R\text{–}I)_C$ system. Unfortunately, because there are no standards available at $(R\text{–}I)_C \gtrsim 2.2$ this transformation cannot be definitively determined for the colour region in which our low mass star sample selection is done, clearly making it impossible for us to place our data definitively on the Kron-Cousins system. The curve shown in Figure 2.2 is a polynomial fit to the data, as follows,

$$\begin{aligned}(r-i)^C_{Pal} - (R\text{-}I)_C = {} & 0.162 - 0.561(R\text{-}I)_C + 0.671(R\text{-}I)^2_C \\ & - 0.360(R\text{-}I)^3_C + 0.0740(R\text{-}I)^4_C \ .\end{aligned} \tag{2.1}$$

2.2.3 - The Reduction of CCD Photometry

All the CCD photometry obtained was reduced using standard aperture photometry techniques with the FOTO routine of the FIGARO data reduction package. Multiple (between three and five) observations were made of Landolt standards hourly over a range of airmasses on each photometric night. These standards were used to calculate a zero point by solving the following equation;

$$i^C_{Pal} = i_{inst} - K_i \sec(ZA) + 2.5\log_{10}(T) - Z_i + 31.0 \tag{2.2}$$

where,

i_{inst} = i-band instrmental magnitude within a given aperture (from FOTO)

K_i = atmospheric extinction in magnitudes/airmass at i-band

ZA = zenith angle of observation

T = exposure time

Z_i = photometric zero point at i-band

in which both K_i and Z_i are possible free parameters. In practice K_i was not seen to vary significantly from the standard Palomar values of K_i = 0.052mag./airmass and K_r = 0.085mag./airmass. Measurements of K_i and K_r typically showed a scatter of

$\sim \pm 0.04$mag./airmass.[4] If our estimate of the extinction coefficient was in error by this much it would introduce a maximum error in the final photometry of $\lesssim 0.04$ mag.as observations were always carried out at sec(ZA) < 2. More typically observations of objects and standards were carried out at airmasses ranging from 1.2 to 1.6, leading to a possible error due to mis-estimation of $K_{i/r}$ of $\sim \pm 0.016$ mag. As we are only attempting to estimate CCD photometry to within $\pm 5\%$, this is a negligible source of uncertainty. Table 2.2 shows the measured Z_i and Z_r for each night, together with the standard deviation in the residuals about each fit. It can be seen that each night's zero-point is typically determined to within ± 0.025 magnitudes.

Stars were chosen by hand from each CCD calibration frame – close double stars and galaxies were avoided, so as to ensure as 'clean' a calibrating sample as possible. Our calibration stars do not therefore represent a complete sample. Positions used for CCD observation were of one of two types; "primary" calibrators and "secondary" observations. First a number of positions (usually five) were chosen for each POSSII/UKSRC field at arbitrary locations (usually at the centre and at the northwest, northeast, southwest and southeast corners of the field 2° from the plate centre) and were observed for $\approx$ 900s at r and $\approx$ 400s at i (exposures times were shortened in good seeing). These CCD images easily reached $\sim$ 1 magnitude fainter than the photographic plate limits, and provide photometry good to $\approx$ 5% at the photographic plate limits. Stars from these images were used as the "primary" calibrators in each field. Many of these long exposures were taken on non-photometric nights with good transparency, and calibrated with short observations of the same positions taken on subsequent photometric nights.

After the "primary" calibration had been performed on each photographic field using these data, a list of very red stars was compiled for each POSSII/UKST field. A sample of these stars was then re-observed in each field with the aim of clarifying the colour term present in the IIIaF/IVN to ri^C_{Pal} transformations. All the stars in these "secondary" CCD images (as well as the very red one of interest) were photometered and included in our database of CCD photometry. The red stars which were observed, were not in general at the photographic plate limits and so many of these exposures were not

[4] This was true with only one notable exception. Photometry was taken on one night (28JAN92) after the eruption of Mt Pinatubo had injected a considerable quantity of dust into the atmosphere. The extinction coefficients on this night were found to be about *three times* the normal values ($K_r = 0.250$, $K_i = 0.220$).

as deep as those taken as primary calibrators. The end result is a large database of CCD photometry with r^C_{Pal}, i^C_{Pal} and $(r-i)^C_{Pal}$ for several hundred stars in each POSS II field. In total 150 positions were observed with CCD11 (FOV=$6.35' \times 6.35'$), altogether containing over 6600 stars.

Section 2.3 - Plate Material, Scanning and Calibration.

The photographic plate material used in this study was acquired as part of the northern and southern all-sky surveys being carried out by Palomar Observatory and the United Kingdom Schmidt Telescope (UKST) Unit. Both use 48″-aperture Schmidt telescopes of almost identical design – the UKST was built as a modified copy of the Oschin Telescope in order to duplicate the original Palomar Sky Survey in the southern sky. The optical and mechanical improvements made to the original 48″ design by the UKST, along with improvements in photographic emulsion technology, allowed the UKST's southern survey to produce plate material of a quality far superior to that of the original Palomar Survey. In 1985 an achromatic corrector plate was installed in the Oschin Telescope (the original corrector produced significant image deterioration for $\lambda \gtrsim 6500$Å) of the same design as that in the UKST (Wynne 1981), and a second epoch of the Palomar Sky Survey was begun (Reid *et al.* 1991).

For this study eleven fields were chosen in four, more-or-less evenly spaced ranges of right ascension.[5] Where possible the fields were chosen to be at high galactic lattitude ($b^{II} > 45°$) and to already have plate material in hand. The complete list of fields chosen and plates eventually used is given in Table 2.3. Fields 829, 831, 832, 868, 889, 890 and 891 all lie on the celestial equator and are accessible from both Palomar and the UKST and so plates were acquired from both sources for these fields. Though both the Northern and Southern Surveys take IIIaJ, IIIaF and IVN plates only IIIaF and IVN plates were used in this study. As noted above (§2.1), the stars we are concentrating on have extremely red colours making observations in the the blue IIIaJ passband of little use. Table 2.3 shows the different cut-on filters used by the Palomar and UKST surveys. For the IVN emulsions these filters are essentially identical – UKST and POSSII IVN photometry can be regarded as being on essentially the same photometric system. The same is not true of the IIIaF emulsions – the OG590, RG610 and RG630 filters cut-on at $\approx$ 5900Å, 6100Å and 6300Å, respectively.

Each 48″-Schmidt plate is 356×356mm (or 14″×14″) in size, which corresponds to a 6.6°×6.6° area on the sky. Unfortunately not all of this exposed plate area is unvignetted – Figure 2.3 shows the vignetting function of the UKST (Tritton 1983), which should be

[5] This choice was motivated by a desire to carry out a parallax programme on stars in the chosen fields - fields spaced 12 hours apart can be observed at large parallax factors on both the morning and evening of the same night.

identical for the Oschin Telescope. The plates are essentially uniformly exposed out to a radius (measured from the plate centre) of 3° and at larger radii become progressively less sensitive. At the largest radii present on the plates (i.e., in the corners) the vignetting corresponds to a magnitude difference of $\approx$ 0.25 mag.Some early UKST plates also suffer from a differential desensitisation (which is largest in the plate corners) due to the presence of moist air trapped between the filter and the plate. Later in the Southern Survey (and throughout POSS II) all plates were flushed with dry nitrogen as they were being taken, eliminating this problem. However, even when this effect is present (which is only likely in a few UKST plates in our plate set) the difference in the apparent vignetting function due to it is unlikely to be greater than 0.04 mag. (Tritton 1983). To ensure our plates are photometrically uniform, we only use the region scanned on each plate within 3° of the plate centre. Figure 2.4 shows the "footprints" of the regions of the plates used in our survey in both equatorial and galactic co-ordinates.

2.3.1 - The COSMOS Scanning Machine.

All the plates listed in Table 2.3 were scanned on the Co-Ordinates, Sizes, Magnitudes and Orientation Scanning machine (COSMOS) machine of the Royal Observatory, Edinburgh. For a complete description of the COSMOS machine and its scanning software see Beard *et al.* (1990) and M^{c}Gillivray & Stobie (1984). A brief summary follows.

COSMOS is a high-speed scanning machine which illuminates the scanned plate with a "flying-spot" produced by a cathode-ray tube. The photographic densities measured are converted into intensities using the 16 calibration spots exposed onto each plate as it is taken (Reid *et al.* 1991). Unfortunately at the time these plates were scanned the precise calibration of these spots appropriate for the Palomar plates used in our study was not available. So a table was arbitrarily chosen for a UKST plate and used instead. This produces non-linearities in the photographic magnitude scale. However, as a CCD-photographic calibration curve was measured for each plate in any case, this does not represent a serious problem.

As mentioned above each 48″-Schmidt plate is 356×356mm in size. Unfortunately, COSMOS can only scan a physical area of 286.7 × 286.7mm – which corresponds to a region 5.35°×5.35°. Figure 2.5(a) shows the geometry of the scanned plate area relative to the entire photographic plate. A point is plotted in the scanned area for each of the 57968 objects detected by COSMOS in this field. The upper left-hand corner of the 16-spot calibration square can be seen extending into the scanned region at the lower right-hand

corner of the scanned region. Figure 2.5(b) & (c) show the final geometries available to our survey (after selecting only objects within 3° of the plate centre) for both a POSSII plate and a UKST plate.

The scanned plate is rendered into a raster grid of 8960×8960 32μm pixels, from which objects are detected by applying a threshold of a few percent above the local sky level (the values used for each plate are listed in Table 2.4). The sky background is estimated by a preliminary fast-scan of the plate which breaks the plate into a 64×64 grid and measures the mode of the transmission value in each box. This 'sky-map' is filtered to remove anomalous values (produced, for example, by bright stars). The local sky background is evaluated for each object by interpolating between the values in this coarse 'sky-map'. The algorithm of Thanisch *et al.* (1984) is used to connect pixels above the sky-threshold into discrete objects, following which a set of parameters is determined for each detected object. It is these parameters (rather than the raw scanned image which is prohibitively large) which are saved and distributed to COSMOS users.

2.3.2 - The COSMOS Data.

For our purposes the most important of the various parameters which COSMOS produces are; the position (both XY co-ordinates within the plate, and Right Ascension (α_{1950}) and Declination (δ_{1950}) determined by fitting a plate model to FK4 positions for bright stars present on the plate); the area of the image (measured in pixels brighter than the sky threshold); the peak intensity of the image; the local sky intensity; and most importantly the COSMOS estimated magnitude (estimated by summing the sky-subtracted intensities for all pixels above the sky threshold level). The absolute (α,δ) determined by COSMOS are accurate to better than 1.5″ – which is more than sufficient for matching objects detected on the various plates used by us.

The plates were also passed through the COSMOS group's "deblending" software (which is described fully in Beard *et al.* (1990)). This code was developed for use in studies at low galactic lattitudes ($|b| < 30°$), where source confusion is a large problem. After the initial thresholding and determination of image parameters, it makes a second pass on the "parent" images. Each "parent" image is re-thresholded at 8 higher levels – the resulting profile is examined to determine whether it is a single image or actually a blend of several "daughter" images. If it determines that an image is blended it assigns pixels (and part pixels using a Gaussian model) to each daughter, and then redetermines all the image

parameters originally determined for the parent image – though the image parameters determined for each daughter have a significantly increased uncertainty.

Most (i.e., > 95%) of the images which COSMOS detects on a given plate are real astronomical objects – however there is a certain amount of contamination of the data set by spurious images. Dust particles and emulsion defects produce small isolated 'images' which can look like stars, but which it turns out are fairly easy to discriminate from real objects by looking at their image parameters (specifically the ratio of their image size and magnitude – as stars have mostly the same point-spread function they fall onto an isolated locus in the size-magnitude plane. Defects and dust have extremely high densities, but are very small and will not lie on this locus – this will be discussed in depth in §2.3.3). More problematic are the large, bright images produced by satellite trails, aeroplane lights, bright stars (and the haloes around them), and bright galaxies – these all tend to be resolved by COSMOS into a "swarm" of smaller images, of which Figure 2.6 shows some typical examples. Most of these contaminating images can be eliminated much as plate defects or dust can, but out of the large number of such images produced, a few will mimic the properties of stars.

For our study in which fields were chosen at high galactic lattitude, source confusion is not a significant problem – the density of stars at $m_V \approx 21$ and $|b| = 30°$ is only $2.8\,\mathrm{arcmin}^{-2}$ (Bahcall & Soneira 1980). We would then only expect $\lesssim 1\%$ of stars to be confused such that they may not be resolved by COSMOS without the use of deblending software (i.e., closer than 3″). In fact we find that for $|b| \sim 50°$, 3-5% of our objects are decomposed into daughter images by COSMOS, however this is not an accurate reflection of the level of source confusion. As described above COSMOS tends to resolve bright, extended objects into discrete components – this is further exascerbated by the deblending software which can "go to town" on a bright star or galaxy and resolve it into hundreds of components. For this reason regions around bright stars and galaxies are excluded from our survey (as we describe in §2.3.3) - when these regions are removed the number of images deblended by COSMOS is $\sim 1 - 2\%$ of the total number of images. As the number of images deblended is so small, it makes little difference one way or the other whether they are included - we have chosen to include them,[6] and use only undeblended and daughter images in our survey.

[6] On the off chance that we find that elusive, world-beating brown dwarf candidate among them.

2.3.3 - COSMOS Calibration

The data processing of the raw COSMOS scans into the final photometric catalogue can be broken into two basic phases; the "calibration" phase and the "cleaning and matching" phase. The calibration of the plates is an essentially straight-forward process. Objects with CCD photometry are matched to objects on the plate, and the COSMOS magnitudes (denoted COSMAGs) are plotted against the CCD r^C_{Pal} and i^C_{Pal} magnitudes. A function is fitted to the resulting locus of points and this function is used to convert all the COSMAGs to r^P_{Pal}/i^P_{Pal} magnitudes (the 'P' is used to denote photographic measures of magnitudes on the r^C_{Pal}/i^C_{Pal} system). To reduce the effects of colour terms only stars in the range $0.0 < (r-i)^C_{Pal} < 1.5$ are used in deriving this transformation.

The CCD objects are 'matched' with the plate objects by plotting all the objects in each CCD field, along with the objects from a $10' \times 10'$ subset of a plate (centred at the CCD frames field centre) on a termial. A few obvious matches are selected by cursor, and a preliminary transformation between the two systems (CCD and plate) is calculated. This preliminary transformation is then used to search for objects on the plate within $4''$ of each CCD object. This set of objects is then used to calculate a final transformation (outlier points are iteratively rejected until the rms of the transformations residuals drops below $0.5''$). The right ascension and declination of each object are then calculated using the absolute position transformation provided by COSMOS.

With these absolute positions known, each plate is searched for objects within $3''$ of each CCD object (if more than one object is detected the nearest neighbour is used), and these matches are used to derive the plate-to-CCD magnitude transformation. Examples of this transformation for both IIIaF and IVN plates are shown in Figure 2.7 - a cubic spline is fitted as the calibrating function, and the residuals about this fitted function are also shown. Cubic splines were chosen (after experimentation with polynomials) because they are best able to represent the sharp 'kink' which occurs in the magnitude transformation a few magnitudes above the plate limit. Usually only one or two knots were used, and these knots were most often placed near the 'kink'. The 'kink' is present because the photographic emulsion is saturated by stellar images several magnitudes above the plate limit. Below this saturation point the relationship between the plate and CCD magnitudes is linear, with a slope of more-or-less one. Above the saturation point the plate is still able to estimate magnitudes – but does so by measuring the *area* of the saturated image, rather than the intensity of the pixels within it – so the relationship between plate and CCD magnitudes is still linear but with a different slope.

Unfortunately working with saturated, or partly saturated, images does introduce some difficulties. The most severe is that when saturated objects are photometered relative to a local sky which varies, their photometry also varies (which does not happen for unsaturated images). This effect is observed to a greater or lesser degree in most of our plates, as variations in the sky background level are present in almost all of our plates. Such sky background variations are produced not only by the vignetting of the plate edges (which we can easily deal with by only using the central 3° of the plate), but also by zodical light, uneven emulsions and uneven hypering and developing. The problems encountered in trying to produce uniform IVN plates are particularly severe, and 10-20% variations in the sky level across these plates are not uncommon. The effects of such sky level variations can be clearly seen when the plate-CCD calibrations curves are plotted separately for different regions of the plates. Figure 2.8 shows some examples; a plate with almost no variations, a plate with some variations (at a level we are able to accept), and a plate with large variations which was rejected from our survey. It should be noted that there does not seem to be any correlation between the grades given to plates by the UKSRC and POSS II surveys, and their level of sky variation. This is not surprising as (except for cases of extremely high fog levels) plates are graded mostly on image quality and/or seeing.

Table 2.5 shows the mean and standard deviation of the residuals about the calibration spline fits for each plate as a function of magnitude. Two points should be especially noted from this table; first the IVN and IIIaF plates can be seen to be complete to $i^C_{Pal} \approx 18$ and $r^C_{Pal} \approx 20.5$ respectively, though there are variations of up to 0.5 magnitudes in this value from plate to plate; secondly, the approximate uncertainty in the photometry at these limits are 0.2 and 0.3 magnitudes respectively – though again these values vary by up to 0.05 magnitudes from plate to plate. For both IVN and IIIaF plates the uncertainties decrease with magnitude, though the photographic photometry never becomes much more precise than about 0.05 magnitudes due to the field effects discussed above.

2.3.4 - Processing of the Calibrated Plates.

Once the individual plates have been trimmed to remove objects more than 3° from the plate centre (which results in each plate covering an area of $\approx$ 25.3 square degrees), filtered to remove the parent images of deblended objects, and calibrated, they are merged together. A single IVN plate is chosen as the *master* plate for each field, and all other plates (called *slave* plates) are searched for matching objects within 4″ of each object on

the master plate. They resulting set of master plate objects and slave plate matches is called a *catalogue*.

Regions around the bright stars ($\lesssim 5-8$ mag.) present in each of the catalogues are then removed. In practice all points in the merged catalogue around the brightest hundred objects in each field were examined by hand. Haloes and diffraction spikes around bright stars, and bright galaxies then become clearly visible and are interactively removed from the catalogue – typically a region a few arcminutes on a side is "zapped." As we are interested in stars with typical distances of $\lesssim$ 200pc it introduces no significant sampling bias to arbitrarily remove regions around bright extra-galactic objects. Almost all of the bright stars deleted are either giants or bright dwarfs at distances > 200pc, and so no bias is introduced into our sample by deleting them, or regions around them.

We then calculate for each image a star/galaxy separation parameter. As was mentioned earlier, stars (which are unresolved by our plates) all have the same point-spread function and can be expected to have a fixed relationship between their image brightness and their image size. The same is not true of galaxies, which can be of more or less arbitrary shape and surface brightness. It is possible then to define quantities calculated using each object's COSMOS parameters which can be used to separate stars from galaxies. Such parameters are discussed in detail in Collins *et al.* (1989) and Picard (1991). We have chosen to calculate the "S-parameter" for all the objects detected in our survey. The S-parameter is defined as follows (Collins *et al.* 1989);

$$S\text{-parameter} = \frac{area}{\log(ipeak + isky) - \log(isky)(1 + cut/100)} \tag{2.3}$$

where,

$area$ = image area in pixels

$ipeak$ = peak intensity of image

$isky$ = local sky intensity

cut = detection threshold in per-cent above local sky

The S-parameter, then, measures how 'centrally concentrated' an object is – typical plots of the S-parameter as a function of r^P_{Pal} and i^P_{Pal} are shown in Figure 2.9. Stars form a clearly delineated ridge in such a diagram, with the galaxies forming a vague 'swarm' of points above that ridge – they have areas larger than stars, for a given magnitude, and so have larger S-parameters. Objects lying below the ridge are usually plate defects or dust

particles, which are extremely dark (and so register to COSMOS as very bright), but have very small area – so their S-parameters are smaller than those of stars.

It will be noticed that at fainter magnitudes the separation of stars and galaxies becomes more difficult as the star-ridge becomes broader. As fewer pixels with poorer signal-to-noise ratio are joined together to make an image, determining 'shape' becomes a less precise excercise. Picard (1991) therefore, introduced a "flattened" version of this parameter (called the ϕ-parameter) which makes the value of the S-parameter independent of magnitude.

$$\phi\text{-parameter} = 100 \times \frac{(S\text{-parameter} - M_{ridge})}{W_{ridge}} \tag{2.4}$$

Put simply, it subtracts off the curve of the star-ridge (M_{ridge}), and then normalises by the width of the star-ridge (W_{ridge} – see Picard 1991 for the details of this procedure). Figure 2.10 shows the ϕ-parameter plot for the same data as Figure 2.9. The ϕ-parameter was also calculated for all objects in our survey.

2.3.5 - Photographic $r_{Pal} - i_{Pal}$ Colours

It is then a straight-forward proceedure to calculate $r^P_{Pal} - i^P_{Pal}$. The plates used to construct the final catalogues in each field are listed in Table 2.4. Lastly, it is necessary to ensure that our $r^P_{Pal} - i^P_{Pal}$ photometry is on the same colour system as our CCD photometry. Figure 2.11 shows a plot of $(r - i)^C_{Pal}$ versus $r^P_{Pal} - i^P_{Pal}$ for the Palomar IVN+RG9/IIIaF+RG610 material in Fields 213, 262, 263 and 513 (along with a second-order polynomial fit). The plot indicates that a sizable colour term is present, which is repeatable for different plates in different fields. Such a colour term clearly represents the difference in effective wavelength (λ_{eff}) between the IIIaF+RG610 combination and the CCD11+Gunn r combination. Moreover, that difference is most pronounced for the latest type stars.

As noted in §2.3 plates taken by the UKST and denoted "R" use a IIIaF+RG630 combination, while those denoted "OR" use a IIIaF+OG590 combination. Each of these have slightly different λ_{eff} than the IIIaF+RG610 combination, however a plot similar to that in Figure 2.10 for these plates (see Figures 2.12 and 2.13 – the polynomial fit to the data in Figure 2.11 is superimposed on both) shows no evidence for a significantly different colour term. We therefore apply the same transformation as that derived for the Palomar material to our UKST material. This transformation was applied to produce a colour which we denote $(r - i)^P_{Pal}$, and which we differentiate from the raw $r^P_{Pal} - i^P_{Pal}$

colour which has *not* been colour-corrected; $(r-i)^P_{Pal}$ is the final colour quoted for objects in our photographic catalogue and is on a photometric system essentially identical to that of our CCD photometry. The plates actually used for calculating this colour in each field are indicated in Table 2.4.

Section 2.4 - Catalogue Evaluation

2.4.1 - Completeness

A fundamental parameter of any catalogue is the level to which it is complete. To examine this we have plotted in Figure 2.14 the differential number counts as a function of magnitude for each field. Also shown are some model predictions for the expected counts of both galaxies and stars – star counts were produced by a Galactic model code due to I.N.Reid (Reid & Majewski 1992), while estimates of the galaxy counts are based on work by numerous authors referenced in Jones *et al.* (1991) and Metcalfe *et al.* (1991). Reid's Galactic model uses four stellar components; a standard old (or "thin") disk population representing stars older than 2 Gyrs with scaleheight 325pc; an intermediate disk population of stars younger than 2 Gyrs with a 250pc scaleheight; an extended (or "thick") disk with a scaleheight of 1kpc; and a halo component represented by a globular cluster luminosity function and colour-magnitude relations in a de Vaucouleur's spheroid with a core radius of 2.6kpc and axial ratio of 0.9. As an examination of Figure 2.14 shows, the Reid model reproduces the observed number counts well for magnitudes ($r^P_{Pal} < 18$, $i^P_{Pal} < 17$) at which the number density of galaxies is small.

Galaxy counts have been produced by numerous authors – we chose to use counts by Jones *et al.* (1991) and Metcalfe *et al.* (1991) who have published both CCD and photographic counts in the R-band and photographic colours in the I-band. While most investigators agree on the slope of the differential galaxy counts in the range $r^P_{Pal} \sim 16 - 21$, the *normalisation* of these counts show little agreement – differences in the normalisation of factors as large as 2 between different fields are common (Metcalfe *et al.* 1991). We, therefore, chose to fit a generalised form to the counts of Jones *et al.* and Metcalfe *et al.*, and then normalise this function to the observed number counts in the range $r^P_{Pal} = 18 - 19.5$. The functional form used is given by;

$$\log(\text{Number Counts}/\square^\circ/0.2 \text{ mag.}) = (0.407 \pm 0.002) \times r^P_{Pal} - (5.6 \pm 0.7). \qquad (2.5)$$

The total model prediction and the normalisation chosen for each field are shown in Figure 2.14 – note that there are definite correlations between the normalisations of adjacent fields, presumably due to the large scale ($\gtrsim 6^\circ$) variations in galaxy counts present over the sky (Picard 1991).

In the absence of any detailed galaxy counts in the I-band, we derive a functional form for the I-band galaxy counts by simply applying the mean colour ($r_F - I \approx 1.0$) observed in two UKST fields by Jones *et al.* 1991, to the form adopted for r^P_{Pal} above, i.e.,

$$\log(\text{Number Counts}/\square^\circ/0.2\text{ mag.}) = (0.407 \pm 0.002) \times i^P_{Pal} - (5.2 \pm 0.7). \qquad (2.6)$$

In each field a normalisation identical to that derived for the r^P_{Pal} counts was used, and the resulting model predictions are shown in Figure 2.14.

Clearly the model predictions provide only an approximate estimate of the number counts one would expect near the plate limits. First, they rely on the completeness of our sample for *galaxies* which dominate the source counts at faint magnitudes. Galaxies have low surface brightness (for a given total magnitude) and are therefore more difficult to detect than stars – one would expect that at a given magnitude our survey is more complete for stars than for galaxies. So any estimate of completness derived using galaxies would be a lower limit to the level for stars. Second, we are forced to rely on a normalisation of our galaxy count model using our galaxy count data – and while our plates should be almost 100% complete for magnitudes as bright as $r^P_{Pal} = 18 - 19.5$ it would be preferable to avoid this. Lastly, the paucity of I-band galaxy counts forces us to use a rather crude technique to evaluate the predicted i^P_{Pal} galaxy counts. Nevertheless, the plots shown in Figure 2.14 are a significantly more useful tool for evaluating our survey than nothing at all. We find that most of our fields have at least one IIIaF plate which is at least 75% complete to $r^P_{Pal} = 20.5$, and one IVN plate which is at least 75% complete to $i^P_{Pal} = 18.0$. We have adopted these as our nominal survey limits – in those fields where our plates are *not* this deep we have adopted a limiting magnitude as the magnitude at which the observed counts fall to 75% of the predicted counts. The limits adopted are shown in Table 2.8. In general then, our survey *may* be incomplete by up to $\sim 25\%$ at the quoted limits, though it is most likely more complete for stars at this magnitude than for galaxies.

2.4.2 - Inter-plate Comparisons

As noted in §2.3.3 we can gain some idea of the uncertainties in our photometry by looking at the residuals about our calibration fits. Unfortunately our CCD calibration samples are not uniformly selected – a better idea of the quality of our data can be gained by looking at the overlap regions of our catalogue, both where we have two or more of the same plate in a field, and in the regions where different fields overlap.

Figures 2.15 and 2.16 show plots of differences between magnitudes (Δi^P_{Pal} and Δr^P_{Pal} respectively) on different plates in the same fields as a function of magnitude. In Fig 2.14 only comparisons of the IIIaF plates used in the construction of our final catalogues are shown – unfortunately only one IVN plate pair was used in our final catalogues (I11526/I7377), so we have plotted the comparisons of two other plate pairs in order to have more than one example.

A number of points should be noted from these diagrams; first it can be seen that there are systematic differences between plates in the same fields – these are due to the difficulty in forcing a cubic-spline fit to reproduce identical functional forms for separate calibrations, even when the same CCD calibratiuon data are being used. Ideally using diagrams like Figures 2.13 & 2.14 such differences could be removed. Unfortunately we have no *a priori* reason for assuming one plate's calibration is any more accurate than another's. In such a situation we are forced to leave the data untouched, and to merely be aware of the possible systematic uncertainties added by the calibration process. Table 2.6 shows the mean and standard deviations in Δi^P_{Pal} and Δr^P_{Pal} when binned as a function of magnitude. We can see that (except for the plate pair I11499/N3601) the systematic errors in the zero-point are always $\lesssim 0.1$ mag. — comparible to the level of the random photometric uncertainties. Moreover, the zero-point errors are always *worst* at the brightest magnitudes. Within a few magnitudes of the plate limits (where most of the interesting objects in a magnitude limited sample of a more-or-less uniform stellar space density will be found) the systematic zero-point errors are a small fraction of the random photometric uncertainties. We therefore do not regard calibration errors as a serious source of uncertainty in our catalogue.

Secondly, we can use Figures 2.13 & 2.14 and Table 2.6 to examine the size of the photometric uncertainties in our catalogue. Of most interest are the photometric uncertainties at our survey limits. The IVN plate-pairs show a standard deviation in Δi^P_{Pal} of 0.3 mag. at $i^P_{Pal} = 18$, which corresponds to an uncertainty in a *single* plate of $0.3/\sqrt{2} = 0.21$ mag. For IIIaF plates, however, this quantity is less striaghtforward to measure. An examination of Figure 2.14 shows that the region of the Δr^P_{Pal}-vs-r^P_{Pal} plane excluded by the completeness limit of the IIIaF plates cuts right through the r^P_{Pal} range we wish to examine. We correct for this by taking the data from each panel of Figure 2.14 in the range $r^P_{Pal} > 18$ and $\Delta r^P_{Pal} > 0.0$. We then 'duplicate' these data for $\Delta r^P_{Pal} < 0.0$ and calculate the standard deviation in Δr^P_{Pal} for these data (obviously the mean of these data will be zero and contains no information). The standard deviations so produced are shown in the last three columns

of Table 2.6. (As a check the standard deviation produced by this method was compared with the standard deviation produced in the normal way for $18 < r^P_{Pal} < 19$ — the results were the same to within 0.01 magnitudes). For the IIIaF plate pairs we find a standard deviation in Δi^P_{Pal} of 0.35 mag. at $r^P_{Pal} = 20.5$, which corresponds to an uncertainty in a *single* plate of $0.35/\sqrt{2} = 0.25$ mag. This means that (adding uncertainties in quadrature) we find a maximum random uncertainty at the plate limits of 0.33 magnitudes for a single $(r-i)^P_{Pal}$ measurement.

We can also examine the overlap regions between plates from different fields – similar plots to Figures 2.15 & 2.16 are shown for these regions in Figures 2.17 & 2.18, and a table similar to Table 2.6 showing the means and standard deviations of the differences binned as a function of magnitude is shown in Table 2.7. The first point to note that (as would be expected) the standard deviations about the mean differences in Table 2.7 show a similar variation with magnitude to that of Table 2.6, though again there are variations from plate to plate. Secondly, it can again be seen that the mean differences between plates show larger systematic offsets at brighter magnitudes (up to 0.2 – 0.3 magnitudes), than at the plate limits where with a few exceptions the mean offsets are less than 0.1 magnitudes. The most notable of these exceptions are the plate pairs FLD889:N3362–FLD890:N3647, FLD262:F2315–FLD213:F2978 and FLD262:F2315–FLD263:F2957, which show significantly larger deviations than all the other plate pairs, *particularly* at the plate limits. Specifically they show offsets of 0.14, 0.18 and 0.21 magnitudes respectively. These offsets are far too large to attribute errors in the CCD calibration, and must represent the effects of a differential de-sensitisation of the plate material. Most of the CCD calibration data was taken within $\sim 2°$ of the plate centre, while the overlap regions lie on the plate edges $\sim 3°$ from the plate centre, and we therefore attribute these offsets to de-sensitisation at the plate edges.

Given the variation in our plate quality, we have attempted to divide our fields into a number of quality ranges. We define a field (i.e., the *complete* catalogue data from that field including the i^P_{Pal} and $(r-i)^P_{Pal}$ data) as being of A-grade if; we can see no evidence for systematic offsets in the photometric zero-point at the plate limits greater than 0.1 magnitudes; the completeness limit in $i^P_{Pal} \geq 18$; and, the completeness limit in $r^P_{Pal} \geq 20.5$. Fields which violate these criteria are graded B-grade. In particular, Field 262 was graded "B" because its IIIaF plate (F2315) shows a systematic offset with both the Field 213 and Field 263 IIIaF plates, which show no offset relative to each other. Field 889 was graded "B" because its IVN plate (N3362) shows an offset with the Field 890 IVN

plate, which shows no offset with respect to the Field 891 IVN plate. Both these fields also happened to be graded "B" because their plates violated the completeness limits.

2.4.3 - Completeness as a Function of Colour.

Lastly we examine the question of completeness in R–I colour — specifically, given the r^P_{Pal} and i^P_{Pal} limits derived in §2.4.1 and the $(r^P_{Pal} - i^P_{Pal})$ to $(r-i)^P_{Pal}$ transformation derived in §2.3.4, to what level is our survey complete in $(r-i)^P_{Pal}$? Figure 2.19 shows the i^P_{Pal} limits imposed by the colour-term as a function of $(r-i)^P_{Pal}$ for several assumed r^P_{Pal} limits. The figure clearly shows how the volume sampled by our survey becomes increasingly smaller for larger and larger R–I colours, due to the presence of the photographic-to-CCD colour term discussed earlier. This dramatically reinforces the importance of understanding the colour terms present in a survey for very red stars – neglecting the colour term in our case would lead to us overestimate the volume we had sampled by a factor of ≈ 4!

2.4.4 - Summary.

To summarise the results of the preceeding sections; we have constructed catalogues from plates in eleven 25.3 square degrees fields in i^P_{Pal}, r^P_{Pal} and $(r-i)^P_{Pal}$ passbands which are similar to the standard I_C, R_C and $(R–I)_C$ passbands. Our catalogues are complete to $i^P_{Pal} \approx 18.0$ and $r^P_{Pal} \approx 20.5$. At those limits the random uncertainties in our photometry are $\sigma(i^P_{Pal}) \approx 0.21$, $\sigma(r^P_{Pal}) \approx 0.25$ leading to maximum photometric uncertainties in our colour estimates of $\sigma((r-i)^P_{Pal}) \approx 0.33$. Systematic uncertainties are seen in some of our "B" grade data - these are $\lesssim 0.1$ magnitudes at the plate limits. Several fields show larger systematic deviations than this at brighter magnitudes ($i^P_{Pal} \lesssim 15$ and $r^P_{Pal} \lesssim 16$), however these are less important than systematic effects at the plate limits, both because at these magnitudes random uncertainties are so small ($\lesssim 0.1$ magnitudes) and because in any magnitude limited survey, most of the objects of interest will be found at the faintest magnitudes. Each individual plate covers an area of ≈ 25.3 square degrees. The $(r-i)^P_{Pal}$ catalogues are complete where the various IIIaF and IVN plates overlap ($\approx 22 - 27$ square degrees per field), giving a total area surveyed in $(r-i)^P_{Pal}$ of 269.79 square degrees.

Section 2.5 - The Stellar Luminosity Function.

In the sections which follow we use the photographic catalogues discussed in the preceeding section to construct a luminosity function for M-dwarfs more luminous than $M_{Bol} \sim 12$, or equivalently, earlier than spectral type M6. Because of the saturation of the very strong TiO bands which dominate the stellar emission in all optical passbands, optical colours provide almost no information on less luminous stars. Leggett & Hawkins (1988) have noted that the R-I colours of very late stars appear to saturate at R–I≈2.5, while their I–J and I–K colours continue to increase with decreasing temperature. Monet *et al.* (1992, c.f. Figure10) found that the tip of the stellar main sequence appears to completely reverse in an M_V:V–I diagram at $M_V \approx 18.5$ or $M_I \approx 14$. Tinney (1992 – Paper III), however finds no evidence for such a reversal in an M_I:I–K diagram, indicating that optical-infrared colours do not suffer from saturation for the latest stars.

We have therefore divided our luminosity function study into two parts; in this paper we derive the stellar luminosity function for $M_{Bol} = 8 - 12.5$ using the photographic plate catalogues we have constructed (we do in fact use our data to construct a luminosity function for fainter magnitudes, but do so only in order to illustrate how systematic errors make such an excercise futile.); we have also used this catalogue to construct complete samples of VLM candidates for study in the infrared. The results of these infrared observations, and the improved luminosity function for stars with $M_{Bol} > 12.5$ – together with mass functions derived from both the photographic (i.e., from this paper) and infrared data – will be presented in Paper IV.

2.5.1 - Definitions.

We define the stellar luminosity function (LF) Φ as follows,

$$\Phi(M_n)\, dM_n = \text{number of stars per cubic parsec in a bin of width } dM_n \text{ centred at } M_n, \tag{2.7}$$

where M_n is a given absolute magnitude, e.g., M_V, M_I, or M_{Bol}. In the discussion which follows we always refer to LFs measured in terms of M_{Bol}. Not only is M_{Bol} the most physically meaningful absolute magnitude for a star, but it is the magnitude most immediately related to its mass – and it is ultimately the derivation of a mass function from an observed LF which is the aim of this study.

We measure the LF then by constructing a volume-limited sample of stars and counting how many stars there are in each luminosity bin. The number of stars in a given

bin of width dM_{Bol} centered on M_{Bol} is then $\Phi(M_{Bol})$. In practice this is difficult to do as the volume limits imposed by a magnitude-limited sample (the type of sample always observed) are almost always dependent on M_{Bol}. If the distance cut-off is chosen such that the sample is 100% complete for the least luminous objects in the sample, useful observations of more luminous objects must be thrown away.

An alternative technique is to construct a complete magnitude-limited sample (in our case, the plate catalogues from each field with their respective $[r^P_{Pal}]_{Lim}$ and $[i^P_{Pal}]_{Lim}$ limits), and to estimate the maximum distance at which each star in this sample could be seen. This distance, and the solid angle covered by the sample, allow a 'maximum volume' (or V_{max}) to be calculated for each star, which is the largest volume of space over which that star could be detected. As was first proposed by Schmidt (1976) and shown by Felten (1976), the sum of the inverse of these V_{max} values in a given luminosity bin is an unbiased estimator of $\Phi(M_{Bol})\ dM_{Bol}$. The $1/Vmax$ technique (as this method of constructing a LF has become known) is essentially a method of allowing the distance limit of a 'distance-limited' sample to vary with luminosity. It allows more intrinsically bright objects to be counted in the sample, so that the maximum available information on the LF is extracted.

To estimate the LF then, we must know for each star; its luminosity (M_{Bol}) and the maximum distance at which it could be detected in our survey (d_{max}). In order to estimate these quantities we are forced to make the fundamental assumption that the stars we are examining lie on the main-sequence, and that M_{Bol}, $M_{i_{Pal}}$ and $M_{r_{Pal}}$ are all single valued functions of stellar colour. Specifically we assume that M_I (throughout this section we use interchangeably "I" and "i_{Pal}") and BC_I (the bolometric correction to i_{Pal} defined such that $M_{Bol} = M_I + BC_I$) are single valued functions of $(r-i)_{Pal}$. In practice, of course, there is both cosmic and observational scatter associated with these absolute magnitude estimates.

One limitation of the $1/V_{max}$ technique is that it assumes stars are uniformly distributed through space. In reality, stars in the solar neighbourhood are concentrated in the plane of the Galactic disk. However the effects of a space-density gradient can be allowed for by assuming a density law, and defining a generalised volume V_{gen} enclosed within a distance d,

$$V_{gen} = \Omega \int_0^d \frac{r^2 \rho\ dr}{\rho_0} \tag{2.8}$$

where Ω is the solid angle covered by the sample, ρ_0 is the local space density and r is a distance. We then make the assumption that the local density can be represented by an exponential disk of scale height h,

$$\frac{\rho}{\rho_0} = e^{-(z/h)}, \tag{2.9}$$

where z is a distance perdendicular to the Galactic plane. (The density changes due to the Galaxy's radial scale length are negligible over the distances we consider here are can be ignored.) In the case where observations are made at the Galactic pole this expression can be integrated by parts to give (Stobie *et al.* 1989),

$$\mathrm{V}_{gen} = \Omega\, h^3\, \{2 - (y^2 + 2y + 2)e^{-y}\}, \tag{2.10}$$

where $y = d/h$. For our samples, however, observations were made at arbitrary Galactic latitudes. In order to evaluate equation 2.8 for this case we note that at galactic latitude b, $z = r \sin b$. In which case,

$$\frac{\rho}{\rho_0} = e^{-\frac{r \sin b}{h}}. \tag{2.11}$$

We then make the assumption that our field of view is small enough that $\frac{\rho}{\rho_0}$ is constant for all points at a given r in the field of view. For the typical parameters of our samples (less than 6° accross at distances of a few hundred parsecs in a 350pc scale height disk) this leads to errors of at most a few percent. By a straightforward substitution we therefore derive,

$$\mathrm{V}_{gen} = \Omega\, \frac{h^3}{\sin^3 b}\{2 - (\xi^2 + 2\xi + 2)e^{-\xi}\}, \tag{2.12}$$

where $\xi = d \sin b/h$. We can then construct (by analogy with the $1/\mathrm{V}_{max}$ LF) an un-biased estimator for the local LF Φ_0 (we use the subscipt "0" to denote that the LF is a local value calculated for an assumed disk scale height) as the sum of the inverses of the maximum values of V_{gen} available to stars in a luminosity bin of width range $d\mathrm{M}_{Bol}$ centred at M_{Bol}. That is, for a star of given M_{Bol} (from which we derive d_{max}), the maximum generalised volume V_a is given by,

$$\mathrm{V}_a = \Omega \int_0^{d_{max}} \frac{r^2 \rho\, dr}{\rho_0} \tag{2.13}$$

which can be evaluated using equation 2.12 for $\xi = (d_{max} \sin b)/h$, and so that,

$$\Phi_0 = \sum \frac{1}{V_a}. \tag{2.14}$$

The variance in this estimator is

$$\mathrm{var}(\Phi_0) = \sum \frac{1}{V_a^2} \tag{2.15}$$

(Felten 1976) so that for mostly similar values of V_a the uncertainties on Φ_0 are essentially Poissonian.

2.5.2 - Adopted Colour-Magnitude Relations and Distance Limits.

Figures 2.20 and 2.21 show the M_I and BC_I relations (as a function of $(r-i)_{Pal}$) which we have adopted. Figure 2.20 was constructed using photometry on the Cousins RI system from the recent compilation of data on low mass stars by Leggett (1992) and triginometric parallaxes from the Yale Catalogue (also reported in Leggett (1992)). Only stars with an uncertainty in $M_I \leq 0.15$ were used to construct this diagram. Photometry on the $(R-I)_C$ system was converted to the $(r-i)_{Pal}$ system using equation 2.1, which is essentially a 1:1 transformation for $(r-i)_{Pal} \lesssim 2.2$. Several stars at $(r-i)_{Pal} > 2.2$ from Paper IV have also been included and were measured directly in the $(r-i)^C_{Pal}$ system as part of the CCD calibration descibed in §2.2. As was noted earlier, equation 2.1 can only be regarded as approximate for $(R-I)_C > 2.2$, however as the uncertainty introduced by its use is not greater than ± 0.07 mag.over the range $2.2 < (R-I)_C < 2.6$, and as data for $(R-I)_C > 2.2$ is only being included for illustrative purposes in any case, the use of the relation is not a difficulty. We derive the following polynomial fit for the colour-magnitude relation,

$$M_I = 5.56037 + 0.458615(r-i)_{Pal} + 1.32084(r-i)^2_{Pal}. \tag{2.16}$$

Figure 2.21 was constructed using the sources of $(R-I)_C$ and $(r-i)_{Pal}$ photometry described above and converted to $(r-i)_{Pal}$ where necessary in the same way. Measurements of BC_I for these objects come from Paper II, and take into account the increasing effects of infrared water vapour absorption which dominate the spectra of these stars. Again a polynomial has been fitted to the data to produce the following relation,

$$BC_I = 0.34842 + 0.708274(r-i)_{Pal} - 0.472678(r-i)^2_{Pal}. \tag{2.17}$$

The scatter about these two relations are (respectively) $\sigma(M_I) = 0.50$ and $\sigma(BC_I) = 0.25$. These scatters are over twice those seen in similar relations as a function of I–K (Paper II, Paper II) indicating how large an effect metallicity variations have on these optical

colours. We can combine equations 2.16 and 2.17 and take the derivative to estimate how the photographic uncertainties in $(r-i)_{Pal}$ map into uncertainties in M_{Bol}. We find that

$$\frac{dM_{Bol}}{d(r-i)_{Pal}} = 1.166892 + 1.69632(r-i)_{Pal}. \tag{2.18}$$

Over the colour range of interest we can see that the uncertainties in $(r-i)_{Pal}$ map into uncertainties in M_{Bol} as large, or larger than, the scatter present in the M_{Bol}:$(r-i)_{Pal}$ relation. Specifically for an uncertainty in $(r-i)_{Pal}$ of ± 0.25 mag.we have uncertainties in M_{Bol} of $\pm 0.7, \pm 1.1$ and ± 1.4 mag.at $(r-i)_{Pal} = 1.0, 2.0$ and 2.5 (respectively). Once again we can see how M_{Bol} estimates based on an optical colour become increasingly less precise for later stars.

It is a straightforward exercise to evaluate for an object of given $(r-i)_{Pal}$ colour and i_{Pal} magnitude the maximum distance d_{max} at which that object could be detected – d_{max} being set by the i_{Pal} and r_{Pal} limits of each field's catalogue (c.f. Table 2.8) and the $(r^P_{Pal} - i^P_{Pal})$ to $(r-i)^P_{Pal}$ colour term (§2.4.3). Figure 2.22 shows d_{max} limits for a range of i_{Pal} and r_{Pal} limits. Notice that the depth of the survey for very red stars is determined by the r_{Pal} limit rather than the i_{Pal} limit, due to the previously mentioned colour term. It is clear that for very red stars no gain is made by sampling beyond a certain depth in i_{Pal}. For $[r_{Pal}]_{lim} = 20.5$ this point is reached at $[i_{Pal}]_{lim} = 17.0$. We have therefore chosen $[i_{Pal}]_{lim} = 17.0$ as the sample limit imposed on all our catalogues for the purpose of constructing a LF. We also impose a lower magnitude limit ($i_{Pal} > 14.0$) so as to minimise the contamination of our sample by giants.

2.5.3 - Contamination of the Samples.

The possible sources of contamination are; a) galaxies, b) plate defects, bright star haloes, poorly deblended images, etc. and c) Galactic giants. We therefore discuss each in turn.

Galaxies are removed from our sample using the star galaxy separator derived in §2.3.3. We have the choice when selecting a ϕ-parameter limit of making it small, (in which case we ensure the sample is composed of only stars), at the risk of rejecting real stellar images, or we can make the ϕ-parameter limit large (and ensure our sample contains almost all the stars in the surveyed area), at the risk of including contaminating galaxies.

We have chosen to reject all objects from our sample which have $|\phi| > 500$. Such a choice errs significantly on the side of including all available stars, with some contamination

by galaxies. However, this contamination is small. At the magnitude levels at which we select objects, stars should be significantly more numerous – an examination of Figure 2.14 shows that the number density of stars in each field at $i_{Pal} = 17$ is 3-10 times the number density of galaxies.

We then select all objects with $(r - i)_{Pal} > 1.0$, since we are only interested in objects with the colours of M-dwarfs. This reduces the number of objects in each field classified as definite galaxies (i.e., $\phi > 500$) by a factors of $\sim 10-30$. This is because galaxies with extremely red colours at these magnitudes are relatively rare. The contamination of our sample by galaxies is then on the order of only 3.0-0.3% even before a galaxy separator is applied. Tests made on the complete samples (i.e., before the colour selection was made) have shown that a ϕ limit of 500 removes between 60-80% of all galaxies. This implies that the selection criteria adopted ensure the total contamination of our samples by galaxies is $\lesssim 1\%$.

The only other question to ask is whether our sample is differentially more contaminated by red galaxies than by blue ones? To examine this it is necessary to look at the relative distributions of the numbers of stars and galaxies in our samples, as a function of colour. By selecting all the objects with $\phi > 500$ from the 9 fields with the best star galaxy separation (Fields 831 and 891 were excluded), we make Figure 2.23(a), which shows the number of 'definite' galaxies (by 'definite' we mean that these objects are almost certainly galaxies) per 0.2 magnitude $(r - i)^P_{Pal}$ bin. By selecting all the objects with $|\phi| < 200$ in the same 9 fields we make Figure 2.23(b), which shows the number of 'definite' stars in the same fields. The number density of stars can be seen to be a much steeper function of colour than the number density of galaxies. In Figure 2.23(c) we show the data from Figure 2.23(b) on the same scale as Figure 2.23(a). The number of 'definite' stars dominates the number of 'definite' galaxies up to about $(r - i)^P_{Pal} \approx 2.2$. And as the number of galaxies actually passed into our sample is $\lesssim 33\%$ of the number of objects shown in Figure 2.23(b), we can see that contamination of our samples by non-stellar images is not significant out to $(r - i)^P_{Pal} \approx 2.2$. At redder colours however, the presence of non-stellar images needs to be considered as a source of systematic bias toward higher number counts, and so, spuriously larger space densities.

It has been assumed throughout the discussion above that all non-stellar images are galaxies. In fact this is not necessarily true. Apparently non-stellar images can also be produced by plate defects and the haloes around bright stars. Most of these images are either rejected by our star-galaxy separation criteria, or removed by the 'zapping' of regions

around bright stars. However a small number of defects will appear to have the ϕ-parameter of a star and be passed into our sample. A further source of confusion is that apparently red stars can be produced when the deblending algorithm fails to separate images on the IVN plate which are deblended on a IIIaF plate. An ellipticity cut was therefore also used on the samples – all objects with $1-b/a > 0.35$ were rejected, where b and a are the minor and major axes for an ellipse fitted to the COSMOS isophotes of each image. This particular value of the cut-off was chosen after an examination by hand of the data for samples of objects in several fields. By superimposing the ellipses determined by COSMOS for all objects within 1 arcminute of each object, it becomes a simple exercise to select images which suffer from deblending problems and objects 'produced' by the chance superposition of plate defects which are usually highly elliptical and oriented in arbitrary directions. To test the reliability of this criteria, the reddest 200 objects detected in 4 randomly selected fields (Fields 262, 832, 889 and 513) were all examined by this super-position technique. Objects were classified as being 'stellar','uncertain', or 'dud'. The results of this excercise are shown in Table 2.9. We find that the $1-b/a$ cutoff removes $\sim 80\%$ of 'dud' images and $\sim 50\%$ of 'uncertain' images.

Table 2.9 also allows us to estimate the degree of contamination of our sample by star-like non-stellar images (i.e., as opposed to galaxy-like images rejected by the star-galaxy separator). We see that $\sim 3\%$ of spurious images (both 'dud' and 'uncertain') are left in the sample by the selection criteria. Again, this is not significant, except possibly at very red $(r-i)_{Pal}$ colours where the number of stars in the sample is small. In fact, it would be expected that the number of spurious star-like images would be more-or-less independent of colour as plate defects should have random 'magnitudes', and the matching of deblended and undeblended objects should produce arbitrary colours. In this case the results shown in Table 2.9 should be interpreted as implying that there are ~ 7 spurious star-like images per magnitude of $(r-i)_{Pal}$ per field, or in the nine-field example above ~ 13 per 0.2 magnitude bin. In this case, once again, colour bins are dominated by stars ($\gtrsim 50$ per 0.2 magnitude bin in 9 fields) for $(r-i)_{Pal} \lesssim 2.2$, but are biased seriously by spurious star-like objects for bins redder than this.

Contamination of our sample by giants will be negligible – an M0III giant has $M_I \approx 2.6$, while an M5III giant has $M_I \approx 3.6$ (Allen 1976). Given the lower limit adopted ($14 < i_{Pal} < 17$) such stars can only be detected at distances of greater then 21kpc and 33kpc respectively. Supergiants are even more luminous and would only be detected at even larger distances. Since the galactic latitudes at which our plates were taken are large

($b \gtrsim 45°$) giants/supergiants at these distances would only fall into our sample if they lay in the Galaxy's outer halo. As stars this late are unknown in the halo we can assume none are detected by our survey.

2.5.3 - Constructing a Luminosity Function.

Luminosity functions were constructed for each of the eleven fields in our survey. Maximum distances at which each object could be detected were estimated using the sample limits described in §2.5.1. Maximum 'generalised' volumes (V_a) were then estimated using equation 2.12. A scale height of 350pc was assumed throughout (Scalo 1986). Because the generalised volume requires this assumption to be made, a further distance limit was imposed so that the impact of any uncertainty in this scale-height estimate was reduced. Distances to all stars were estimated using the observed $(r-i)^P_{Pal}$ colour, i^P_{Pal} magnitude and the colour-magnitude relation of equation 2.16. Stars more distant than 150pc were removed from the sample – this allows us to sample reasonable number statistics for the more luminous M-dwarfs, while keeping the distance limit small enough that uncertainties in the disk scale height do not cause significant uncertainties in V_a. The luminosity of each star was estimated using the observed $(r-i)^P_{Pal}$ colour and equations 2.16 and 2.17. Luminosity functions (Φ_0) were then constructed in each field by binning the data in M_{Bol} and calculating the sum of the $1/V_a$ values in each bin. Uncertainties for each bin were estimated as the square root of the variance in each bin, as defined by equation 2.15.

The use of an $(r-i)^P_{Pal}$ limit produces some incompleteness at the bright end of these LFs. The typical uncertainty for an $(r-i)^P_{Pal}$ estimate is ± 0.29 mag.(This is based on the estimates of uncertainties for a single observation in §2.4.2 for $r^P_{Pal} \leq 20.5$ and on the data from Table 2.6 for $i_{Pal} \leq 17$.) Since there is an uncertainty in $(r-i)^P_{Pal}$ of ± 0.29 mag., some fraction of the stars with *actual* $(r-i)^P_{Pal}$ values redder than this limit are rejected because they are *measured* to have a colour bluer than the limit. We therefore only evaluate the LF for $M_{Bol} > 8.5$ where (for a Guassian distribution of uncertainties in $(r-i)^P_{Pal}$) the data is more than 84% complete. Of course, the measurement error in $(r-i)^P_{Pal}$ – as well as the scatter about the M_I:$(r-i)_{Pal}$ relation – will scatter stars into the sample which are actually bluer than the colour limit, (or equivalently more luminous than the corresponding M_{Bol} limit). The systematic effects of this on our determination of the LF will be discussed below when Malmquist-type effects are considered.

These eleven LFs were then averaged to produce a single LF estimate. (The average taken as the mean value of Φ_0, when weighted by the volume sampled for an object

with M_{Bol} equal to the bin centre value.) The final uncertainties quoted are the Poisson counting errors given by the number of objects in each bin. This LF (in two binnings) is shown in Figure 2.24 and Table 2.10. A previously determined LF in this luminosity range (Reid 1987) is also shown. The Reid LF is based on nearby star data (i.e., stars with measured triginometric parallaxes) for $M_{Bol} < 10$ and on photometric data from 48″-Schmidt studies (like this one) for fainter data. In general the photometric samples on which the faint Reid LF is based, add up to only a fraction of the volume sampled in this study.

In order to indicate how systematic effects produced by uncertainties in the exact disk scale height affect our results, we have plotted in Figure 2.25 the LF from one of the binnings in Figure 2.24, along with the LFs produced when the same sample is reduced for an distance limit of $d_{max} = 200$pc (*squares*) and for an assumed scale height $h = 300$pc (*triangles*). (These LFs are only plotted for $M_{Bol} < 12.5$ as Φ_0 values fainter than this are seriously contaminated by non-stellar objects – see §2.5.5). As would be expected the difference between the two is negligible for low luminosity stars where the sample is limited to distances $\ll 100$pc. For brighter stars however differences of up to 10% are seen.

It should also be noted that the completeness limits used to set the volumes sampled (see §2.4.1) were chosen to be the magnitudes at which $> 80\%$ of the predicted galaxy counts on each plate were counted. This means our LF estimates have a *maximum* possible systematic uncertainty due to incompleteness of 20%. In practice our samples are more complete for stars than for galaxies, and for magnitudes more than ~ 0.5 magnitudes above the completeness limits in Table 2.8 our data should be essentially 100% complete. So this 20% value should be regarded as an worst-case upper limit.

2.5.4 - Malmquist-type effects.

Systematic biases (normally referred to under the general heading of "Malmquist bias") are introduced into a distance limited sample when an imperfect colour-magnitude relation is used to estimate luminosities and sampled volumes. An examination of the number counts in our sample (Table 2.10) as a function of bolometric luminosity, shows that the number counts increase steeply for more luminous stars. Uncertainty in our $M_I{:}(r-i)^P_{Pal}$ relation will therefore have the effect of scattering more intrinsically luminous stars into a given absolute magnitude bin than are scattered out of it. There is a systematic bias toward overestimating the number of stars in a given bolometric luminosity bin. Alternatively, we systematically underestimate the average bolometric luminosity of stars in a

given colour bin, because stars in that bin are (on average) bluer than they would be in the absence of uncertainties. This is the classical Malmquist bias (Malmquist 1927, Mihalas & Binney 1981), and can be dealt with by essentially 'shifting' the LF to brighter bolometric magnitudes.

However, the colour-magnitude relation is also used to estimate the volumes sampled by stars in a given luminosity (or colour) bin. Scatter in the colour-magnitude relation will lead to this volume being systematically under-estimated, because absolute magnitude uncertainties will scatter more over-luminous stars into the sample volume than they scatter sub-luminous stars out of it. This means we actually sample objects to a larger distance than we expect. This second bias is sometimes known as the "Malmquist effect." The correction for these biases is discussed in detail in Stobie *et al.* (1989), and we follow their technique for estimating correction for it. They derive (for a uniform space density of stars and an uncertainty in the absolute magnitude σ) a correction $\Delta\Phi$ which must be added to the actual luminosity function Φ to produce the observed luminosity function Φ_{obs},

$$\frac{\Delta\Phi}{\Phi} = \frac{1}{2}\sigma^2\left[(0.6\ln 10)^2 - 1.2\ln 10\,\frac{\Phi'}{\Phi} + \frac{\Phi''}{\Phi}\right]. \tag{2.19}$$

Stobie *et al.* then use this to choose a model of the luminosity function which produces an observed luminosity function which matches their LF data. Once they have a model of the 'true' LF, they use it to determine estimates of V_a corrected for Malmquist biases (which they denote V_a^*) and so derive a Malmquist-corrected LF. We do not attempt to carry out a detailed correction for Malmquist biases here, however we have used equation 2.19 to obtain a first-order estimate of the the size of these corrections. That is, we assume,

$$\begin{aligned}\frac{\Delta\Phi}{\Phi} &\approx \frac{\Delta\Phi_{obs}}{\Phi_{obs}} \\ &= \frac{1}{2}\sigma^2\left[(0.6\ln 10)^2 - 1.2\ln 10\,\frac{\Phi'_{obs}}{\Phi_{obs}} + \frac{\Phi''_{obs}}{\Phi_{obs}}\right]\end{aligned} \tag{2.20}$$

and evaluate an approximation to the true LF by subtracting corrections from the observed LF,

$$\Phi \approx \Phi_{obs} - \frac{\Delta\Phi_{obs}}{\Phi_{obs}}. \tag{2.21}$$

The results of this are shown in Figure 2.26, where a smoothing-spline (de Boor 1978) has been fitted to each of the luminosity functions shown in Figure 2.24, and first-order corrections for Malmquist biases evaluated using equation 2.21 and 2.20 to give the LFs

plotted as square symbols. (The second-order term from equation 2.20 was ignored.) As would be expected the major effect is to shift the LF to more luminous magnitudes (i.e., remove the classical Malmquist bias) and to decrease the LF overall (i.e., correct for over estimated volume sampling). The effects are most noticeable in the slope of the LF between $M_{Bol} \approx 10 - 12$ which is made considerably steeper – again as would be expected. Overall the major effect of these biases is to 'sharpen' the apparent maximum at $M_{Bol} \approx 10$ and to steepen the fall-off in the LF seen at fainter magnitudes – which was the major conclusion of Stobie *et al.*

2.5.5 - Discussion.

A few points about the LFs in Figure 2.24 are immediately noticeable. A pronounced peak is seen in the LF at $M_{Bol} \approx 10$ and a pronounced minima at $M_{Bol} \approx 12.5$. Both these features have been seen in previous determinations of the low mass LF (Reid 1987, Hawkins & Bessell 1988, Leggett & Hawkins 1988, Stobie *et al.* 1989). Confusingly they seem to be particularly apparent in LFs based on photometric data for more distant stars (d$\sim$ 10 – 30pc), while LFs based on nearby stars (for which trigonometric parallaxes are available) show less convincing evidence of the dip. Figure 2.24, however, clearly shows that the difference can no longer be negated by apealling to poor number statistics in the photometric survey data. Note also that neither the effects of systematic errors in the volume estimation (Fig 2.25), nor the effects of Malquist-type biases (Figure2.27), are sufficient to make the $M_{Bol} \approx 12.5$ minima go away. Correction for Malmquist-type bias in particular only makes the minimum even more pronounced. Because the nature of this feature depends so strongly on the form of the LF for $M_{Bol} > 12.5$, further discussion of this discrepancy is deferred to Paper IV in which an infrared LF for these stars is derived.

The other major point to note is the pronounced up-turn in the LF which is seen for $M_{Bol} > 13$. This upturn is very similar to that seen in several previous luminosity functions measured with optical data (see Reid (1987) and references therein). However in light of the results derived for the contamination of our sample by both galaxies and spurious star-like images (§2.5.3), as well as the increased scatter in the M_{Bol} estimates of these stars due to the steepening of the $dM_{Bol}/d(r-i)_{Pal}$ relation (§2.5.4), it can be seen that the Φ_0 estimates in this region *are completely spurious.* That these Φ_0 values have no meaning has been dramatically shown by our programme of infrared observations. Wheras the LF shown in Table 2.10 implies that $\sim$ 8 stars are present in our sample with

$M_{Bol} > 14$, we in fact found that there are *no* stars this faint in our sample when K-band observations were made of all candidates in the same fields (Paper IV).

A last question to ask is whether averaging these independent LFs is a valid procedure? Are the LFs estimated for each field really estimates of the same underlying LF, or does the LF vary from field to field. We have plotted in Figure 2.27 (in two separate binnings) the four LFs produced by averaging only adjacent fields (i.e., Field 213,262 and 263; Fields 513 and 868; Fields 829,831 and 832; and Fields 889,890 and 891. The galactic coordinates of these fields are given in Table 2.3 and shown in Figure 2.4) Figure 2.27 shows that while slight normalisation differences ($\sim \pm 25\%$) are seen at a marginally significant level between the different directions in which our study was carried out, the overall shape of the LFs are much the same. The shape of the field LF seems to be independent of the direction in which it is examined.

Section 2.6 - A Sample of VLM Candidates.

It has been clearly shown above that optical colours are essentially useless for studying the luminosity function for VLM stars (i.e., stars with $M_{Bol} \gtrsim 12.5$). Not only are our samples of such objects contaminated by galaxies and spurious images, but the M_{Bol} estimates for these objects are extremely poor with uncertainties as high as ± 1.4 magnitudes. We have therefore used our plate catalogues to select complete samples of VLM candidates in each field. In general these samples were chosen to be all objects redder than $(r - i)^P_{Pal} = 2.0$ for $i^P_{Pal} < 17 - 17.5$. These samples have been observed at the infrared K-band, and the $i^P_{Pal} - K$ colours so constructed (which we hereafter refer to simply as I–K) have been used to estimate more precise bolometric luminosities.

Because all K-band observations were made with an infrared array, the detection of contaminating galaxies and undeblended binaries is very straightforward. Moreover, spurious objects will be seen as non-detections at K-band, eliminating their contamination. We have therefore selected our VLM candidate sample using an extremely conservative star-galaxy separation criterion. Objects are rejected from our sample only if it is clear that their star/galaxy separation parameters make it impossible for them to be stars - this translates to requiring them to be more than 1.5 magnitudes above the plate limit, and to have $|\phi| > 600$ (i.e., more than 6-sigma away from the star-ridge) in *at least* two plates.

The results of this VLM survey will be presented in Tinney, Reid & Mould (1992 - Paper IV) along with improved determinations of the inital mass function based on this new data for stars with mass below $0.4M_{\odot}$.

Section 2.7 - Conclusions.

We have constructed a 270 square degree photographic catalogue from IIIaF and IVN plates of the UKSRC and POSSII sky surveys. These catalogues are complete to $i_{Pal} \approx 18$ and $r_{Pal} \approx 20.5$. The photometric uncertainties at the respective limits are ± 0.21 and 0.25 magnitudes. These parameters should be taken as representive for those considering scientific programmes with generation of digital catalogues currently being produced from both the UKSRC and POSSII plate catalogues. However, while these values are representative there can be considerable variation in quality from plate to plate – in particular for IVN plates – and prospective users are warned that systematic variations in magnitudes of up to ± 0.2 are possible. The usefulness of the catalogues will be directly proportional to the amount of calibration data which can be acquired in each field.

Our catalogues have been calibrated on to a photometric system created for this project (which we denote $r_{Pal}i_{Pal}$) defined by Cousins system standards observed over a narrow range of colour through Gunn-system r and i filters. This system was chosen in order to minimise colour terms between the photographic plate passbands and the calibrating CCD sequence passbands. Despite this we find there to be a significant colour term present between the magnitude produced by IIIaF plates and CCD r filter observations. This colour term results in our survey being limited by the depth of the IIIaF plates (rather than the IVN plates) for very red stars. We find that no gain in survey depth for VLM stars is produced by using objects fainter than $i_{Pal} \approx 17 - 17.5$.

We have evaluated colour-magnitude and bolometric correction relations suitable for the study of early M-dwarfs (M0-M7 or $1.0 \gtrsim (r-i)_{Pal} \lesssim 2.2$), and use these to measure the stellar luminosity function for $8.5 < M_{Bol} < 12.5$ over a volume of space almost and order of magnitude larger than previous studies. We derive a form of the $1/V_{max}$ LF which allows for an exponential gradient in the stellar density of the disk, for observations made at arbitrary galactic latitude. We find that we essentially reproduce the results of earlier studies of this type, though with higher precision.

Our 270 square degree catalogue detects almost 600,000 objects within the magnitude limits described above. In evaluating the LF we have selected from this sample only 3551 objects within 150pc of the sun – around 99.4% of the objects detected are ignored. With such a small fraction of the objects detected being used to construct a LF it is clear that the contamination of the final sample by spurious objects must be well understood! As the number of stars detected is a strongly decreasing function of M_{Bol}, this is even more important for fainter stars. We find that the inability of our selection criteria to reject *all* non-stellar objects is not significant for $M_{Bol} \lesssim 12$. At fainter absolute magnitudes however our sample becomes heavily contaminated, simply because the number of actual very late stars detected is so small. Moreover, M_{Bol} becomes a steeper function of $(r-i)_{Pal}$ for very late stars, resulting in small uncertainties in the photometry ($\sim \pm 0.25$) producing large uncertainties in the M_{Bol} estimates. Also, as the maximum volumes sampled by stars decrease strongly with increasing M_{Bol} stars scattered into larger M_{Bol} bins by photometric uncertainties and/or cosmic scatter in the colour-magnitude relation will contribute disproportionately to larger estimates of Φ_0.

These effects combine to make the faint end of the LF determined by photometric studies so subject to systematic bias as to be useless. When we calculate the LF for $M_{Bol} > 12$ we find that we reproduce early LF results in this region, which have been taken to allow

for a strongly increasing number density of stars near the bottom of the main sequence. However, we find these Φ_0 estimates to be completely spurious. The only way in which to study the LF at the very bottom of the main sequence is to make infrared observations, both because they allow non-stellar objects to be rejected, and because infrared colour-magnitude relations for these objects produce much more precise luminosity estimates (Papers II & III). We have therefore selected samples from our photographic catalogues for further observation in the infrared, the results of this study being presented in Paper IV.

Lastly we have used our observations in eleven fields (carried out in approximately four directions through the Galactic disk) to see whether there are strong variations in the disk LF. We find no evidence for significant variation in the form of the LF, though we do find marginally significant evidence for $\sim 20\%$ variations in the normalisation of the LF.

The authors wish to thank Harvey M^{c}Gillivray for all his assistance in expediting the scanning of the UKSRC and POSSII plates used in this programme. Thanks also go to all the staff at Palomar Mountain, who made acquiring the enormous amount of CCD calibration data required for this programme possible.

References

Allen, C.W. 1976, *Astrophysical Quantities*, Athlone Press : London

Bahcall, J.N. & Soneira, R.M., 1980, ApJSupl, 44 73

Beard, S., M^{c}Gillivray, H.T., Thanisch, P.F. 1990, MNRAS, 247, 311

Bessell, M. 1979, PASP, 91, 589

Bessell, M. 1986, PASP, 98, 1303

Cousins 1976, Mem.R.Astron, 81, 25

Collins, C.A., Heydon-Dumbleton, N.H. & MacGillivray, H.T. 1989, MNRAS, 236, 7p

Common, A.A. 1883, MNRAS, 43, 255

de Boor, C. 1978, *A Practical Guide to Splines* Springer-Verlag : New York

Draper, J.W. 1840, Phil.Mag., 17, 217

Felten, J.E., 1976, ApJ, 207, 700

Hawkins, M.R.S, & Bessell, M.S. 1988, MNRAS, 234, 177

Jones, L.R. *et al.* 1991, MNRAS, 249, 481

Landolt, A. 1983, Astron.J., 88, 999

Leggett, S.K. & Hawkins, M.R.S. 1988, MNRAS, 334, 1065

Leggett, S.K. 1992, ApJSupp, 82, 351

Malmquist, K.G. 1927, Lund.Medd.Series 11, No. 37

Metcalfe, N., *et al.* 1991, MNRAS 249, 498

M^{c}Gillivray, H.T. & Stobie, R.S. 1984, Vistas.Astr., 27, 433

Mihalas, D.M. & Binney, J. 1981, *Galactic Astronomy: Structure and Kinematics*, 2nd Edition, p.239. W.H.Freeman : San Fransisco

Monet, D.G. 1992, AJ, 103, 638

Picard, A. 1991, AJ, 102, 445

Reid, I.N. 1987, MNRAS, 225, 873

Reid, I.N. *et al.* 1991, PASP, 103, 661

Reid, I.N. & Majewski, S. 1992, ApJ, *submitted*

Scalo, J.M. 1986, Fund.Cosmic.Phys., 11,1

Schmidt, M. 1968, ApJ, 151, 393

Stobie, R.S., Ishida, K., Peacock, J.A., 1989, MNRAS, 238, 709

Thanisch, P.F., McNally, B.V. & Robin, A. 1984. *Image and Vision Computing*, 2, 191

Thuan & Gunn 1976, PASP, 88, 543

Tinney, C.G., Mould, J.R., Reid, I.N. 1992a, ApJ, 396, 173

Tinney, C.G., Mould, J.R., Reid, I.N. 1992b, AJ, *in press.* (Paper II)

Tinney, C.G., 1992a, AJ, *in press.* (Paper III)

Tinney, C.G., 1992b, ApJ, *submitted.* (Paper IV)

Tritton, S., 1983. *The U.K Schimdt Telescope Unit Handboook* Royal Observatory Edinburgh : Edindurgh

Wynne, C. 1981, QJRAS, 22 146

Tables to Chapter 2

Table 2.1 - A List of CCD Observations.

Date (UT)	Quality	Observer	Date (UT)	Quality	Observer
20APR90	No Obs	Tinney	15MAY91	Phot	Mould[a]
21APR90	No Obs	Tinney	16MAY91	Phot	Mould[a]
22APR90	Non-Phot	Tinney	17MAY91	Phot	Mould[a]
6JUN90	No Obs	Tinney	2JUN91	Phot	Mould[a]
7JUN90	No Obs	Tinney	3JUN91	Phot	Tinney
8JUN90	Non-Phot	Tinney	4JUN91	Phot	Tinney
9JUN90	No Obs	Tinney	23JUN91	Phot	Tinney
24JUN90	Non-Phot	Tinney	24JUN91	Non-Phot	Tinney
25JUN90	Phot	Tinney	25JUN91	Phot	Tinney
26JUN90	Phot	Tinney	7JUL91	Non-Phot	Tinney
15AUG90	Non-Phot	Tinney	8JUL91	Non-Phot	Tinney
16AUG90	Phot	Tinney	7AUG91	Phot	Weir[a]
20AUG90	Phot	Tinney	20AUG91	Non-Phot	Reid[b]
21AUG90	Phot	Tinney	21AUG91	Non-Phot	Reid[b]
23SEP90	Non-Phot	Tinney	16SEP91	Non-Phot	Tinney
24SEP90	Phot	Tinney	23NOV91	Non-Phot	Tinney
25NOV90	Phot	Tinney	24NOV91	Non-Phot	Tinney
1DEC90	Phot	Tinney	25NOV91	Non-Phot	Tinney
2DEC90	Non-Phot	Tinney	29NOV91	Non-Phot	Tinney
26JAN91	Non-Phot	Tinney	30NOV91	Non-Phot	Tinney
27JAN91	Non-Phot	Tinney	1DEC91	Non-Phot	Tinney
28JAN91	Non-Phot	Tinney	2DEC91	Non-Phot	Tinney
29JAN91	No Obs	Tinney	3DEC91	Non-Phot	Tinney
23APR91	No Obs	Tinney	4DEC91	Non-Phot	Tinney
24APR91	Non-Phot	Tinney	27JAN92	Non-Phot	Tinney
25APR91	No Obs	Tinney	28JAN92	Phot	Tinney
			29JAN92	Non-Phot	Tinney
			30JAN92	Non-Phot	Tinney

Notes to Table.

[a] - JRM and W.N.Weir kindly made observations on nights allocated for other projects.

[b] - INR kindly observed while CGT was observing at Las Campanas, Chile.

Table 2.2 - Photometric CCD Observations.

Date (UT)	Z_r[a]	Z_i[a]	Seeing
25JUN90	8.756 ± 0.026 (10)	9.296 ± 0.016 (10)	1.1-1.5″
26JUN90	8.798 ± 0.032 (13)	9.324 ± 0.017 (12)	1.5-2.0″
16AUG90	8.700 ± 0.028 (10)	9.277 ± 0.021 (15)	1.3-2.0″
20AUG90	8.729 ± 0.040 (6)	9.318 ± 0.030 (6)	1.5-2.0″
21AUG90	8.724 ± 0.054 (10)	9.317 ± 0.039 (11)	1.1-1.5″
24SEP90	8.760 ± 0.032 (16)	9.364 ± 0.027 (17)	1.2-1.7″
25NOV90	8.628 ± 0.025 (11)	9.190 ± 0.017 (11)	1.4-1.7″
1DEC90	8.608 ± 0.015 (10)	9.168 ± 0.010 (9)	1.3-1.8″
15MAY91	8.759 ± 0.035 (10)	9.306 ± 0.027 (10)	1.3-1.5″
16MAY91	8.811 ± 0.044 (11)	9.351 ± 0.035 (10)	1.5-2.0″
17MAY91	8.747 ± 0.039 (11)	9.286 ± 0.029 (9)	2.0-2.5″
2JUN91	9.020 ± 0.020 (7)	9.566 ± 0.029 (9)	1.3-1.5″
3JUN91	8.878 ± 0.035 (10)	9.435 ± 0.025 (13)	1.1-1.8″
4JUN91	8.859 ± 0.026 (8)	9.419 ± 0.025 (9)	1.1-1.5″
23JUN91	8.802 ± 0.024 (9)	9.358 ± 0.014 (9)	1.1-2.0″
25JUN91	8.794 ± 0.009 (4)	9.357 ± 0.010 (4)	1.5-2.5″
23JUL91	8.689 ± 0.028 (5)	9.206 ± 0.024 (6)	1.0-1.4″
28JAN92	8.661 ± 0.029 (8)	9.134 ± 0.044 (8)	1.3-1.8″

Notes to Table.

[a] - See Equation (2.2) in text for definition of Z_i and Z_r. Uncertainties quoted are standard deviations about the fitted zero-points – the numbers of parenthesis are the number of standard stars observed to get each zero-point. Each standard star was observed 4–5 times in a 'multiple' exposure with a single CCD read.

Table 2.3 - Plate Material Scanned.

Field	Field Centre α δ (1950.0)	Field Centre l^{II}	Field Centre b^{II}	Observ.	Plate[a] Number	Epoch	Grade[b]
829	02^h00^m +00°	157.8	-57.7	UKSRC	I12254	1987.83	B3
				POSSII	F768	1986.70	A
				UKSRC	R8222	1982.86	A3
831	02^h40^m +00°	171.8	-51.8	UKSRC	I11526	1986.94	A2
				UKSRC	I7377	1981.92	B4
				POSSII	F2889	1989.85	C2
				UKSRC	R4446	1978.61	A4
				UKSRC	R7376	1981.92	A
832	03^h00^m +00°	177.4	-48.3	UKSRC	I11499	1986.89	C5
				POSSII	N3601	1990.78	B
				UKSRC	OR11502	1986.90	C5
				POSSII	F1469	1987.72	R
				POSSII	F3004	1989.97	C1
263	09^h50^m +45°	172.7	+54.8	POSSII	N3100	1990.20	C1
				POSSII	F2957	1989.92	A
213	10^h00^m +50°	166.1	+50.8	POSSII	N2291	1989.09	C1
				POSSII	F1096	1987.29	R
				POSSII	F2978	1989.93	A
262	10^h15^m +45°	174.5	+50.5	POSSII	N2940	1989.89	A
				POSSII	F1091	1987.23	R
				POSSII	F2315	1989.16	C2
513	15^h00^m +25°	35.8	+60.6	POSSII	N1197	1987.34	R
				POSSII	F1094	1987.23	R
868	15^h00^m +00°	357.4	+48.3	UKSRC	I11801	1987.30	A
				UKSRC	I11802	1987.30	A
				UKSRC	I9992	1985.20	B
				POSSII	F1178	1987.32	R
				POSSII	F2428	1989.40	C3
				UKSRC	R5780	1980.22	A2
889	22^h00^m +00°	59.9	-41.1	POSSII	N3362	1990.55	B
				POSSII	F3386	1990.56	R
				POSSII	F3479	1990.64	B
				POSSII	F3561	1990.72	R
890	22^h20^m +00°	64.2	-45.0	POSSII	N3647	1990.82	C1
				UKSRC	OR11286	1986.61	B3
				UKSRC	OR11414	1986.76	A3
				POSSII	F1342	1987.58	R
				POSSII	F1415	1987.82	R
				POSSII	F3493	1990.64	B
891	22^h40^m +00°	68.3	-48.9	POSSII	N3584	1990.74	C1
				POSSII	F742	1986.67	C1

Notes to Table 2.3

[a] - The letter before each plate number denotes the emulsion/filter combination used. Palomar plates are denoted; F = IIIaF emulsion + RG610 filter, N = IVN + RG9. UK Schmidt plates are denoted; R = IIIaF + RG630, OR = IIIaF + OG590, I = IVN + RG715.

[b] - The grading codes (assigned by each observatory) give information on the quality of each plate. Palomar grades its plates from A (best) to R (rejected by the survey) – A, B, C1, C2, C3, R (Reid *et al.* 1991). The UKST takes both survey and non-survey plates. All plates receive a letter grade from A (best) to C (worst). Plates taken for the Survey also receive a number grade - the lower the better (Tritton 1983).

Table 2.4 - Plate Material Used in Final Catalogues.

Field	Plate Number	Epoch	Sky[a] Thresh.	Area[b] Tresh.	Deblend[c] Used	Area[d] ($\square^\circ$)	Used for[e] $(r-i)^P_{Pal}$
829	I12254	1987.83	8	4	Y	25.32	Y
	F768	1986.70	5	4	Y	25.19	Y
	R8222	1982.86	6	4	Y	25.41	N
831	I11526	1986.94	7	4	Y	27.27	Y
	I7377	1981.92	6	3	N	25.33	Y
	F2889	1989.85	6	4	Y	25.34	Y
	R4446	1978.61	7	3	N	25.33	N
	R7376	1981.92	10	4	N	25.24	Y
832	I11499	1986.89	5	4	Y	25.32	Y
	N3601	1990.78	5	4	Y	25.35	Y
	OR11502	1986.90	7	4	Y	25.25	Y
	F1469	1987.72	6	4	Y	25.31	Y
	F3004	1989.97	6	4	Y	25.33	N
263	N3100	1990.20	5	4	Y	25.27	Y
	F2957	1989.92	6	4	Y	25.19	Y
213	N2291	1989.09	7	4	Y	25.34	Y
	F1096	1987.28	6	4	Y	25.35	N
	F2978	1989.93	7	4	Y	25.31	Y
262	N2940	1989.89	5	4	Y	25.32	Y
	F1091	1987.23	6	4	Y	25.35	N
	F2315	1989.16	5	4	Y	25.31	Y
513	N1197	1987.34	6	4	Y	25.37	Y
	F1094	1987.23	7	4	Y	25.29	Y
868	I11801	1987.30	5	4	Y	25.29	Y
	I9992	1985.20	6	3	N	25.25	N
	F1178	1987.32	7	4	Y	25.32	Y
	F2428	1989.40	8	4	Y	25.35	Y
889	N3362	1990.55	5	4	Y	25.30	Y
	F3386	1990.56	6	4	Y	25.35	Y
	F3479	1990.64	7	4	Y	25.38	Y
	F3561	1990.72	6	4	Y	25.25	Y
890	N3647	1990.82	5	4	Y	25.34	Y
	OR11286	1986.61	6	4	Y	25.29	N
	OR11414	1986.76	8	4	Y	25.29	Y
	F1342	1987.58	8	4	Y	25.24	Y
	F1415	1987.82	8	4	Y	25.30	N
	F3493	1990.64	7	4	Y	25.44	Y
891	N3584	1990.74	5	4	Y	25.28	Y
	F742	1986.67	5	4	Y	25.26	Y

Notes to Table 2.4

[a] - Sky threshold (in percent above local sky) applied by COSMOS when selecting images (§2.3.1)

[b] - Area threshold (in 32μm pixels) applied by COSMOS when selecting images (§2.3.1)

[c] - Y means the COSMOS group's deblending software was applied to this plate; N means it was not.

[d] - Area in square degrees ($\square^\circ$) covered by the plate once a 3° 'cookie' has been excised, but *before* bad regions were removed as described in §2.3.3. Bad regions removal decreases this area by less than 0.3 square degrees.

[e] - Y means that this plate's photometry was used to calculate $(r-i)^P_{Pal}$ values for objects in this field; N means it was not.

Table 2.5(a) – Calibration Residuals for IVN Plates.

i^C_{Pal} Bin	I12254	I11526	I7377	I11499	N3601	N3100	N2291
12.25	0.076±0.000 (1)	-0.003±0.000 (1)		0.010±0.000 (1)	-0.029±0.000 (1)		-0.048±0.000 (1)
12.75	-0.062±0.068 (2)	-0.012±0.010 (2)	0.002±0.006 (2)			0.009±0.039 (6)	
13.25	0.030±0.038 (2)	0.022±0.038 (6)	-0.013±0.023 (4)	-0.023±0.000 (1)	0.020±0.000 (1)	-0.005±0.040 (6)	-0.011±0.014 (3)
13.75	-0.009±0.065 (3)	-0.019±0.030 (7)	-0.011±0.052 (7)	0.002±0.013 (3)	0.023±0.047 (4)	0.010±0.016 (4)	0.012±0.036 (5)
14.25	-0.063±0.037 (5)	-0.015±0.038 (11)	0.000±0.067 (10)	0.037±0.028 (4)	0.016±0.016 (4)	-0.070±0.056 (4)	0.007±0.049 (4)
14.75	0.020±0.033 (6)	-0.023±0.048 (14)	-0.007±0.049 (12)	0.043±0.040 (4)	0.068±0.000 (1)	0.001±0.047 (12)	-0.003±0.066 (8)
15.25	0.026±0.017 (3)	-0.024±0.044 (15)	0.013±0.065 (15)	0.007±0.074 (7)	-0.005±0.057 (6)	0.033±0.054 (13)	0.012±0.061 (14)
15.75	0.063±0.050 (6)	-0.005±0.049 (16)	0.010±0.067 (19)	-0.017±0.061 (9)	-0.006±0.055 (7)	-0.003±0.068 (15)	0.003±0.060 (17)
16.25	0.052±0.080 (19)	0.026±0.064 (24)	-0.001±0.069 (18)	0.028±0.052 (5)	-0.022±0.016 (5)	0.004±0.060 (15)	-0.004±0.102 (20)
16.75	-0.054±0.091 (15)	0.015±0.090 (32)	0.007±0.062 (29)	-0.005±0.100 (21)	0.008±0.078 (12)	0.026±0.080 (18)	-0.029±0.113 (14)
17.25	-0.017±0.120 (16)	0.018±0.121 (38)	-0.044±0.117 (33)	0.018±0.090 (12)	0.023±0.112 (5)	-0.004±0.128 (21)	-0.024±0.123 (24)
17.75	-0.127±0.196 (11)	-0.017±0.187 (47)	-0.053±0.158 (45)	-0.042±0.177 (19)	0.099±0.209 (12)	0.072±0.108 (20)	0.026±0.154 (25)
18.25	0.062±0.273 (24)	-0.019±0.252 (72)	0.023±0.245 (69)	0.003±0.249 (32)	0.145±0.218 (11)	-0.044±0.196 (25)	0.033±0.230 (23)
Total	118	285	263	118	70	159	159

i^C_{Pal} Bin	N2940	N1197	I11801	I9992	N3362	N3647	N3584
12.25		0.013±0.020 (5)	0.036±0.026 (4)	0.066±0.034 (3)	0.048±0.010 (2)	0.023±0.014 (2)	-0.006±0.134 (3)
12.75	-0.056±0.043 (2)	0.012±0.027 (3)	0.005±0.053 (3)	0.052±0.082 (6)	-0.008±0.035 (5)	0.022±0.015 (5)	-0.002±0.145 (3)
13.25	0.042±0.045 (3)	0.034±0.029 (5)	-0.002±0.065 (6)	-0.047±0.124 (8)	0.004±0.049 (15)	-0.013±0.036 (7)	0.012±0.151 (2)
13.75	-0.005±0.054 (5)	-0.014±0.069 (9)	0.000±0.054 (9)	0.065±0.111 (9)	-0.036±0.064 (8)	-0.014±0.055 (13)	-0.077±0.044 (3)
14.25	0.013±0.050 (5)	-0.011±0.072 (14)	-0.015±0.039 (13)	0.085±0.046 (13)	0.042±0.066 (10)	0.053±0.046 (10)	0.086±0.092 (6)
14.75	-0.075±0.000 (1)	0.000±0.082 (10)	0.010±0.065 (21)	0.061±0.099 (25)	-0.013±0.078 (12)	0.024±0.069 (19)	0.003±0.105 (10)
15.25	-0.017±0.041 (7)	0.007±0.084 (13)	0.038±0.045 (24)	0.076±0.119 (25)	-0.005±0.077 (23)	0.001±0.059 (22)	0.001±0.159 (4)
15.75	0.032±0.059 (6)	0.004±0.094 (19)	-0.004±0.087 (26)	-0.033±0.151 (28)	-0.003±0.074 (27)	0.002±0.072 (28)	-0.026±0.151 (7)
16.25	-0.006±0.063 (9)	0.033±0.089 (30)	0.022±0.089 (42)	0.019±0.111 (43)	-0.017±0.073 (26)	0.006±0.085 (38)	-0.079±0.057 (7)
16.75	0.043±0.089 (10)	0.064±0.086 (34)	0.015±0.080 (37)	0.022±0.151 (35)	0.017±0.061 (55)	0.028±0.110 (45)	0.030±0.134 (9)
17.25	0.011±0.105 (15)	-0.029±0.128 (33)	-0.009±0.134 (47)	0.035±0.137 (54)	0.006±0.091 (58)	0.012±0.137 (49)	-0.072±0.188 (17)
17.75	0.058±0.160 (15)	-0.015±0.171 (44)	-0.032±0.186 (46)	0.008±0.179 (64)	0.029±0.127 (73)	0.070±0.159 (56)	-0.003±0.182 (25)
18.25	0.110±0.204 (13)	0.023±0.201 (21)	0.041±0.223 (38)	-0.011±0.268 (57)	0.032±0.166 (70)	0.102±0.269 (66)	0.029±0.264 (16)
Total	94	243	320	374	385	361	113

Table 2.5(b) – Calibration Residuals for IIIaF Plates.

r_{Pal}^{C} Bin	r768		r2889		r7376		r11502		r1469		r2957	
13.25	-0.007±0.039	(2)	-0.041±0.063	(3)	-0.031±0.061	(3)	0.029±0.001	(2)	0.023±0.012	(2)	-0.003±0.024	(7)
13.75	0.093±0.032	(2)	0.016±0.030	(3)	0.028±0.025	(3)	0.074±0.000	(1)	0.045±0.000	(1)	0.022±0.008	(3)
14.25	0.008±0.022	(2)	-0.014±0.042	(2)	0.017±0.023	(2)	0.066±0.015	(2)	0.013±0.006	(2)	-0.006±0.025	(3)
14.75	-0.060±0.116	(4)	0.026±0.042	(4)	0.014±0.028	(3)	0.048±0.000	(1)	0.000±0.000	(1)	-0.013±0.076	(4)
15.25	-0.053±0.086	(5)	-0.003±0.040	(10)	-0.015±0.032	(8)	0.013±0.025	(4)	0.017±0.000	(1)	0.012±0.029	(9)
15.75	0.082±0.081	(5)	0.000±0.052	(10)	-0.019±0.029	(8)	-0.008±0.030	(4)	-0.030±0.049	(3)	-0.006±0.059	(10)
16.25	0.011±0.050	(7)	0.015±0.072	(18)	-0.035±0.040	(15)	-0.034±0.031	(4)	-0.037±0.024	(2)	-0.010±0.047	(10)
16.75	-0.002±0.057	(16)	0.027±0.093	(16)	0.014±0.057	(14)	-0.005±0.062	(12)	-0.064±0.060	(8)	0.008±0.053	(11)
17.25	0.044±0.075	(9)	-0.010±0.089	(20)	0.001±0.080	(17)	-0.023±0.023	(7)	0.014±0.084	(2)	0.002±0.062	(13)
17.75	-0.007±0.107	(12)	0.003±0.101	(29)	0.021±0.090	(24)	0.028±0.060	(13)	-0.061±0.034	(3)	0.063±0.089	(13)
18.25	0.046±0.102	(11)	0.016±0.151	(25)	-0.004±0.135	(22)	0.102±0.097	(16)	0.061±0.095	(8)	0.045±0.100	(11)
18.75	0.017±0.076	(8)	0.047±0.130	(35)	-0.011±0.162	(32)	0.091±0.096	(10)	-0.026±0.105	(5)	0.019±0.169	(28)
19.25	-0.032±0.163	(10)	-0.002±0.210	(47)	0.017±0.271	(41)	-0.003±0.213	(18)	0.088±0.149	(12)	0.043±0.249	(23)
19.75	0.001±0.198	(24)	0.048±0.290	(53)	0.007±0.387	(44)	-0.018±0.271	(23)	0.069±0.257	(6)	0.057±0.351	(29)
20.25	-0.026±0.336	(32)	0.002±0.261	(39)	-0.032±0.272	(28)	0.013±0.319	(22)	0.085±0.152	(9)	0.076±0.312	(29)
20.75	0.080±0.339	(10)	-0.369±0.000	(1)			-0.003±0.469	(7)	-0.382±0.053	(3)	0.100±0.166	(5)
Total		161		316		265		151		70		208

r_{Pal}^{C} Bin	r2978		r2315		r1094		r1178		r2428		r3386	
13.25	-0.003±0.000	(1)	-0.034±0.043	(2)	0.013±0.011	(3)	-0.021±0.043	(2)	-0.026±0.039	(2)	0.018±0.023	(4)
13.75	0.015±0.003	(2)	0.014±0.023	(4)	0.002±0.022	(7)	0.043±0.054	(6)	0.025±0.061	(6)	-0.008±0.041	(10)
14.25	0.022±0.000	(1)	0.004±0.040	(4)	-0.014±0.032	(11)	0.024±0.068	(10)	-0.009±0.120	(9)	-0.012±0.025	(10)
14.75	0.020±0.002	(2)	-0.013±0.034	(5)	0.017±0.053	(11)	0.016±0.074	(10)	0.002±0.062	(9)	0.013±0.042	(10)
15.25	-0.010±0.034	(6)	0.049±0.048	(3)	0.000±0.037	(7)	0.006±0.065	(15)	-0.004±0.072	(13)	-0.004±0.043	(10)
15.75	0.002±0.024	(10)	-0.014±0.033	(4)	-0.002±0.057	(9)	0.014±0.083	(17)	0.002±0.082	(13)	0.017±0.042	(19)
16.25	0.020±0.054	(10)	-0.003±0.027	(8)	0.008±0.049	(14)	-0.013±0.068	(17)	0.060±0.093	(17)	-0.005±0.057	(20)
16.75	0.008±0.026	(12)	0.011±0.060	(8)	-0.025±0.038	(15)	0.003±0.070	(30)	0.053±0.100	(26)	-0.009±0.058	(27)
17.25	0.037±0.051	(9)	0.009±0.082	(5)	0.005±0.058	(26)	0.015±0.084	(28)	0.026±0.104	(28)	-0.008±0.059	(42)
17.75	-0.025±0.067	(17)	0.009±0.063	(12)	0.002±0.074	(33)	0.020±0.107	(47)	0.027±0.095	(48)	-0.004±0.074	(45)
18.25	0.019±0.097	(18)	-0.013±0.091	(12)	0.004±0.083	(34)	-0.006±0.105	(41)	0.015±0.113	(45)	0.021±0.091	(49)
18.75	0.043±0.146	(19)	0.038±0.094	(14)	-0.015±0.087	(47)	0.003±0.143	(55)	0.004±0.154	(58)	0.021±0.110	(60)
19.25	0.039±0.235	(21)	0.122±0.191	(8)	0.024±0.131	(57)	0.003±0.195	(64)	0.067±0.233	(73)	0.106±0.190	(68)
19.75	0.072±0.262	(14)	0.006±0.333	(21)	0.008±0.192	(55)	0.061±0.283	(46)	0.062±0.216	(45)	0.046±0.233	(66)
20.25	-0.014±0.292	(16)	-0.006±0.301	(21)	0.002±0.349	(40)	-0.025±0.349	(26)	0.107±0.323	(31)	-0.005±0.266	(34)
20.75			-0.006±0.263	(14)	-0.012±0.297	(11)	-0.128±0.226	(5)	-0.023±0.162	(5)	-0.310±0.000	(1)
Total		165		146		388		422		432		479

Table 2.5(b) – Calibration Residuals for IIIaF Plates.

r^C_{Pal} Bin	r3479		r3561		r11414		r1342		r3493		r742	
13.25	0.025±0.052	(4)	0.030±0.027	(4)	0.005±0.062	(7)	0.003±0.054	(6)	-0.019±0.046	(6)	-0.035±0.036	(2)
13.75	0.026±0.061	(9)	-0.012±0.052	(9)	-0.001±0.055	(7)	0.024±0.044	(5)	-0.046±0.043	(6)	0.033±0.000	(1)
14.25	-0.056±0.043	(9)	-0.023±0.031	(10)	-0.033±0.064	(11)	0.031±0.042	(9)	-0.006±0.040	(10)	-0.013±0.021	(3)
14.75	0.023±0.065	(10)	0.017±0.044	(9)	0.023±0.063	(16)	0.017±0.051	(15)	0.022±0.049	(15)	0.024±0.047	(4)
15.25	-0.017±0.051	(12)	0.018±0.048	(12)	0.002±0.051	(19)	0.005±0.052	(18)	-0.002±0.044	(17)	0.014±0.040	(9)
15.75	0.026±0.086	(21)	0.010±0.048	(21)	0.034±0.058	(22)	0.024±0.047	(17)	0.029±0.043	(18)	0.055±0.049	(6)
16.25	0.012±0.074	(20)	-0.010±0.071	(22)	0.002±0.057	(28)	0.010±0.063	(27)	0.002±0.057	(28)	0.001±0.067	(8)
16.75	-0.013±0.090	(30)	-0.006±0.073	(30)	-0.009±0.083	(39)	-0.016±0.074	(30)	-0.009±0.071	(37)	-0.024±0.079	(8)
17.25	0.014±0.080	(44)	-0.005±0.085	(43)	-0.012±0.089	(37)	-0.004±0.084	(27)	-0.002±0.080	(31)	-0.021±0.067	(6)
17.75	-0.009±0.077	(48)	0.020±0.085	(52)	-0.015±0.096	(52)	-0.003±0.073	(41)	0.016±0.088	(45)	-0.039±0.025	(8)
18.25	0.011±0.112	(48)	0.027±0.105	(48)	-0.036±0.114	(43)	-0.010±0.096	(40)	0.017±0.102	(43)	-0.002±0.091	(18)
18.75	0.018±0.134	(65)	0.043±0.150	(67)	-0.013±0.143	(70)	0.009±0.122	(71)	0.029±0.138	(65)	-0.012±0.162	(17)
19.25	0.071±0.183	(71)	0.078±0.249	(80)	0.006±0.176	(63)	0.030±0.159	(65)	0.120±0.201	(57)	-0.089±0.154	(24)
19.75	0.025±0.234	(62)	0.099±0.296	(75)	0.074±0.266	(58)	0.018±0.226	(70)	0.066±0.245	(55)	0.054±0.256	(40)
20.25	0.066±0.270	(35)	-0.024±0.285	(38)	-0.029±0.304	(37)	0.028±0.317	(59)	-0.032±0.270	(26)	0.049±0.294	(24)
20.75	-0.053±0.159	(5)			-0.244±0.116	(6)	-0.077±0.301	(22)	-0.201±0.000	(1)	-0.221±0.135	(5)
Total		497		524		519		526		464		186

Table 2.6 - Comparison of Multiple Plates.

Field	Plate Pair	$<\Delta> \pm \sigma(\Delta)^a$								
		IVN Plates[a]								
		[12,14][c]	[14,15]	[15,16]	[16,17]	[17,17.5]	[17.5,18]			
831	I11526 – I7377	0.00 ± 0.18	-0.07 ± 0.17	-0.06 ± 0.16	0.00 ± 0.17	0.02 ± 0.20	-0.03 ± 0.27			
832	I11499 – N3601	-0.16 ± 0.18	-0.14 ± 0.17	-0.12 ± 0.17	-0.13 ± 0.21	-0.14 ± 0.20	-0.18 ± 0.26			
868	I11801 – I9992	-0.07 ± 0.19	-0.08 ± 0.16	-0.05 ± 0.17	0.01 ± 0.16	0.01 ± 0.20	-0.02 ± 0.26			
		IIIaF Plates[d]								
		[12,14][e]	[14,15]	[15,16]	[16,17]	[17,18]	[18,19]	[19,20.0][f]	[20,20.5][f]	[20.5,21][f]
831	F2889 – R7376	0.05 ± 0.14	0.00 ± 0.15	0.05 ± 0.13	0.06 ± 0.17	0.00 ± 0.18	0.07 ± 0.26	± 0.35	± 0.55	
832	R11502 – F1469	-0.04 ± 0.18	0.09 ± 0.11	0.12 ± 0.10	0.12 ± 0.14	0.06 ± 0.16	0.03 ± 0.17	± 0.19	± 0.23	± 0.30
868	F1178 – F2428	0.05 ± 0.12	0.06 ± 0.14	-0.03 ± 0.15	-0.07 ± 0.14	-0.05 ± 0.13	-0.02 ± 0.16	± 0.24	± 0.33	± 0.43
889	F3386 – F3479	-0.04 ± 0.13	-0.04 ± 0.13	-0.03 ± 0.14	-0.02 ± 0.14	-0.03 ± 0.15	-0.02 ± 0.16	± 0.21	± 0.26	
889	F3386 – F3561	-0.01 ± 0.11	-0.01 ± 0.11	-0.04 ± 0.12	-0.07 ± 0.15	-0.07 ± 0.17	-0.04 ± 0.17	± 0.22	± 0.26	
890	F1342 – F3493	0.03 ± 0.15	0.06 ± 0.14	0.02 ± 0.15	-0.01 ± 0.15	-0.02 ± 0.16	-0.05 ± 0.19	± 0.22	± 0.27	± 0.38
890	F1342 – R11414	-0.08 ± 0.22	0.02 ± 0.15	-0.02 ± 0.14	-0.04 ± 0.14	-0.04 ± 0.16	-0.02 ± 0.18	± 0.25	± 0.32	± 0.41

Notes to Table 2.6

[a] - Mean and Standard deviations of the Magnitude differences between the listed plates. Each magnitude bin contains over 2000 points.

[b] - Plates I11499 and I9992 were not used in the deriving the final $(r-i)^P_{Pal}$.

[c] - Magnitude (i^P_{Pal}) bin.

[d] - Only plates used in deriving the final $(r-i)^P_{Pal}$ catalogue are shown.

[e] - Magnitude (r^P_{Pal}) bin.

[f] - Standard deviations corrected for incompleteness as described in text.

Table 2.7 - Comparison of Overlap Regions .

Field:Plate – Field:PlatePair	$<\Delta> \pm \sigma(\Delta)$[a]				
	IVN Plates[b]				
	[12,14][c]	[14,16]	[16,17]	[17,18]	
FLD262:N2940 – FLD213:N2291	0.18 ± 0.09	0.24 ± 0.11	0.11 ± 0.12	0.08 ± 0.18	
FLD262:N2940 – FLD263:N3100	0.19 ± 0.12	0.07 ± 0.11	0.04 ± 0.14	0.05 ± 0.17	
FLD263:N3100 – FLD213:N2291	0.16 ± 0.14	0.24 ± 0.14	0.05 ± 0.12	0.03 ± 0.16	
FLD889:N3362 – FLD890:N3647	-0.30 ± 0.20	-0.26 ± 0.19	-0.20 ± 0.19	-0.14 ± 0.20	
FLD890:N3647 – FLD891:N3584	-0.03 ± 0.12	-0.10 ± 0.12	-0.07 ± 0.15	-0.01 ± 0.19	
	IIIaF Plates[b]				
	[12,14][d]	[14,16]	[16,18]	[18,19]	[19,20]
FLD262:F2315 – FLD213:F2978	-0.12 ± 0.09	-0.13 ± 0.09	-0.15 ± 0.16	-0.15 ± 0.20	-0.18 ± 0.26
FLD262:F2315 – FLD263:F2957	0.00 ± 0.10	-0.03 ± 0.10	-0.10 ± 0.18	-0.13 ± 0.19	-0.21 ± 0.27
FLD263:F2957 – FLD213:F2978	-0.04 ± 0.08	-0.02 ± 0.08	0.20 ± 0.10	0.01 ± 0.16	0.04 ± 0.23
FLD831:R7376 – FLD832:R11502	0.21 ± 0.09	-0.01 ± 0.09	0.05 ± 0.17	0.02 ± 0.25	0.00 ± 0.31
FLD831:F2889 – FLD832:F1469	-0.03 ± 0.11	-0.07 ± 0.08	0.00 ± 0.12	-0.04 ± 0.18	-0.06 ± 0.24
FLD889:F3386 – FLD890:F1342	-0.11 ± 0.11	-0.13 ± 0.09	-0.08 ± 0.11	-0.05 ± 0.14	-0.02 ± 0.20
FLD889:F3386 – FLD890:F3493	0.02 ± 0.17	-0.05 ± 0.11	-0.09 ± 0.13	-0.08 ± 0.16	-0.10 ± 0.23
FLD889:F3386 – FLD890:R11414	-0.11 ± 0.15	-0.11 ± 0.13	-0.10 ± 0.14	-0.04 ± 0.15	-0.04 ± 0.23
FLD889:F3479 – FLD890:F1342	-0.05 ± 0.08	-0.02 ± 0.08	0.00 ± 0.11	0.02 ± 0.15	0.01 ± 0.20
FLD889:F3479 – FLD890:F3493	0.07 ± 0.09	0.07 ± 0.12	-0.01 ± 0.14	-0.01 ± 0.16	-0.08 ± 0.23
FLD889:F3479 – FLD890:R11414	-0.01 ± 0.21	0.02 ± 0.15	-0.01 ± 0.14	0.01 ± 0.16	-0.03 ± 0.23
FLD889:F3561 – FLD890:F1342	-0.21 ± 0.09	-0.17 ± 0.14	-0.07 ± 0.12	-0.02 ± 0.17	0.01 ± 0.22
FLD889:F3561 – FLD890:F3493	-0.09 ± 0.09	-0.12 ± 0.09	-0.07 ± 0.17	-0.04 ± 0.20	0.07 ± 0.24
FLD889:F3561 – FLD890:FR11414	-0.13 ± 0.12	-0.09 ± 0.11	-0.04 ± 0.13	-0.01 ± 0.17	0.00 ± 0.23
FLD890:F1342 – FLD891:F742	-0.06 ± 0.08	-0.09 ± 0.11	-0.08 ± 0.12	-0.05 ± 0.16	-0.09 ± 0.25
FLD890:F3493 – FLD891:F742	-0.04 ± 0.08	-0.05 ± 0.11	0.00 ± 0.13	0.04 ± 0.16	0.06 ± 0.24

Notes to Table 2.6

[a] - Mean and Standard deviations of the Magnitude differences between the listed plates

[b] - Only plates used in deriving the final $(r-i)^P_{Pal}$ catalogue are shown.

[c] - Magnitude (i^P_{Pal}) bin. Each bin contains (respectively) at least 40, 80, 80 &120 points.

[d] - Magnitude (r^P_{Pal}) bin. Each bin contains (respectively) at least 50, 250, 600, 600 & 1000 points.

Table 2.8 - Final Catalogue Parameters.

Field : Grade	Plate	$(r^P_{Pal})_{Lim}$[a] /$(i^P_{Pal})_{Lim}$	Compl.[b] (%)	Area[c] (□°)	Grade Comments (see text)
829 : A	I12254	18.0	78%	22.38[d]	
	F768	20.5	87%		
	R8222	20.1	96%		
831 : A	I11526	18.0	99%	24.61	
	I7377	18.0	73%		
	F2889	20.1	65%		
	R7376	20.7	75%		
832 : A	I11499	18.0	84%	27.68	
	N3601	18.0	65%		
	OR11502	20.7	82%		
	F1469	20.7	91%		
263 : A	N3100	18.0	86%	25.05	
	F2957	20.5	75%		
213 : B	N2291	17.5	75%	25.13	N2291 violates limit.
	F2978	20.3	75%		F2978 violates limit.
262 : B	N2940	18.0	80%	24.96	
	F2315	20.3	79%		F2315 shows offset & violates limit.
513 : B	N1197	17.5	85%	23.13	N1197 viloates limit.
	F1094	20.5	75%		
868 : A	I11801	18.0	80%	22.69	
	I9992	18.0	90%		
	F1178	20.5	75%		
	F2428	20.5	52%		
889 : B	N3362	18.0	83%	25.10	N3362 shows offset.
	F3386	20.3	94%		F3386 viloates limit.
	F3479	20.1	75%		F3479 viloates limit.
	F3561	20.3	76%		F3561 viloates limit.
890 : A	N3647	18.0	80%	25.22	
	OR11414	20.5	82%		
	F1342	20.7	83%		
	F3493	19.7	76%		
891 : A	N3584	18.0	83%	24.91	
	F742	20.5	82%		

Notes to Table 2.8

[a] - Magnitude limit as described in text.

[b] - Completeness level at the magnitude limit for this plate. Calculated using predicted counts from a Galactic model and a (normalised) galaxy count model, as descibed in text.

[c] - The area quoted is that of the total region in that field in which $(r-i)^P_{Pal}$ could be measured. Some of the adjacent fields overlapped slightly – the total region of overlap was 3.48□°, giving a total surveyed area of 269.79□°.

[d] - This area is for the overlap region of I12254 with F768. A small region (2.41□°) from R8222 which overlapped I12254, but *not* F768 was also surveyed, though only for $i^P_{Pal} < 17.0$.

Table 2.9 - Sample Contamination Tests for Reddest 200 Stars in Four Field.

Field	$(r-i)^P_{Pal}$ Max.	N_{Dud}	N_{Unc}	N_{Good}	N_{Dud} Left	N_{Unc} Left
Field 889	1.73	24	8	174	1	5
Field 262	1.63	0	8	197	0	5
Field 832	1.75	2	2	197	2	1
Field 513	1.66	3	6	192	1	1

Notes to Table 2.9

$(r-i)^P_{Pal}$ Max. is the colour of the bluest star examined; N_{Dud},N_{Unc} and N_{Good} are the number of stars designated (respectively) 'dud','uncertain' or 'stellar' (see text); N_{Dud} Left and N_{Unc} Left are the number of 'dud' and 'uncertain' stars left in the sample after application of the '1-b/a' cut.

Table 2.10 - The Stellar Luminosity Function.

Binning 1					Binning 2				
M_{Bol}[a]	Φ_0[b] ($pc^{-3}mag.^{-1}$)	$\sigma(\Phi_0)$[b]	#	Volume[c] (10^3pc^3)	M_{Bol}	Φ_0 ($pc^{-3}mag.^{-1}$)	$\sigma(\Phi_0)$	#	Volume (10^3pc^3)
8.75	22.197	1.783	155	12.01	9.00	27.007	1.431	356	30.58
9.25	25.946	1.118	539	43.64	9.50	27.622	1.043	702	52.72
9.75	32.074	1.052	930	58.97	10.00	30.879	0.997	960	63.25
10.25	24.944	0.871	820	66.15	10.50	21.554	0.798	730	68.11
10.75	16.190	0.684	560	69.42	11.00	13.123	0.619	449	70.29
11.25	11.419	0.629	330	57.75	11.50	10.567	0.736	206	38.64
11.75	8.779	0.801	120	25.70	12.00	7.658	0.943	66	16.99
12.25	9.561	1.313	53	11.18	12.50	10.385	1.663	39	7.32
12.75	8.114	1.771	21	4.78	13.00	6.810	2.053	11	3.11
13.25	13.798	3.827	13	2.01	13.50	11.876	3.959	9	1.30
13.75	10.008	5.004	4	0.84	14.00	22.307	9.107	6	0.52
14.25	29.799	13.326	5	0.33	14.50	50.619	25.310	4	0.12
14.75	54.866	31.677	3	0.12					

Notes to Table 2.10

[a] - Bolometric magnitude of bins centre. All bins have width 0.5 magnitudes.

[b] - Values of Φ_0 and $\sigma(\Phi_0)$ are $\times 10^3$.

[c] - Volume sampled by survey (in 10^3 cubic parsecs) for a stars with M_{Bol} equal to the bin centre value.

Figure Captions.

Figure 2.1 - Bandpasses for Various RI Magnitude Systems. Bandpasses for the Cousins (R_C & I_C) systems are shown as heavy lines; for the photographic (IIIaF+OG590, IIIaF+RG630 & IVN) systems as lighter lines; and for the Gunn (r & i) systems as the lightest lines. Also shown superimposed is the spectra of the VLM star LHS2065 (spectral type M8-M9). All filter tracings are due to Bessell (1986) except the Gunn i which is due to J. Cohen (priv. comm.).

Figure 2.2 - $ri_{Palomar}$ to $RI_{Cousins}$ Colour Terms. These figures represent the combined observations of standards on the Cousins system using Gunn r and i filters and a TEKTRONIX unthinned CCD. Each night's zero-point was calculated using standards in the range $(R–I)_C \approx 0.5 \pm 0.1$. **(a)** shows the transformation derived for $(r - i)^C_{Pal}$. Each point represents a separate observation with uncertainty $\approx$ 0.03mag. The curve is a fourth-order least-squares polynomial, which provides a good fit to the data (Coefficients; $a_0 = 0.162$, $a_1 = -0.561$, $a_2 = 0.671$, $a_3 = -0.360$, $a_4 = 0.0740$) over the range $0.1 < (R - I)_C < 2.2$. This gives a 1-σ residual for a single observation of 0.012 mag. **(b)** shows the transformation derived for i^C_{Pal}. Each point represents a separate observation with uncertainty $\approx$ 0.05mag. A first order fit gives coefficients, $a_0 = 0.009 \pm 0.004$, $a_1 = -0.014 \pm 0.004$. Considering the typical uncertainties of the observations, the uncertainty on the coefficient a_1 and the fact that this slope is primarily determined by the reddest stars which are also the most uncertain, we consider a zeroth order fit with $a_0 = -0.046 \pm 0.004$ to be more appropriate, which gives a 1-σ residual for a single observation of 0.022mag.

Figure 2.3 - UKST Vignetting Function (from Tritton 1983) Shown are the values of $V(\alpha) = \frac{I(\alpha)}{I(0)}$ and $\Delta m(\alpha) = -2.5 \log \frac{I(\alpha)}{I(0)}$ where α = angular radius in degrees, and I = intensity. Notice that the plates are essentially uniformly exposed out to a radius of three degrees.

Figure 2.4 - Survey 'Footprints' in both Equatorial (a) and Galactic (b) Co-ordinates.

Figure 2.5 - The Geometry of Scanned Plate Regions. (a) - The COSMOS scan of POSSII plate N2291; COSMOS scans only a 5.35°×5.35° region (inner box) of the 6.6°×6.6° plate (outer box). A point is plotted for each COSMOS detected object. (b) - The same figure as (a) is plotted for POSSII plate F2428, with objects more than 3° from the plate centre removed. (c) - The same figure as (b) is plotted for UKST plate R5780. The UKST plate has been rotated so that it is the same

orientation as the Palomar plate - the slightly different areas of the plate scanned can be seen when the (b) and (c) are compared.

Figure 2.6 - Some Example of Spurious COSMOS Images Produced by Bright or Extended Objects on plate R5780. The objects shown are (a) NGC 5850 (m_{pg} = 13.6), (b) NGC 5838 (m_{pg} = 12.1), (c) SAO 120813 (m_V = 7.7), and (d) SAO 120809 (m_V = 4.6).

Figure 2.7 - Sample r^P_{Pal} and i^P_{Pal} Calibration Curves. (a) for POSSII plate N2291, and (b) for UKST plate R5780.

Figure 2.8 - An Example of the Offsets produced by Field Effects. Each CCD calibration field has been plotted with a separate symbol. Notice how different symbols more or less reproduce the same function but are offset from each other - these offsets are particularly pronounced for brighter (i.e., saturated) images.

Figure 2.9 - Sample S-parameter plots for both IVN ((a) Plate I11801) and IIIaF ((b) Plate R5780) plates. r^P_{Pal} and r^P_{Pal} magnitudes have been multiplied by 100.

Figure 2.10 - Sample ϕ-parameter plots for both IVN ((a) Plate I11801) and IIIaF ((b) Plate R5780) plates. r^P_{Pal} and r^P_{Pal} magnitudes have been multiplied by 100.

Figure 2.11 - Photographic-CCD $(r - i)_{Pal}$ Colour Term : IIIaF+RG610 & IVN combination (i.e., appropriate for Palomar F plates). Colours have been multiplied by 100.

Figure 2.12 - Photographic-CCD $(r - i)_{Pal}$ Colour Term : IIIaF+OG590 & IVN combination (i.e., appropriate for UKST OR plates). Colours have been multiplied by 100.

Figure 2.13 - Photographic-CCD $(r - i)_{Pal}$ Colour Term : IIIaF+RG630 & IVN combination (i.e., appropriate for UKST R plates). Colours have been multiplied by 100.

Figure 2.14 - Observed Differential Number Counts. Observed counts are plotted as the indicated symbols. The dashed lines represent star counts as predicted by the Galactic model of Reid. The dot-dashed lines are galaxy counts normalised for each field as described in the text. The solid lines are the total predicted objects counts (i.e., stars + galaxies).

Figure 2.15 - Comparison of Magnitudes from Duplicate IVN Plates. E.g., in panel (a) differences are displayed in the sense Δi^P_{Pal} = (I11526 magnitude - I7377 magnitude) $\times 100$.

Figure 2.16 - Comparison of Magnitudes from Duplicate IIIaF Plates. See Fig 2.15 caption.

Figure 2.17 - Comparison of Overlapping IVN Plates. See Fig 2.15 caption.

Figure 2.18 - Comparsion of Overlapping IIIaF Plates. See Fig 2.15 caption.

Figure 2.19 - Region of the i_{Pal} limits as a function of $(r-i)^P_{Pal}$ for a physical limit to a plate of $i_{Pal} = 18$, and r^P_{Pal} limits of 20.3 (dashed line), 20.5 (dot-dashed line) and 20.7 (dotted line) magnitudes.

Figure 2.20 - Adopted M_I:$(r-i)_{Pal}$ colour-magnitude relation.

Figure 2.21 - Adopted BC_I:$(r-i)_{Pal}$ relation.

Figure 2.22 - Survey distance limits as a function of sample limits and $(r-i)_{Pal}$ colour.

Figure 2.23 - Number densities of stars (a,c) and galaxies (b) as a function of $(r-i)_{Pal}$ in nine fields (see text). Panel (b) and (c) are plotted on an identical scale for ease of comparison.

Figure 2.24 - $1/V_a$ LF for all eleven fields in the survey. The solid line shown is a LF due to Reid (1987) which summarises much of the previous work. The Reid LF is based on the nearby star sample of Weilen *et al.* (1983) for $M_{Bol} < 10$ and several photometric surveys based (like this study) on optical colours from 48″-Schmidt plates.

Figure 2.25 - $1/V_a$ LF for; *circles* – standard assumptions, i.e., $d_{lim} = 150$pc, $h = 350$pc; *squares* – $d_{lim} = 200$pc, $h = 350$pc; *triangles* – $d_{lim} = 150$pc, $h = 300$pc.

Figure 2.26 - $1/V_a$ LF corrected to first-order for Malmquist-type biases. *circles* – raw LF. *solidline* – smoothing spline fit to raw LF. *squares* – raw LF corrected for biases as described in text.

Figure 2.27 - $1/V_a$ LF in each of the four directions studied. These are; *circles* - Fields 213,262 and 263. $\langle b \rangle \sim 48, \langle l \rangle \sim 165$; *crosses* - Fields 513 and 868. $\langle b \rangle \sim 55, \langle l \rangle \sim 165$; *squares* - Fields 829, 831 and 832. $\langle b \rangle \sim -53, \langle l \rangle \sim 170$; *triangles* - Fields 889,890 and 891. $\langle b \rangle \sim -44, \langle l \rangle \sim 64$.

Figure 2.1

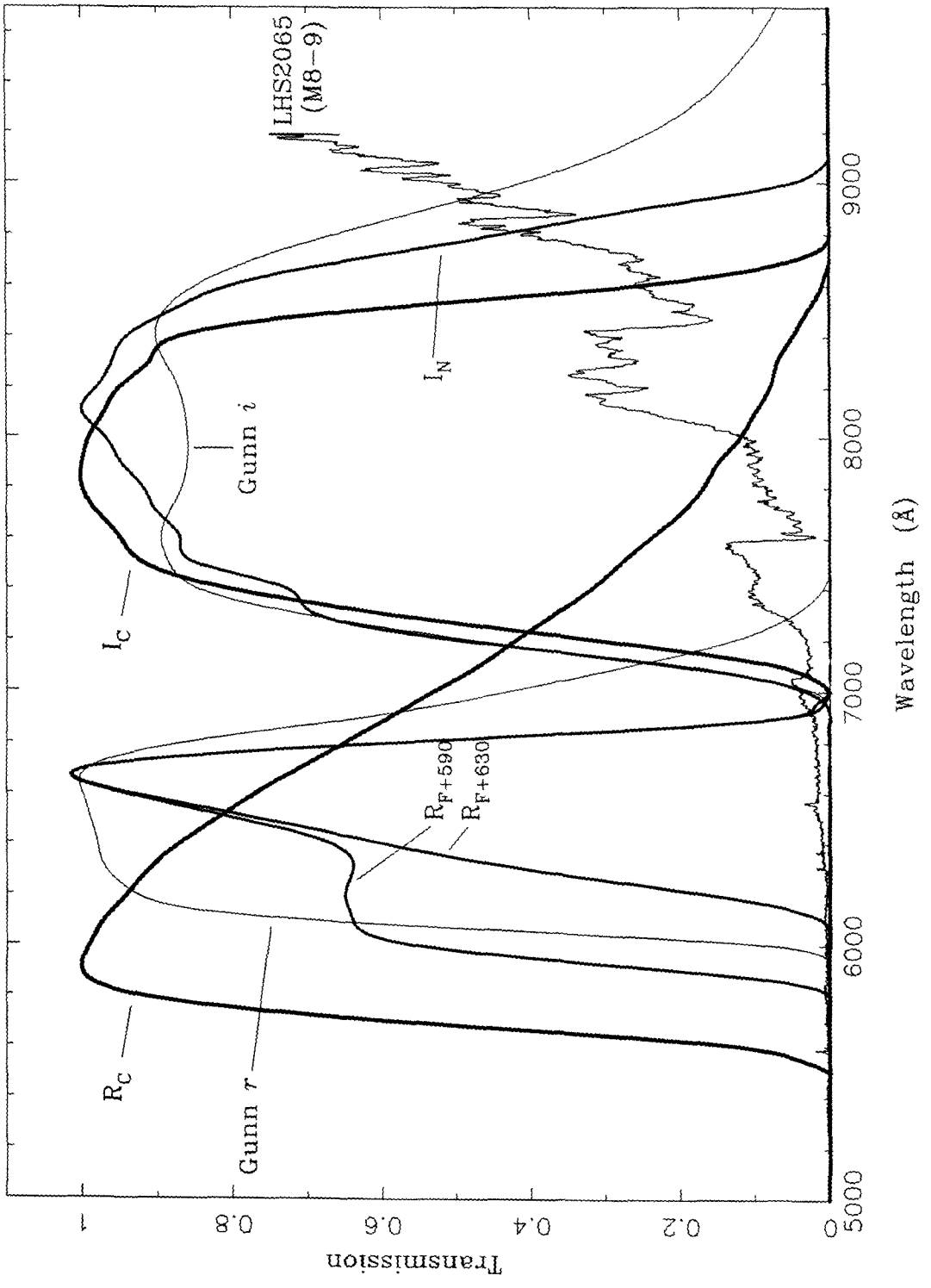
LHS2065
(M8−9)
I_N
Gunn i
I_C
R_{F+590}
R_{F+630}
R_C
Gunn r
Transmission
0
0.2
0.4
0.6
0.8
1
5000
6000
7000
8000
9000
Wavelength (Å)

Figure 2.2

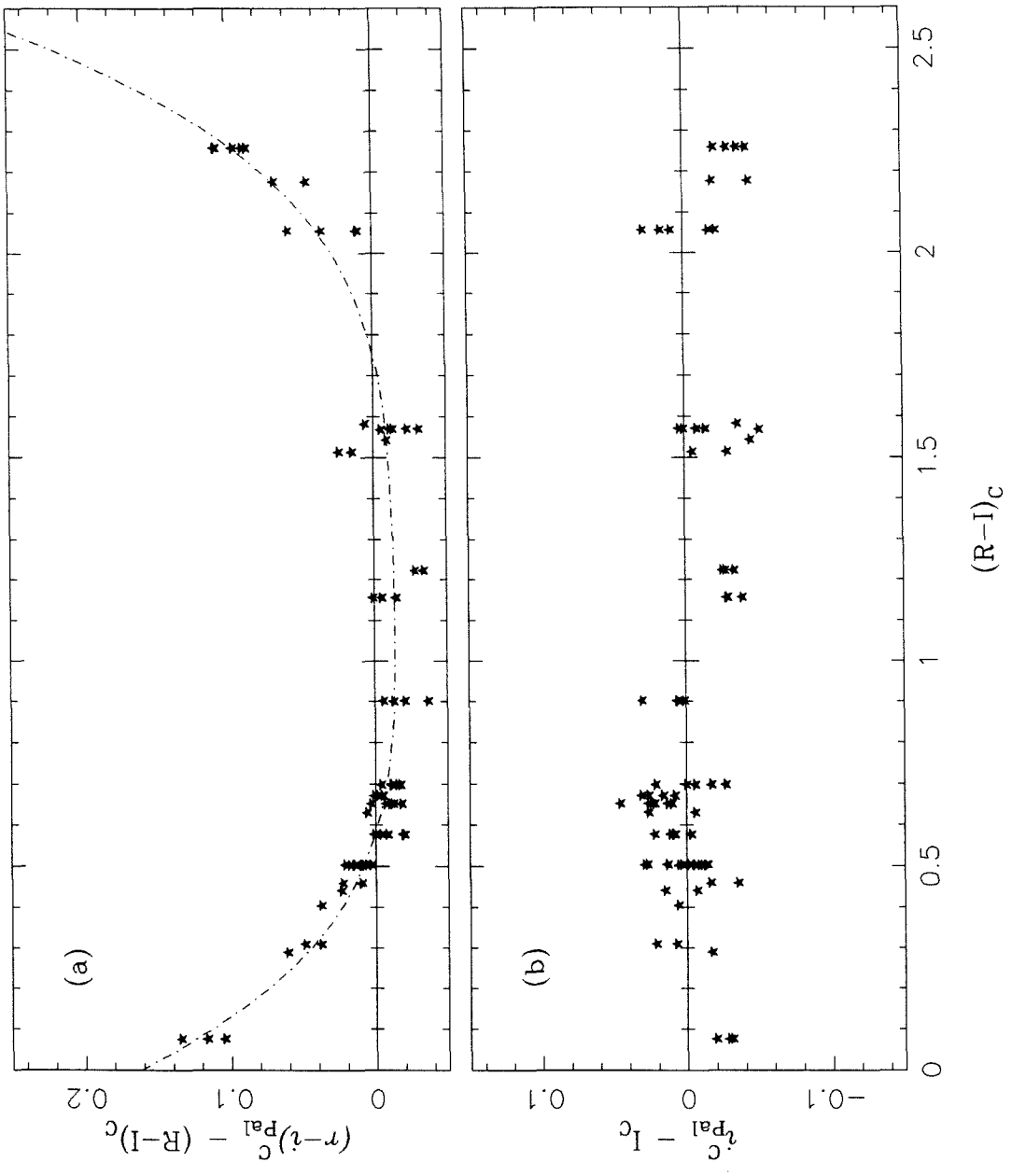

Figure 2.3

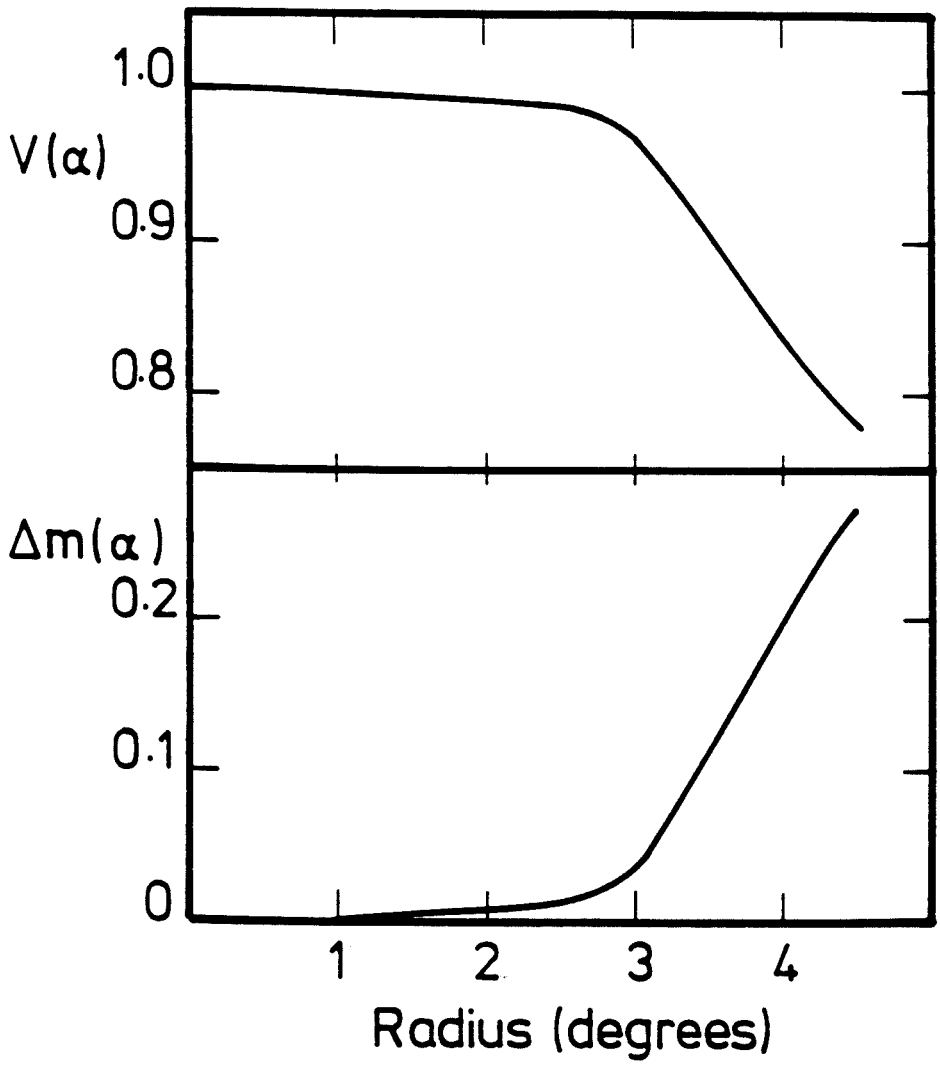

Figure 2.4(a),(b) - Survey Footprints

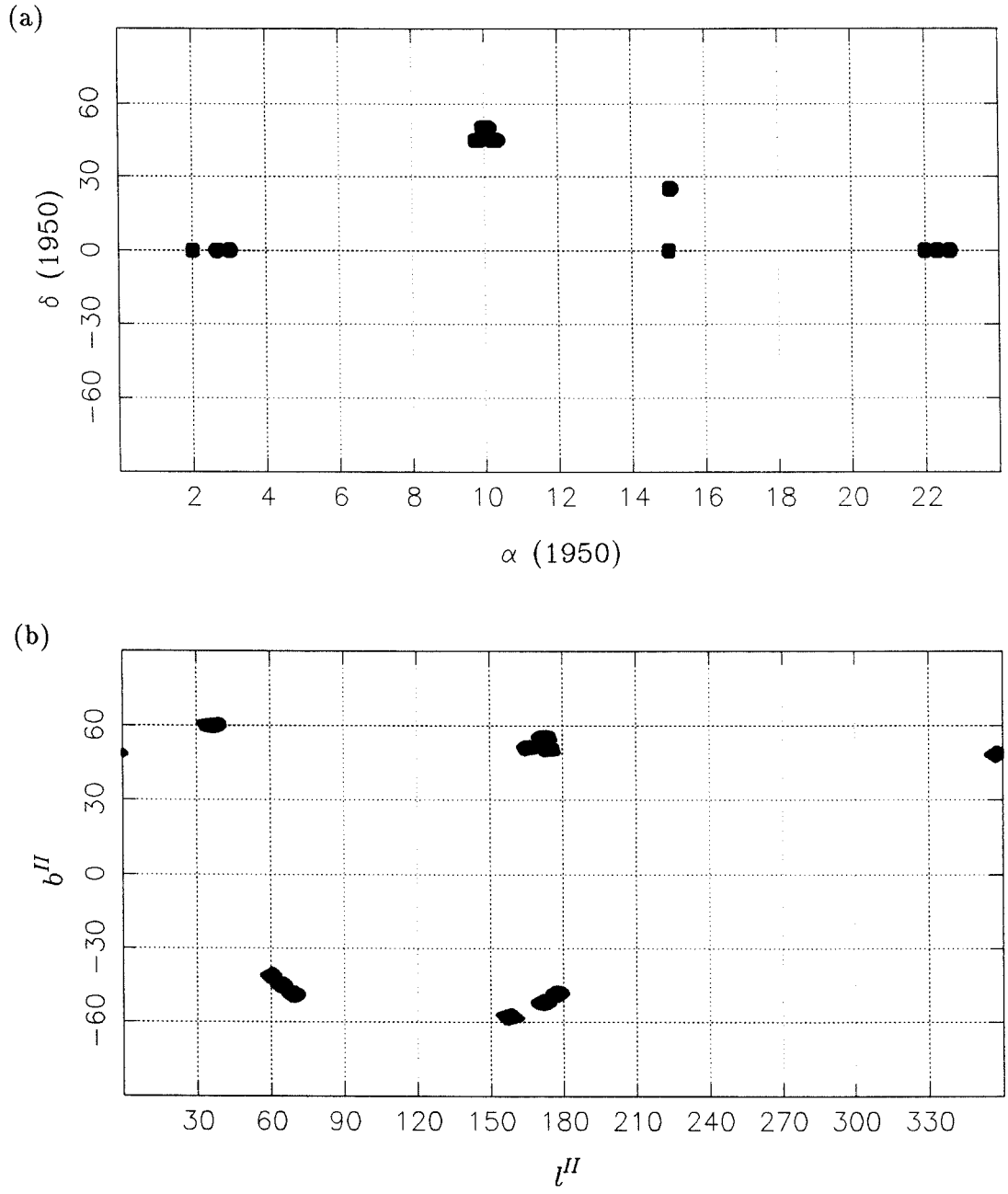

Figure 2.5(a)

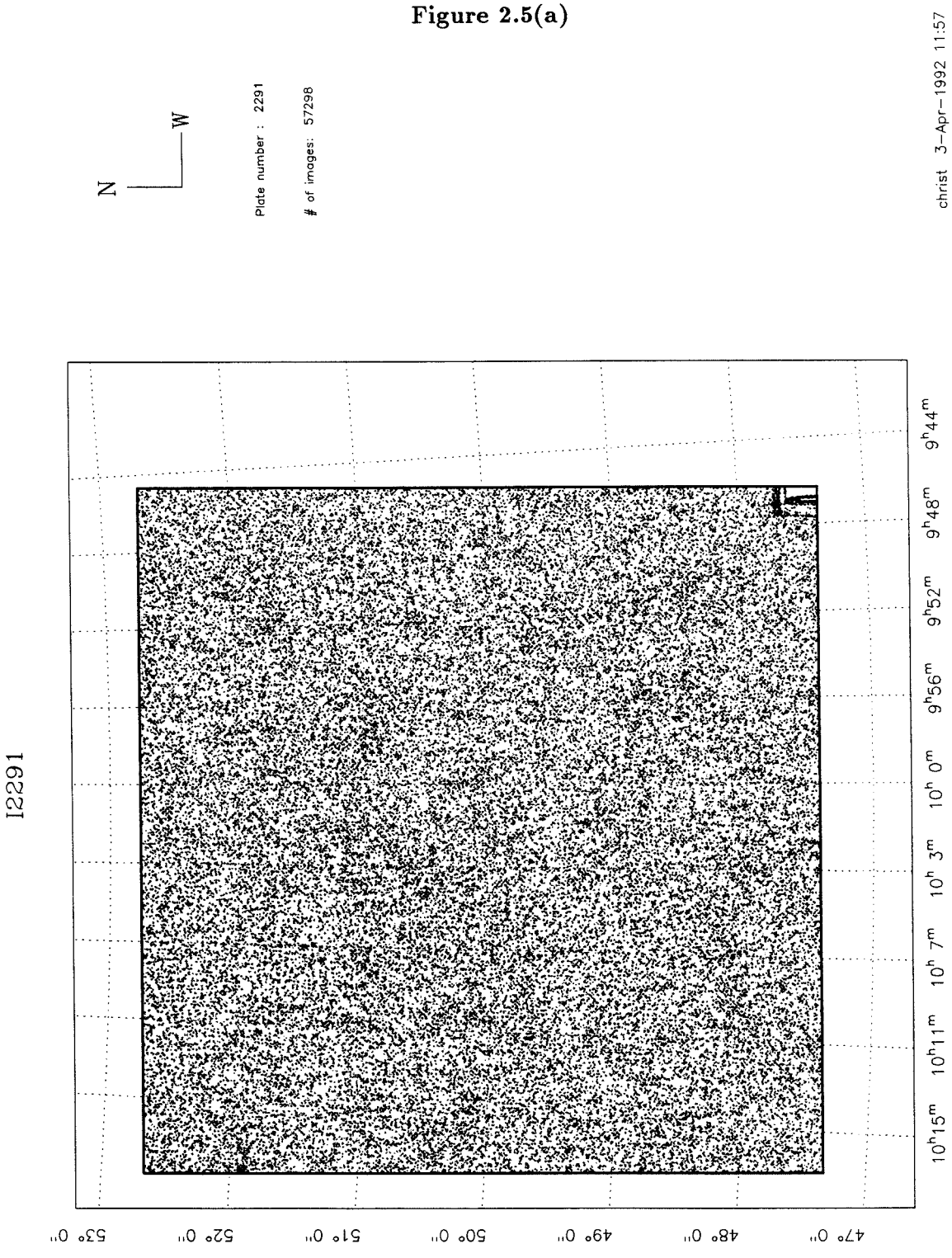
N
W
Plate number : 2291
# of images: 57298
christ 3-Apr-1992 11:57
I2291
53° 0′
52° 0′
51° 0′
50° 0′
49° 0′
48° 0′
47° 0′
10h15m
10h11m
10h 7m
10h 3m
10h 0m
9h56m
9h52m
9h48m
9h44m

Figure 2.5(b)

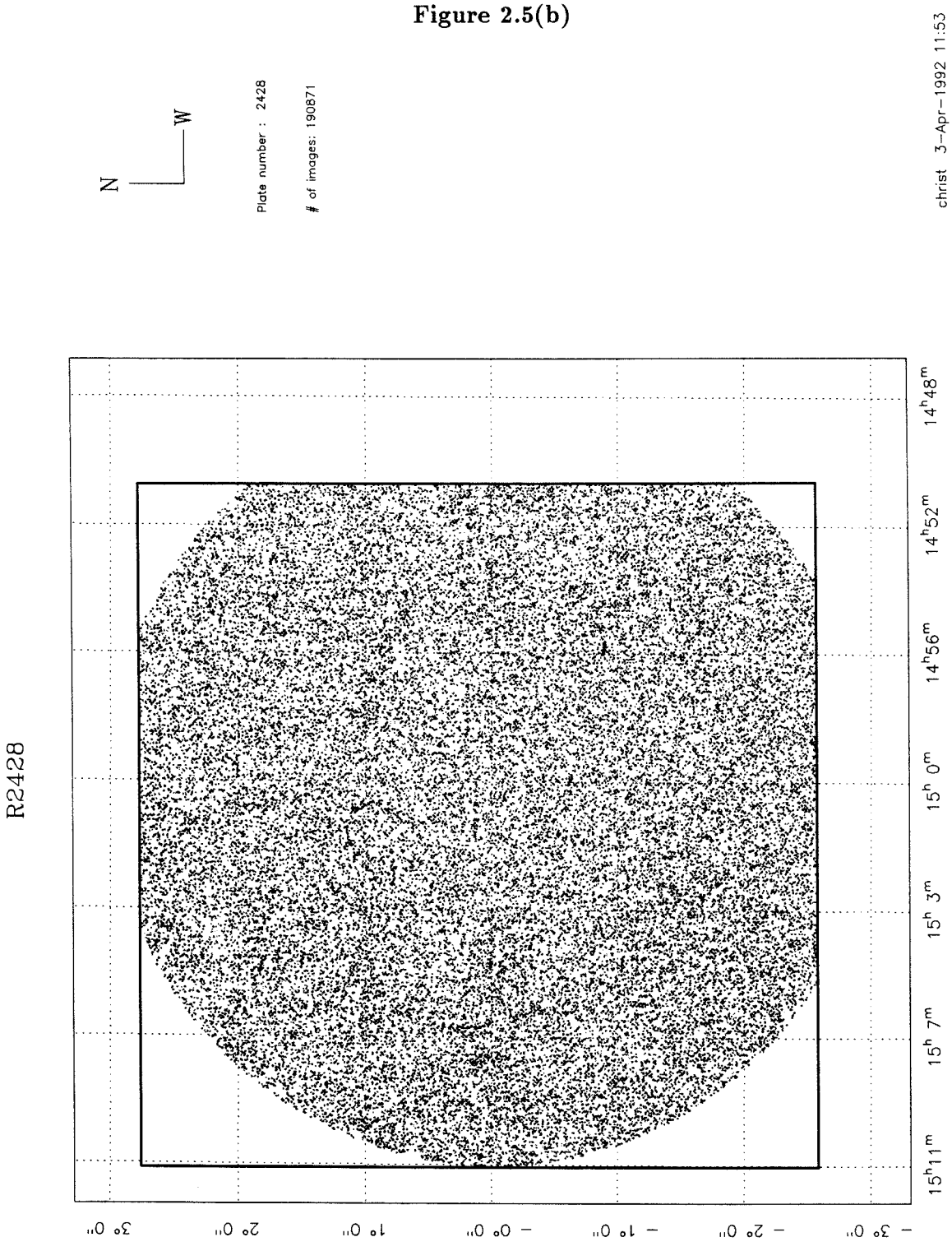
N
W
Plate number : 2428
# of images: 190871
christ 3-Apr-1992 11:53
R2428
15h11m
15h 7m
15h 3m
15h 0m
14h56m
14h52m
14h48m
– 30° 0"
– 20° 0"
– 10° 0"
– 0° 0"
10° 0"
20° 0"
30° 0"

Figure 2.5(c)

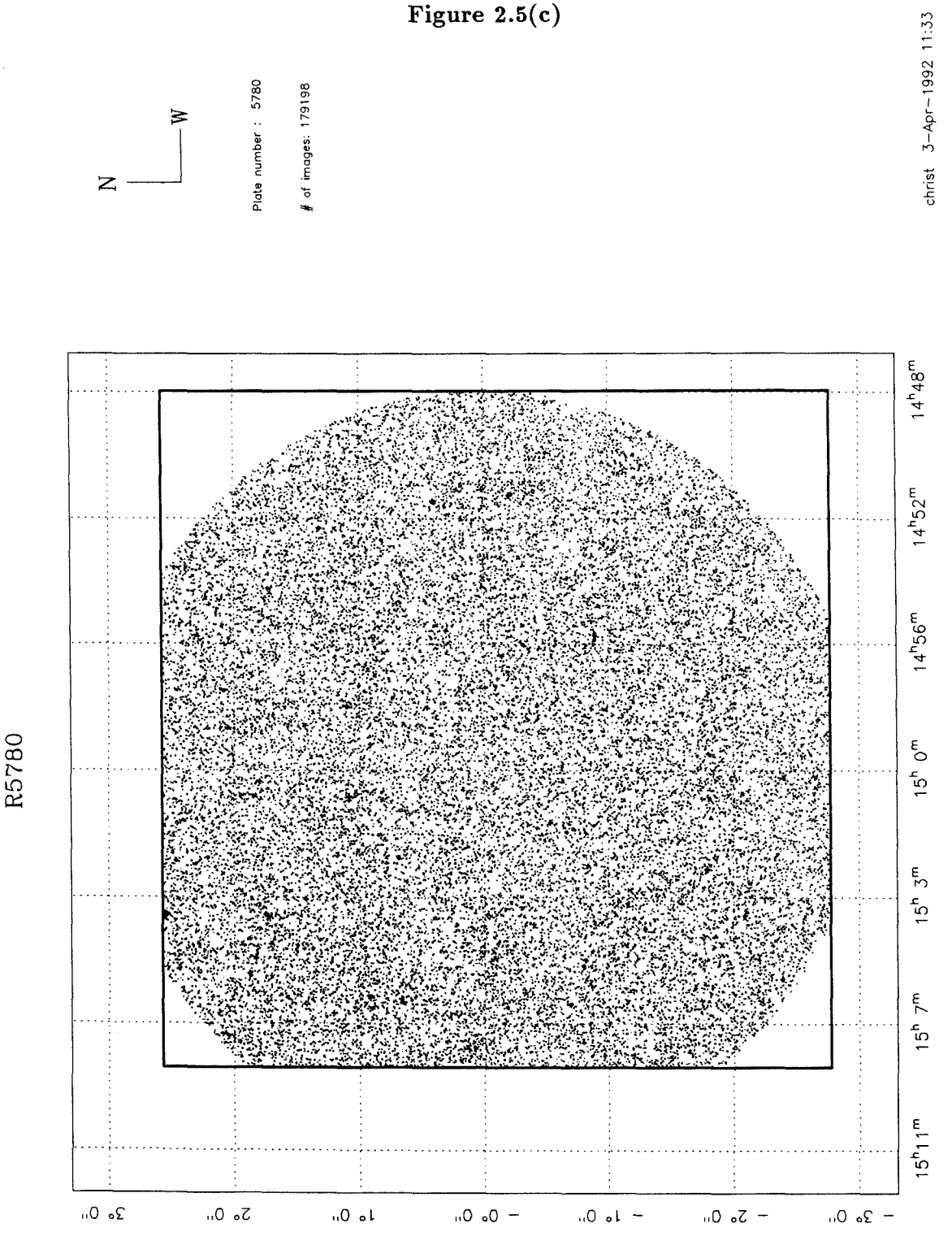
N
W
Plate number : 5780
# of images: 179198
christ 3-Apr-1992 11:33
R5780
15h11m
15h 7m
15h 3m
15h 0m
14h56m
14h52m
14h48m
30° 0'
20° 0'
10° 0'
0° 0'
-10° 0'
-20° 0'
-30° 0'

Figure 2.6

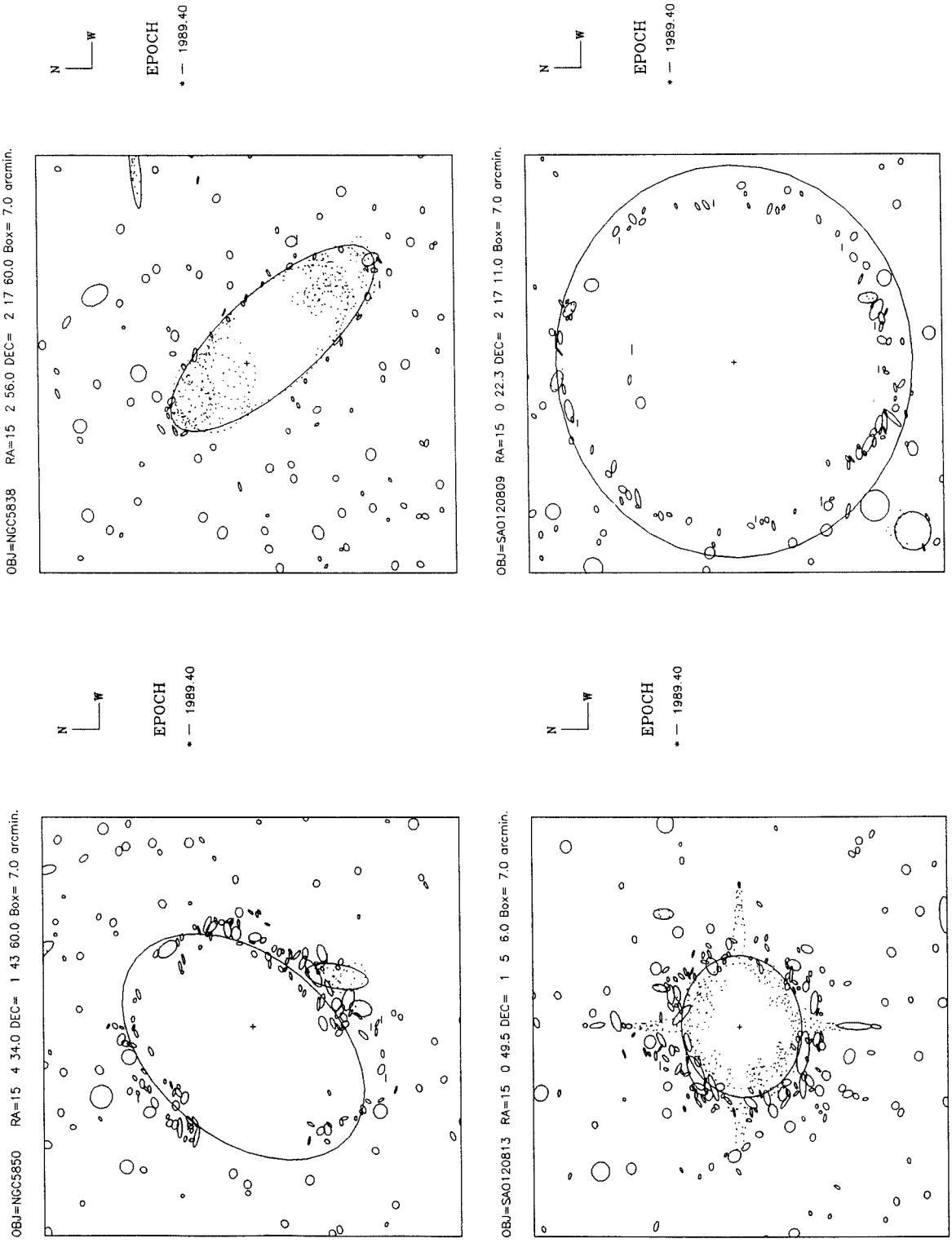
OBJ=NGC5838 RA=15 2 56.0 DEC= 2 17 60.0 Box= 7.0 arcmin.
N
W
EPOCH
* — 1989.40
OBJ=SA0120809 RA=15 0 22.3 DEC= 2 17 11.0 Box= 7.0 arcmin.
N
W
EPOCH
* — 1989.40
OBJ=NGC5850 RA=15 4 34.0 DEC= 1 43 60.0 Box= 7.0 arcmin.
N
W
EPOCH
* — 1989.40
OBJ=SA0120813 RA=15 0 49.5 DEC= 1 5 6.0 Box= 7.0 arcmin.
N
W
EPOCH
* — 1989.40

Figure 2.7(a)

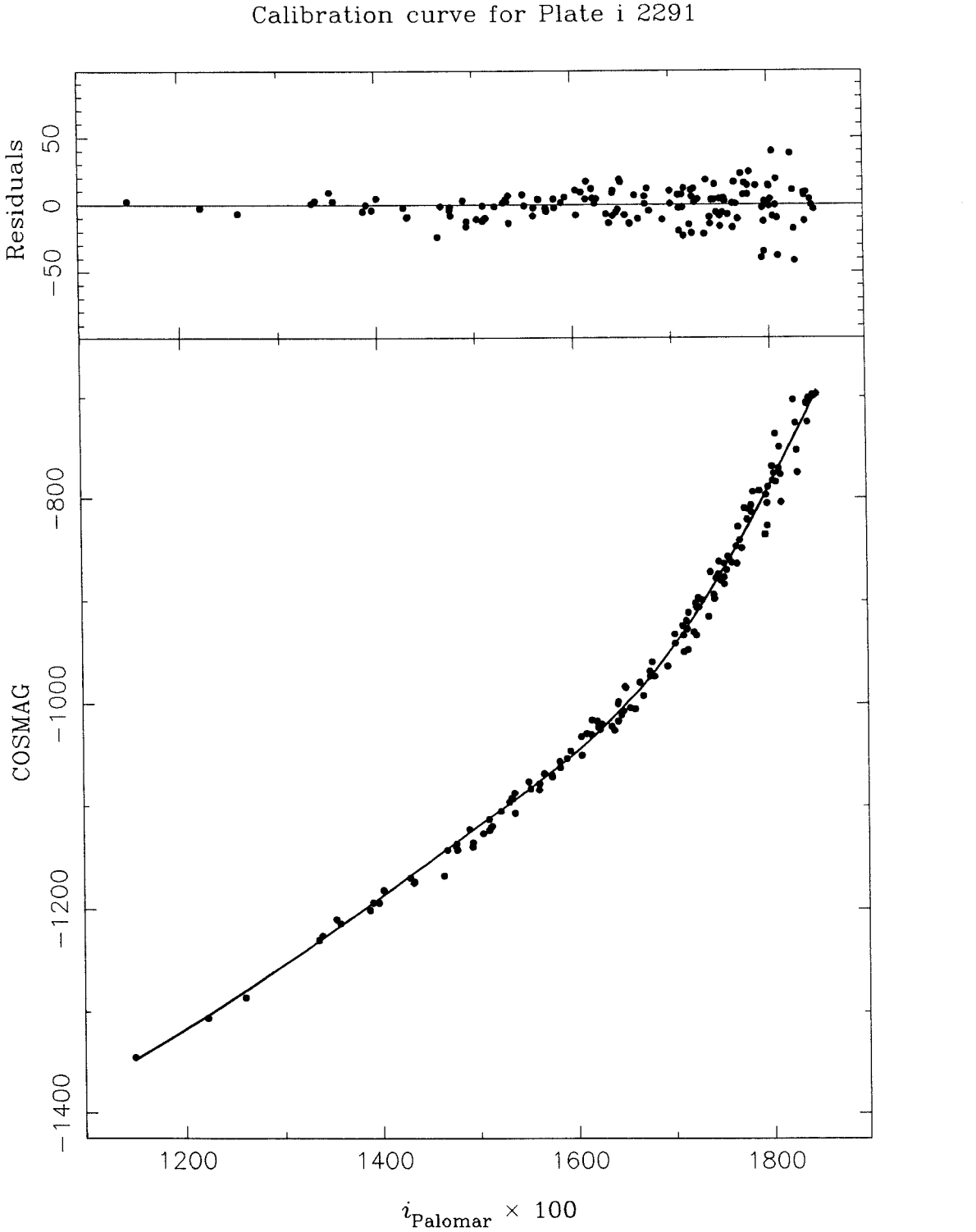
Calibration curve for Plate i 2291
Residuals
50
0
-50
COSMAG
-800
-1000
-1200
-1400
1200
1400
1600
1800
$i_{\text{Palomar}} \times 100$
christ 8-Mar-1992 14:17

Figure 2.7(b)

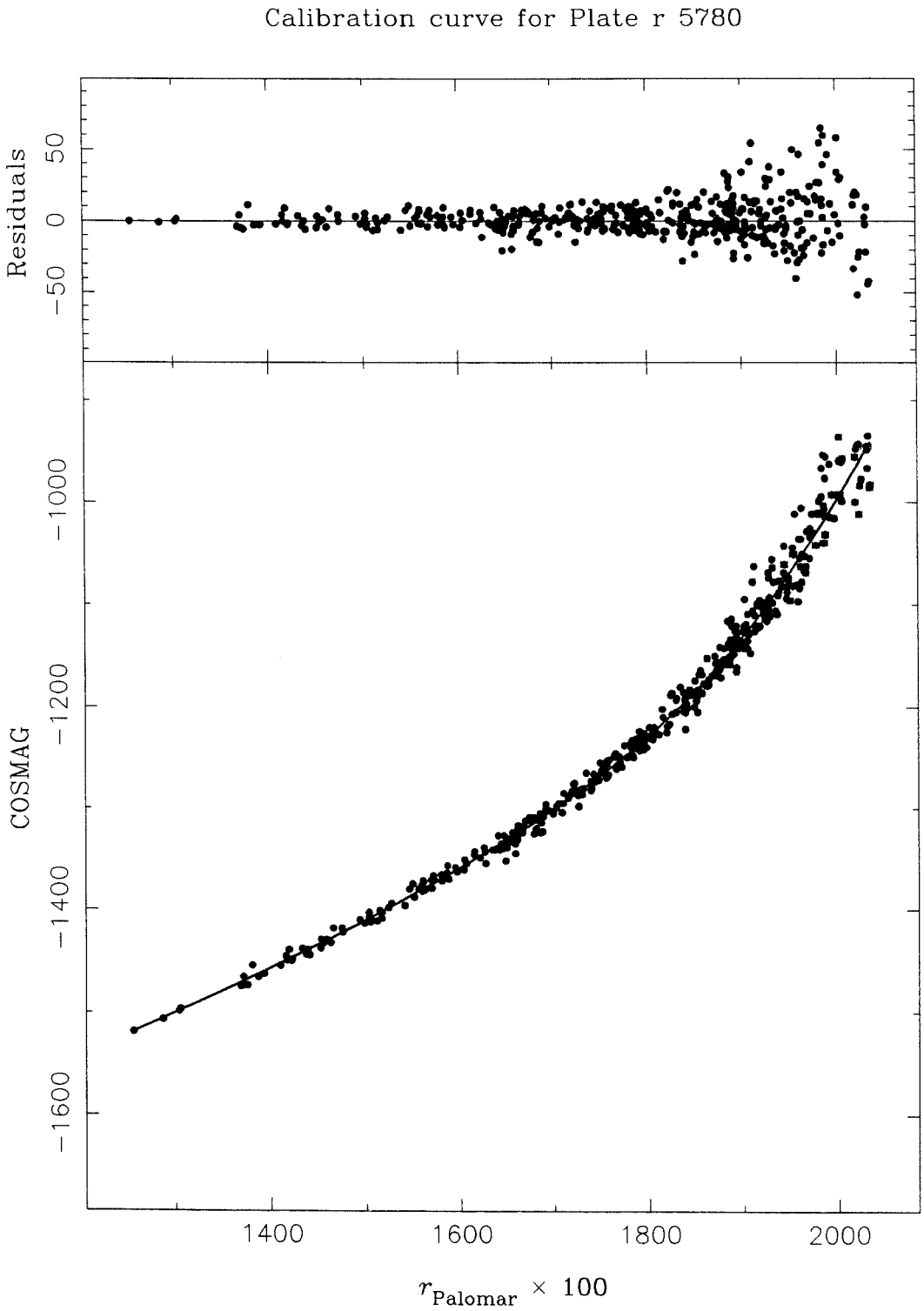
Calibration curve for Plate r 5780
Residuals
50
0
−50
COSMAG
−1000
−1200
−1400
−1600
1400
1600
1800
2000
$r_{\text{Palomar}} \times 100$
christ 8-Mar-1992 14:59

Figure 2.8

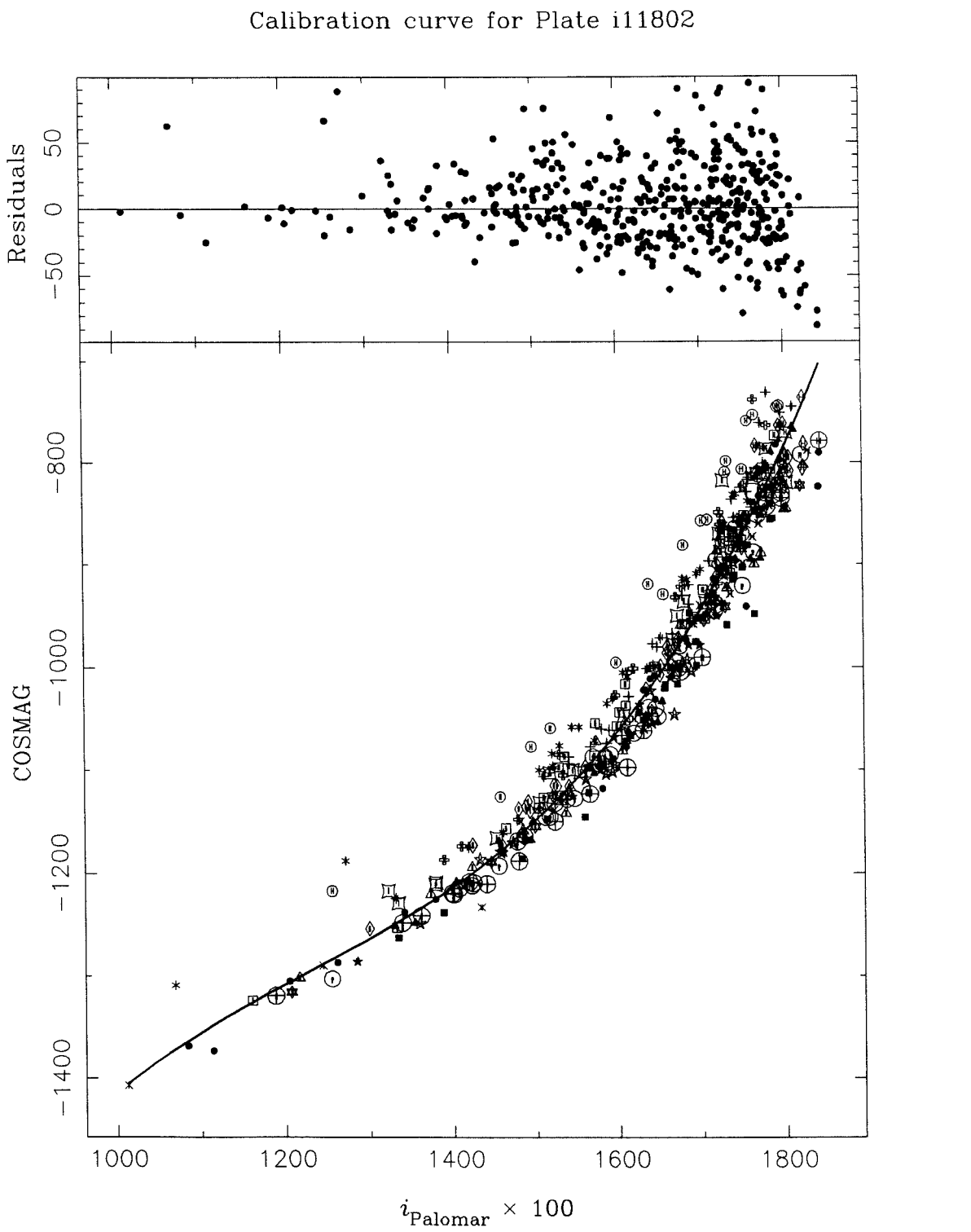
Calibration curve for Plate i11802
Residuals
50
0
−50
COSMAG
−800
−1000
−1200
−1400
1000
1200
1400
1600
1800
$i_{\text{Palomar}} \times 100$
christ 4-Apr-1992 16:18

Figure 2.9(a)

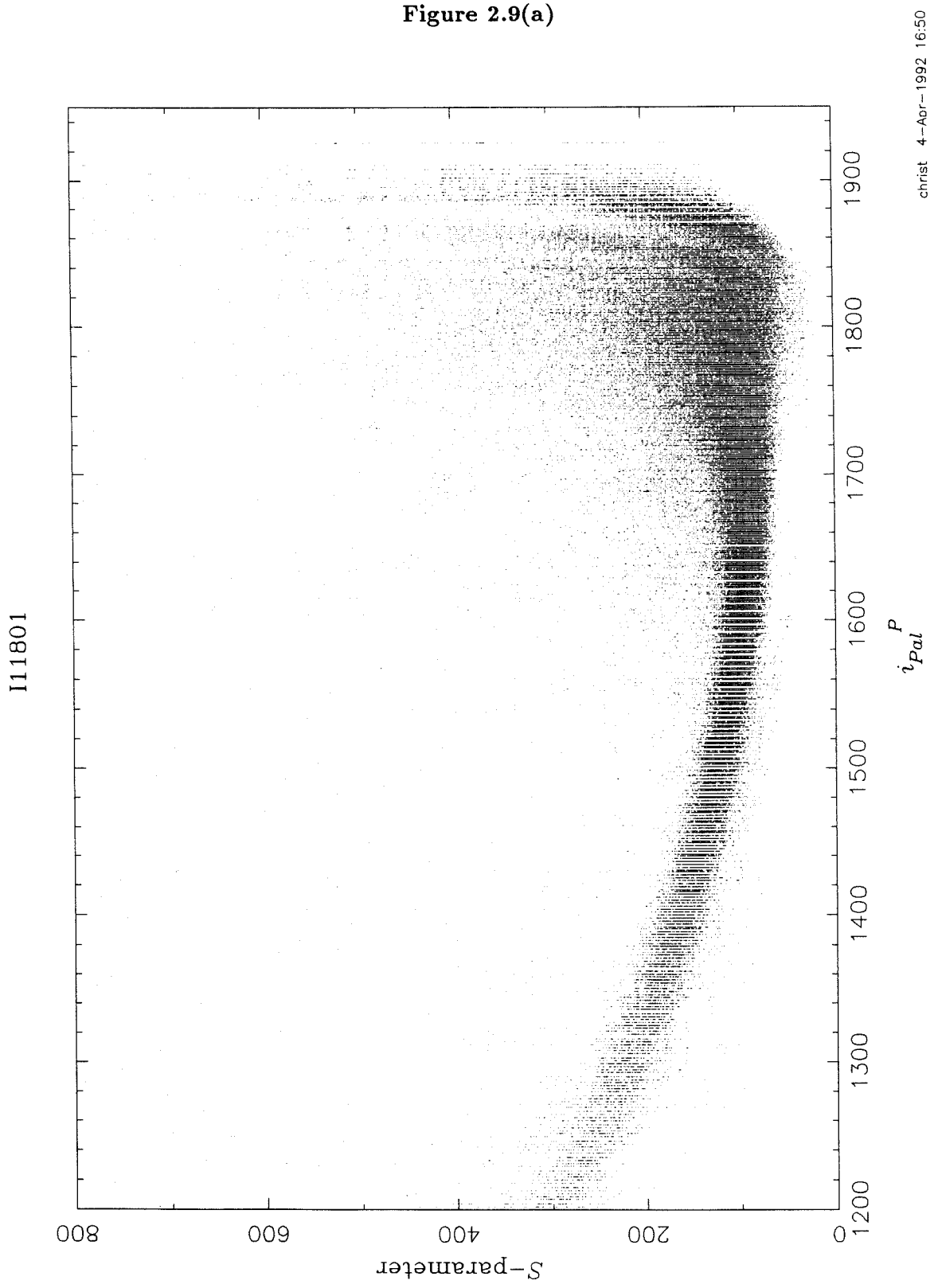
I11801
christ 4-Apr-1992 16:50
i_{Pal}^{P}
1200
1300
1400
1500
1600
1700
1800
1900
0
200
400
600
800
S–parameter

Figure 2.9(b)

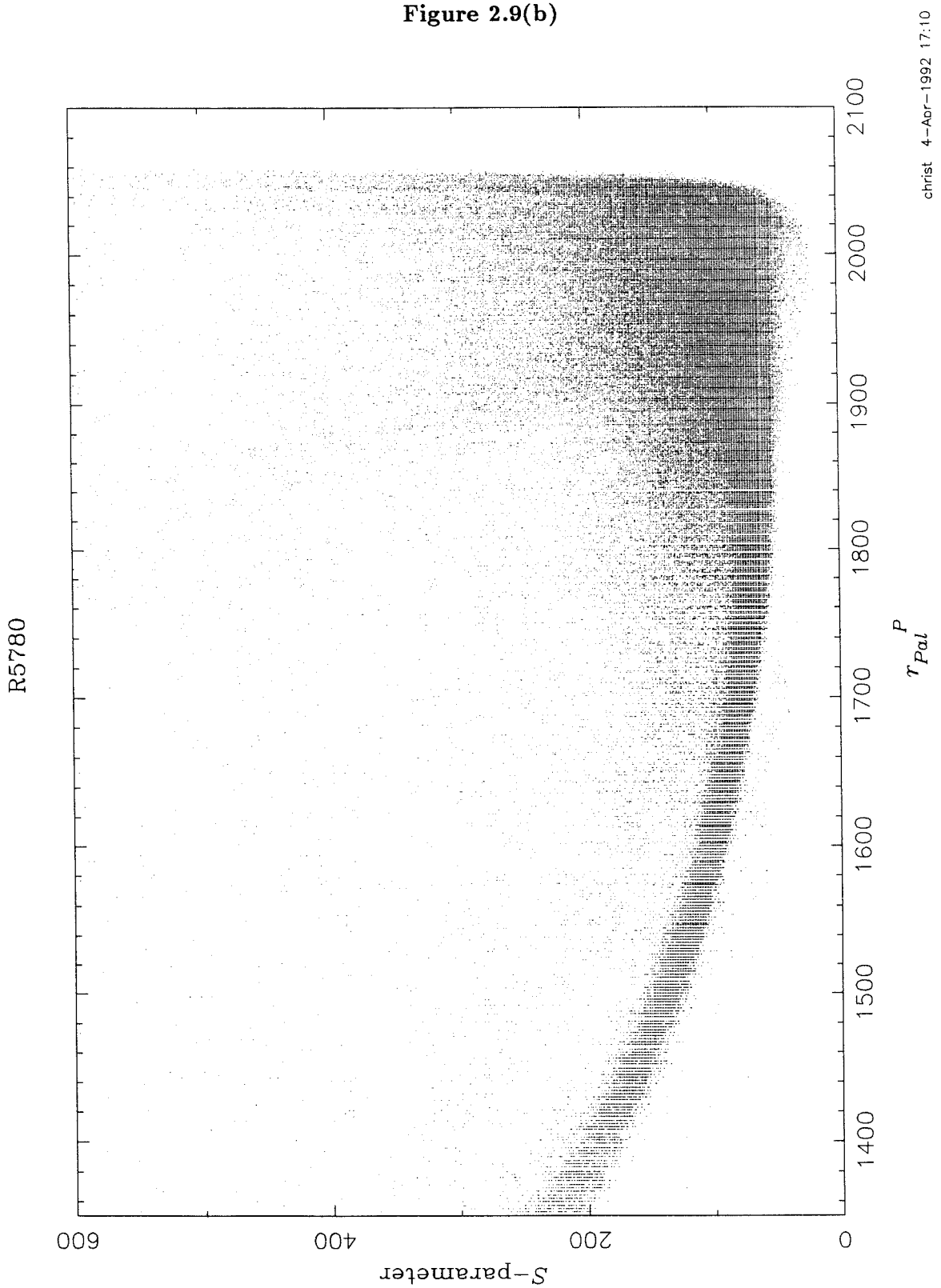
R5780
S–parameter
0
200
400
600
1400
1500
1600
1700
1800
1900
2000
2100
r_{Pal}^{P}
christ 4-Apr-1992 17:10

Figure 2.10(a)

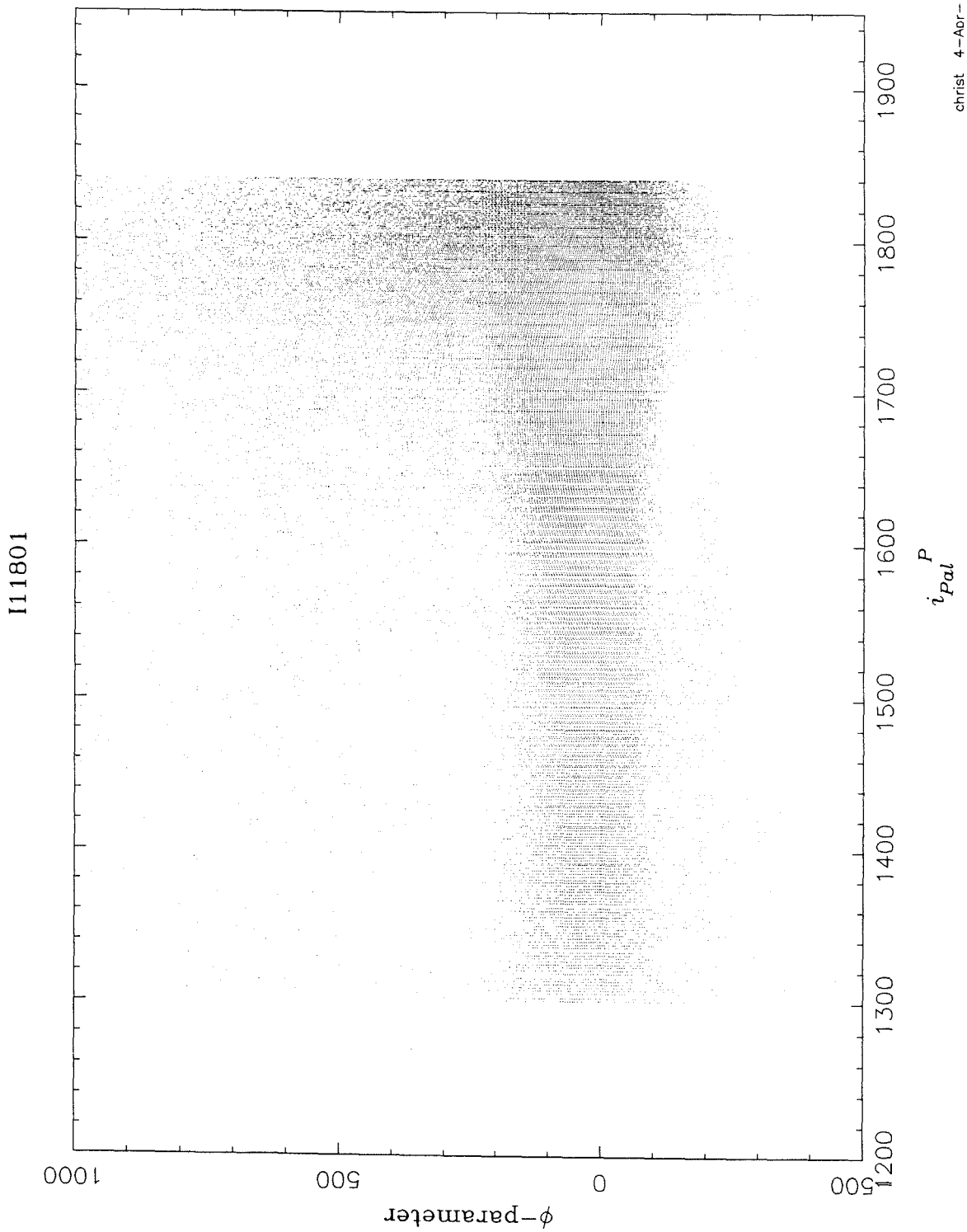
I11801
i^P_{Pal}
1900
1800
1700
1600
1500
1400
1300
1200
1000
500
0
500
ϕ–parameter
christ 4–Abr–1992 16:53

Figure 2.10(b)

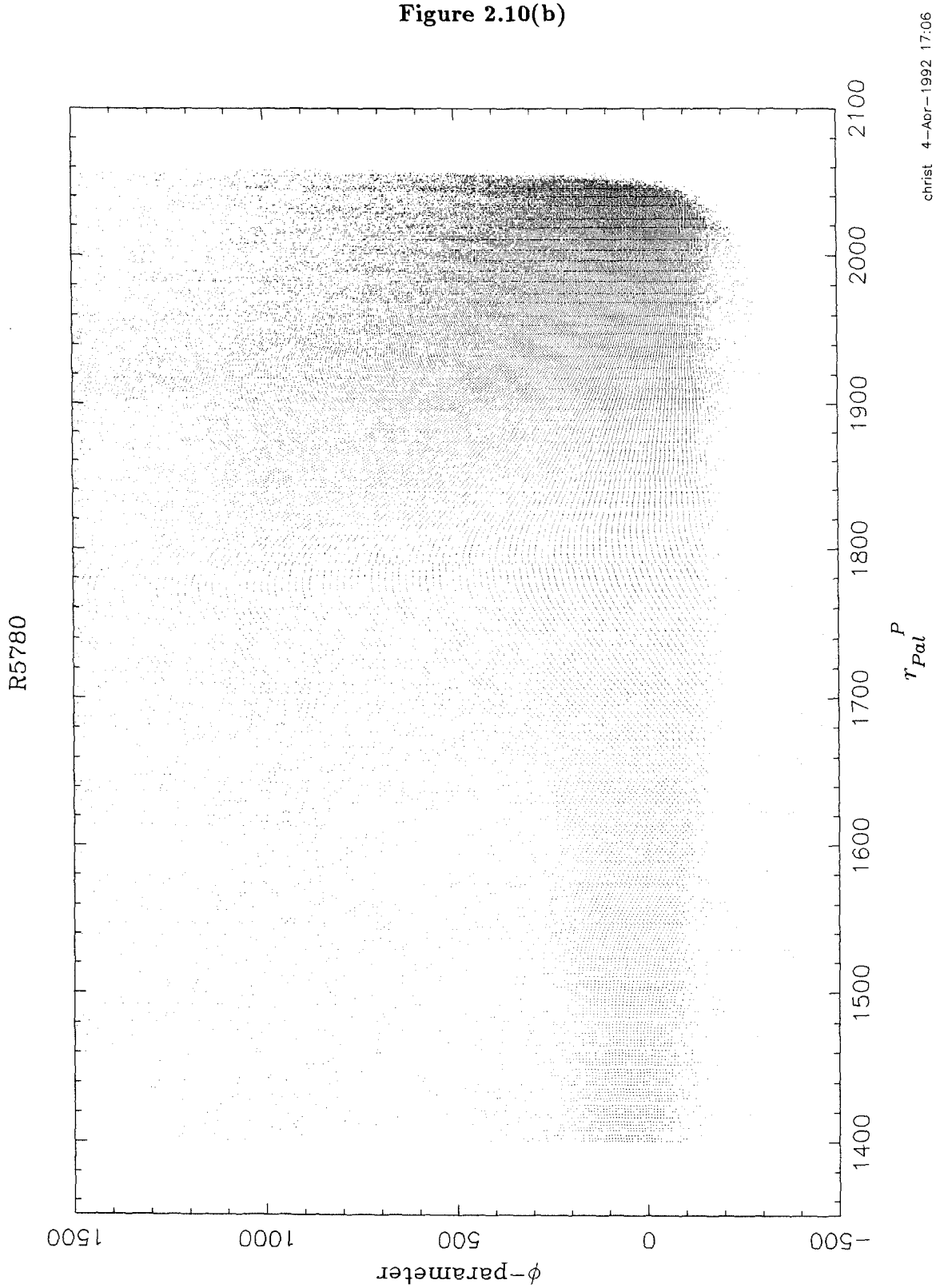
R5780
r_{Pal}^{P}
ϕ–parameter
2100
2000
1900
1800
1700
1600
1500
1400
1500
1000
500
0
−500
christ 4–Apr–1992 17:06

Figure 2.11

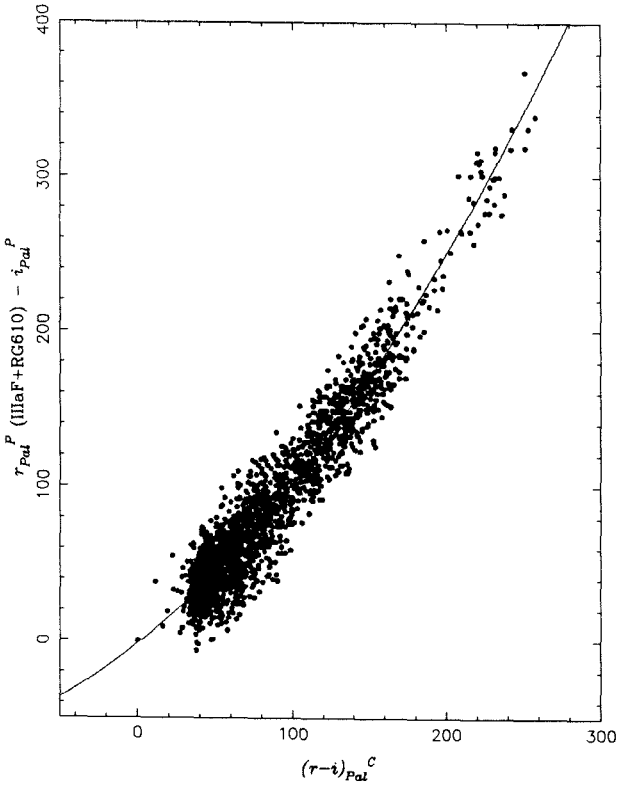

Figure 2.12

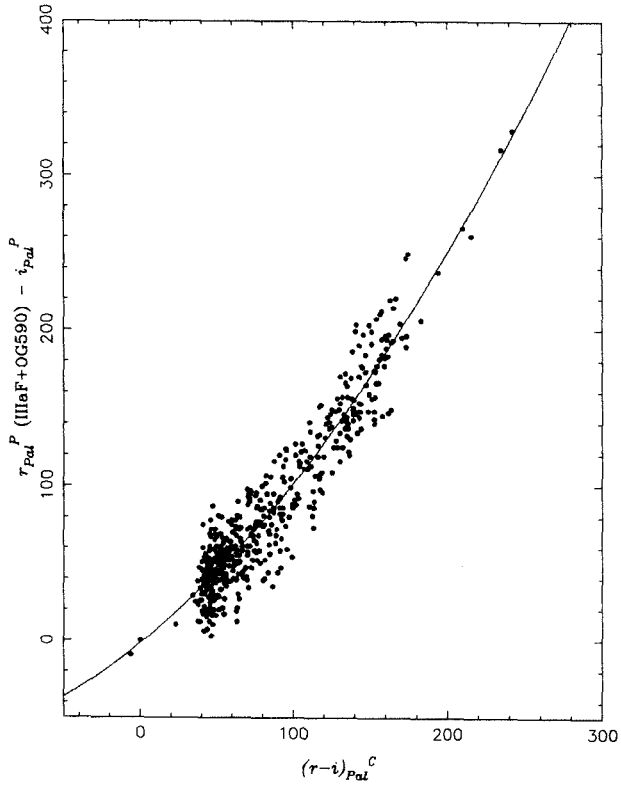

Figure 2.13

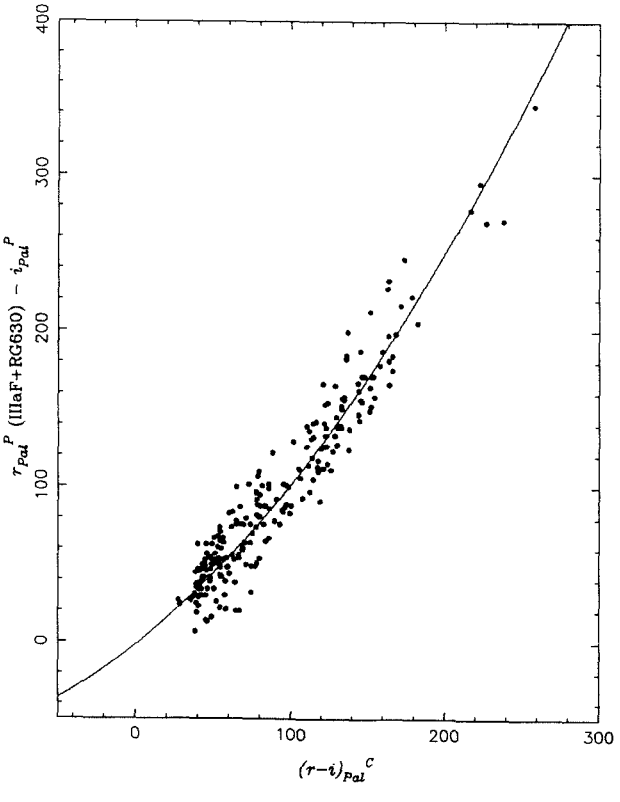

Figure 2.14 - Star and Galaxy Counts

(a) FLD829

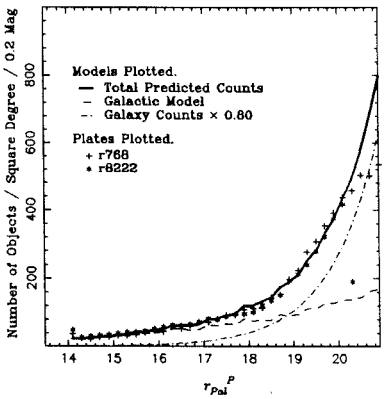

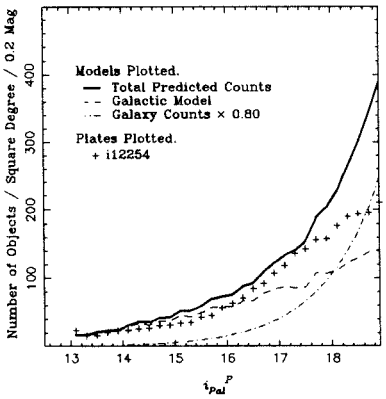

(b) FLD831

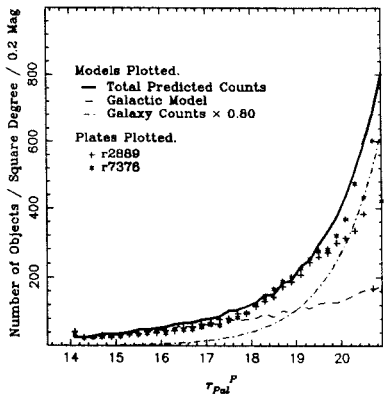

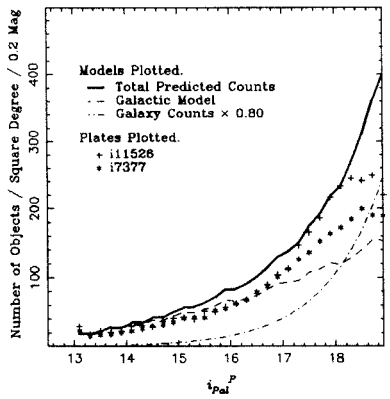

(c) FLD832

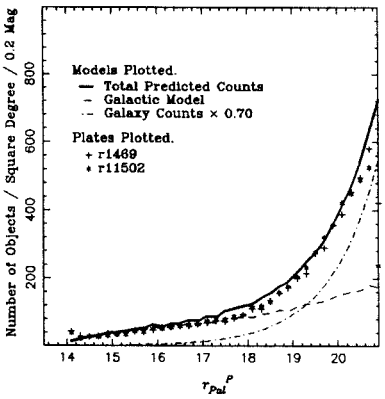

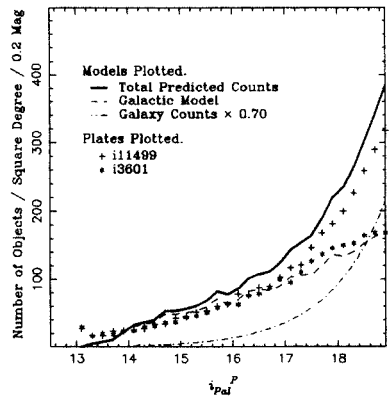

(d) FLD262

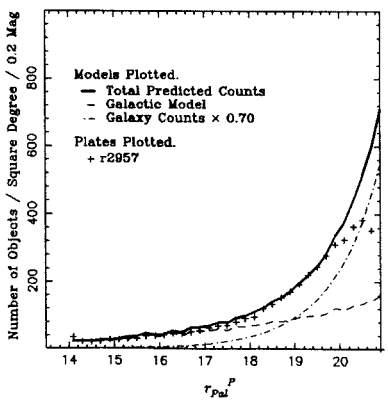

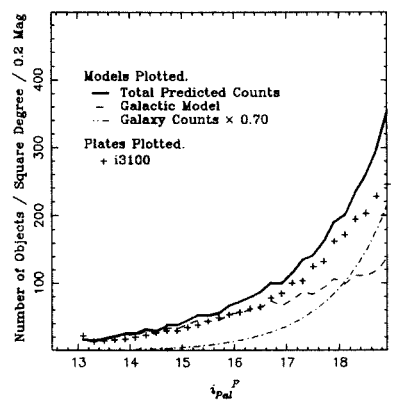

Figure 2.14 - Star and Galaxy Counts(cont.)

(a) FLD213

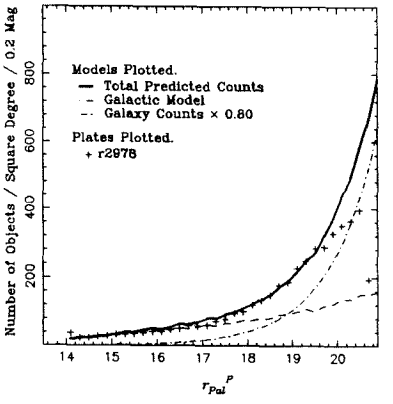

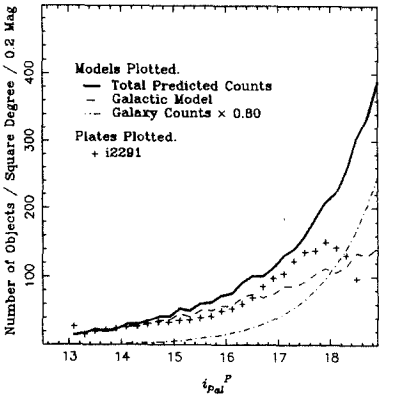

(b) FLD262

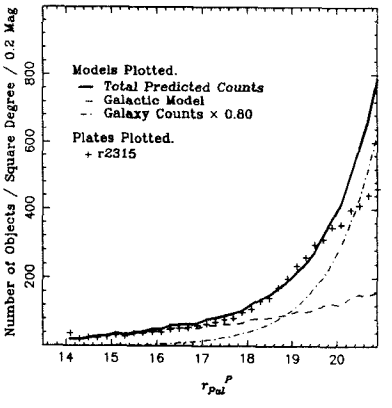

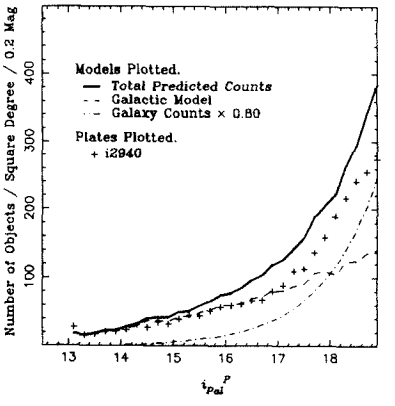

(c) FLD513

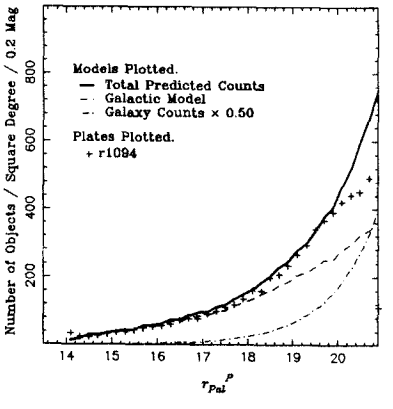

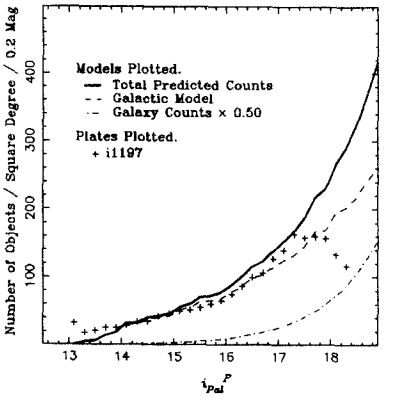

(d) FLD868

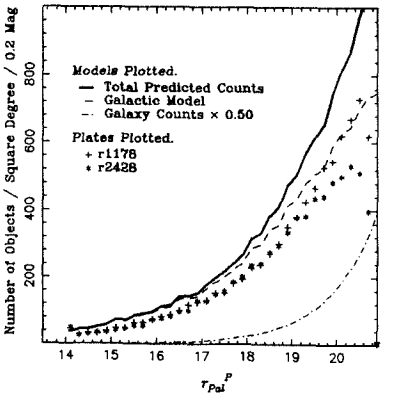

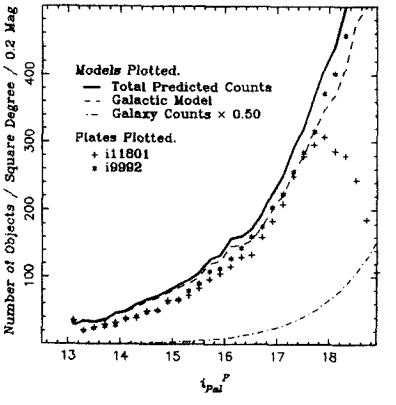

Figure 2.14 - Star and Galaxy Counts(cont.)

(a) FLD889

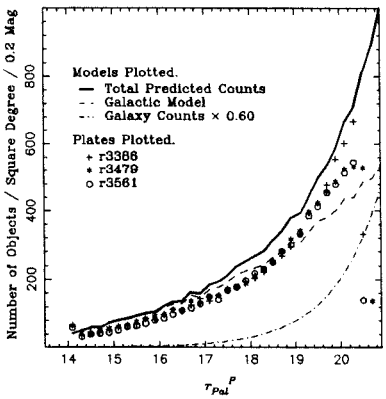

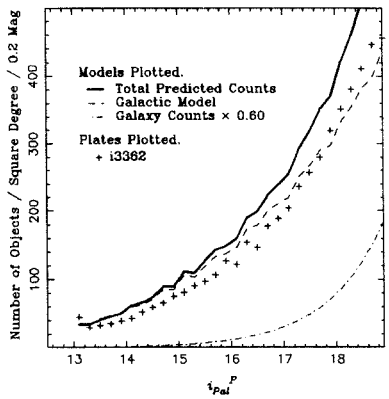

(b) FLD890

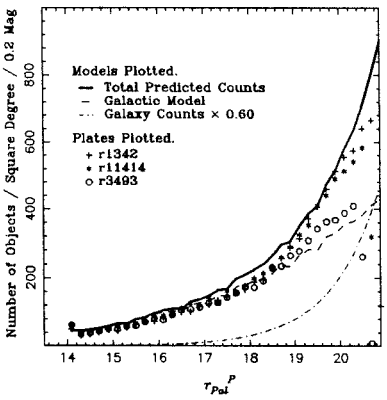

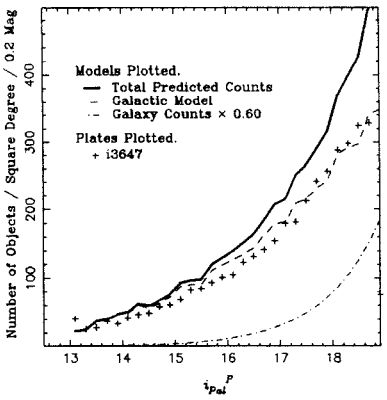

(c) FLD891

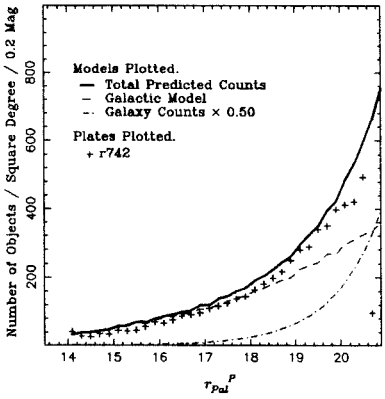

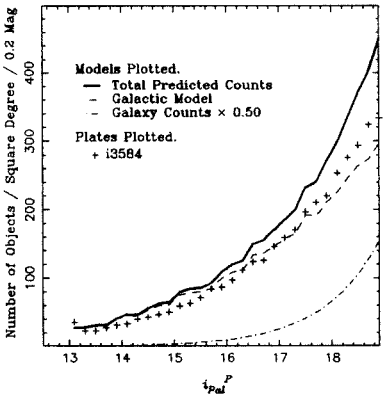

Figure 2.15

(a) Field 831 : I11526 – I7377

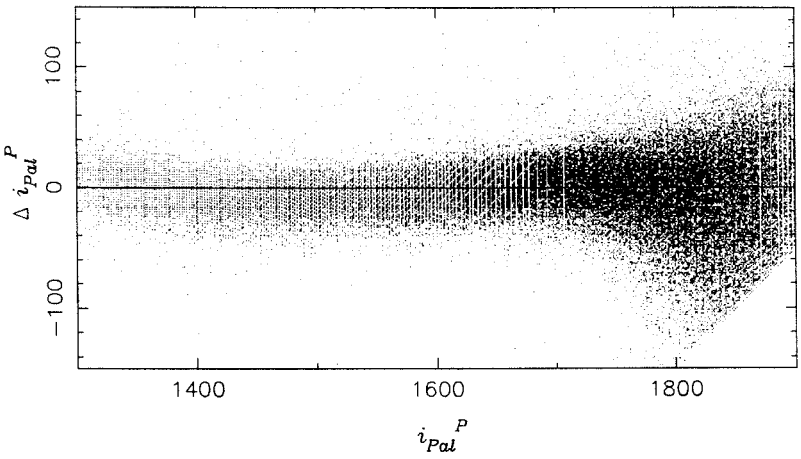

(b) Field 832 : I11499 – N3601

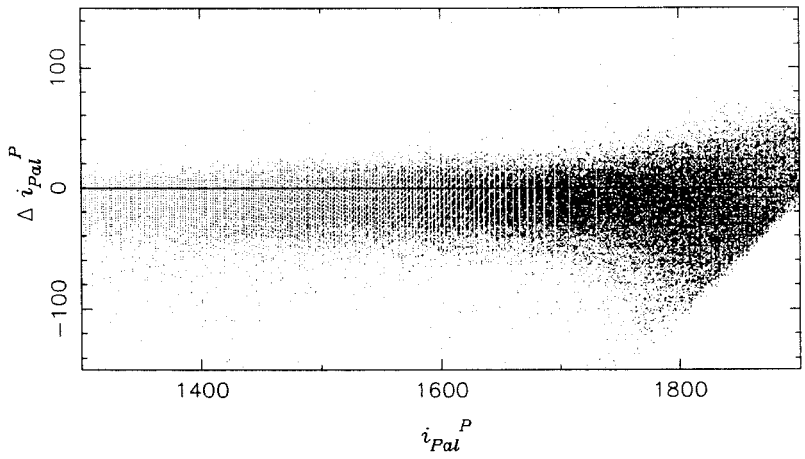

(c) Field 868 : I11801 – I9992

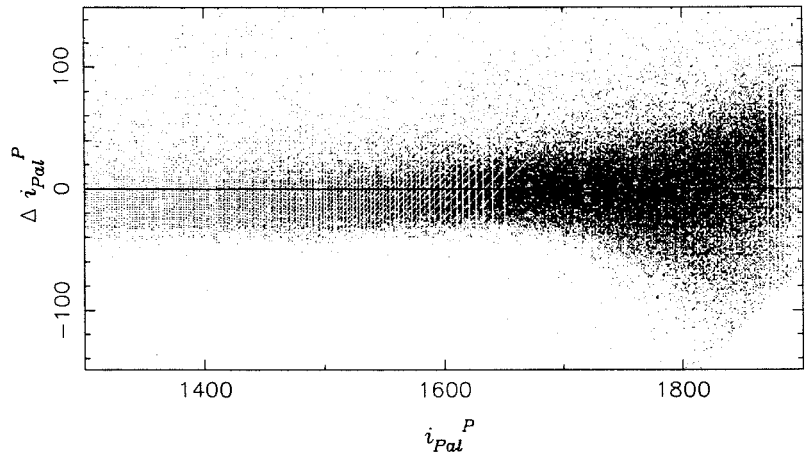

Figure 2.16

(a) Field 831 : F2889 – R7376

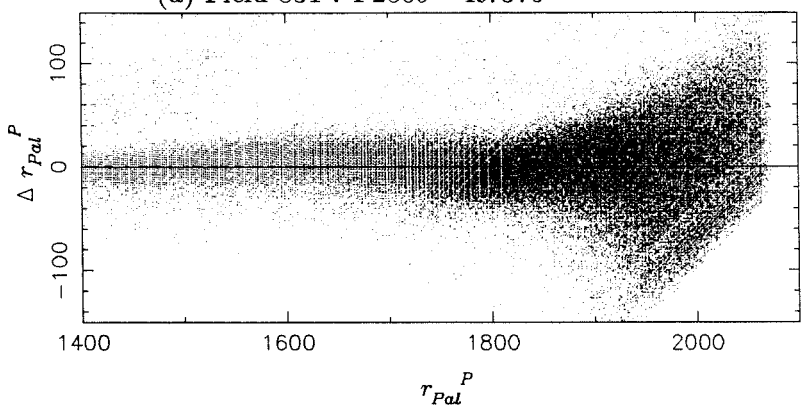

(b) Field 832 : R11502 - F1469

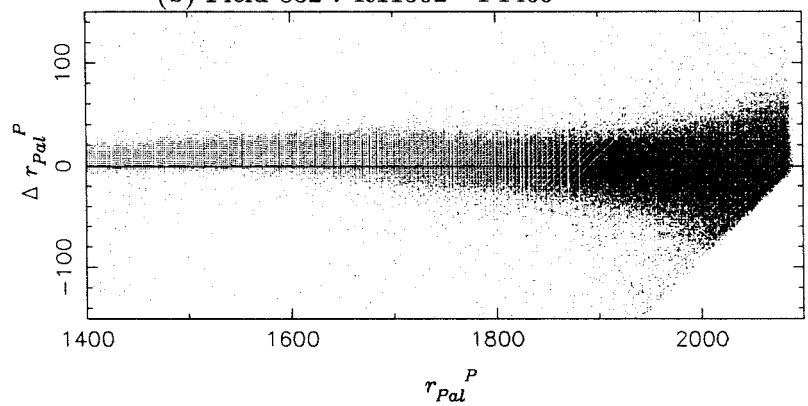

(c) Field 868 : F1178 – F2428

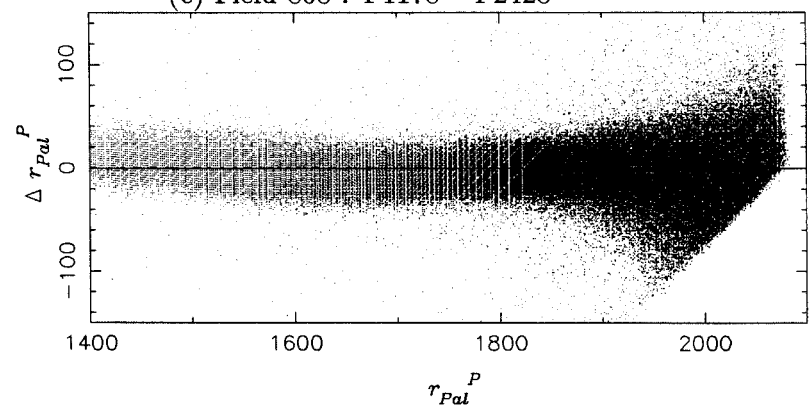

(d) Field 889 : F3386 – F3479

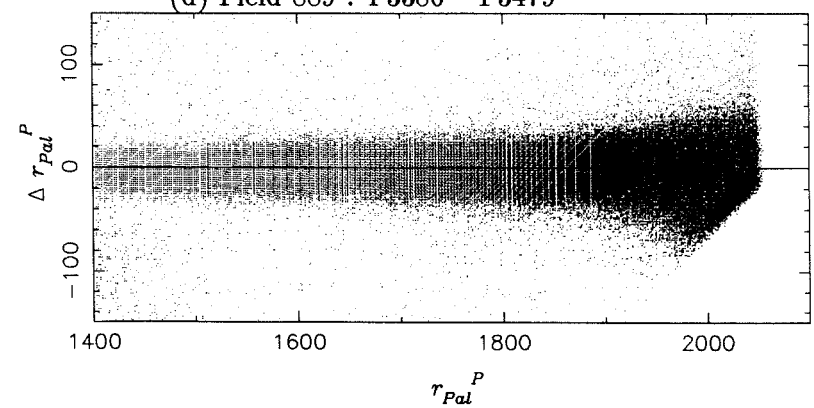

Figure 2.16 (cont)

(e) Field 889 : F3386 – F3584

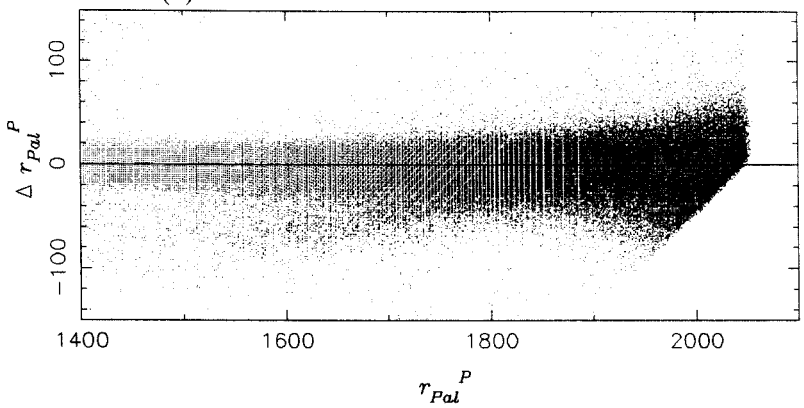

(f) Field 890 : F1342 – F3493

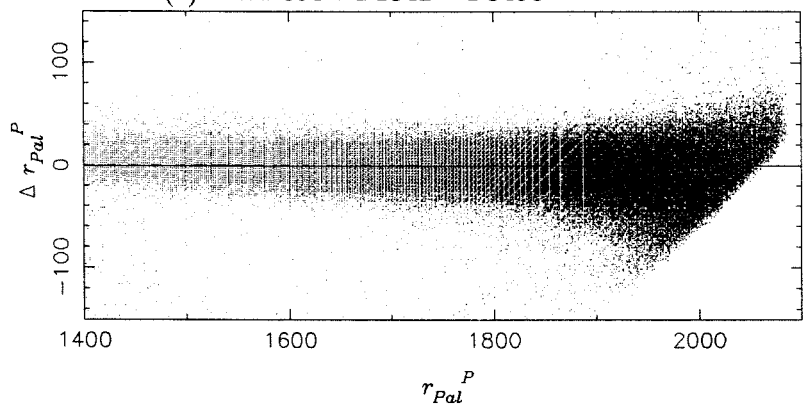

(g) Field 890 : F1342 – R11414

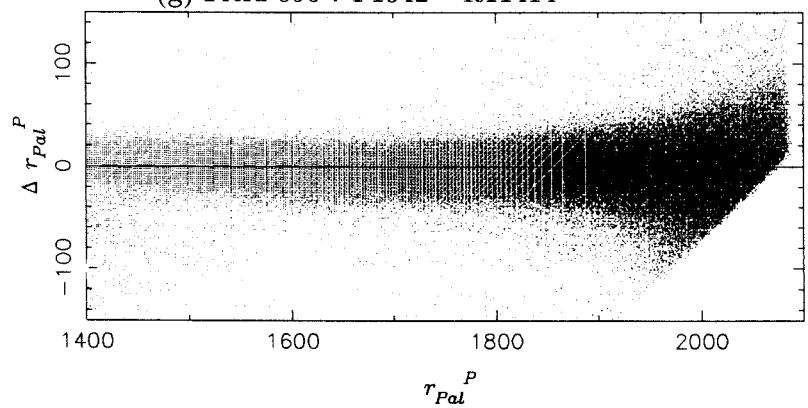

Figure 2.17

(a) FLD262:N2940 – FLD213:N2291

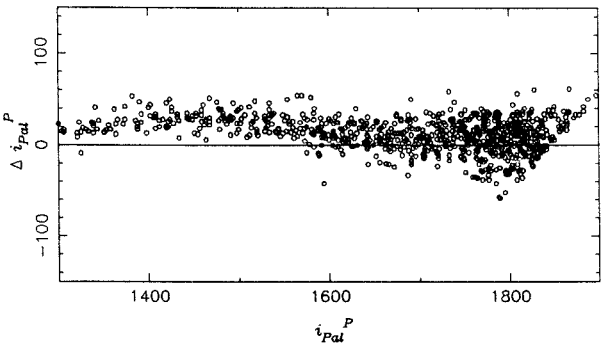

(b) FLD262:N2940 – FLD263:N3100

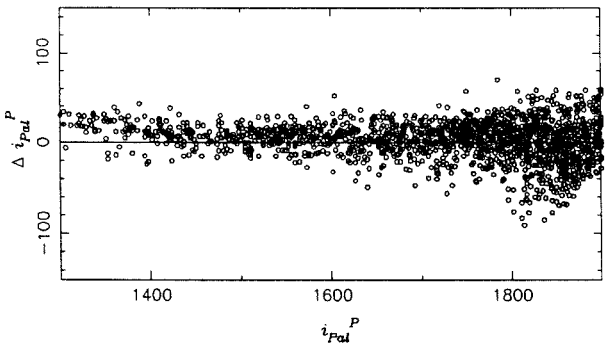

(c) FLD263:N3100 – FLD213:N2291

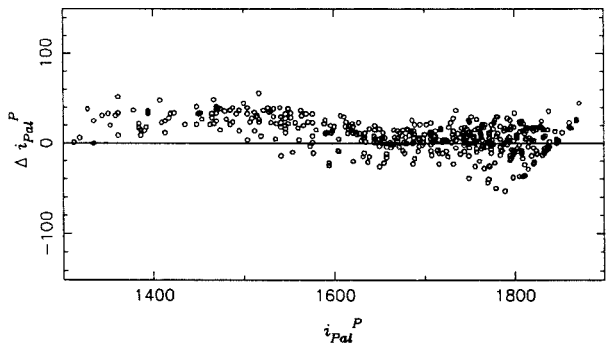

(e) FLD889:N3362 – FLD890:N3647

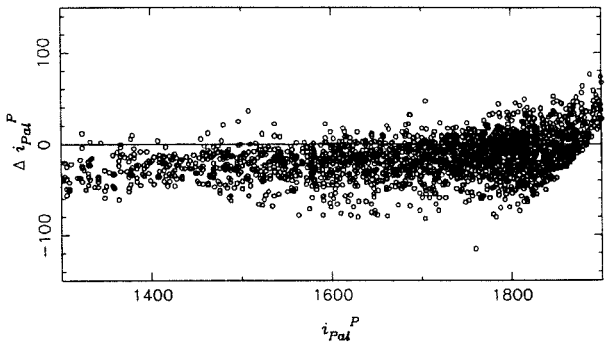

(f) FLD890:N3647 – FLD891:N3584

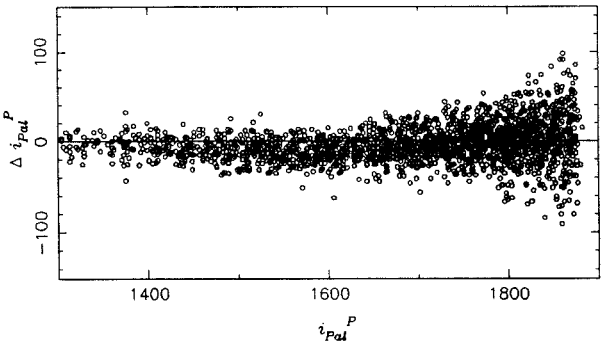

Figure 2.18

(a) FLD262:F2315 – FLD213:F2978

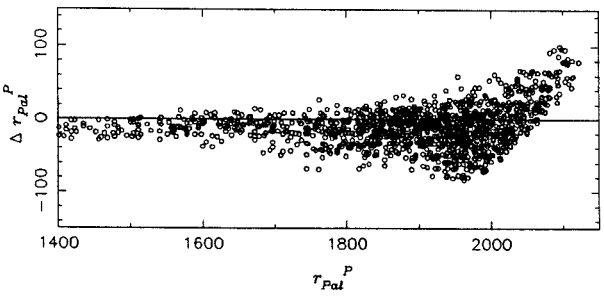

(b) FLD262:F2315 – FLD263:F2957

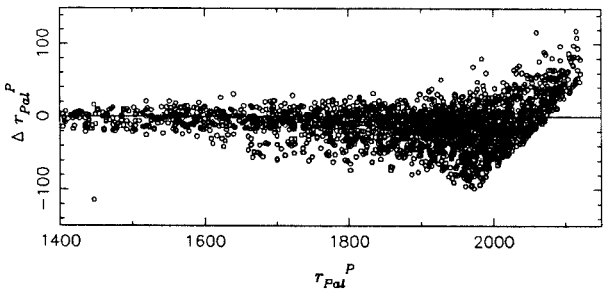

(c) FLD263:F2957 – FLD213:F2978

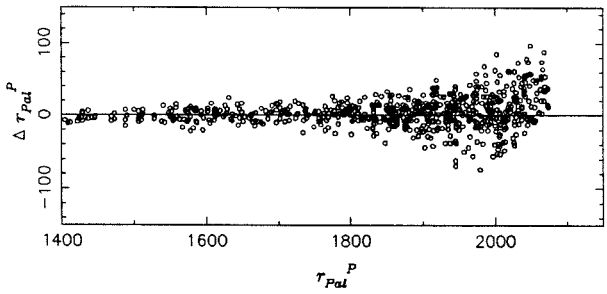

(d) FLD831:R7376 – FLD832:R11502

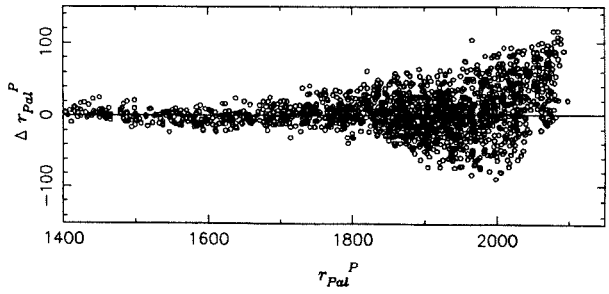

(e) FLD831:F2889 – FLD832:F1469

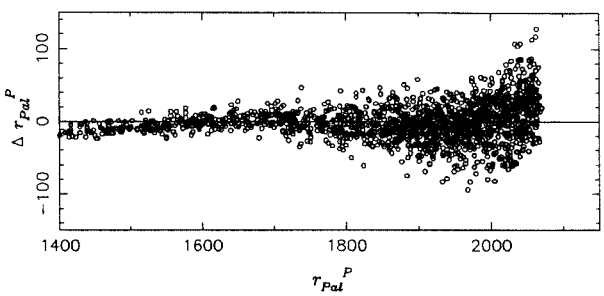

(f) FLD889:F3386 – FLD890:F1342

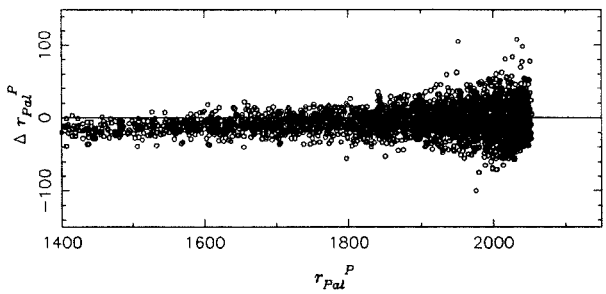

(g) FLD889:F3386 – FLD890:F3493

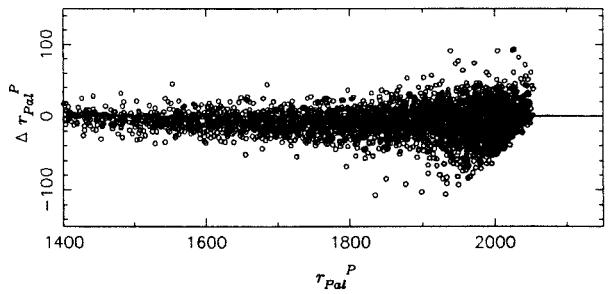

(h) FLD889:F3386 – FLD890:R11414

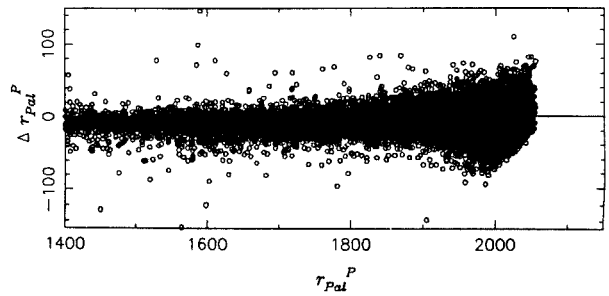

Figure 2.18 (cont)

(i) FLD889:F3479 – FLD890:F1342

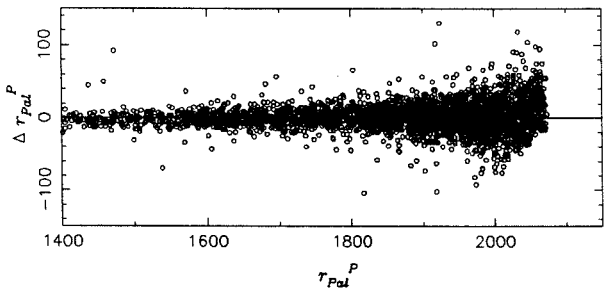

(j) FLD889:F3479 – FLD890:F3493

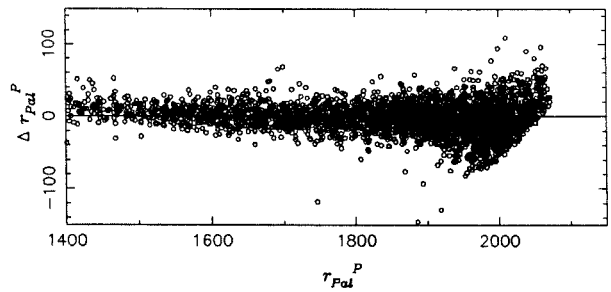

(k) FLD889:F3479 – FLD890:R11414

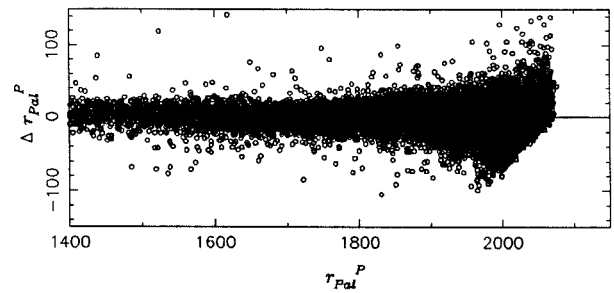

(l) FLD889:F3561 – FLD890:F1342

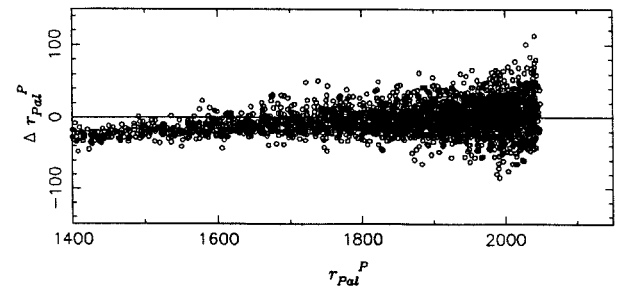

(m) FLD889:F3561 – FLD890:F3493

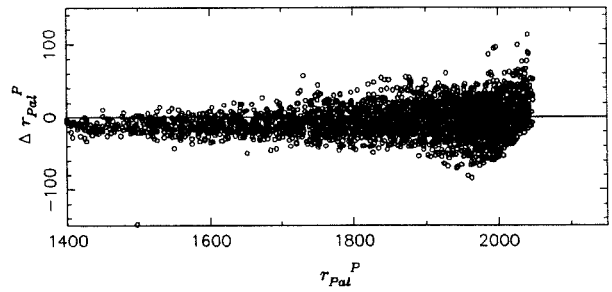

(n) FLD889:F3561 – FLD890:FR11414

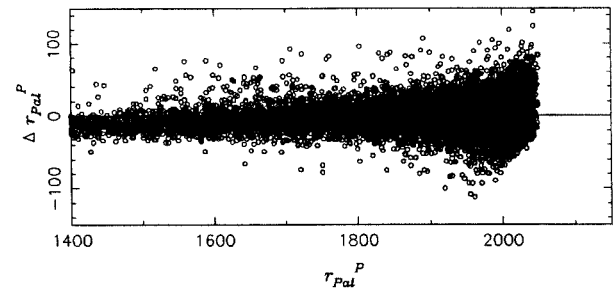

(o) FLD890:F1342 – FLD891:F742

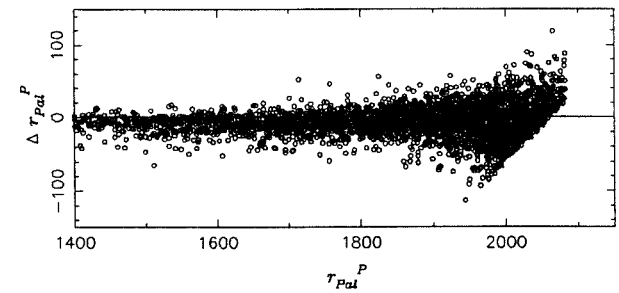

(p) FLD890:F3493 – FLD891:F742

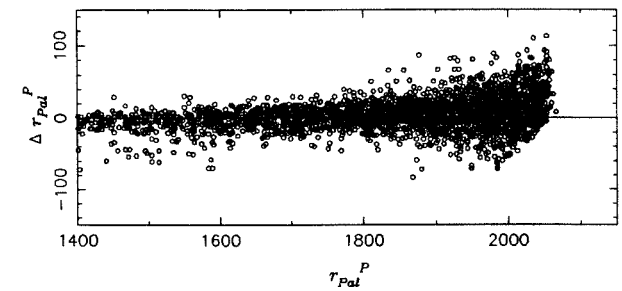

Figure 2.19

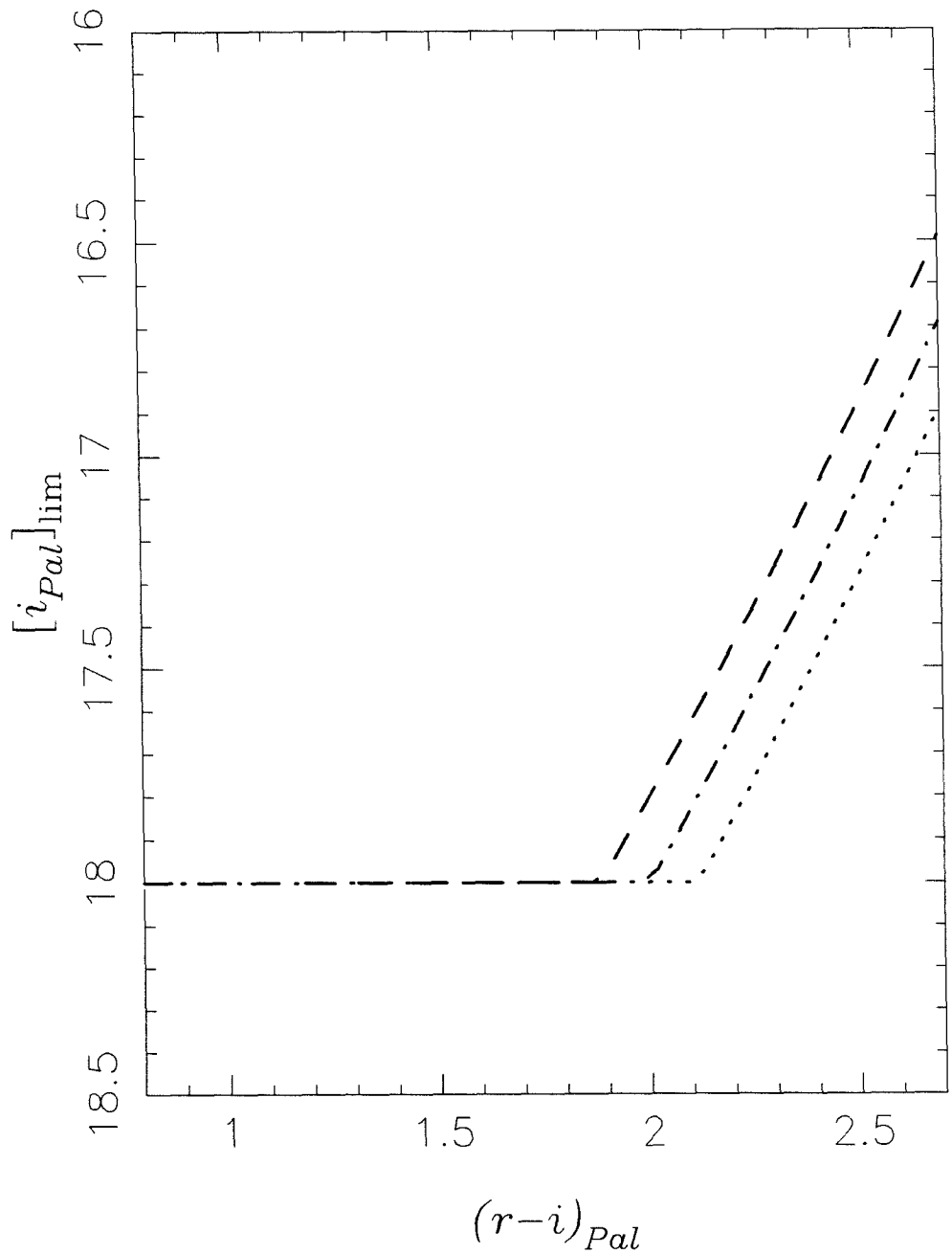

Figure 2.20

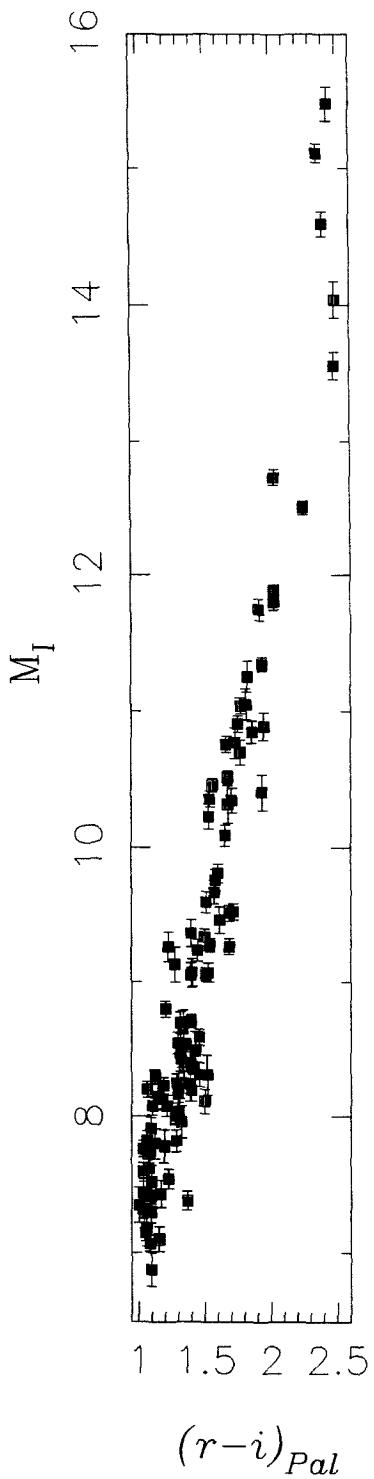

Figure 2.21

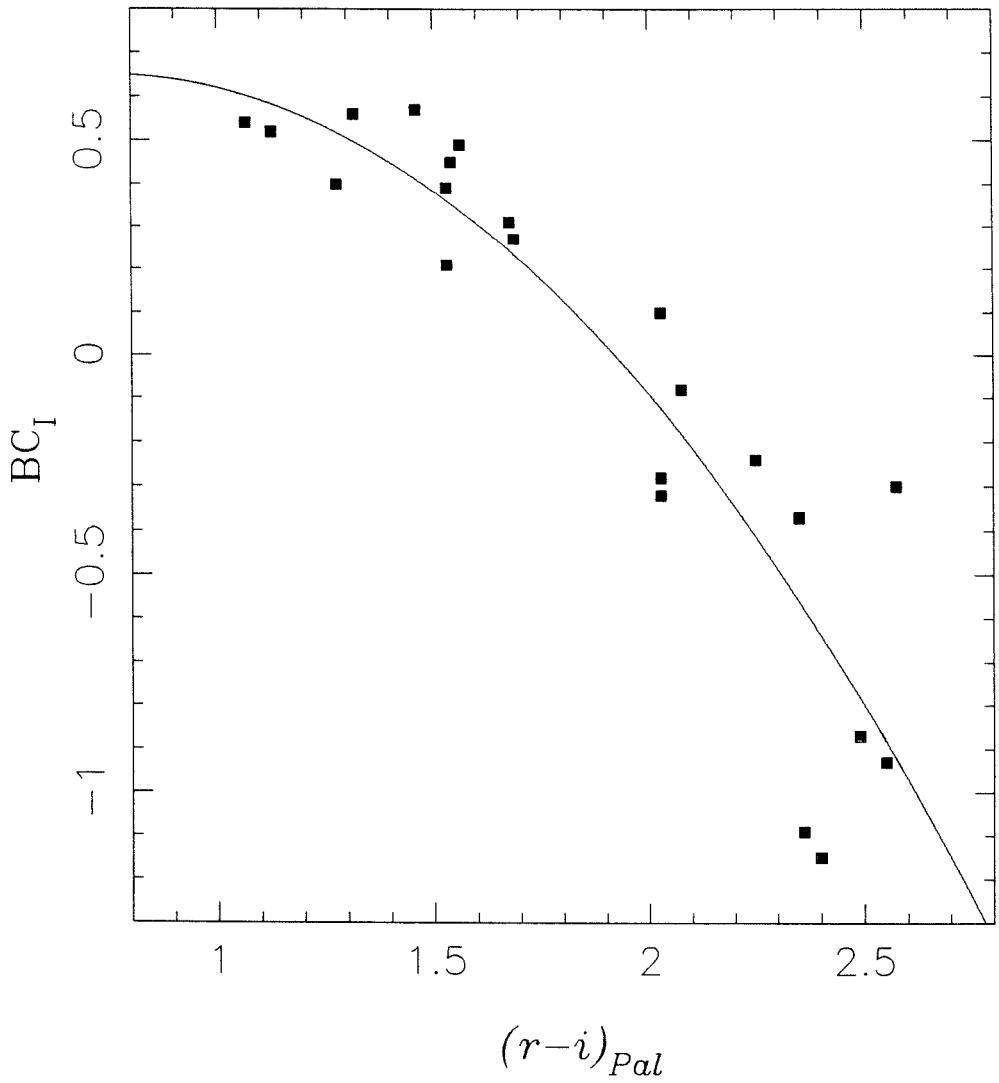

Figure 2.22

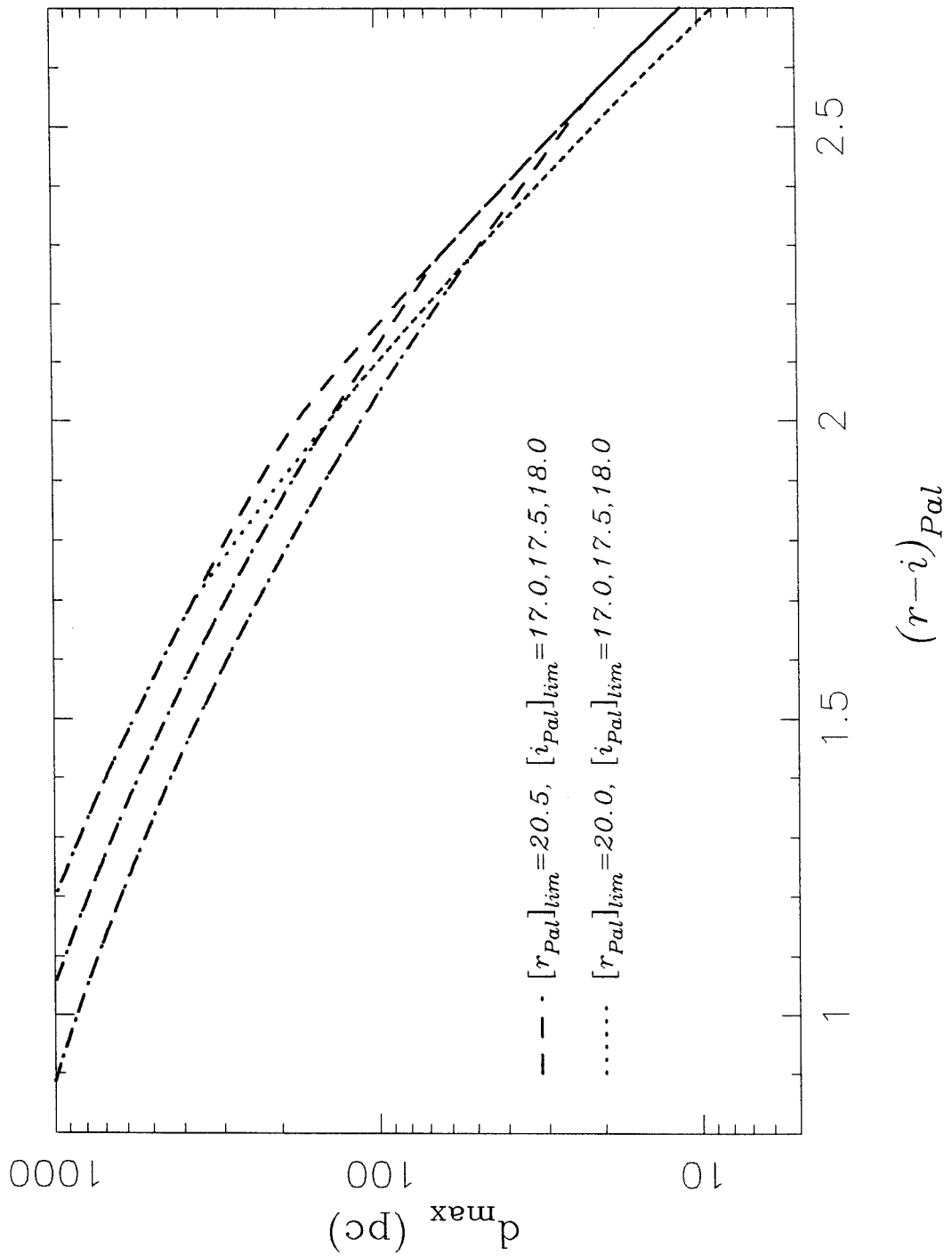
d_max (pc)
1000
100
10
1
1.5
2
2.5
(r−i)_Pal
– – · [r_Pal]_lim=20.5, [i_Pal]_lim=17.0,17.5,18.0
····· [r_Pal]_lim=20.0, [i_Pal]_lim=17.0,17.5,18.0

Figure 2.23(a)

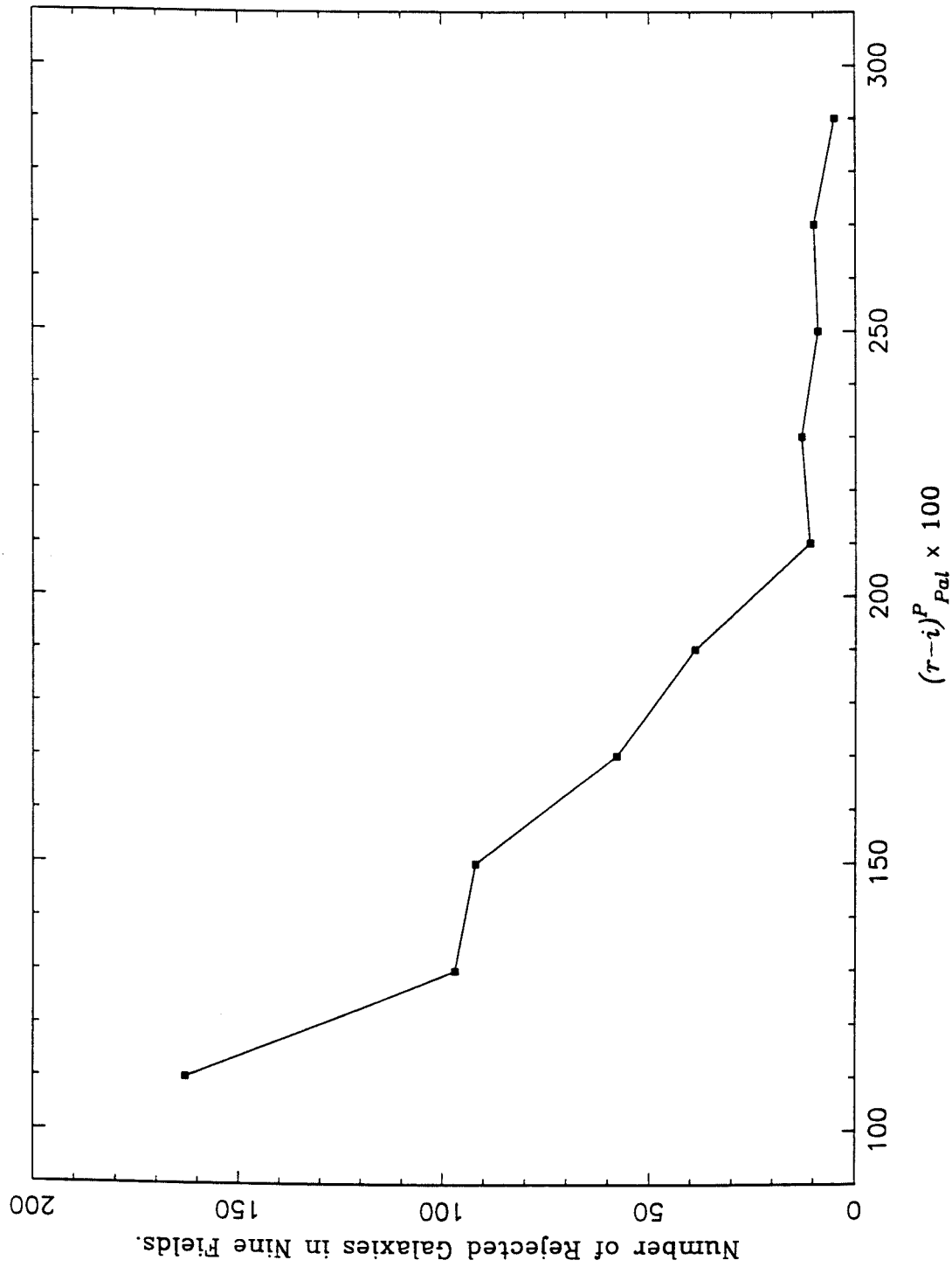
Number of Rejected Galaxies in Nine Fields.
0
50
100
150
200
100
150
200
250
300
$(r-i)^P_{Pal}$ x 100

Figure 2.23(b)

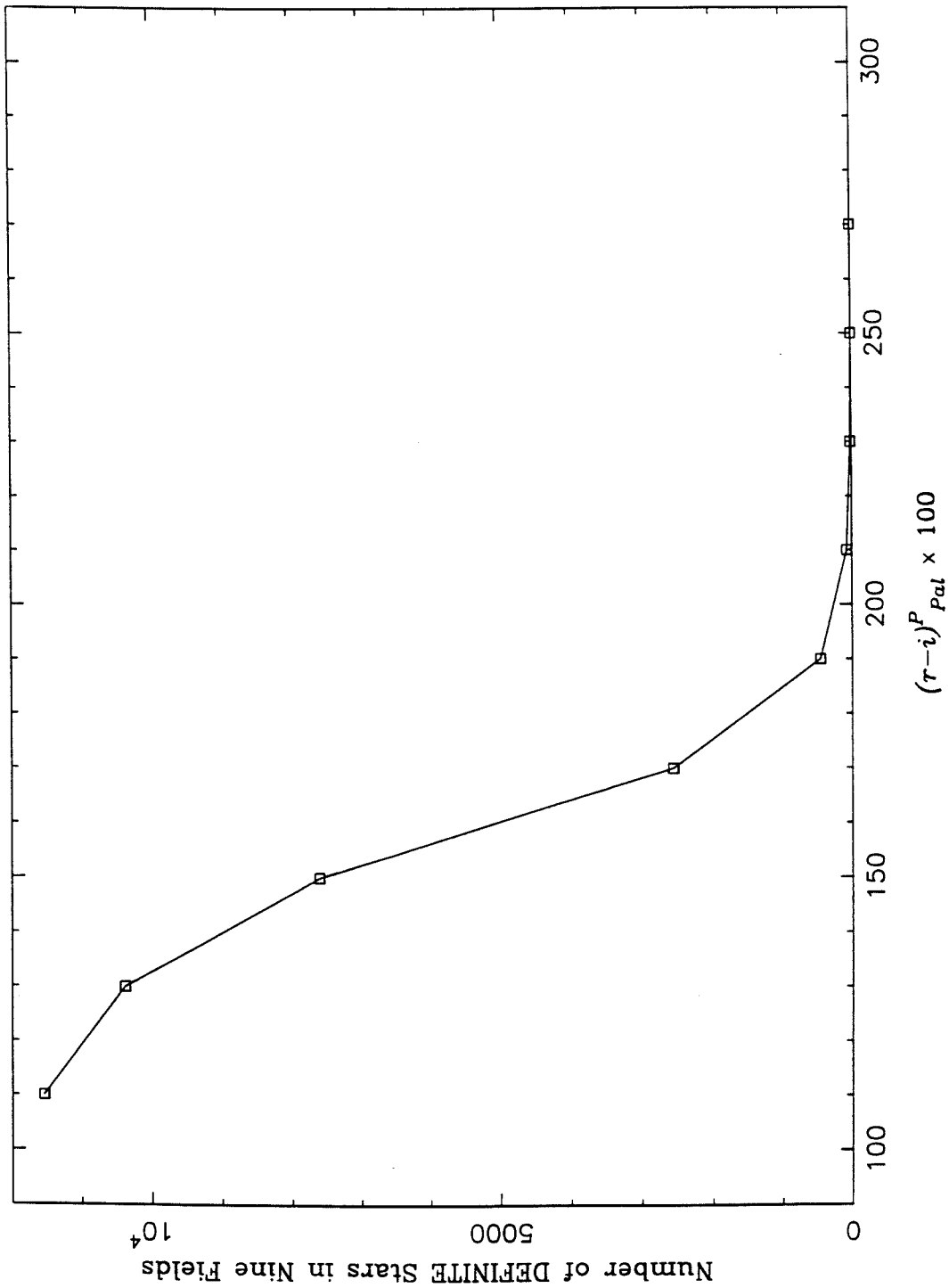
Number of DEFINITE Stars in Nine Fields
0
5000
10^4
100
150
200
250
300
(r−i)^P_Pal x 100

Figure 2.23(c)

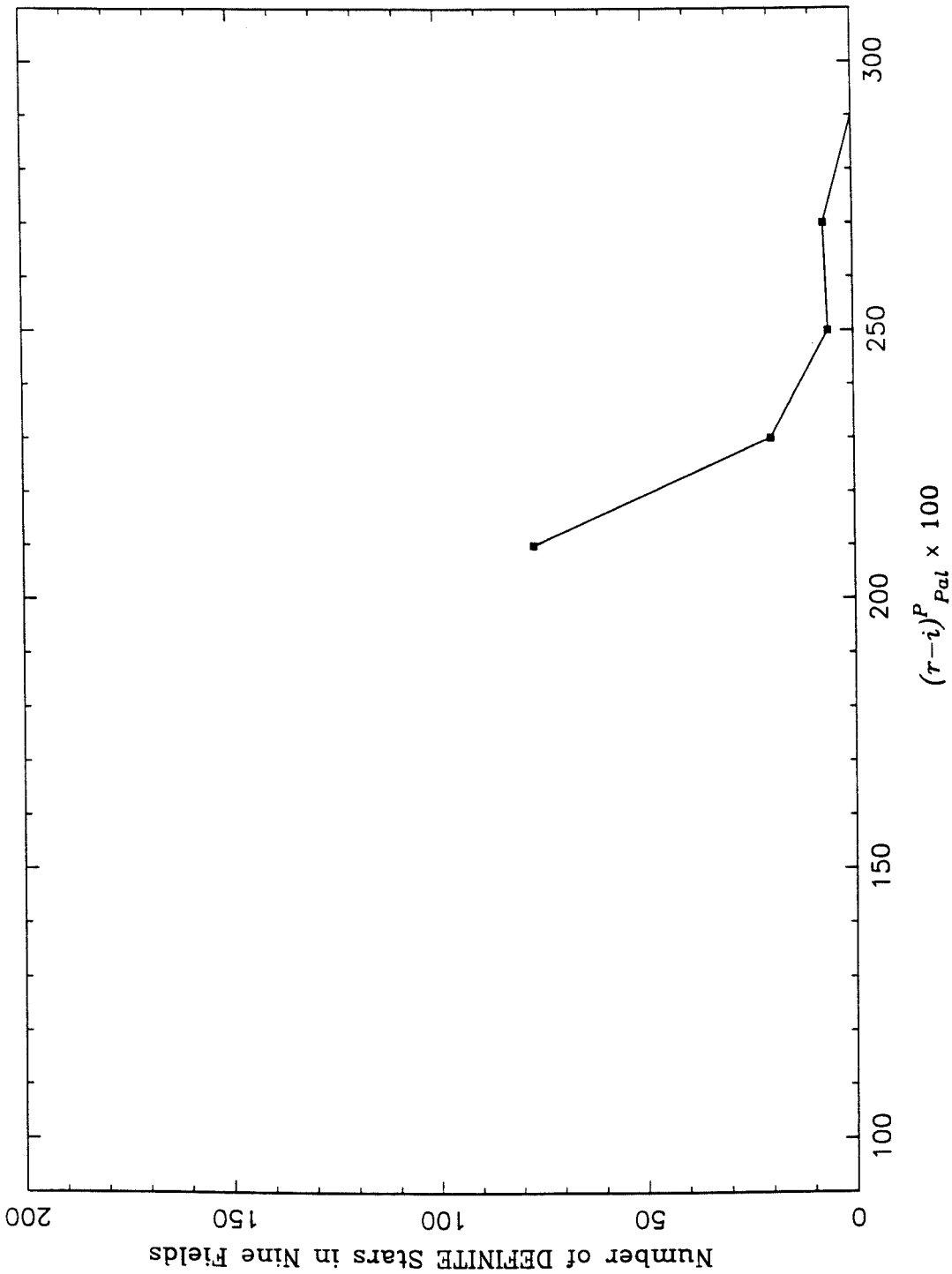
Number of DEFINITE Stars in Nine Fields
0
50
100
150
200
$(r-i)^P_{Pal}$ x 100
100
150
200
250
300

Figure 2.24

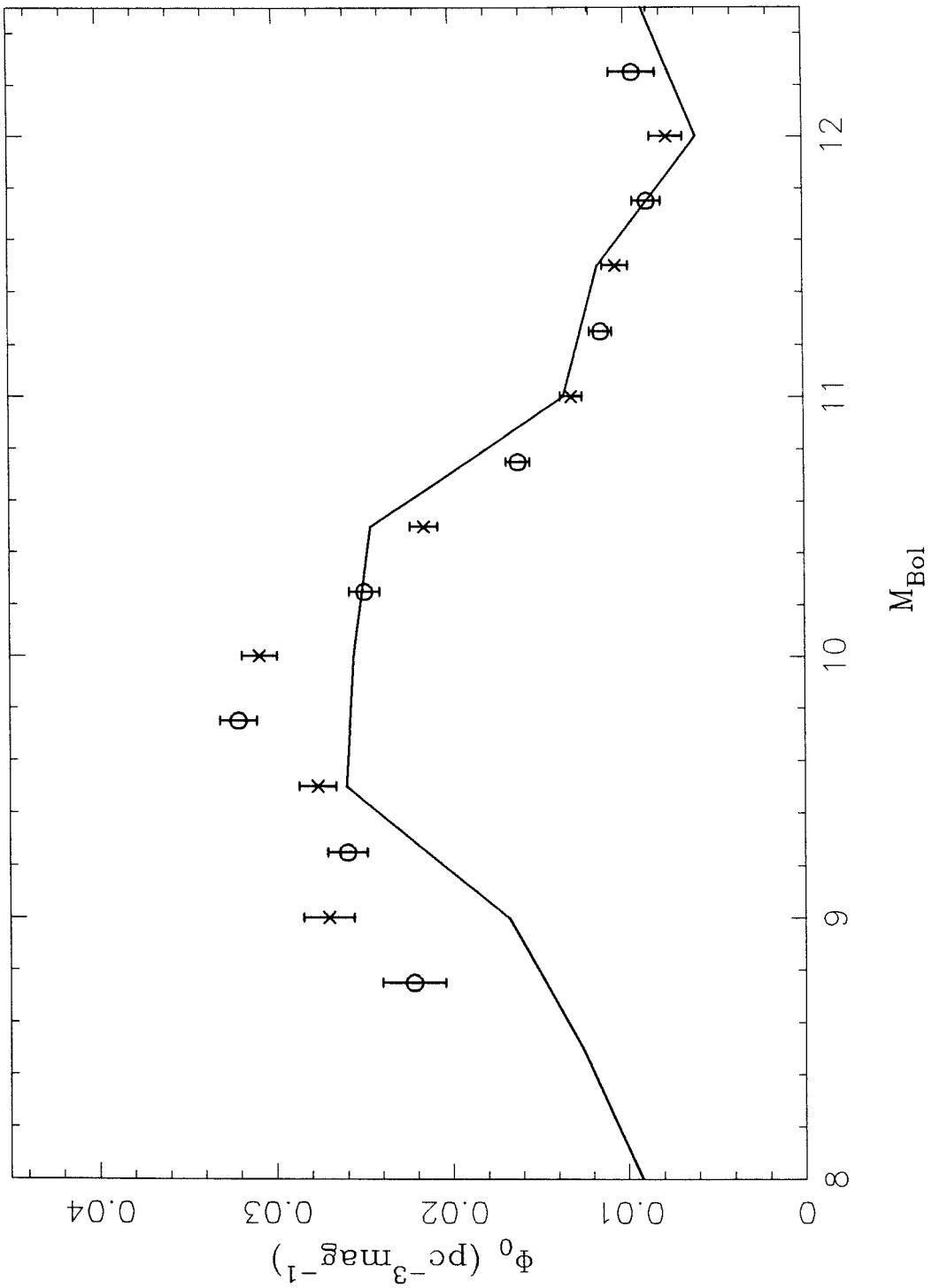

Figure 2.25

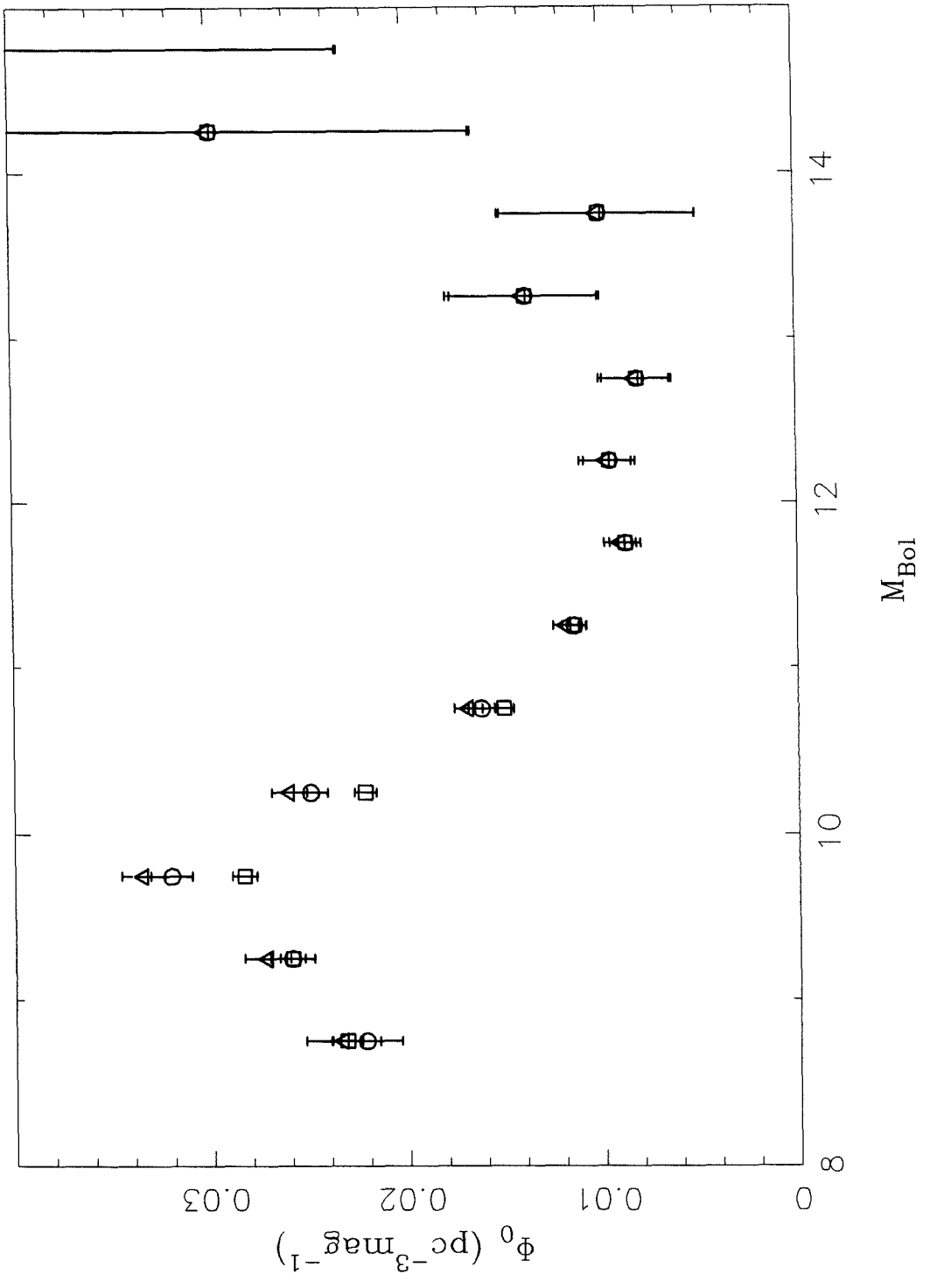

Figure 2.26(a)

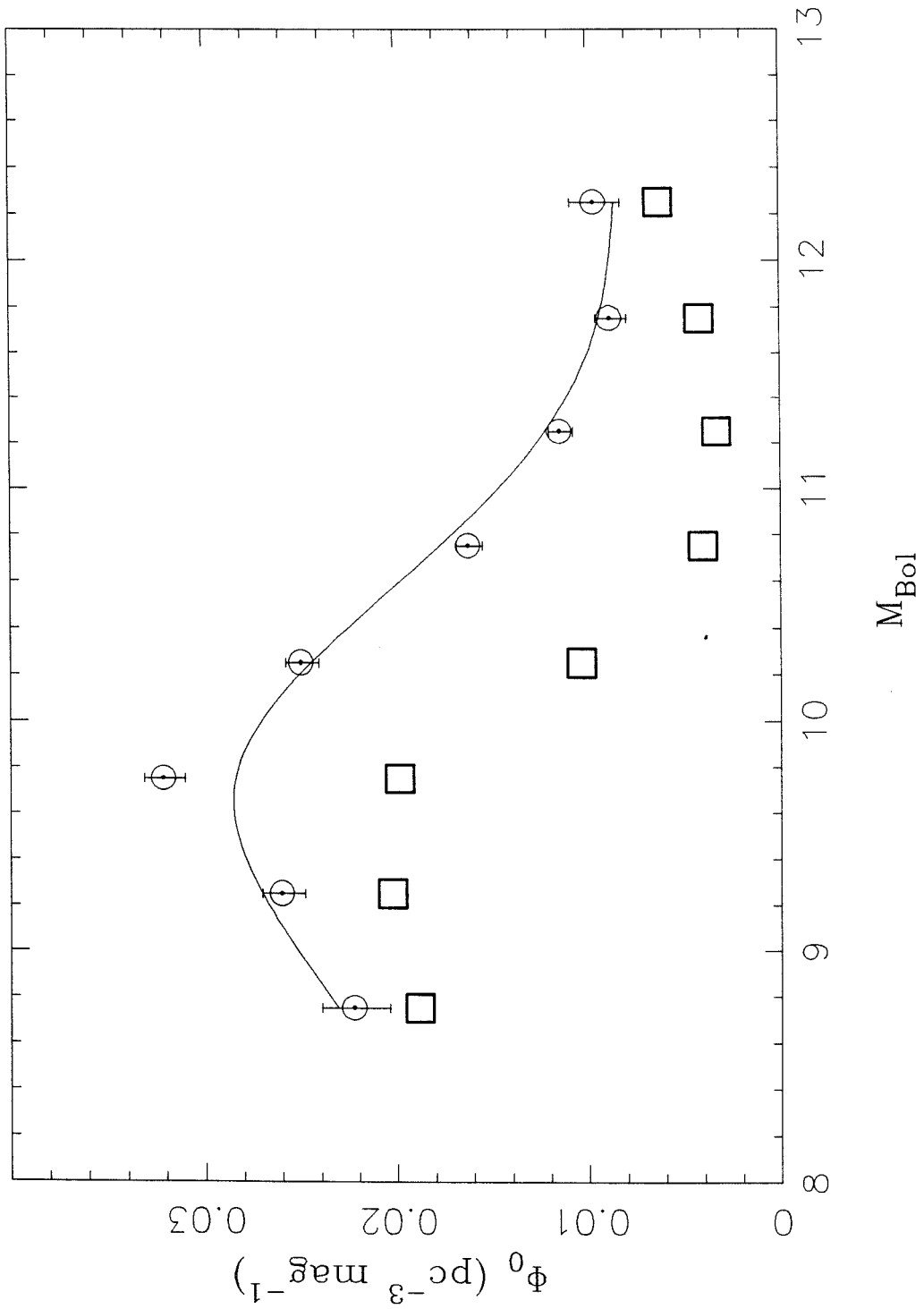

Figure 2.26(b)

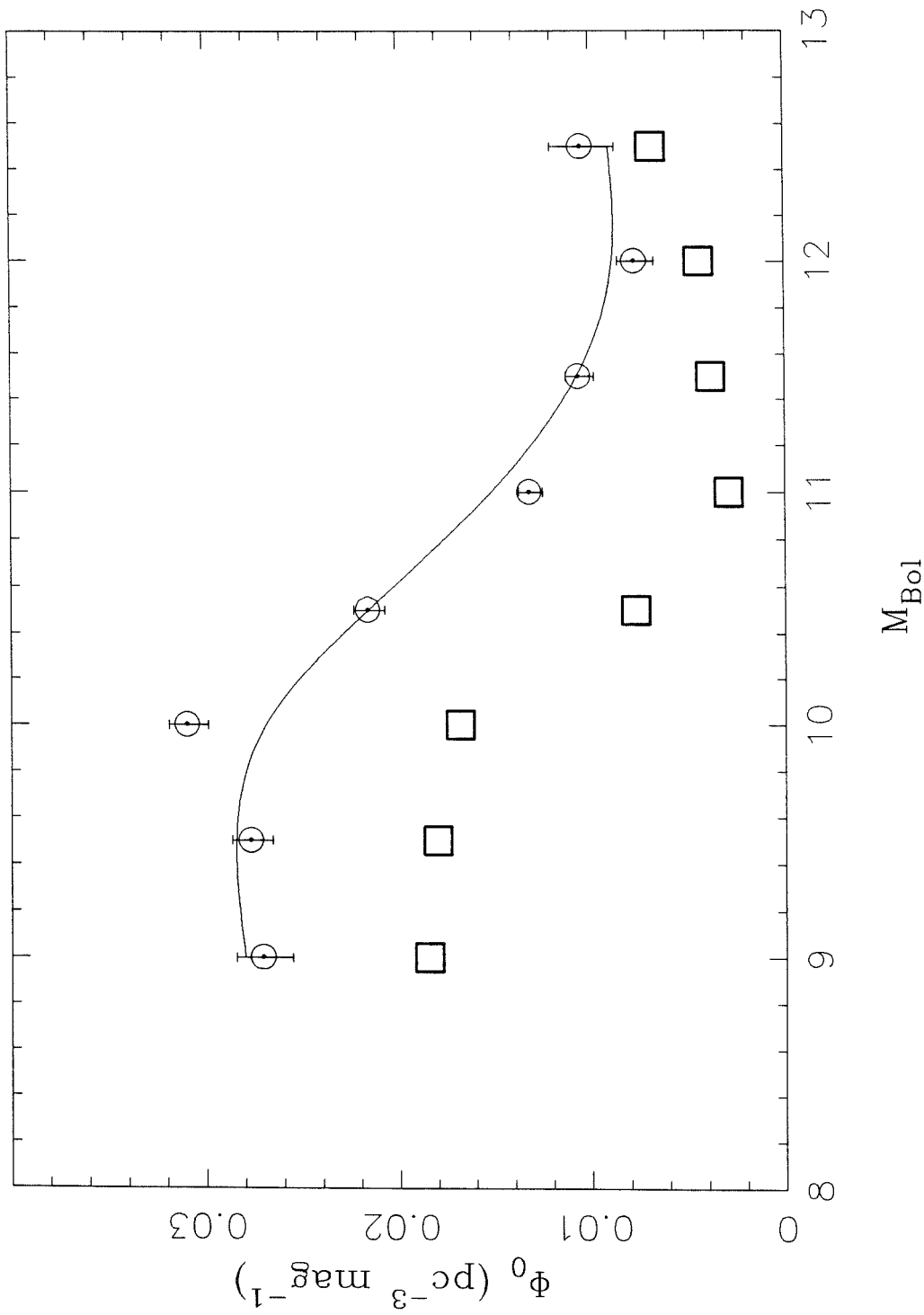

Figure 2.27(a)

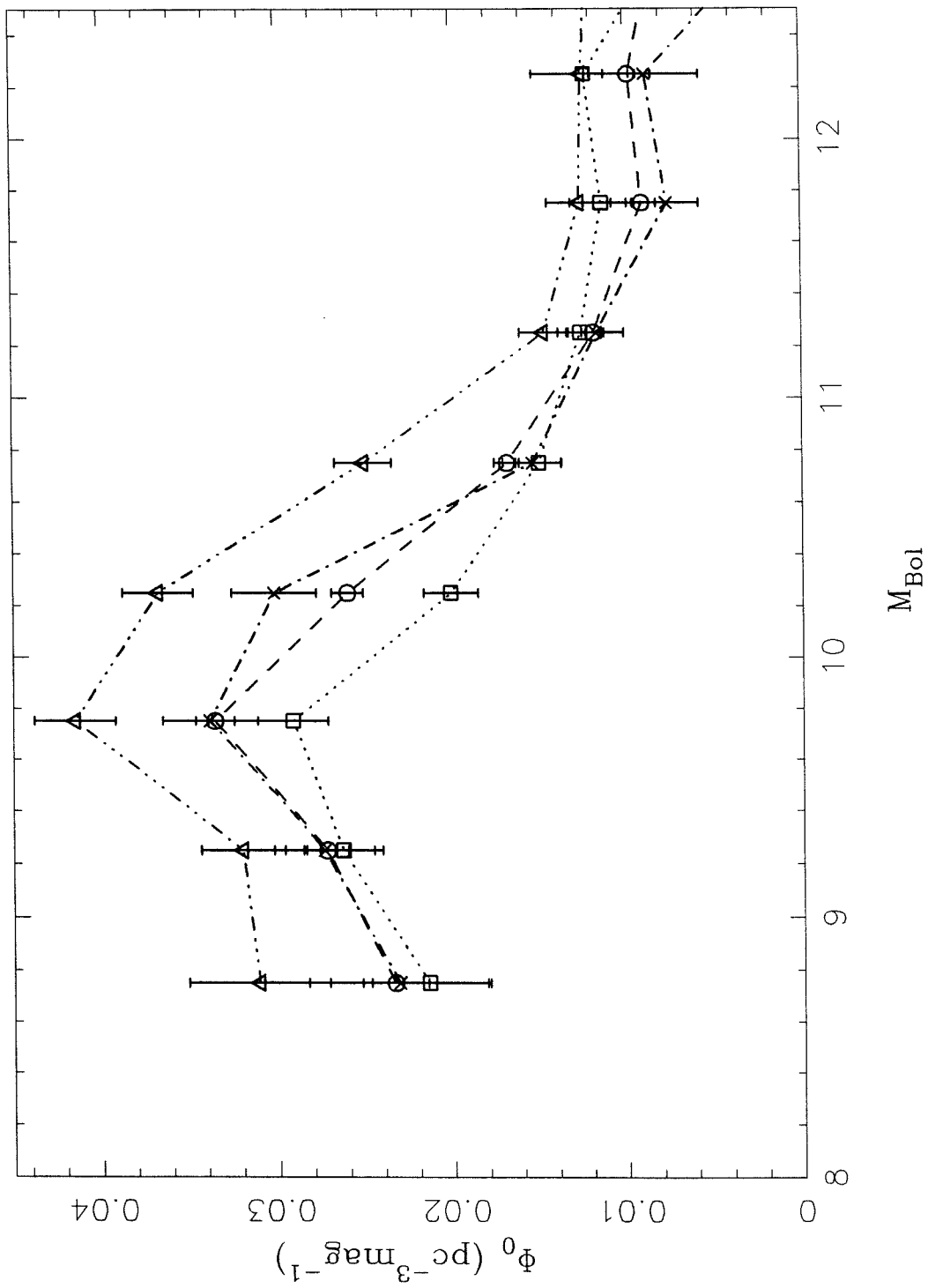

Figure 2.27(b)

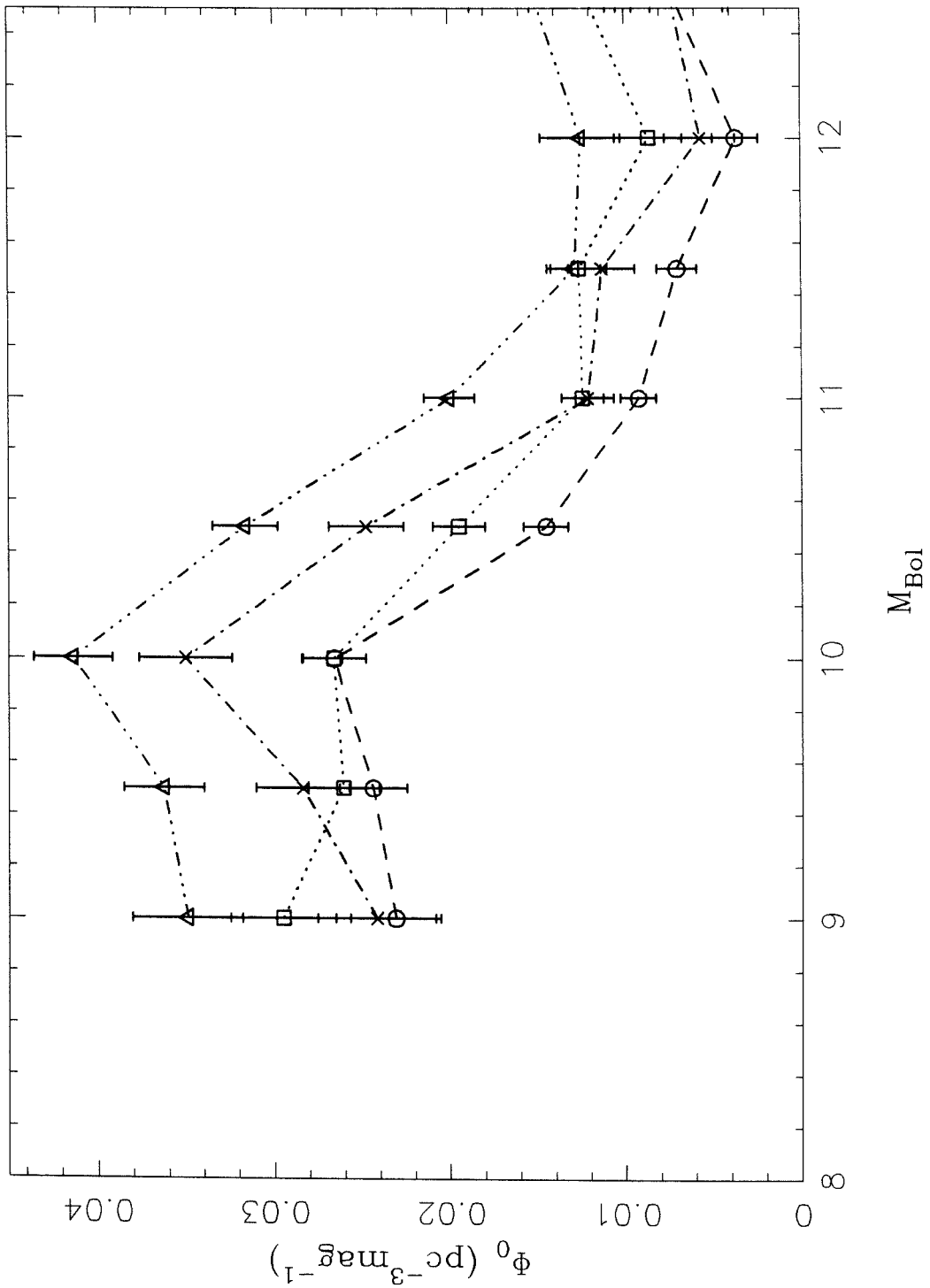

Chapter 3 - The Faintest Stars : Infrared Photometry, Spectra, and Bolometric Magnitudes.[1]

Abstract

We present infrared JHKLL′ photometry (obtained with the IRTF telescope on Mauna Kea) for a selection of the latest stars known. We also present low resolution ($\Delta\lambda/\lambda \sim 150 - 300$) infrared spectra covering the range $\lambda \approx 1.0 - 2.5\mu$m (obtained with the UKIRT telescope, also on Mauna Kea). Because of the dry site at which these data were obtained we are able to correct for the presence of terrestrial H_2O absorption and study the *stellar* H_2O bands which dominate the atmospheres of these stars. We find that the L band fluxes of these stars are considerably depressed (relative to L′ fluxes) by the presence of stellar H_2O absorption in the $2.5 - 3.3\mu$m band. Strong H_2O absorption is also seen in the $1.3 - 1.5\mu$m, $1.8 - 2.1\mu$m and $2.3 - 3.0\mu$m bands of our spectra - we examine the amount of flux which is 'overcounted' when these absorption bands are ignored and bolometric fluxes are calculated using broadband photometry alone. We find that a correction of only $\sim 5 - 10\%$ is required to correct for the 'flux overcounting' produced by using only broadband observations. The combined photometric and spectral data is used to evaluate bolometric corrections and bolometric magnitudes of a sample of late type M-dwarfs which extends almost 2-magnitudes fainter than the faintest previously measured objects. Lastly, we examine some of the current problems associated with the effective temperature scale for very low mass stars.

Section 3.1 - Introduction

In recent years numerous surveys have set out to study the space density of stars at the bottom of the main sequence (Hawkins & Bessell 1988, Leggett & Hawkins 1988 and 1989, Henry & M^{c}Carthy 1992, Tinney, Mould & Reid 1992a, Tinney, Reid & Mould 1992 (Paper I), Tinney 1992b (Paper IV)). Such studies have all been motivated by the desire to either find sub-stellar objects (i.e., brown dwarfs), or to understand the possible density of such objects by the extrapolation of the mass function for objects above the hydrogen-burning limit to masses below that limit. But, while the number of extremely

[1] Observations were made partially on the 60-inch telescope at Palomar Mountain which is jointly owned by the California Institute of Technology and the Carnegie Institution of Washington.

faint M-dwarfs and/or brown-dwarf candidates has increased dramatically in the last five years, our understanding of the *properties* of the stars so discovered has more or less stood still. In particular, the M_{bol} and T_{eff} scales used to convert observed optical or infrared colours into estimated luminosities and temperatures (and by extension into estimates of the mass) are poorly defined – it is this area which we primarily seek to address in this work.

The spectra of late M-dwarfs ($M_{bol} \gtrsim 11$) are dominated in the infrared (where most of their energy is radiated) by the presence of broad water vapour absorption bands centred at approximately 1.4, 1.9, 2.8 and 4.4μm. Early studies of the luminosities and temperatures of late M-dwarfs (Greenstein *et al.* 1970, Veeder 1974, Mould & Hyland 1976) relied on optical and near-infrared photometry alone to estimate luminosities, while Reid & Gilmore (1984) used CVF spectrophotometry to estimate the effects of H_2O absorption in a few relatively bright M-dwarfs from $1.4 - 2.4\mu$m. Beyond 2.2μm, the spectra were generally assumed to follow a Rayleigh-Jeans (RJ) tail, and shortward of 2.2μm luminosities were evaluated by interpolating between the observed broadband fluxes, essentially ignoring the presence of H_2O absorption. Berriman & Reid (1987, hereafter BR) were the first to study systematically the stellar water vapour absorption bands by using CVF spectrophotometry between 1.3 and 2.5μm and between 3.0 and 4.0μm from the high, dry site of Mauna Kea. They found that a simple-minded approach to the interpolation of the broad-band fluxes could lead to significant errors in the estimation of M_{bol}. Unfortunately BR were severely limited by both the sensitivity of the then available detectors, and the small number of very late M-dwarfs known, with the result that the latest star they were able to study was VB8, for which they derived a luminosity of $M_{bol} = 12.84$. This is almost 2 magnitudes brighter than the canonical luminosity of an object at the very bottom of the main-sequence (Burrows *et al.* 1989). We have, therefore, extended the work of BR by examining the infrared photometry and spectra of a sample of much later stars. Our sample includes objects discovered in proper motion surveys (LHS2924, LHS2065, LHS2397a (Luyten 1979)), large scale photometric surveys (TVLM-stars (Papers I and IV), BRI-stars (Irwin *et al.* 1991, Irwin *et al.* 1992, Irwin 1992)), surveys of companions to nearby stars (GD165B (Becklin & Zuckerman 1988)), a serendipitously discovered object (PC 0025+0447 (Schneider *et al.* 1991)) and several stars from the 25pc sample (Gliese 1969, Gliese & Jahreiss 1979) some of which overlap the BR sample. A list of positions for objects observed which do not have previously published positions, or for which the published positions are not sufficiently precise to allow easy identification, is included in Appendix 1.

Section 3.2 - Infrared Photometry

3.2.1 - Observations

Infrared JHKLL′ photometry of a sample of late-type dwarfs was measured with the 'ProtoCAM' camera of the NASA Infrared Telescope Facility, Mauna Kea, Hawaii on the nights of 20-24 June 1992 (UT). ProtoCAM uses as 58×62 SBRC InSb array in a He-cooled dewar, with a pixel scale of $0.35''$/pixel. Seeing over the run varied from $0.7''$ to $1.5''$. Observations were carried out by taking pairs of exposures at each passband for each star, with the telescope being moved a standard offset in between. The second exposure of each pair was used as a sky frame for the first exposure, and *vice versa*, allowing simultaneous observation of sky and object. Previous experience with ProtoCAM had shown that even after flat fielding the camera produces photometry which has systematic offsets between different parts of the array. Therefore at the beginning of our run two 'standard regions' of the array were chosen (i.e., two $\approx 10 \times 10$ pixel regions free of bad pixels), and all standards and objects were photometered within those two regions.

A standard data reduction procedure was followed : the data were bias subtracted, linearised, flat fielded, cleaned and then pair-subtracted. The pair-subtracted images were then aperture photometered using the FOTO routine of the FIGARO data reduction package. The linearity correction was evaluated by observing a hot-load placed in front of the dewar with integration times ranging from 1s to 100s. A single correction (derived from counts in one of the 'standard' regions of the array) was applied to the entire array. As a test a linearity correction was derived in the other 'standard' region – no difference in the derived linearity correction was found. The linearity correction was also derived for 'hot-load' data from three different nights – again no significant difference was found. The final linearity correction adopted was of the form;

$$\text{Linear Counts} = x - 2.6120 \times 10^{-6} x^2 + 1.7891 \times 10^{-10} x^3 \qquad (3.1)$$

where x =raw counts, and indicates a maximum deviation from linearity in the array of $\approx 8\%$ at 30,000 counts. This correction was applied to all four night's data. Flat fields were constructed at J, H and K for each night's data by observing a smooth section of the dome illuminated by the dome's interior lights, and then with the dome's lights off. By subtracting the two images the thermal background due to the dome and the telescope is removed, and the resultant image was used to flatten the data. At L and L′, flats were constructed by observing the dome with the interior lights off, and then rotating the

dome (keeping the telescope stationary) and observing the sky. Subtracting these images removes the thermal contribution of the telescope from the resulting flat field. The array has numerous bad pixels, both 'hot' and 'dead' – these were cleaned by linear interpolation.

Each standard was photometered through a 8.4″ diameter aperture, which includes 99.5% of the total flux. Each object was photometered using a smaller aperture (4.2″ at JHK and 2.8″ at LL′, except for extremely faint objects where apertures as small as 2.1″were used), and an aperture correction derived from the bright standard stars was applied. The aperture corrections were seen to vary by ±0.02 magnitudes at JHK and ±0.03 magnitudes at LL′ as a result of seeing variations over the course of each night – these variations have been included in our final estimated uncertainties.. Extinction coefficients were derived for each night's data by observations of one of the standards of Elias *et al.* (1982) over a range of airmasses, and from these mean coefficents were derived and used for the entire run. The measured values of the airmass coefficients were; K_J(mag/airmass) = 0.18 ± 0.03, $K_H = 0.10 \pm 0.02$, $K_K = 0.10 \pm 0.02$, $K_L = 0.14 \pm 0.02$, $K_{L'} = 0.12 \pm 0.03$. These values are about twice those normally seen at Mauna Kea, presumably due to dust injected into the upper atmosphere by volcanic eruptions within the last two years.

The J, H, K and L photometry was calibrated onto the CIT/CTIO infrared photometric system, using standards due to Elias *et al.* 1982, while the L′ photometry was calibrated onto the Mauna Kea Observatories (MKO) L′ system using IRTF standards (Tokunaga 1986) and UKIRT standards (Leggett 1992). Because the filters installed in ProtoCAM are not identical to those used to define the CIT/CTIO JHKL systems, considerable care was taken to observe a number of standards over a wide range of colour. As well as the Elias *et al.* standards, several stars from the UKIRT standard list which have photometry transformed into the CIT/CTIO system by Leggett (1992) were observed. The standard stars observed are summarised in Table 3.1. Only blue Elias standards (i.e., A-stars) were used to calculate the photometric zero point for each night's data. The scatter in the residuals about each photometric solution were always less than 0.02 magnitudes in the J,H and K bands, and less than 0.03 magnitudes in the L and L′ bands. Fig 3.1 shows the residuals in J–H, H–K, and K–L as a function of J–K. No evidence for a colour term is seen in any of these colours at the level of ~ 0.02 magnitudes. We therefore conclude that at the level of precision of our photometry and over the colour ranges we are interested in, no colour term is present. Modelling of observations of blackbody spectra using the ProtoCAM filter profiles by M.Ressler (1992), supports this conclusion. Lastly, we also

observed the Elias stars used as L standards, at L′, and we report their L′ magnitudes on the MKO system in Table 3.1.

3.2.2 - Discussion

The JHKLL′ photometry derived for all the M-dwarfs observed is shown in Table (a). (Table 3.2(b) shows photometry for several objects discussed in §3.3). Uncertainties for the brighter programme objects (K< 12) are typically ±0.03 at JHK and ±0.05 at LL′. Fainter objects typically have the following uncertainties; ±0.05 at J, H and K and ±0.10 magnitudes at L and L′; a few objects have poorer photometry and they are so denoted in Table 3.2(a). Also shown in Table 3.2(a) are V and I_C for each of the listed stars. Most of this photometry is due to a compilation of photometry for low mass stars due to Leggett (1992), however a few of the stars observed are from the Very Low Mass Star Survey of Tinney *et al.* (Papers I and IV) and the photometry reported was acquired with the Direct Imaging CCD Camera on the Palomar 60″ telescope as part of that programme.

Figure 3.2 shows the J-H/H-K diagram for all the stars in Table 3.2, along with both a dwarf and giant sequence (Leggett 1992, Bessell & Brett 1988). The J-H/H-K diagram discriminates between late-type giants and late-type dwarfs of roughly the same T_{eff} because of the pronounced H^- opacity minimum seen in dwarfs, which corresponds closely in wavelength with the H bandpass. With the exception of TVLM 890-49148, BRI2339-0447 and GD165B, all the stars in Table 3.2 fall within the dwarf region of this diagram. (TVLM 890-49148 is clearly a giant, and a Palomar 200″spectrum acquired as part of a radial velocity programme has clearly shown BRI2339-0447 to be a giant also.) GD165B (H–K=0.61, J–H=1.03) occupies a position suggestively separated from the rest of the dwarf sequence – however, Zuckerman & Becklin (1992) have recently reported that it shares a common proper motion with its white-dwarf primary making it very unlikely that it could be a giant. Given its almost certain status as a dwarf, it suggests that the dwarf sequence can be extended to spectral types later than M9 and to colours significantly redder than the previous limits of H–K $\approx$ 0.5 and J–H $\approx$ 0.75.

Veeder (1974) first noted that the flux in the L band (which with $\lambda_{eff} = 3.5\mu$m extends considerably into the $2.5 - 3.5\mu$m water band) is probably depressed by stellar H_2O absorption. BR found that their CVF spectrscopy bore this prediction out - late M-dwarfs do have significant stellar absorption in this region. We can use our L and L′ photometry to investigate this effect in stars later than BR were able to measure, by using the L-L′

colour as a long wavelength H_2O index. Because the L filter extends considerably into the stellar water band, while L′ ($\lambda_{eff} = 3.8\mu$m) is substantially clear of water absorption, the difference L–L′ acts as a crude H_2O index, much like the narrow band H_2O index defined at 2μm by Persson *et al.* (1977). Figure 3.3(a) shows a plot of L–L′ against J–K, with the L–L′ colours measured for several A-type Elias *et al.* standards shown for comparison. We also plot in Figure 3.3(b) the observed K–L and K–L′ colours as a function of I–K, together with polynomial fits to the data. The figures clearly show how H_2O absorption depresses the L band relative to the L′ band, and further that the depression becomes stronger for later type stars. Unfortunately because of the large bandpasses involved, L–L′ can only provide a crude handle on the water vapour absorption – while the L band does extend substantially into the 3μm H_2O band, it also includes some 'unabsorbed' stellar continuum, 'washing out' the effects of stellar H_2O absorption. However, the L–L′ data does indicate that for the latest M-dwarfs (J–K $\gtrsim$ 1.2 or spectral types M8-9 and later) that H_2O absorption at $3 - 3.5\mu$m is *at least* twice as strong as that seen by BR in earlier (J–K $\lesssim$ 1.0, spectral types M6-7 and earlier) stars.

Section 3.3 - Infrared Spectra

3.3.1 - Observations

Infrared spectral observations were carried out on the nights of 23-24 January 1992 (UT), using CGS4 on the United Kingdom Infrared Telescope (UKIRT), Mauna Kea, Hawaii. CGS4 is a cooled grating spectrograph mounted in a closed-cycle liquid-nitrogen cooled dewar. It currently uses a 58×62 SBRC InSb array, which can be moved along the spectrograph's focal plane in order to Nyquist sample the spectrum. For our run a 75 line/mm grating was used in six different configurations, which are summarised in Table 3.3. These configurations were chosen to cover the complete wavelength range from $1.0 - 2.5\mu$m with some overlap between each spectral segment.

In all six stars were observed over the course of the two nights. LHS2924, LHS2065, LHS2397a, and TVLM 832-10443 were observed in all six configurations. GJ1111 was observed in configurations 2-6, while data for GJ1002 was acquired only in configurations 1 and 2. Either before, or after (and often both before and after) each programme star observation in each configuration, a nearby atmospheric standard was observed. Late F-type and early G-type dwarfs were chosen from the *Bright Star Catalogue* (Hoffleit & Jaschek 1982) for use as atmospheric standards. Except for Paschen and Brackett series hydrogen lines and weak CO bands in the G-dwarfs, these spectra are featureless and well

described by a Rayleigh-Jeans tail. By chosing them to be as close as possible (on the sky) to our programme objects we were able to ensure that our atmospheric standard observations were never made more than 0.22 airmasses away from our programme stars, and most were observed within 0.05 airmasses of our programme stars. The standards chosen for use with each object are summarised in Table 3.4

Each star was observed by taking pairs of observations with the programme star being moved a standard distance along the slit by 'nodding' the telescope in between. Typically many pairs were taken on a given object and later added together. The wavelength scales were calibrated using argon arc spectra taken each time the grating was moved to a new configuration. Spectra were then extracted from the resulting images using the standard extraction (ANAL) routine of the FIGARO package. Before using the atmospheric standards to correct terrestrial H_2O absorption, several Paschen and Brackett series absorption lines of hydrogen were interpolated across in the standards. In particular the Pa_γ (1.0941μm), Pa_β (1.2822μm), Br_{12-4} (1.6412μm), Br_{11-4} (1.6811μm), Br_{10-4} (1.17367μm), Br_{9-4} (1.8179μm) and Br_γ (2.1661μm) lines were removed. Because the Pa_α and Br_δ lines fall within the terrestrial water vapour bands at 1.9μm, it turned out to be almost impossible to disentangle them from the complex terrestrial water vapour structure, which at these resolutions breaks up into a series of deep bandheads. They were therefore left uncorrected. The first overtone ^{12}CO bandheads (2.2935, 2.3227, 2.3525 and 2.3830 μm) are very weak in G0-G5 dwarfs, and undetectable in F-dwarfs. We measured depths for the 2.2935μm CO bandhead in the later G-dwarfs we observed (which had spectra types between G3V and G5V) of 3%. The CO bands in all our atmospheric standards were therefore left uncorrected.

The spectra of the programme stars were then divided by the atmospheric standards, and multiplied by a blackbody spectrum of a T_{eff} appropriate to that standard. The effective temperatures used are listed in Table 3.4, and were chosen to be appropriate for each spectral type (Johnson 1966). The segments from configurations 1 and 2, 3 and 4, and 5 and 6 were then joined together by equalising the fluxes in their respective overlapping regions, to produce 3 spectrum segments, more or less corresponding to the J, H and K filter windows. We found it was not possible to use the same technique between the segments of configurations 2 and 3, and 4 and 5, because in these cases the overlapping regions are in the heart of the terrestrial H_2O bands. Small errors in the cancellation of the terrestrial bands (presumably due to temporal H_2O variations, as well as airmass differences) tend to lead to large errors ($\sim$ 20%) in the estimated flux of the programme

objects in these regions. The programme spectra are also considerably more noisy in these regions. Each of the the 'J', 'H' and 'K' segments were therefore normalised using existing JHKLL′. Most of the photometry used is presented in Tables 3.2(a) – which is discussed in §3.2 – and 3.2(b) – which is drawn from the compilation of Leggett (1992) and from Paper IV. All the photometry used was on the CIT/CTIO system.

The normalisation was carried out by multiplying each spectrum segment by the appropriate J, H, or K bandpass (Ressler 1992), calculating the resultant flux density in that band and comparing with the broad-band photometric flux density. The broad-band flux densities were calculated for a magnitude system which assumes Vega has zero magnitude at all wavelengths. The flux densities corresponding to zero-magnitude and effective wavelengths adopted are listed in Appendix 2. They are based on the the combined calibrations due to several authors as summarised in Tokunaga (1986) for JHKLL′, and on the work of Reid & Gilmore (1984) in the optical. The flux density zero points have had small ($\approx$ 5%) corrections applied (Ressler 1992) to correct for the slightly non-standard ProtoCAM filter responses.

The resulting spectra are plotted in Figure 3.4 as normalised flux (F_ν) *versus* wavelength. Despite the efforts made to ensure that the removal of atmospheric features was as accurate as possible, it is clear that data obtained deep in the heart of the terrestrial water bands are not very accurate – it is simply a very difficult measurement to perform. In at least two stars, one of the water vapour bands appeared in the final spectra in 'emission'. We have marked on Figure 3.4 the wavelength ranges where the atmospheric transmission is worst - in particular the ranges 1.35 – 1.45μm, 1.8 – 1.85μm and 2.55 – 2.8μm. Exactly how good the data is in these ranges can be tested only by repeat observations, however they should probably not be trusted to more than $\pm$40% as is indicated by the differences seen between overlapping regions in LHS2924 and TVLM 832-10443. Outside these ranges we estimate our absolute spectrophotometry to be good to better than $\pm$10%.

The dominant feature of these spectra are obviously the strong H_2O absorption bands. It is fortunate that in extremely low-luminosity stars the stellar water vapour bands are much wider than those produced by the earth's atmosphere. So while the data we obtained in the heart of the terrestrial bands may be questionable, the wings of the stellar bands are observationally well constrained. It is especially interesting to note that the underlying structure of the bands seems to vary considerably from star to star. In general it appears that as the bands become stronger their "wings" extend further and further into the JHK windows. In Figure 3.4 we have attempted to display the observed

stars in what appears to be the order of their H_2O band strength, and a clear sequence can be seen in which stronger water vapour absorption 'eats' away more and more of the underlying spectrum. Take, for example, the red "wing" of the 2μm band; there seems to be a definite sequence from the weak absorption in GJ1111 which extends to only $\lambda \sim 2.1\mu$m; to the H_2O absorption in LHS2397a and TVLM 832-10443 which appears to extend to $\lambda \sim 2.2\mu$m; to the strong absorption in LHS2924 which appears to extend all the way $\lambda \sim 2.2\mu$m, where it effectively 'meets' the blue edge of the 2.5μm H_2O band. It is clear that the structure of these bands should give us a powerful handle on the properties of these stars. Unfortunately it is also clear that the existing stellar models do not accurately describe the behaviour of these bands. We have shown in Figure 3.4 three models for very late M-dwarfs (log $g = 5$, $[M/H] = 0.0$) due to Allard (1990, 1992) at T_{eff}=2250K, 2500K and 3000K. All of the models and spectra shown have been normalised at 1.7μm. These models are improved versions of those presented in Allard (1990), which include the effects of FeH and some neutral metals.

BR derived a temperature for GJ1111 of 2450 ± 110K – the 3000K model would appear to be too hot for this star, since it does not predict enough flux in the K band although it does predict something like the right shaped H_2O bands, even if somewhat too strong. The 2500K model (which is close the BR derived temperature) predicts almost the correct fluxes in the J, H and K windows, but displays H_2O bands which are *far* too strong. The situation is even more confusing at lower temperatures; we estimate the effective temperature of LHS2924 to lie within the range 2350-2050K (cf. §3.4) - however, neither a 2500K, 2250K, nor 2000K (not shown) model is a good match to the data. The water vapour bands of the 2000K and 2250K models are far too strong, while the 2500K model predicts too much flux in the J-band window. Both the 2000K and 2250K models over-predict CO absorption. Moreover, none of the models predict H_2O bands of the same shape as those seen in LHS2924. The models have a pronounced "knee" in the spectrum at 2.18μm, right at the edge of the H_2O band. LHS2924, unlike the other stars observed, has no such "knee" – it's spectrum is essentially straight from 1.9 to 2.3μm. A more serious difficulty is that *none* of the models come within 10% - 30% of the observed flux in the K-window for *any* of the stars we observed. It is clear that while the latest generation of models are a significant improvement over those previously available, significant problems remain to be resolved.

Section 3.4 - Bolometric Magnitudes

In order to estimate bolometric fluxes for a sample of stars later than BR studied, we have compiled all the available data on the flux distribution of late stars. In particular we have collected together; the CVF spectrophotometry, L′- and M-band photometry, and far-infrared photometry reported in BR; near-infrared grism spectra and optical spectra of the star PC 0025+0447 (Graham *et al.*1992, Schneider *et al.* 1991); optical spectra of the stars GJ1111, GL406, VB10, VB8, LHS2924 and TVLM 832-10443 acquired with the 4-Shooter Spectrograph on the Palomar 200" Telescope by J.Mould and by D.Hamilton; optical spectra of the star LHS2065 acquired with the Double Spectrograph on the Palomar 200" telescope by W.Sargent; V- and I-band photometry from Leggett (1992); and the infared spectrophotometry and photometry described above. Optical spectroscopy was placed on a flux scale using the available broadband photometry.

In Figure 3.5 we plot the data for all objects with either optical or infrared spectrophotometry, as well as the broadband fluxes for the unusual object GD165B. In each case a Rayleigh-Jeans (RJ) tail has been plotted extending longwards of the longest wavelength photometric point. Comparison of the existing far-infrared data, (which admittedly is not extensive), with the RJ extrapolation seems to indicate that this procedure is reasonable. These plots clearly show how important L or L′ photometry is to measurement of the luminosities of these faint stars – $\sim$ 30% of the energy emitted by stars later than M9 is emitted longward of 2.5μm, and it is clear that extrapolation using a RJ tail of the either K-band data, or the longest point in the K-window spectra, will severely under-estimate the luminosities of these stars. For two of the stars shown in Figure 3.5 (PC 0025+0447 and TVLM 832-10443) no L or L′ photometry was available. For these objects we have estimated K–L and K–L′ colours using their I–K colour and the relations of Figure 3.3(b), and these are plotted in Figure 3.5. Bolometric fluxes for the stars shown in Figure 3.5 have been estimated by simple linear interpolation of the available data (as indicated by the dotted lines in Figure 3.4) redward of the V-band (λ = 0.556μm). It should be noted that much less than 1% of the bolometric flux of these extremely late-type stars is emitted blueward of the V-band.

In Table 3.5(a) we show the apparent bolometric magnitudes (m_{bol}) so derived for each object. Given the large quantity of broadband photometry currently available for these stars, and the small number of objects with infrared spectrophotometry an obvious question to ask is "How much is the bolometric flux of a late M-dwarf over-estimated when broadband magnitudes alone are used?" We can attempt to answer this by comparing

the fluxes we produce by interpolating broadband fluxes across the stellar water vapour bands, with the fluxes produced by integrating the spectra accross the same wavelength range. The results of this experiment are summarised in Table 3.6. The scatter in the "flux deficit" values presented in Table 3.6 bears out the difficulty of doing spectrophotometry through the atmospheric H_2O bands. However they represent the best available data on the flux deficit produced by stellar water vapour bands. We have calculated a straight mean for the H_2O deficits in two luminosity ranges (I–K $<$ 4.0 and I–K $>$ 4.0) and for each of the wavelength ranges in Table 3.6. (VB8 was not used in deriving this mean - its anolmalously high H_2O deficits appear to be due to a photometric offset of $\sim$ 10% between our broadband photometry for this star and the BR spectrophotometry). Reid & Gilmore (1984) also attempted to measure the "flux deficits" in a small sample of brighter M-dwarfs between $1.38 - 2.49\mu$m - they obtained deficits of between 1% and 6%, which are consistent with the values we show in Table 3.6.

Even given the uncertainties present in the spectrophotometry, it is clear that stellar water vapour only induces an overcounting of between 5 and 10% in the estimated bolometric flux of a star. This is stated, however, with a *caveat.* At present the exact shape of the H_2O absorption band between 2.5 and 3.5μm remains a mystery for stars later than GL406 and VB8 (which were observed by BR). We have simple-mindedly interpolated the existing spectral data from 2.5 to 3.5μm for later-type stars (which for GL406 and VB8 reasonably mimics the observed behaviour). In doing so we estimate the H_2O absorption in LHS2065, LHS2397a and TVLM 832-10443 to be half as much again as that seen in VB8 and GL406. Given that scatter in the observed H_2O deficits, this is consistent with our conclusion in §3.2.2 that (based on their L-L′ colours) H_2O absorption (in this band) must be more than twice that seen in M6-7 stars. If our interpolation is reasonable then the conclusions about flux over-counting will remain correct. However, in the (unlikely) event that this band is much stronger than all the other bands, we may be more seriously overestimating the luminosities of these stars. Further observations in the $3 - 4\mu$m window are clearly called for. It should be noted that the available models do *not* predict this band to be significantly stronger than those at shorter wavelengths.

We have used the available broadband colours to estimate m_{bol} for the rest of the stars in Table 3.2, applying a 8% correction for flux over-counting in stars redder than I–K = 4.0 and a 6.2% correction for flux-over-counting in stars bluer than I–K = 4.0. The results are shown in Table 3.5(b). The objects TVLM 513-46546, TVLM 513-8328, TVLM 868-110639, TVLM 868-54745, TVLM 868-84947, TVLM 890-60235 and GD165B

were integrated in the absence of any V photometry, however this should not seriously affect our results as only $\lesssim 3\%$ of the flux of these stars is emitted shortward of the the I-band at 0.82μm. Also shown in Table 3.5 are parallax estimates for these stars - either trigonometric parallaxes (van Altena *et al.* 1992, Tinney 1992a (Paper III)), or photometric parallaxes based on main sequence M_K:I–K and M_J:I–J relations (Paper III). Using these parallaxes we derive estimates of M_{bol}, which are also shown. For objects with trigonometric parallaxes, the uncertainties in the final M_{bol} estimates are dominated by uncertainties in the bolometric flux (typically $\sim \pm 10\%$), as the parallax estimates are typically good to better than 5%. This is not true for objects with photometric parallaxes which have typical uncertainties of $\pm 30\%$. The photometric parallax for GD165B shown in Table 3.5 is derived from that of its white dwarf companion GD165A (Becklin & Zuckerman 1992), and is consistent with that of GD165B considering the large uncertainty introduced by the necessity of extrapolating the dwarf main sequence to the extreme colours of GD165B.

We calculated bolometric corrections using the *apparent* magnitudes of Table 3.5 ($BC_K = m_{bol} - K$), and these are shown plotted in Figure 3.6 as a function of I–K. The figure shows an extremely tight correlation of BC_K with I–K – the scatter of the residuals about the quadratic fit shown is only 0.05 magnitudes. Moreover, no systematic difference is seen between the points derived from integrated spectra (plotted as squares) and integrated broadband photometry (plotted as circles). We have also shown in Figure 3.6 (as the dotted line) the BC_K as a function of I–K relation derived from Bessell (1991). Bessell's absolute magnitude scale is based on the integration of broad-band magnitudes, and therefore overestimates the luminosities of late M-dwarfs, producing the systematic difference between his bolometric corrections and ours. We have also been able to obtain data on more extremely late stars – the new relation is clearly to be preferred.

Figure 3.7 shows the M_{bol} versus I–K diagram. Stars with trigonometric parallaxes are shown as squares, those with photometric parallaxes as triangles – no systematic difference can be seen here either. A third order fit is shown in the figure, which has a scatter in the residuals (over the range of most interest; $3.0 < M_{bol} < 5.1$) of 0.26 magnitudes. Given the tight BC_K relationship seen in Figure 3.6, almost all of this scatter must be inherent in the trigonometric and photometric parallaxes, i.e., represent either observational or cosmic scatter in the absolute-magnitude / colour relations. As scatter due to the observational uncertainties in the trigonometric parallaxes is $\lesssim 0.05$ magnitudes, the scatter in at least the square points in Figure 3.7 must be cosmic. It is possible that metallicity effects may be be causing some of this scatter, since metal poor stars will be subluminous for a given

colour. At present there are too few stars with good trigonometric parallaxes and known space motions, and the behaviour of these extremely late-type atmospheres with changes in metallicity are too poorly understood to really examine this question, though clearly it needs to be addressed. Leggett (1992) has used a much larger sample with good parallaxes and photometry to empirically define metallicity classes in earlier M-dwarfs. Once more data has been acquired such a classification may be possible for objects at the bottom of the main sequence.

One of the objects observed deserves further mention : GD165B. This object was discovered by Becklin & Zuckerman (1988) as a companion to the white dwarf GD165. It has, by far, the lowest known luminosity of any extra-solar system object. As can be seen in Figure 3.5(f), it's flux distribution is also much cooler than any of the other objects in our sample, emitting as much flux (F_ν) at 3.5μm as it does at 2.2μm.

We derive a bolometric magnitude of M_{bol} = 14.72, which represents the best current estimate of its luminosity, though a few *caveats* should be added. Whereas for most of the stars in our sample, flux estimates are not seriously in error as a result of extending the spectrum with a Rayleigh-Jeans tail longward of 3.5μm, it is not clear that this is true for GD165B – we may be underestimating its luminosity by not counting flux longward of 3.5μm. On the other hand GD165B may be expected to have much stronger H_2O bands than any of the other objects in our sample, which would lead us to overestimate its flux. An optical spectrum of GD165B obtained by Kirkpatrick *et al.* (1992b) has served to muddy the water even further. They find that its spectrum is unlike that of any other late type star (though they are able to rule out the presence of molecular bands like those seen in the Jovian planets) and suggest that it may have absorptions in previously identified molecules present. Obviously future study of this intriguing object is called for!

Section 3.5 - Effective Temperatures and Model Atmospheres.

Effective temperatures for very low mass stars have proved both difficult to estimate and controversial to interpret. The greatest difficulty to date has been that no *real* effective temperatures measurements have yet been made for these objects. An effective temperature is, strictly speaking, defined as follows;

$$L = 4\pi R^2 \, \sigma T_{eff}{}^4, \tag{3.1}$$

where L is the luminosity of the star in question, and R is the radius of its photosphere. In the (usual) absence of stellar radius data, effective temperatures are estimated using a model atmosphere where, given a set of input parameters (gravity, metallicity, radius, effective temperature, etc), an emergent flux distribution is predicted. When an observed star's flux distribution matches that of a model, we can say we have estimates for those parameters – including the effective temperature.

Kirkpatrick *et al.* (1992a) have recently presented $0.6 - 1.5\mu$m spectra for a sample 8 late M-dwarfs (though only two have $M_{bol} > 13.0$). They estimated effective temperatures for the reddest stars in their sample using fits of Allard's models in the $1.0 - 1.35\mu$m range. In this way they estimate effective temperatures systematically $\sim$ 500K hotter than those estimated by BR and Veeder (1974). As we discuss later, current interiors models and the effects of backwarming make it possibile that the BR and Veeder temperatures are systematically low. However, it is not clear to us that the current atmospheric models match the observed spectra well enough to be able to determine this. As was discussed in §3.2, while the models can produce reasonable fits to the observed spectra in the J-band window (and indeed also in the H-band window), they cannot simultaneously match the spectra in the K-band window. And their discrepancy at longer wavelengths is even worse. To illustrate this we show in Figure 3.8 the complete flux distribution of LHS2924 along with a 2500K and a 2000K Allard model. The 2500K model (which is the Allard model closest to the temperature for LHS2924 estimated by Kirkpatrick *et al.*) severely underestimates the flux observed for this star longer than 2μm. A 2000K model more nearly reproduces the observed longer wavelength fluxes (though it too underestimates the fluxes at K and L′ bands), but enormously over-predicts the depth of the H_2O bands.

The inability of the current models to reproduce the observed broadband colours and H_2O bands has been remarked upon by several investigators - Leggett (1992) observed that the models cannot reproduce the observed JHK colours, while Kirkpatrick *et al.* were unable to simultaneously fit the models to both optical and near-infrared spectra. Allard (1990) herself derived synthetic photometry from the models and observed the effect noted above, i.e., that J–H and H–K get *bluer* for the cooler models, even though these colours are observed to get *redder* in cooler stars. Mould (1976) remarked on the over-prediction of the H_2O band strengths, and suggested that this could be produced by the use of mean, rather than detailed, opacities for H_2O. H_2O absorptions are not (as is currently assumed by models) smooth and broad – at high resolution they break up into a 'picket fence' of bandheads, which once saturated absorb no more flux. A mean opacity however, can

continue to estimate higher and higher levels of absorption after H_2O is actually completely saturated.

In summary, then, as the models are currently unable to reproduce the gross, broadband properties of these stars, it is probably premature to attempt to use them in deriving effective temperatures. It bears emphasis that given we can neither measure the radii of these stars, nor predict their flux distribution with a model atmosphere, we cannot, strictly speaking, estimate an effective temperature.

In this situation we are forced to rely on various empirical derivations of quantities related to the effective temperature. Greenstein *et al.* (1970) and Veeder (1974) estimated temperatures by fitting a modified black-body curve through the observed broad-band UBVRIHKL photometry. They allowed for a small amounts of absorption at short wavelengths using a grey-body model. However, this technique essentially ignores the $\sim$ 10% of a star's flux absorbed by the infrared H_2O bands, which must be redistributed through the windows between those bands. BR estimated what we will call an "equivalent temperature", or T_{eqv}, by finding the temperature at which a blackbody, normalised to the observed flux density at 2.2μm, will have the same intregrated flux as is measured by integration of the observed spectrum. This is essentially a colour technique – it seeks a temperature at which the ratio of the observed flux (at a given wavelength) to the total integrated flux is the same as that for a blackbody of temperature T_{eqv} (Berriman *et al.* 1992). Obviously if the star's spectrum is *close* to a black-body, the derived T_{eqv} will be *close* to the effective temperature. (Errors were later found (Stringfellow 1991) in some of the optical photometry used by BR, however these produce no significant errors in the T_{eqv} values derived (Berriman *et al.* 1992).)

We have used the BR technique to derive T_{eqv} (normalised in our case to the observed flux at 3.82μm) for all the stars in our sample. These temperatures are shown in Table 3.5. For the 4 stars we have in common with BR we find a difference between our temperatures and theirs of 15 ± 38K (we ignore GL447 for which BR had no $1 - 2.5\mu$m spectroscopy). We further estimated equivalent temperatures anchored at 2.2μm for 12 of our stars later than those observed by BR, and found a mean difference between the 2.2μm and 3.8μm temperatures of 32 ± 109K – no significant difference seems to be introduced by our use of L′ (3.82μm) rather than K (2.3μm) to anchor our T_{eqv} estimate. We use our M_{bol} and T_{eqv} estimates to produce the H-R diagram shown in Figure 3.9 (we assume $M_{bol\odot} = 4.72$). It should be noted that the temperature uncertainties shown in Figure 3.9 are the uncertainties in our ability to estimate T_{eqv} – they do not reflect possible

systematic differences between T_{eqv} and T_{eff}. Also shown in Figure 3.9 are two predicted main-sequences based on interior/grey-body models for low mass stars and brown-dwarfs due to Burrows, Hubbard and Lunine (1989, hereafter BHL). The two models are for stars with age 10^9 years (by 10^9 years stellar objects have essentially settled onto the main sequence – older stars lie on essentially the same sequence). Model B assumes a standard convective mixing-length parameter ($\alpha = 1.0$); Model D assumes a more extreme mixing-length parameter ($\alpha = 0.1$). (Because no L′ photometry was available for GD165B we derived a T_{eqv} estimate using the existing L photometry and for a range of probable values for L-L′ (cf. Figure 3.2). For the following values of L-L′ we estimate T_{eqv}; L-L′ = 0.25, T_{eqv} = 1660K; L-L′ = 0.00, T_{eqv} = 1880K – the T_{eqv} shown in Table 3.5 is what we estimate to be the most likely value, L-L′= 0.20, T_{eqv} = 1700K.)

The now well-known offset between the observed 'empirical' main-sequence and the theoretical prediction can be clearly seen. The adoption of an extreme mixing-length parameter goes some way towards resolving the discrepancy for hotter objects ($T_{eqv} \sim$ 2800K), but at lower temperatures there remains a clear offset of $\sim$ 300K. Given the difficulties described above in estimating real effective temperatures for these low mass objects, and the relatively straightforward procedure for measuring luminosities, it seems most likely that the offset observed is due to problems in the T_{eff} scale rather than the luminosity scale. It is at present unclear whether this offset is due to the technique used in deriving T_{eqv}, or whether it reflects problems with the theoretical (interiors) models. It is interesting to note however that only a single temperature offset would be necessary to bring the observed and theoretical main-sequences into excellent agreement.

The fundamental assumption used to derive T_{eqv} is that the region around 3.82μm is both clear of stellar absorption *and* 'extra' stellar emission – that it represents some 'underlying' continuum. But this is almost certainly not true. The observed 300K offset would be produced if the ratio of the observed flux density at 3.82μm to the total flux were $\sim 10-15\%$ higher than that which would be predicted by a blackbody spectrum. However, we *know* that $\lesssim 10\%$ of the star's total flux is being absorbed by the infrared H_2O bands. This flux must be being re-radiated in the 'windows' between these bands – and it is in precisely these locations that we attempt to normalise our data in order to estimate T_{eqv}. The shaky bedrock of this technique is further demonstrated when we consider what would happen if we estimated T_{eqv} using the flux at 3.5μm (L band). In §3.2 it was seen that water vapour depresses L fluxes relative to L′ by up to 20%. T_{eqv} estimates 'anchored' at this band will be 15 – 20% *hotter* than those produced using the 3.82μm fluxes. The fact that

temperature estimates can vary depending on where they are made clearly indicates that a much better understanding of the physics of these atmospheres is required – in short, real effective temperatures will be obtainable *only* once atmospheric models which substantially match the observed spectra are available. Until that time quantities like T_{eqv} may well represent the best temperature estimate available, however they must be used with their inherent flaws firmly in mind.

3.5.2 - Brown Dwarves?

Mass is the parameter most commonly used to define a difference between stars (i.e., hydrogen-burning objects) and brown dwarves (i.e., objects unable to ignite hydrogen burning whose main energy source is gravitational contraction) – the "brown dwarf" limit most commonly adopted is $0.08M_{\odot}$. If the HR diagram of Figure 3.9 is examined (and we assume for the time being that the observed T_{eqv} values should be shifted by $\sim$ 300K to bring them into alignment with the theoretical tracks), then several objects would appear to lie well below this mass, and would be considered to be brown dwarves.

However it is worth remembering that the so-called 'brown-dwarf limit' is *not* a sharply defined one. It refers to the smallest mass at which an object can successfully reach the main sequence and derive all its luminosity from nuclear burning. But objects below $0.08M_{\odot}$ can spend several times 10^9 years fitfully burning hydrogen before they 'fail' to reach the main sequence. During this period an appreciable fraction of their luminosity can come from nuclear burning. This can be appreciated by examing Figure 7 of BHL. It shows that while there is an appreciable 'step' in the mass-luminosity relationship near $0.08M_{\odot}$, that 'step' is fairly shallow at 10^9 years and only becomes sharp by 10^{10} years. Objects with masses in the range $0.06 - 0.08M_{\odot}$ can spend several times 10^9 years as "transition" objects – neither fully burning hydrogen, nor rapidly cooling like lower mass objects (BHL).

All of the stars which lie below the $0.08M_{\odot}$ "brown-dwarf" limit in Figure 3.9 also lie above $0.06\ M_{\odot}$ – they seem to fill the "transition" regime. While they may not be fully supported by nuclear burning, it is also unlikely that *no* nuclear burning is taking place within them. Whether such objects are then classified as "brown-dwarves" is more a matter of semantics, than physics. Of all the objects shown in Figure 3.9, GD165B is clearly the best candidate for being a *bona-fide* brown dwarf. Its luminosity is outstandingly lower than that of any other known object, its temperature (even given the questions of temperature measurement raised above) is much lower than that of any other known object, and its spectrum is unlike that of any other late M-dwarf. The models of BHL would predict a

mass of M = $0.08M_\odot$ if it is 10^{10} years old and M = $0.06M_\odot$ if it is 10^9 years old. In either case it is clearly the lowest mass "star-like" object known.

Section 3.6 - Infrared Absorption Lines.

A detailed discussion of the numerous absorption lines the UKIRT spectra display for these stars is deferred to a later paper. However, as we believe some of these lines have been detected for the first time, we present here measured wavelengths, equivalent widths and identifications for some of the strongest lines in our spectra.

Figure 3.10 shows details of the more prominent absorption lines in LHS2924 – particularly the Na and K lines in the $1.1 - 1.3\mu$m window, and the Na, Ca and Ti lines in the $2.2 - 2.4\mu$m window. We present wavelengths and equivalent widths for these lines (measured using the ABLINE routine of the FIGARO data reduction package), averaged over the six stars for which we have spectra, in Table 3.7. Because of the low resolution used and the complex molecular bands dissecting the spectra, setting continuum levels around these lines is problematic. As a result the equivalent widths presented in Table 3.7 are rather uncertain, and are only accurate to ±35% in the J windows and ±50% in the H and K windows. Some of these lines have previously been observed in FTS spectra of earlier M-dwarfs (Mould 1978) – we have made preliminary identifications of as many of the rest of the lines as possible using the *Atlas of Infrared Spectra of the Solar Photosphere and Sunspot Umbrae* (Hall 1973). The temperatures of sunspot umbrae are approximately the same as those in very late M-dwarfs, simplifying the identification of lines which are strong in low-temperature photospheres. When searching the Atlas near the measured wavelength, we particularly looked for lines which were strong in the umbral spectra. As can be seen in Table 3.7, these generally turned out to be strong lines ($\log gf > -0.5$) of low ionization potential in transitions with small lower-energy-level potentials ($\sim 1.5-4.5$eV). Neutral Na, K, Ca and Ti are clearly abundant in the low temperature atmospheres of these dwarfs. Several weak lines (($\log gf \sim -2.0$) of Ti are also seen in the region of $2.22 - 2.23\mu$m. Again these are due to transitions with small (1.73eV) lower-energy-level potentials. We were unable to identify several of the apparently strong lines in the J and H windows.

Section 3.7 - Conclusion.

By using both JHKLL′ photometry and near infra-red spectra we have measured the complete flux distribution for a sample of objects which extends to the bottom of the main sequence – and possibly beyond. Photometry beyond 3μm is essential to deriving

luminosities for objects in the 2500 – 1800K effective temperature range. However we find that once the absorption to the infrared water vapour bands is taken into account we are able to determine *apparent* bolometric fluxes to better than 10% – the paucity of trigonometric parallaxes is the factor currently limiting the precision of the low mass luminosity scale.

Current atmospheric models fail to fit the observed infrared spectra of these stars, both in broad photometric passbands, and in the structure of the infrared H_2O bands which are generally predicted to be too strong. Given this, *effective temperatures for these stars can not be measured* and we are forced into adopting an empirical temperature scale. The BR technique for estimating equivalent temperatures, even when 'anchored' at 3.8μm rather than 2.2μm, continues to produce temperature estimates which show a $\sim$ 300K offset from the predicted H-R diagram. However, this temperature estimation is sensitive to the band-pass at which its normalisation is carried out and systematic offsets in the temperature scale may well be present. Until the re-radiation of the flux absorbed by the infrared water vapour bands is better understood, the empirical temperatures will continue to be suspect. What is most clear is that low-temperature dwarf atmospheres are an area crying out for more modelling. The new generation of infrared instruments are producing data which reveal serious problems with the existing theoretical work – it is time to go back and iterate again!

The authors gratefully acknowledge the staff of UKIRT and IRTF for their efficient, skillful and friendly assistance at the telescopes. We particularly wish to thank Drs T. Hawarden, G. Wright, M. Shure and T. Herbst. Dr J.L. Greenstein offered us many helpful insights, while Drs D. Hamilton and W. Sargent provided several optical spectra – for both we are very grateful. Dr M.Irwin helpfully provided pre-publication data on several of the BRI objects. We are extremely grateful to Dr F.Allard for providing the latest versions of her stellar models. CGT gratefully acknowledges a grant from the Sigma Xi Foundation which supported part of the travel expenses involved in carrying out this work.

References

Becklin, E.E. & Zuckerman, B., 1988, Nature, 336 656

Berriman, G. & Reid, I.N., 1987. MNRAS, 227, 315

Berriman, G., Reid, I.N. & Leggett, S.K. 1992, ApJLett, 392, L31

Bessell, M., 1991, AJ, 101, 662

Bessell, M. & Brett, J. 1988, PASP, 100, 1138

Burrows, A., Hubbard, W.B., Lunine, J.I. (BHL), 1989. ApJ 345, 939

Elias, J.H., *et al.* 1982, AJ, 87, 1029

Hall, D.N.B., 1973. *Atlas of Infrared Spectra of the Solar Photosphere and Sunspot Umbrae*, Kitt Peak National Observatory

Hawkins, M.R.S. & Bessell, M.S., 1988, MNRAS, 234, 177

Henry, T.J. & M^{c}Carthy, D.W., 1992, ApJ, 350, 334

Hoffleit, D. & Jaschek, C. 1982, *The Bright Star Catalogue.* (New Haven: Yale University Observatory)

Gliese, W., 1969, *Catalogue of Nearby Stars, Veroff. Astr. Rechen. Inst. Heidelberg No 22*

Gliese, W. & Jahreiss, H., 1979. A&ASupl, 38, 423

Graham, J.R., *et al.* 1992, AJ *in press*

Greenstein, J.L., *et al.* 1970. ApJ 161, 519

Irwin, M., M^{c}Mahon, R.G., Reid. N. 1991. MNRAS, 252, 61p

Irwin, M. *et al.* 1992. *in preperation*

Irwin, M. 1992. *private communication*

Kirkpatrick, J.D., Kelly, D.M., Rieke, G.H., Liebert, J., Allard, F., Wehrse, R. 1992a. ApJ *in press*

Kirkpatrick, J.D., Henry, T.J, Liebert, J. 1992b. ApJ *submitted*

Kurucz, R.L. & Peytremann, E., 1975. *A Table of Semi-Empirical gf Values*, SAO Special Report 362. (Cambridge: Smithsonian Astrophysical Observatory)

Johnson, H.L. 1966, ARAA, 4, 193

Leggett, S.K. 1992, ApJSuppl, 82, 351

Leggett, S.K. & Hawkins, M.R.S., 1988, MNRAS, 234, 1065

Leggett, S.K. & Hawkins, M.R.S., 1989, MNRAS, 238, 145

Luyten, W.J., 1979, *LHS Catalogue* (Minneapolis: University of Minnesota)

Mould, J.R., 1976. A&A, 48, 443

Mould, J.R. & Hyland, A.R., 1976. ApJ, 208, 399

Reid, I.N. & Gilmore, G., 1984. MNRAS, 206, 19

Ressler, M. 1992 *private communication*

Schneider, D.P., *et al.* 1991, AJ, 102, 1180

Stringfellow, G.S. 1991, ApJLett, 375, L21

Tinney, C.G., Mould, J.R., Reid, I.N. 1992a, ApJ, 396, 173

Tinney, C.G., Reid, I.N., Mould, J.R., 1992, ApJSuppl, *submitted.* (Paper I)

Tinney, C.G., 1992a, AJ, *in press.* (Paper III)

Tinney, C.G., 1992b, ApJ, *submitted.* (Paper IV)

Tokunaga, A.T., 1986, *IRTF Photometry Manual* (Honolulu: University of Hawaii)

Veeder, G.J., 1974. AJ 79, 1056

Zuckerman, B. & Becklin, E.E., 1992, ApJ, 386, 260

Table 3.1 - ProtoCam Photometry of Elias *et al.* Standards.

Object	J_{CIT}		H_{CIT}		K_{CIT}		L_{CIT}		L'_{MKO}[a]		SRC[c]	SRC[c]
	Obs.	Res.[b]	Obs.	Res.	Obs.	Res.	Obs.	Res.	Obs.	Res.	1	2
HD1160	7.077	-0.017	7.049	-0.009	7.045	-0.005	7.037	-0.012	7.035	-0.035	E	UM
HD129653	6.994	0.014	6.940	0.000	6.932	-0.012	6.927	-	6.915		E	
HD129655	6.809	0.006	6.708	0.002	6.691	-0.001	6.673	-0.008	6.669		E	
HD201941	6.681	-0.011	6.626	0.014	6.610	0.010	6.612	-0.002	6.619		E	
GJ1002	8.292	0.013	7.728	0.027	7.418	0.012	7.089	-	6.931	0.029	E	UM
GL406	7.060	0.000	6.436	0.004	6.082	-0.002	5.709	0.021	5.565		E	
GL748AB	7.090	-0.015	6.566	-0.021	6.348	-0.043	6.087	-	5.969	0.001	E	UM
GL811.1	7.759	-0.004	7.149	0.001	6.932	-0.002	6.726	0.014	6.661		E	
GL447	6.506	-0.016	5.946	-0.036	5.670	-0.040	5.371	-0.041	5.262		U	
GL876	5.861	0.059	5.274	0.046	5.018	0.042	4.785	0.015	4.697		U	
GL729	6.172	0.040	5.615	0.055	5.354	0.036	5.077	-	4.975		U	
BS8551	2.930	-0.020	2.393	-0.023	2.314	-0.014	2.219	0.030	2.219	0.020	E	IM
BS4689	-		-		3.766	0.011	3.730	0.030	3.759	0.021	E	IM
BS6707	-		-		3.251	-0.041	3.180	-0.030	3.194	-0.024	E	IM

Notes to Table 3.1

a - Except for BS4689, BS6707 and BS8551 which define the zero-point for these observations, this column reports new values for the L′ magnitudes of these objects.

b - Defined in the sense Residual = Standard – Object.

c - The column labelled SRC1 gives the source for the JHKL photometry on the CIT/CTIO system, SRC2 gives the source for the L′ photometry on the Mauna Kea Observatories system; E = Elias *et al.* 1982, U = UKIRT Standards due to Krisciunas (1990) and transformed to CIT/CTIO system by Leggett (1992), M = IRTF MKO L′ standards (Tokunaga 1986), UM = UKIRT MKO L′ stds (Krisciunas 1990).

Table 3.2 - VIJHKLL′ Photometry of Low Mass Stars.

Object	V[1]	I_C[2]	J_{CIT}	H_{CIT}	K_{CIT}	L_{CIT}	L'_{MKO}	J-H	H-K	I-K	Q1[3]	Q2[3]
(a) Objects with IRTF Photometry.												
LHS2397a	19.57	14.95	12.00	11.26	10.84	10.26	10.02	0.74	0.42	4.11	a	b
TVLM 513-46546	-	15.09	11.96	11.31	10.77	10.20	9.97	0.65	0.54	4.32	a	b
TVLM 513-8328	-	17.14	14.17	13.48	13.03	12.42	12.26	0.69	0.45	4.11	a	c
TVLM 868-110639	-	15.79	12.72	11.93	11.44	10.67	10.51	0.79	0.49	4.35	a	b
TVLM 868-54745	-	14.90	12.74	12.09	11.73	11.12	11.11	0.65	0.36	3.17	a	c
TVLM 868-84947	-	16.28	14.14	13.40	12.93	12.57	12.35	0.74	0.47	3.35	b	c
TVLM 890-60235	-	16.65	14.17	13.56	13.22	12.61	-	0.61	0.34	3.43	b	c
BRI 0021-0214	-	15.07	11.90	11.13	10.64	9.88	9.71	0.77	0.49	4.43	a	b
BRI 1222-1222	-	-	12.61	11.90	11.43	10.71	10.75	0.71	0.47	-	a	b
BRI 2202-1119	-	13.66	11.71	11.17	10.84	10.36	-	0.54	0.33	2.82	a	b
BRI 2339-0447	-	11.70	9.57	8.67	8.14	7.35	-	0.90	0.53	3.56	a	b
GD165B	-	19.25	15.80	14.78	14.17	13.27	-	1.02	0.61	5.08	b	c
GJ1002	13.76	10.16	8.29	7.73	7.42	7.09	6.93	0.59	0.31	2.74	a	a
GL406	13.45	9.39	7.06	6.44	6.08	5.71	5.57	0.62	0.36	3.31	a	a
GL447	11.12	8.14	6.51	5.95	5.67	5.37	5.26	0.56	0.28	2.47	a	a
GL699	9.55	6.77	5.28	4.77	4.52	4.22	4.12	0.51	0.25	2.25	a	a
GL729	10.47	7.69	6.17	5.62	5.35	5.08	4.98	0.55	0.27	2.34	a	a
GL748AB	11.07	8.48	7.09	6.57	6.35	6.09	5.97	0.52	0.22	2.13	a	a
GL811.1	11.50	9.11	7.76	7.15	6.93	6.73	6.66	0.61	0.22	2.18	a	a
GL831	12.01	9.02	7.31	6.70	6.42	6.12	6.00	0.61	0.28	2.60	a	a
GL866AB	12.33	8.62	6.48	5.89	5.56	5.21	5.08	0.59	0.33	3.06	a	a
GL876	10.18	7.45	5.86	5.27	5.02	4.79	4.70	0.59	0.25	2.43	a	a
VB10	17.50	12.80	9.91	9.25	8.82	8.35	8.15	0.66	0.43	3.98	a	a
(b) Other Objects.												
LHS2065[4]	18.80	14.44	11.24	10.49	9.98	-	9.19	0.75	0.51	4.46	b	b
GJ1111[4]	14.79	10.53	8.20	7.62	7.26	-	-	0.58	0.36	3.27	b	
TVLM 832-10443[5]	-	16.06	13.16	12.58	12.04	-	-	0.58	0.54	4.02	b	

Notes to Table 2

1 V band photometry from Leggett (1992).

2 I_C band photometry from Leggett (1992), except for TVLM and BRI stars which was acquired on the Palomar 60″ telescope.

3 Q1 is a quality flag giving uncertainties for JHK photometry – a < ±0.03 ; b < ±0.05 ; c < ±0.10.Q2 is a quality flag giving uncertainties for LL′ photometry, – a < ±0.05 ; b < ±0.10 ; c < ±0.20.

4 JHKL′ Photometry from Leggett (1992).

5 Photometry taken with the Cassegrain IR Camera of the Palomar 200″ telescope as part of Very Low Mass Star Survey (Paper IV).

Table 3.3 - CGS4 Grating Positions.

Configuration	λ_{cen} (μm)	Order	λ Range (μm)	Dispersion (nm/pix)	Resolution ($\frac{\lambda}{\Delta\lambda}$)
1	1.10	II	1.006 – 1.203	1.635	337
2	1.27	II	1.171 – 1.374	1.685	383
3	1.44	II	1.344 – 1.545	1.676	441
4	1.65	I	1.448 – 1.857	3.366	253
5	2.00	I	1.803 – 2.210	3.350	306
6	2.35	I	2.155 – 2.563	3.344	360

Table 3.4 - CGS4 Programme Objects and Standards.

Object	Standard	Type[a]	T_{eff}[b]
LHS2065	BS3538	G3V	5700
LHS2924	BS5534	G0-2V	5835
LHS2397a	BS4529	F7V	6130
TVLM 832-10443	BS996	G5V	5660
GJ1111	BS3299	F6V	6270
GJ1002	BS72	G0V	5900

Notes to Table 3.4

a - Spectral type are from the *Bright Star Catalogue* (Hoffleit & Jaschek 1982)

b - T_{eff} derived using the spectra type and the T_{eff}-spectral type relations of Johnson (1966).

Table 3.5 - Bolometric Magnitudes for Low Mass Stars.

Object	K	I–K	m_{bol}	BC_K	π_T[a] (mas)	π_P[b] (mas)	M_{bol}	T_{equ}[c] (K)	Notes
(a) Objects with Infrared Spectra and Broadband Photometry									
PC 0025+0447	14.87	4.66	18.06	3.19		14±4	13.79	2010	*d*
LHS2065	9.98	4.46	13.17	3.19	118.0±1.7		13.53	2150	
LHS2924	10.84	4.37	14.06	3.22	93.3±1.5		14.06	2080	
LHS2397a	10.80	4.15	13.92	3.12	70.9±2.4		13.17	2150	
TVLM 832-10443	12.04	4.02	15.19	3.15	39.4±2.2		13.17	2230	*d*
VB8	8.82	3.42	11.94	3.12	155.7±0.7		12.90	2450	
GL406	6.08	3.31	9.15	3.07	418.9±2.0		12.26	2580	
GJ1111	7.26	3.27	10.25	2.99	275.8±3.0		12.46	-	*e*
			10.21	2.95	275.8±3.0		12.42	-	*f*
GL866AB	5.56	3.06	8.54	2.98	293.0±2.7		10.88	2720	
GL447	5.67	2.47	8.49	2.78	299.4±1.5		10.87	2580	JH
GL699	4.52	2.25	7.26	2.74	546.7±0.8		10.83	3110	
(b) Objects with Broadband Photometry Only									
GD165B	14.17	5.08	17.50	3.33	27.8±3.4		14.74	1700[g]	JHK
BRI 0021-0214	10.64	4.43	13.84	3.20	82.5±3.4		13.42	1980	JHK
TVLM 868-110639	11.44	4.35	14.64	3.20	57.5±1.9		13.44	1975	JHK
TVLM 513-46546	10.77	4.32	14.00	3.23	100.8±2.3		14.02	2080	JHK
TVLM 513-8328	13.03	4.11	16.21	3.18		25±8	13.20	2180	JHK
VB10	8.82	3.98	11.95	3.13	172.8±0.8		13.13	2330	JHK
TVLM 890-60235	13.22	3.43	16.28	3.06		20±6	12.79	-	JHK
TVLM 868-84947	12.93	3.35	16.13	3.20		18±6	12.41	2350	JHK
TVLM 868-54745	11.73	3.17	14.80	3.07		32±10	12.33	2450	JHK
GJ1002	7.42	2.74	10.26	2.84	212.8±3.3		11.90	2910	HK
GL831	6.42	2.60	9.29	2.87	125.5±1.9		9.78	2920	JHK
GL876	5.02	2.43	7.84	2.82	211.1±4.8		9.46	3090	JHK
GL729	5.35	2.34	8.14	2.79	342.3±5.0		10.81	3070	JHK
GL811.1	6.93	2.18	9.67	2.74	56.7±5.7		8.44	3260	JHK
GL748AB	6.35	2.13	9.05	2.70	100.0±2.2		9.05	3180	JHK

Notes to Table 3.5

a - Absolute Trigonometric Parallaxes from the Yale General Catalogue of Trigonometric Stellar Parallaxes (van Altena, Lee & Hoffleit 1992), except for TVLM 832-10443, 868-110639, 513-46546 and BRI0021-0214 which are from Paper III, and GD165B which has a preliminary parallax in Zuckerman & Becklin (1992).

b - Photometric Parallaxes derived from M_K:I–K and M_J:I–J relation of Paper III. The uncertainties quoted are determined by the spread about the colour-magnitude relations (±0.3 magnitudes) and the difference in the parallaxes determined using both M_K:I–K and M_J:I–K.

c - See text (§3.5) for definition of T_{equ}.

d - L and L′ estimated using I–K colour and the relations of Figure 3.3(b).

e - Calculated using infrared spectrophotometry presented in this paper.

f - Calculated using infrared spectrophotometry of BR.

g - See text (§3.5) for discussion of this value.

J - Correction of 2.5% (I–K > 4.0) or 1.8% (I–K < 4.0) applied to m_{bol} and M_{bol} for flux 'missed' between J and H bands.

H - Correction of 2.7% (I–K > 4.0) or 2.4% (I–K < 4.0) applied to m_{bol} and M_{bol} for flux 'missed' between H and K bands.

K - Correction of 3.0% (I–K > 4.0) or 2.0% (I–K < 4.0) applied to m_{bol} and M_{bol} for flux 'missed' between K and L bands.

Table 3.6 - Flux 'Overcounting' Produced by Broadband Magnitudes.

Object	I–K	Flux Overcounted as Percentage of Bolometric Flux J to H (1.29 – 1.67μm)	H to K (1.67 – 2.23μm)	K to L (2.23 – 3.55μm)	Notes
PC 0025+0447	4.66	2.4%	2.3%	-	*a*
LHS2065	4.46	-	-	4.8%	
LHS2924	4.37	2.4%	3.4%	-	
LHS2397a	4.15	-	2.3%	4.1%	
TVLM 832-10443	4.02	2.8%	2.8%	3.0%	*b*
VB8	3.42	8.0%	4.4%	3.6%	
GL406	3.31	1.5%	3.0%	2.6%	
GJ1111	3.27	2.1%	1.2%	1.3%	*b*
GJ1111	3.27	0.3%	1.3%	2.7%	*c*
GL866AB	3.06	2.1%	3.1%	2.9%	
GJ1002	2.74	3.1%	-	-	
GL447	2.47	-	-	2.1%	
GL699	2.25	1.5%	3.4%	1.4%	
I–K > 4.0		2.5%	2.7%	3.0%	
I–K < 4.0		1.8%	2.4%	2.0%	

Notes to Table 3.6

Blank entries indicate that either no spectra were available in this wavelength range, or that no measurable flux deficit was found.

a - L and L′ estimated using I–K colour and the relations of Figure 3.3(b).

b - Calculated using infrared spectrophotometry presented in this paper.

c - Calculated using infrared spectrophotometry of BR.

Table 3.7 - Strong Infrared Absorption Lines.

λ_{obs}[a] (μm)	λ_{ID}[b] (μm)	Species	Eq. Width[c] (nm)	log gf[d]
1.1409	1.140379	Na I	1.7	-0.18
1.1701	1.169020	K I	0.7	0.21
1.1778	1.177282, 1.176960	K I	1.0	0.46,-0.49
1.1992[e]		FeH	1.8	
1.2110	1.210354	Si I	0.6	-0.39
1.2426	1.243225	K I	0.9	-0.46
1.2518	1.252209	K I	1.0	-0.15
1.583			0.24	
1.594			0.11	
1.603			0.20	
1.614	1.613688	Ca I	0.39	-0.53
1.627			0.72	
2.096	2.096241, 2.097253	Ca I	0.23	-0.79,-0.59
2.207	2.205643, 2.208368	Na I	0.62	0.29,-0.27
2.220	2.221122, 2.223292	Ti I	0.15	-1.85,-1.74
2.233	2.231063	Ti I	0.14	-2.21
2.262	2.260792, 2.262495,2.265131	Ca I	0.11	-0.42,0.20,0.46
2.337	2.337915, 2.334848	Na I	0.30	-0.42,0.53

Notes to Table 3.7

a - Observed line centroid. Good to $\sim \pm 0.0005\mu$m in J window, to $\sim \pm 0.001\mu$m in H windows and to $\sim \pm 0.002\mu$m in K window.

b - Line indentifications from Hall (1973). Where more than one wavelength is shown, lines would have been detected as blended by CGS4.

c - Equivalent widths are good to $\sim \pm 35\%$ in J window, and $\pm 50\%$ in H and K windows.

d - log gf values are due to Kurucz & Peytremann (1975).

e - FeH absorption band (Kirkpatrick *et al.* 1992a).

Appendix 1 - Positions for Observed Objects.

We provide positions for those objects listed in Table 3.2 which either have no previously published positions (Tinney *et al.* and some Irwin *et al.* sources), or for which the previously published positions are not very precise (LHS stars and GD165B). We do not provide new positions for the GL/GJ stars, as these objects are sufficiently bright that finding them is trivial. The positions quoted below are good to $\pm 1''$, and are derived from either COSMOS scans of Palomar or UK Schmidt Survey plates (Tinney *et al.* sources), or IRTF/UKIRT telescope co-ordinates. In particular the position for PC00 is better than that provided in the discovery paper (Schneider *et al.* 1991). All positions are B1950.0 equinox.

Object	α	δ	Epoch
BRI 0021-0214	$00^h\ 21^m\ 51.1^s$	$-02°\ 14'\ 59''$	1992.5
PC 0025+0447	$00^h\ 25^m\ 07.6^s$	$+04°\ 47'\ 04''$	1991.5
LHS2065	$08^h\ 51^m\ 05.6^s$	$-03°\ 18'\ 07''$	1992.1
LHS2397a	$11^h\ 19^m\ 18.1^s$	$-12°\ 56'\ 46''$	1992.1
BRI 1222-1222	$12^h\ 22^m\ 17.1^s$	$-12°\ 21'\ 58''$	1992.5
GD165B	$14^h\ 22^m\ 12.0^s$	$+09°\ 30'\ 45''$	1992.5
LHS2924	$14^h\ 26^m\ 36.3^s$	$+33°\ 24'\ 06''$	1992.1
TVLM 868-54745	$14^h\ 57^m\ 59.6^s$	$-00°\ 47'\ 54''$	1986.1
TVLM 513-46546	$14^h\ 58^m\ 54.5^s$	$+23°\ 01'\ 50''$	1987.3
TVLM 868-84947	$15^h\ 03^m\ 26.0^s$	$+00°\ 05'\ 05''$	1986.1
TVLM 868-110639	$15^h\ 07^m\ 41.2^s$	$-02°\ 29'\ 47''$	1986.1
TVLM 513-8328	$15^h\ 12^m\ 08.9^s$	$+23°\ 52'\ 12''$	1987.3
BRI 2202-1119	$22^h\ 02^m\ 55.6^s$	$-11°\ 19'\ 06''$	1992.5
TVLM 890-60235	$22^h\ 20^m\ 32.0^s$	$+00°\ 14'\ 59''$	1989.7
BRI 2339-0447	$23^h\ 39^m\ 27.9^s$	$-04°\ 47'\ 44''$	1992.5

Appendix 2 - Adopted Flux Zero-Points and Effective Wavelengths.

The following effective wavelengths and flux densities for a zero magnitude star were adopted. JHKLL' values are for stars observed with the ProtoCAM JHKLL' filters. They are modifications of the values presented in Tokunaga (1986) for the ProtoCAM filter profiles (Ressler 1992), and assume Vega has zero magnitude at all wavelengths. VI_C values are from Reid & Gilmore (1984).

	V	I_C	J	H	K	L	L'
λ_{eff} (μm)	0.556	0.82	1.29	1.67	2.23	3.55	3.82
F_ν(Jy) for 0 mag.	3708	2550	1530	1000	644	279	250

Figure Captions

Figure 3.1 - ProtoCAM-to-CIT/CTIO Colour Terms. Each panel shows the residuals (in the sense standard minus observation) of the observed standards for each of J–H, H–K, K–L, K-L′ as a function of J–K. The sources of the standard photometry are descibed in the text.

Figure 3.2 - J–H/H–K Diagram for Stars in Table 3.2. Also shown is a dwarf sequence *(dashed line)* due to Leggett (1992) and a giant sequence *(dot-dashed line)* due to Besell & Brett (1988). The names of the latest M-dwarfs are noted.

Figure 3.3(a) - L–L′ as a Function of J–K for Stars in Table 3.2. The line is a least squares fit to the data; $L–L' = -0.007 + 0.125(K–L) + 1.98618(K–L)^2$, $\sigma(L–L') = 0.06$.

Figure 3.3(b) - K–L and K–L′ as a Function of I–K for Stars in Table 3.2. *Filled Circles*: K–L′, *Filled Squares*: K–L. The lines are least squares fits to the data. $K–L = 0.10552 + 8.98689 \times 10^{-5}(I–K) + 0.030258(I–K)^2$; $\sigma(K–L) = 0.07$. $K–L' = 0.140721 + 0.0207674(I–K) + 0.0329135(I–K)^2$; $\sigma(K–L') = 0.05$.

Figure 3.4 - Infrared Spectra of Low Mass Stars. The spectra of five objects with substantially complete $1.0 – 2.5\mu$m spectra are shown. Each flux calibrated spectrum was normalised by its flux in the range $\lambda = 1.0695 – 1.075\mu$m, and offset. The normalisation constants and offsets used are as follows; LHS2924: 34.321mJy, 4.0; TVLM 832-10443: 10.194mJy, 3.0; LHS2937a: 32.668mJy, 2.0; LHS2065: 69.183mJy, 1.0; GJ1111: 958.44mJy, 0.0. Also shown for reference are model spectra due to Allard (1990 - 2500K and 2000K) and Mould (1976 - 3000K), which have been similarly normalised.

Figure 3.5 - The Flux Distributions of the Lowest Mass Stars. The sources of the infrared photometry and spectrophotometry are described in the text. Broadband fluxes are shown as large circles, UKIRT spectrophotometry is shown as a thin line. Spectrophotometry due to BR and Graham *et al.* is shown as small dots. The dotted lines used to connect points and sections of spectrum show the linear interpolations used in calculating the bolometric fluxes described in the text.

Figure 3.6 - Bolometric Correction B_K versus I–K. *Squares* – stars with bolometric fluxes derived from infrared spectra. *Circles* – stars with bolometric fluxes derived from broadband photometry, corrected as descibed in the text. The solid line shown is a fit to the data; $BC_K = 0.731089 + 1.50089(I–K) – 0.328693(I–K)^2 + 0.0261465(I–K)^3$; $\sigma(BC_K) = 0.04$. The dotted line is the BC_K relation of Bessell (1991).

Figure 3.7 - Absolute Bolometric Magnitude M_{bol} versus I–K. *Squares* – stars with trigonometric parallaxes. *Triangles* - stars with photometric parallaxes. The line is a fit to the data; $M_{bol} = -14.8545+18.8384(I–K)–4.35502(I–K)^2+0.351274(I–K)^3$; $\sigma(3.0 < M_{bol} < 5.1) = 0.26$.

Figure 3.8 - LHS2924 and 2250K and 2000K Models due to Allard. Symbols used are the same as those in Figure 3.5. The models of Allard are shown as a dashed line.

Figure 3.9 - HR Diagram for Very Low Mass Stars. *Squares* – stars with trigonometric parallaxes. *Circles* - stars with photometric parallaxes derived from I–K colours. Temperatures are derived as T_{eqv} which is defined in the text. Models are due to Burrows, Hubbard & Lunine (1989). The small circles on the tracks show the locations of (going from high luminosity to low) 0.20, 0.15, 0.125, 0.11, 0.10, 0.095, 0.090, 0.085, 0.080, 0.075, 0.070 and $0.060 M_{\odot}$ models.

Figure 3.10 - The Infrared Spectrum of LHS2924 - Identifications for the indicated lines are shown in Table 3.7

Figure 3.1

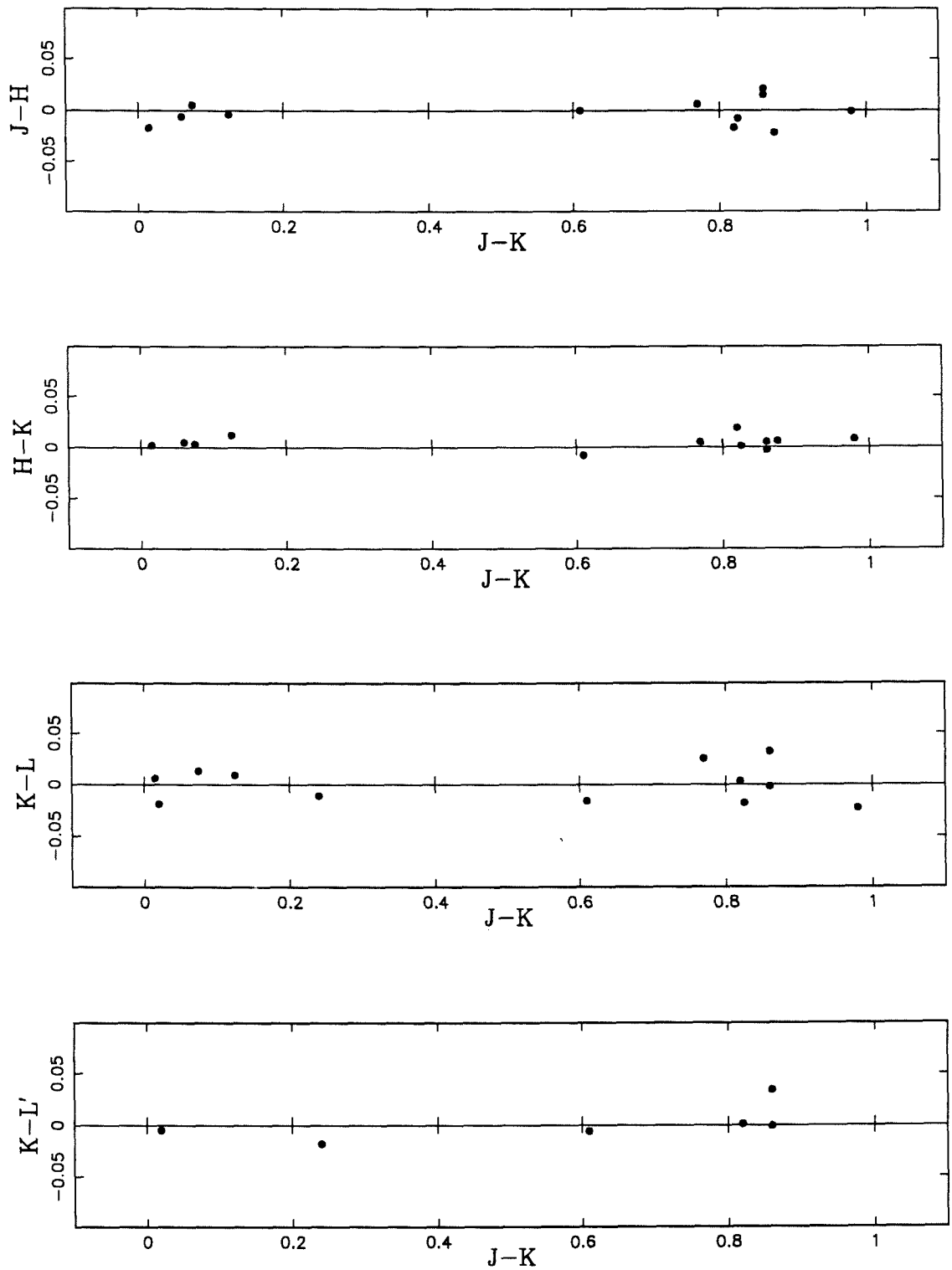
J−H
0.05
0
−0.05
0
0.2
0.4
0.6
0.8
1
J−K
H−K
0.05
0
−0.05
0
0.2
0.4
0.6
0.8
1
J−K
K−L
0.05
0
−0.05
0
0.2
0.4
0.6
0.8
1
J−K
K−L′
0.05
0
−0.05
0
0.2
0.4
0.6
0.8
1
J−K

Figure 3.2

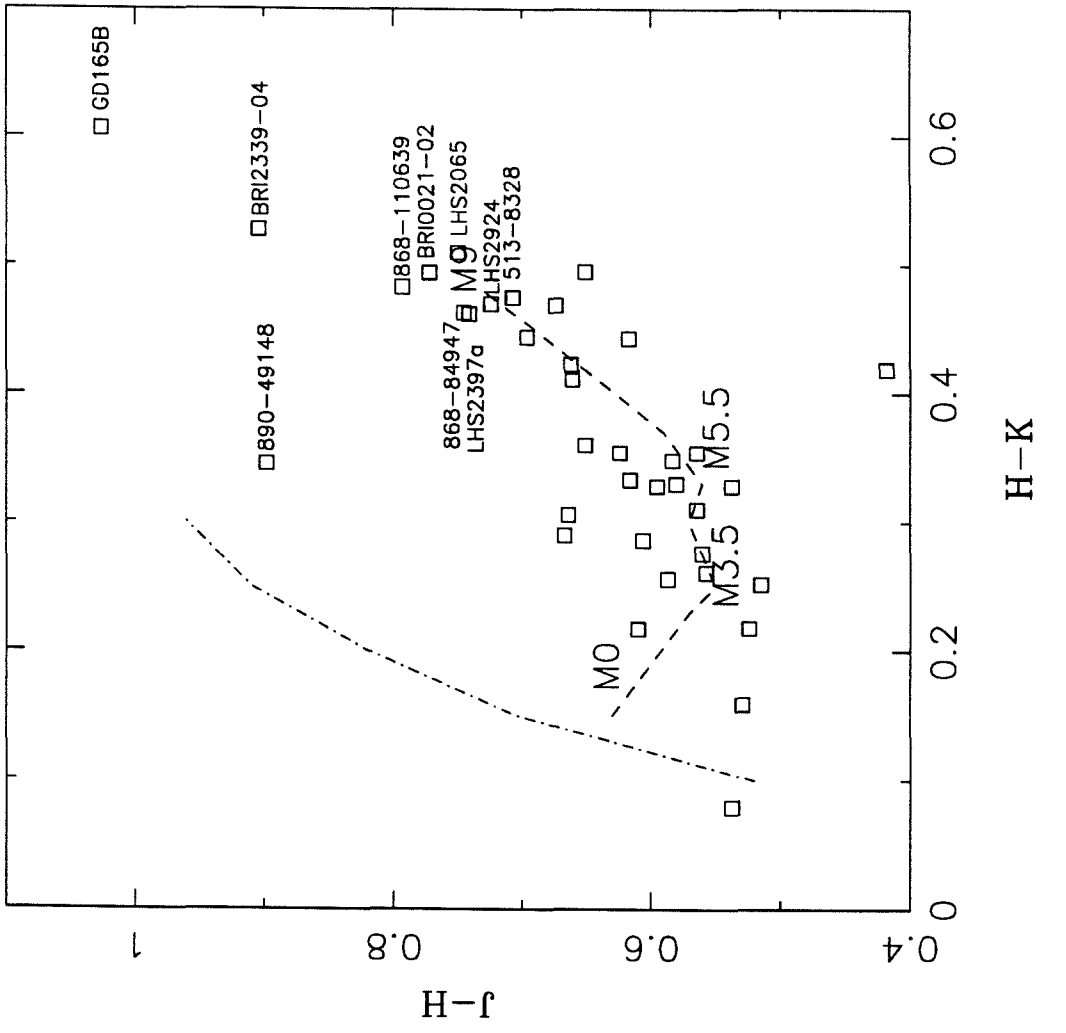

christ 3-Aug-1992 15:44

Figure 3.3(a)

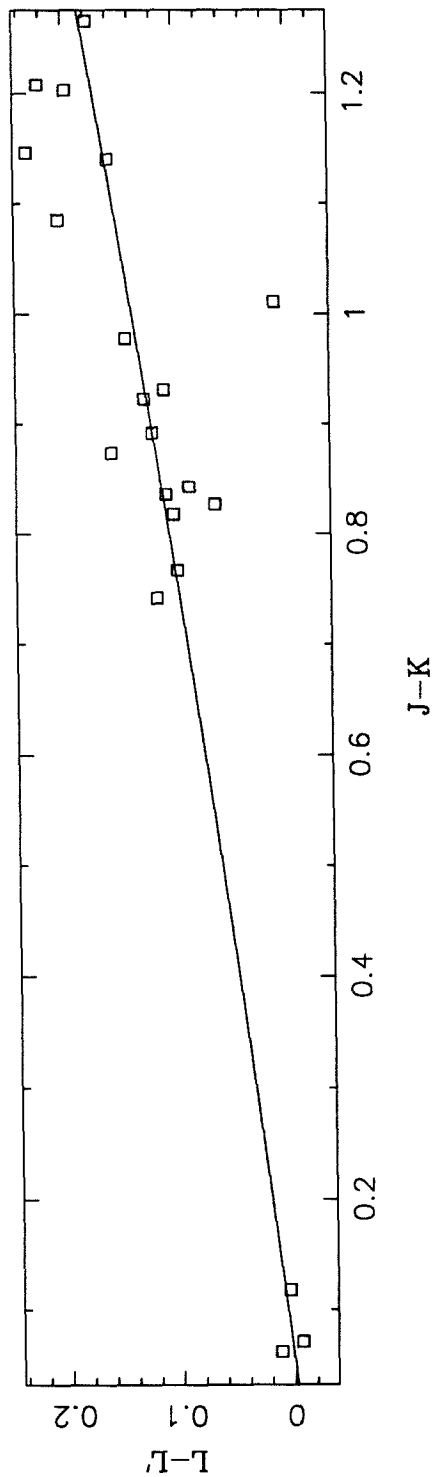

Figure 3.3(b)

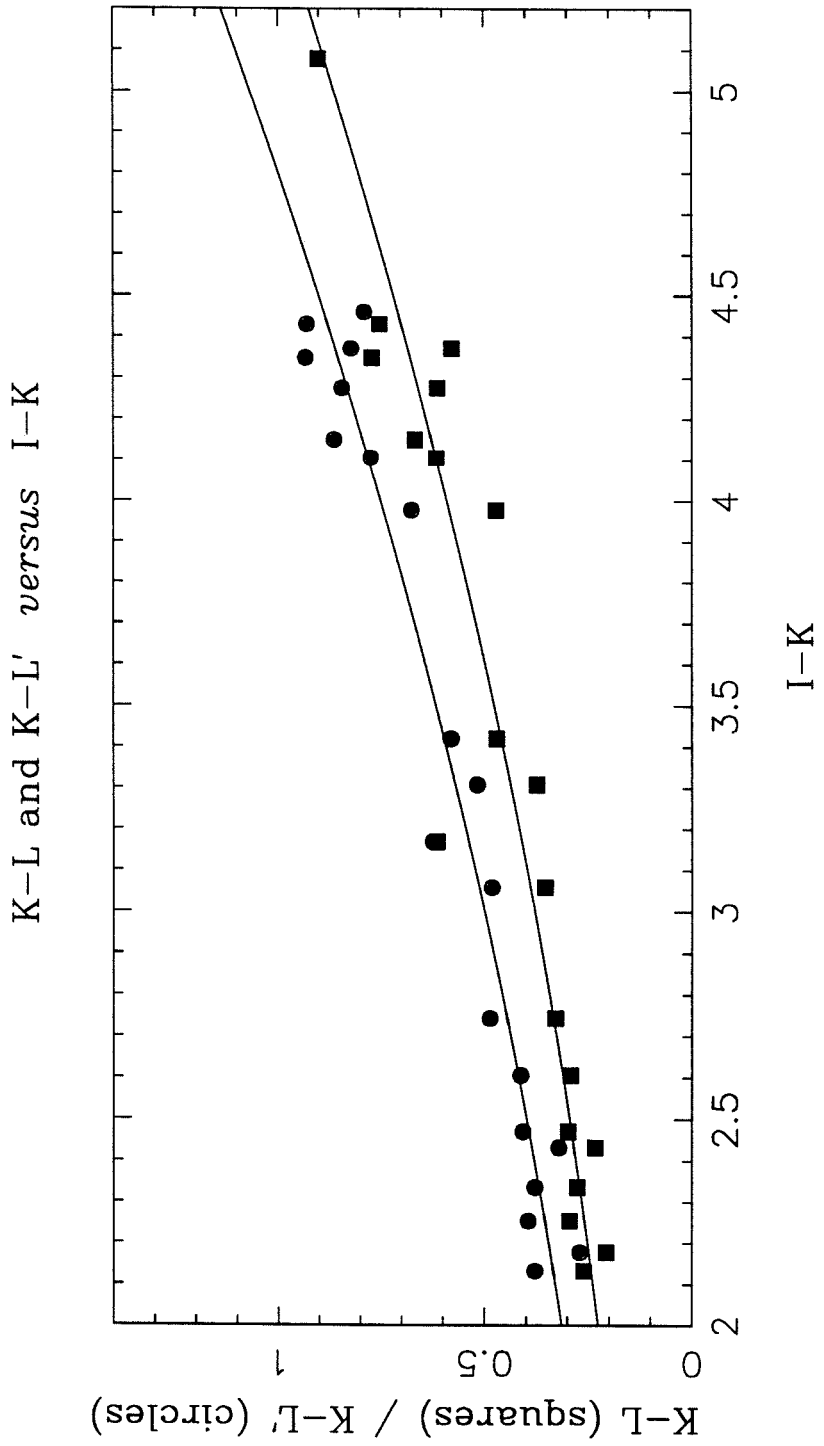

Figure 3.4

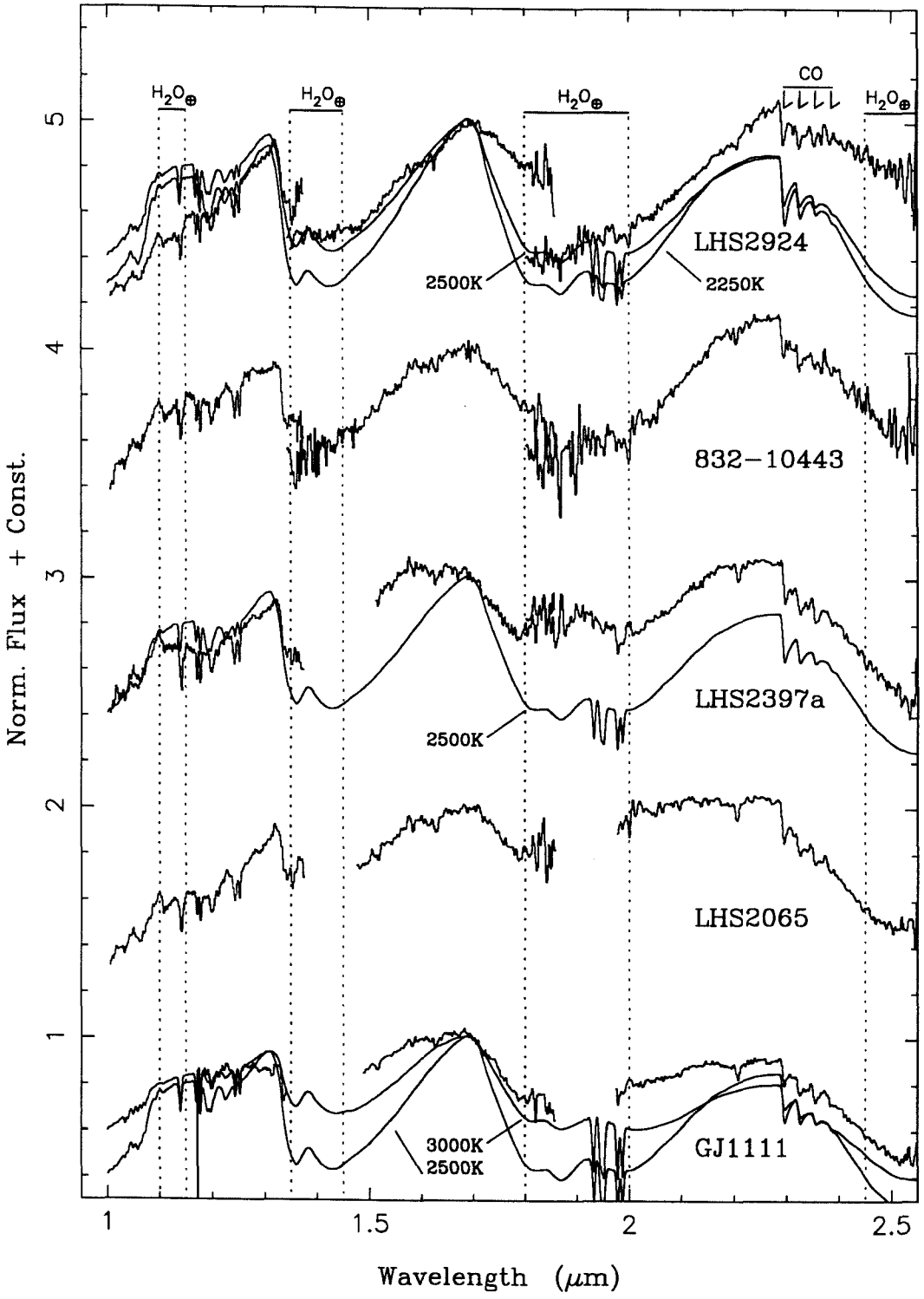
H2O⊕
H2O⊕
H2O⊕
CO
H2O⊕
LHS2924
2500K
2250K
832−10443
LHS2397a
2500K
LHS2065
3000K
2500K
GJ1111
Norm. Flux + Const.
Wavelength (μm)
1
1.5
2
2.5
1
2
3
4
5

Figure 3.5(a),(b)

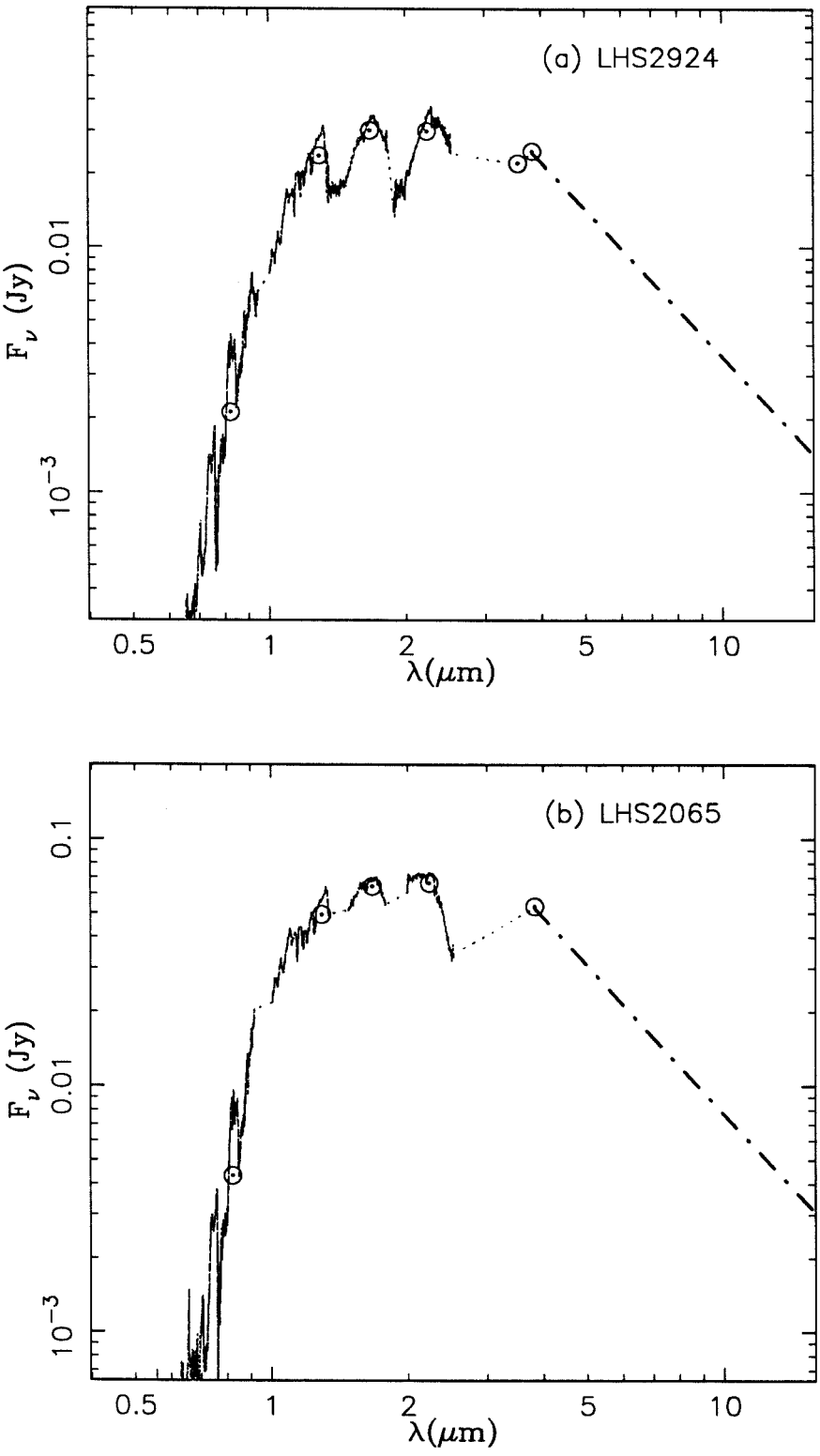
(a) LHS2924
F_ν (Jy)
0.01
10^{-3}
0.5
1
2
5
10
$\lambda(\mu m)$
(b) LHS2065
F_ν (Jy)
0.1
0.01
10^{-3}
0.5
1
2
5
10
$\lambda(\mu m)$

Figure 3.5(c),(d)

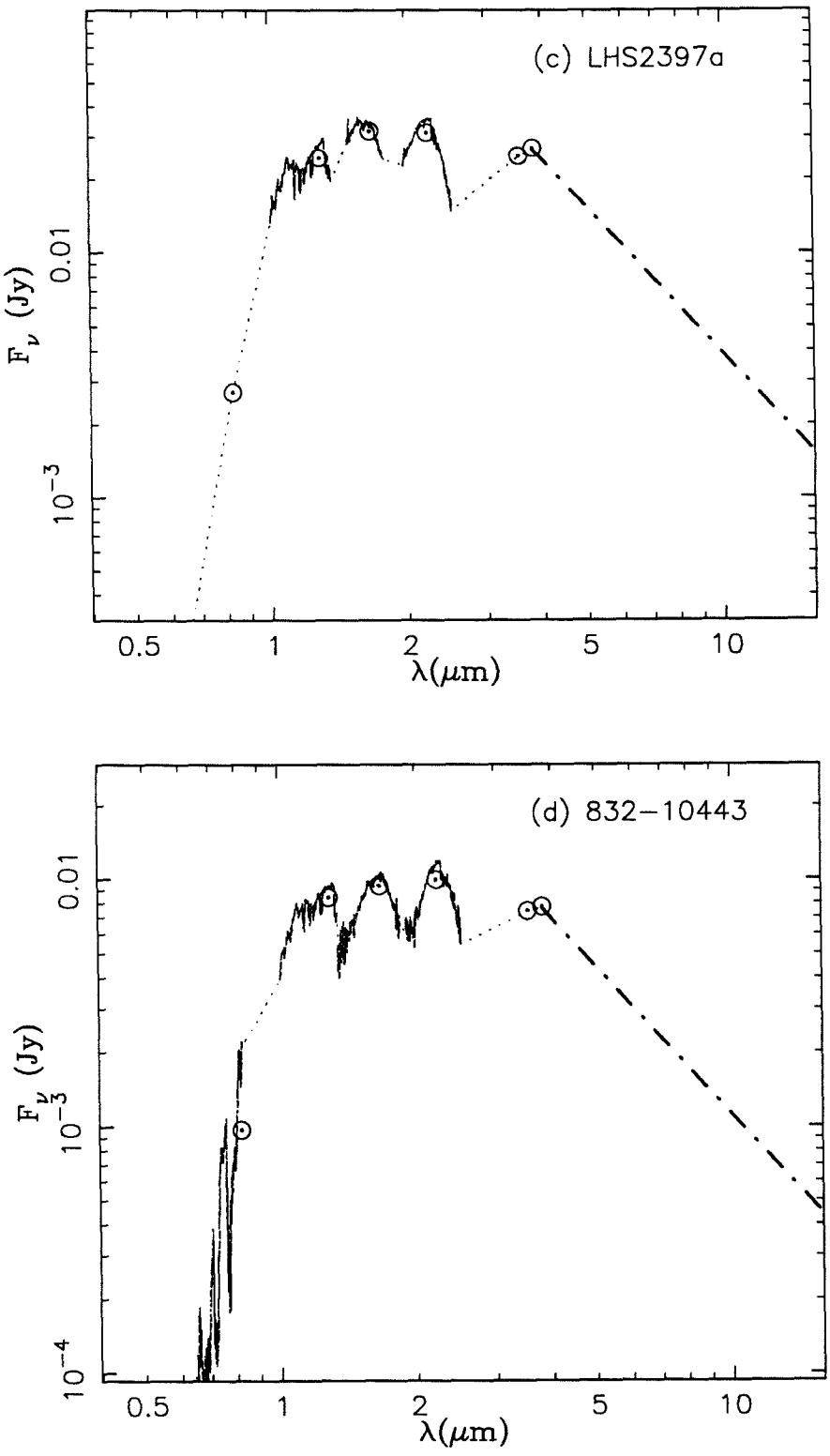
(c) LHS2397a
F_ν (Jy)
0.01
10^{-3}
0.5
1
2
5
10
λ(μm)
(d) 832−10443
F_ν (Jy)
0.01
10^{-3}
10^{-4}
0.5
1
2
5
10
λ(μm)

Figure 3.5(e),(f)

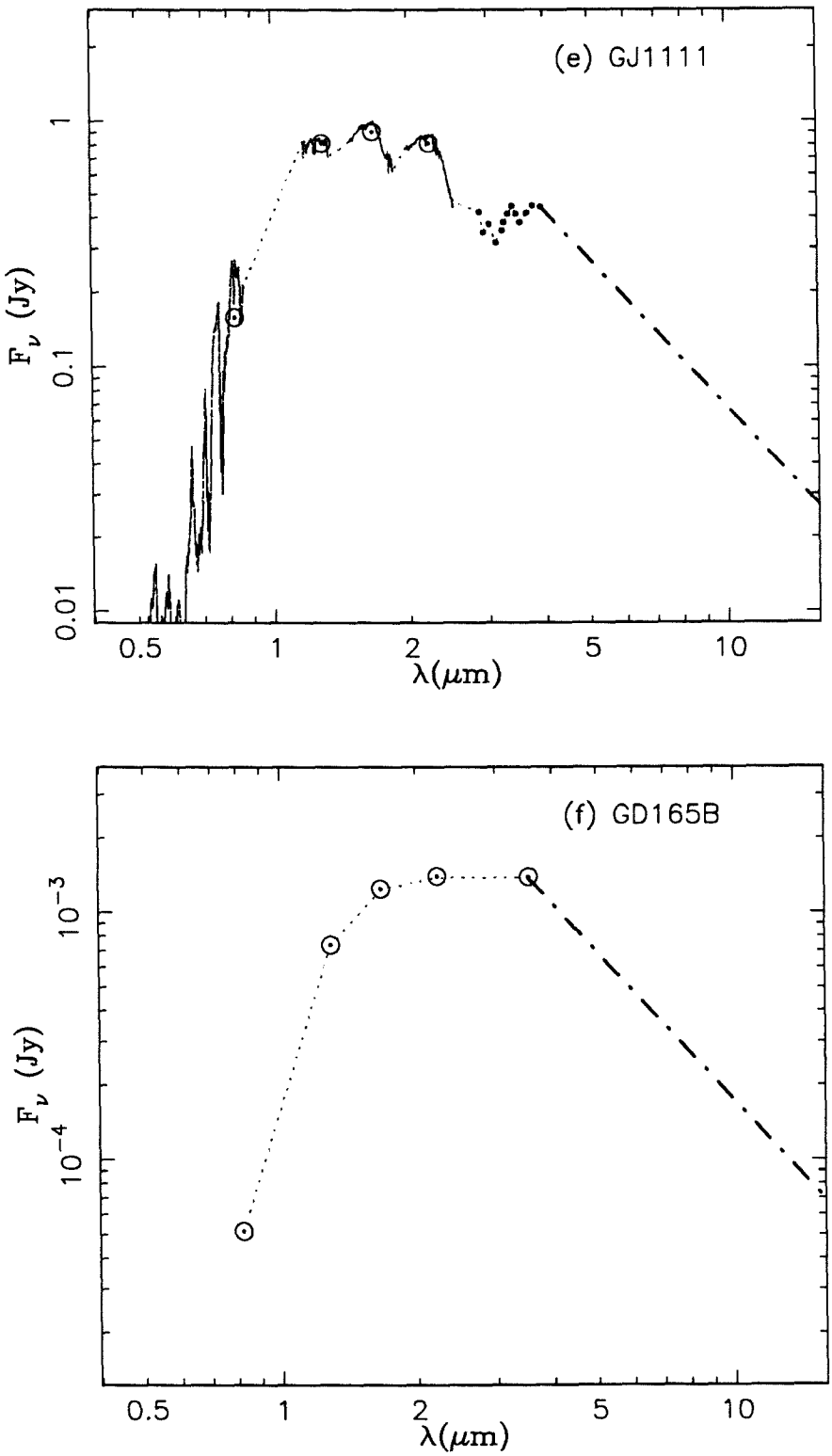
(e) GJ1111
F_ν (Jy)
1
0.1
0.01
0.5
1
2
5
10
λ(μm)
(f) GD165B
F_ν (Jy)
10^{-3}
10^{-4}
0.5
1
2
5
10
λ(μm)

Figure 3.5(g),(h)

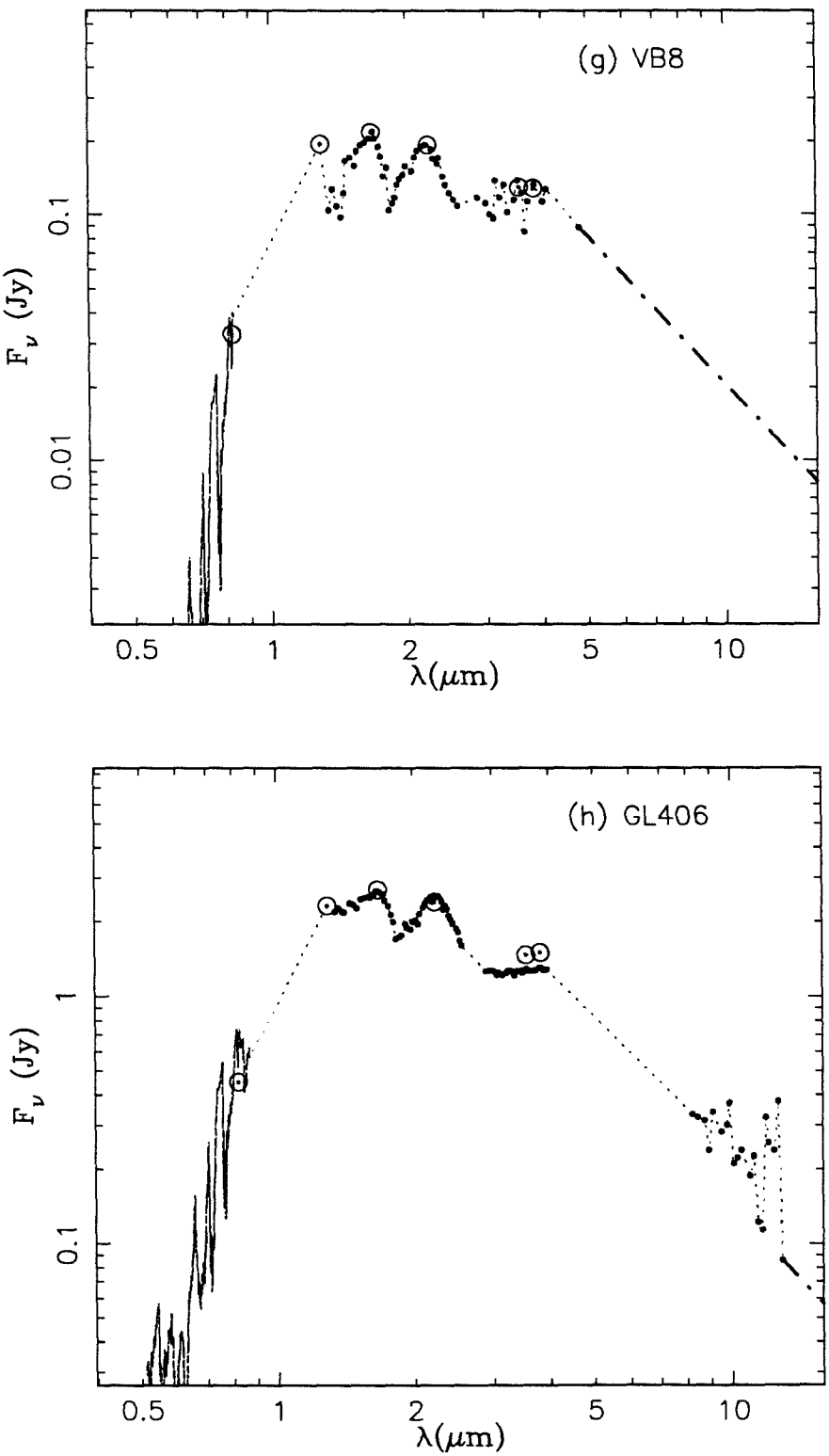

Figure 3.5(i),(j)

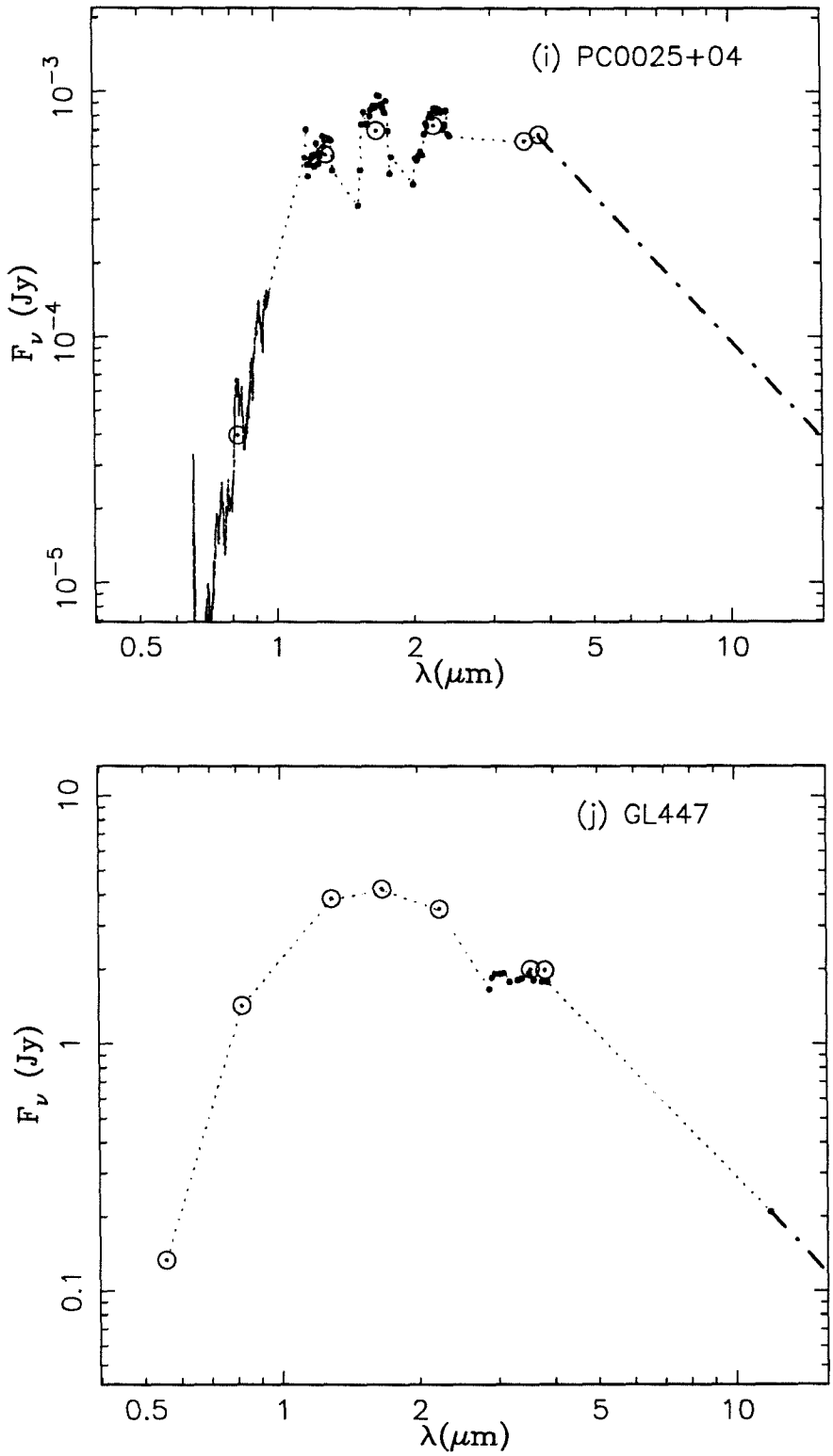
(i) PC0025+04
F_ν (Jy)
10^{-3}
10^{-4}
10^{-5}
0.5
1
2
5
10
λ(μm)
(j) GL447
F_ν (Jy)
10
1
0.1
0.5
1
2
5
10
λ(μm)

Figure 3.5(k),(l)

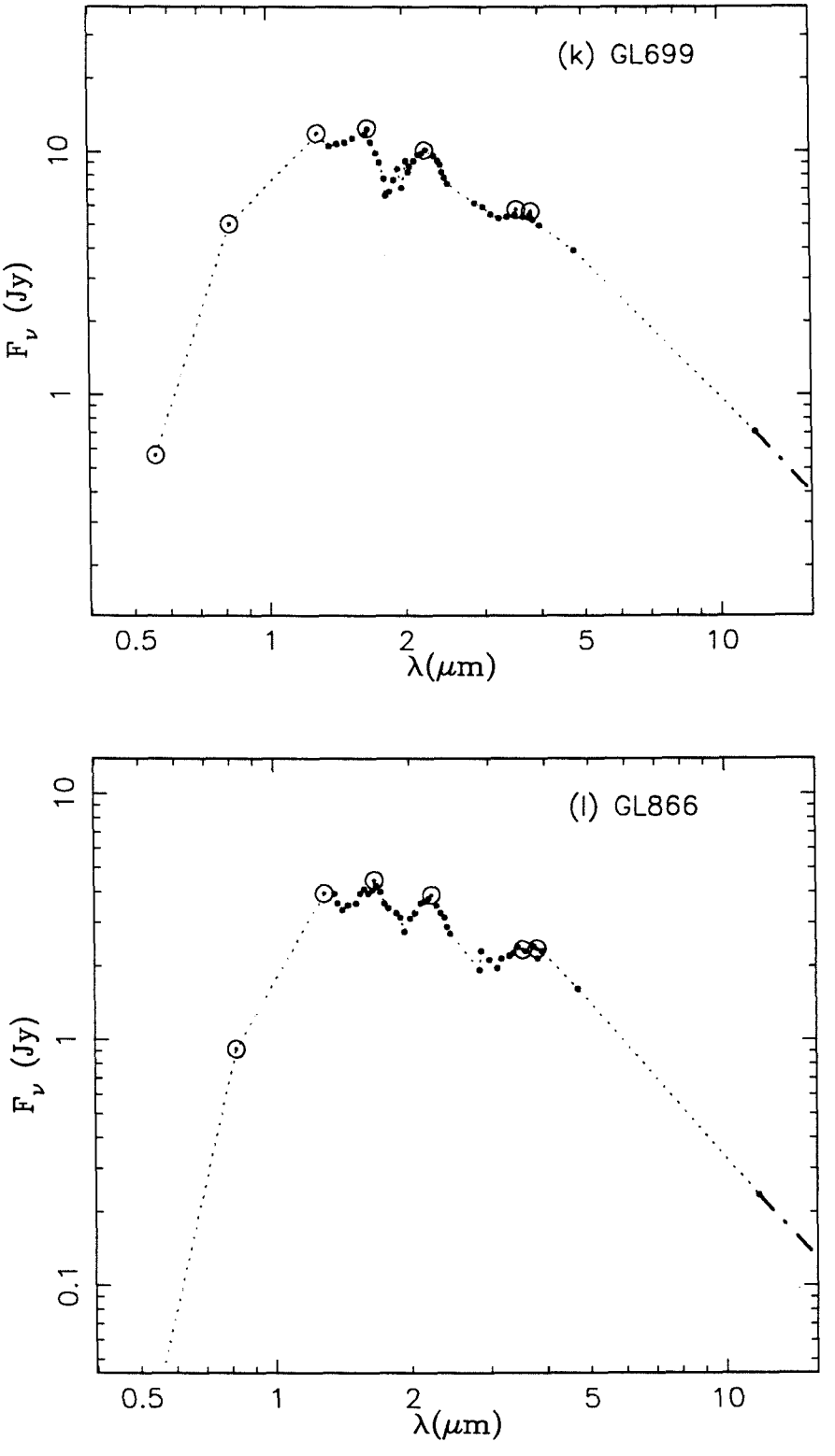
(k) GL699
10
1
F_ν (Jy)
0.5
1
2
5
10
λ(μm)
(l) GL866
10
1
0.1
F_ν (Jy)
0.5
1
2
5
10
λ(μm)

Figure 3.5(m),(n)

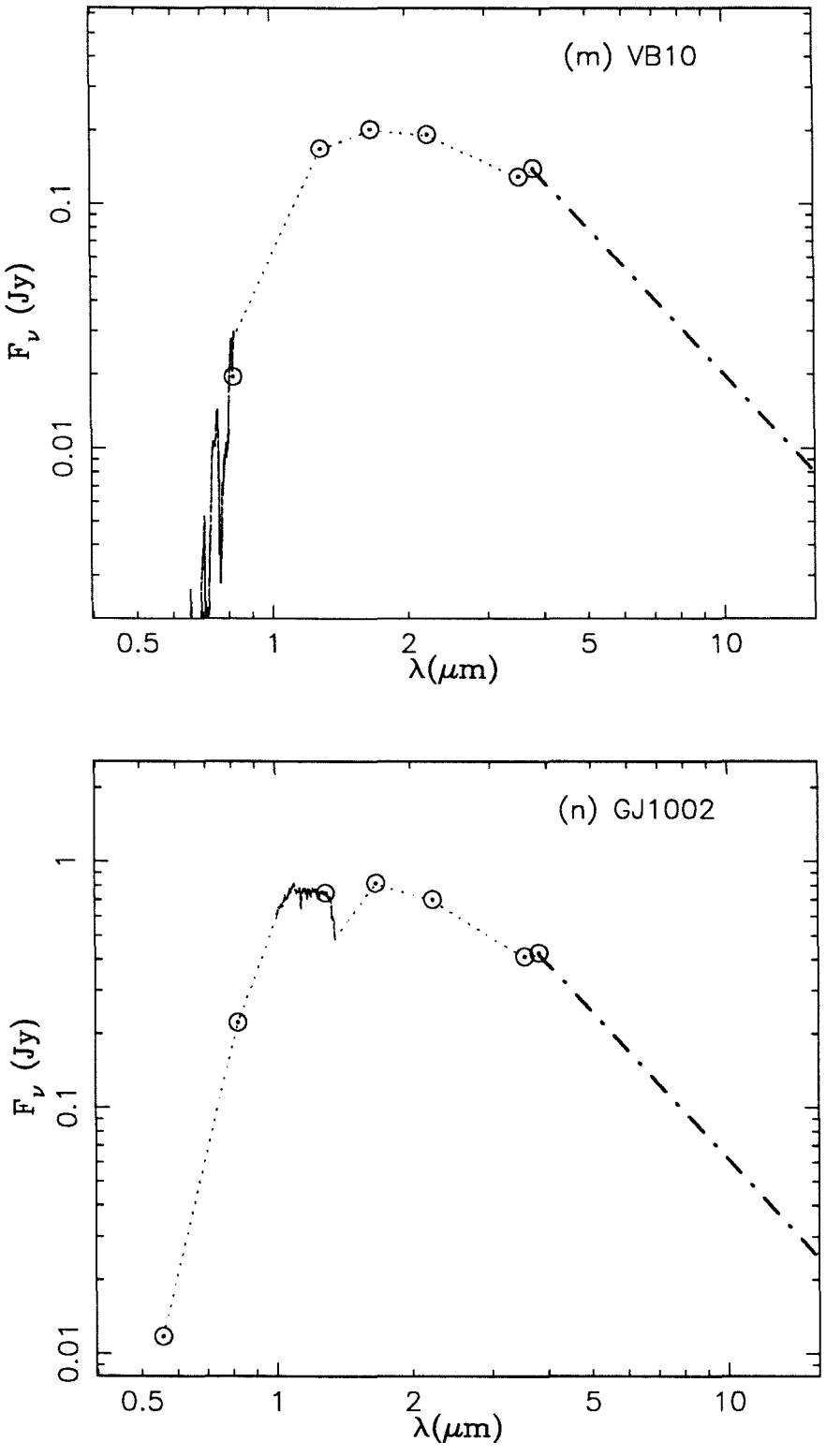
(m) VB10
0.1
0.01
F_ν (Jy)
0.5
1
2
5
10
λ(μm)
(n) GJ1002
1
0.1
0.01
F_ν (Jy)
0.5
1
2
5
10
λ(μm)

Figure 3.6

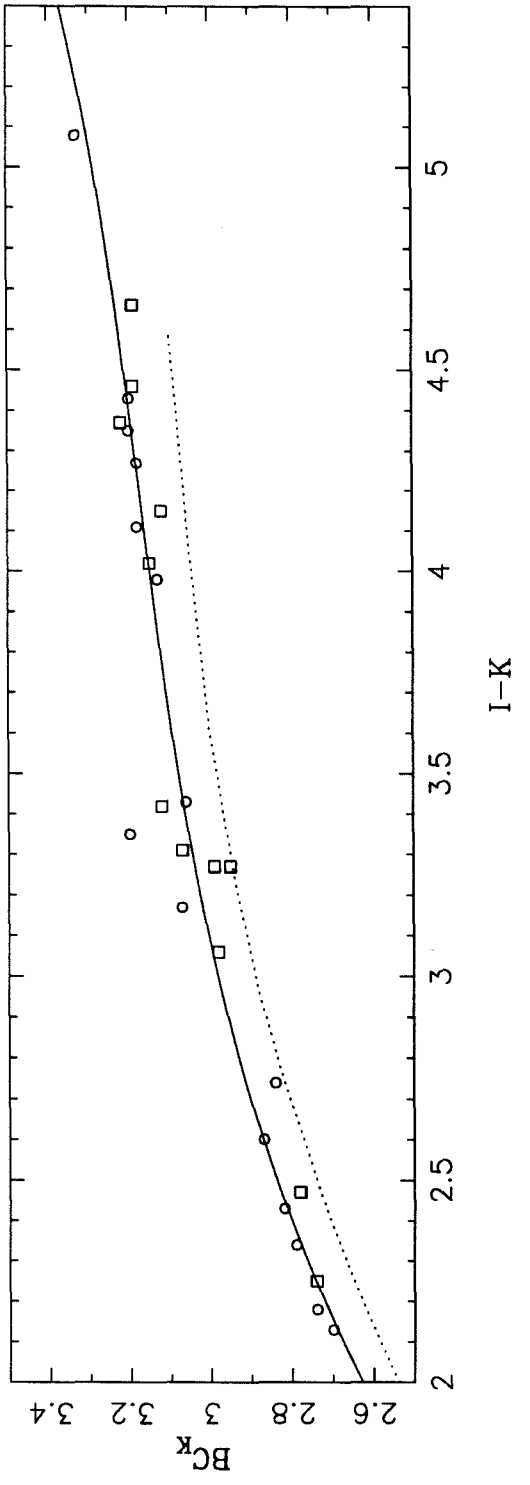

Figure 3.7

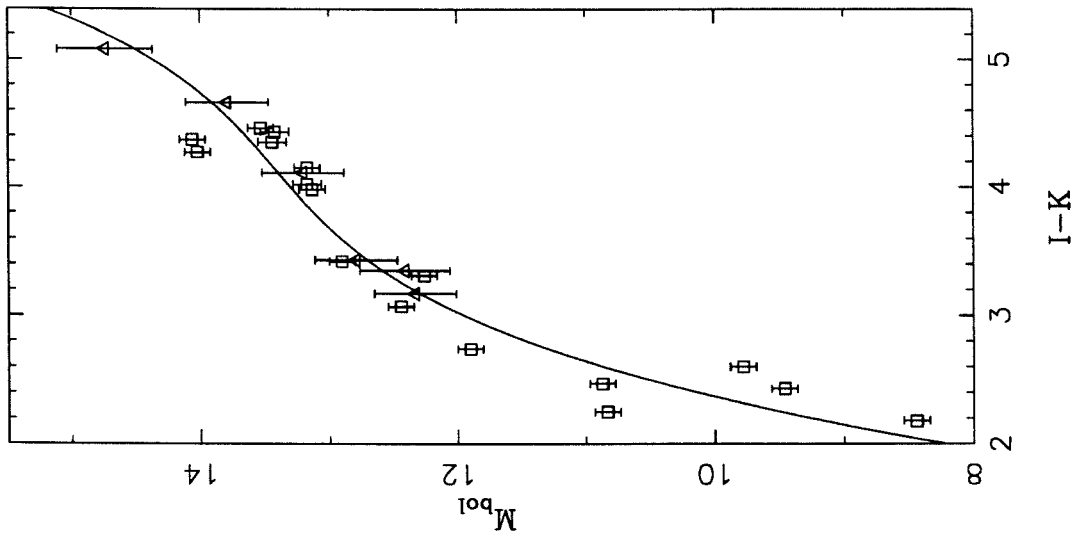

Figure 3.8(a),(b)

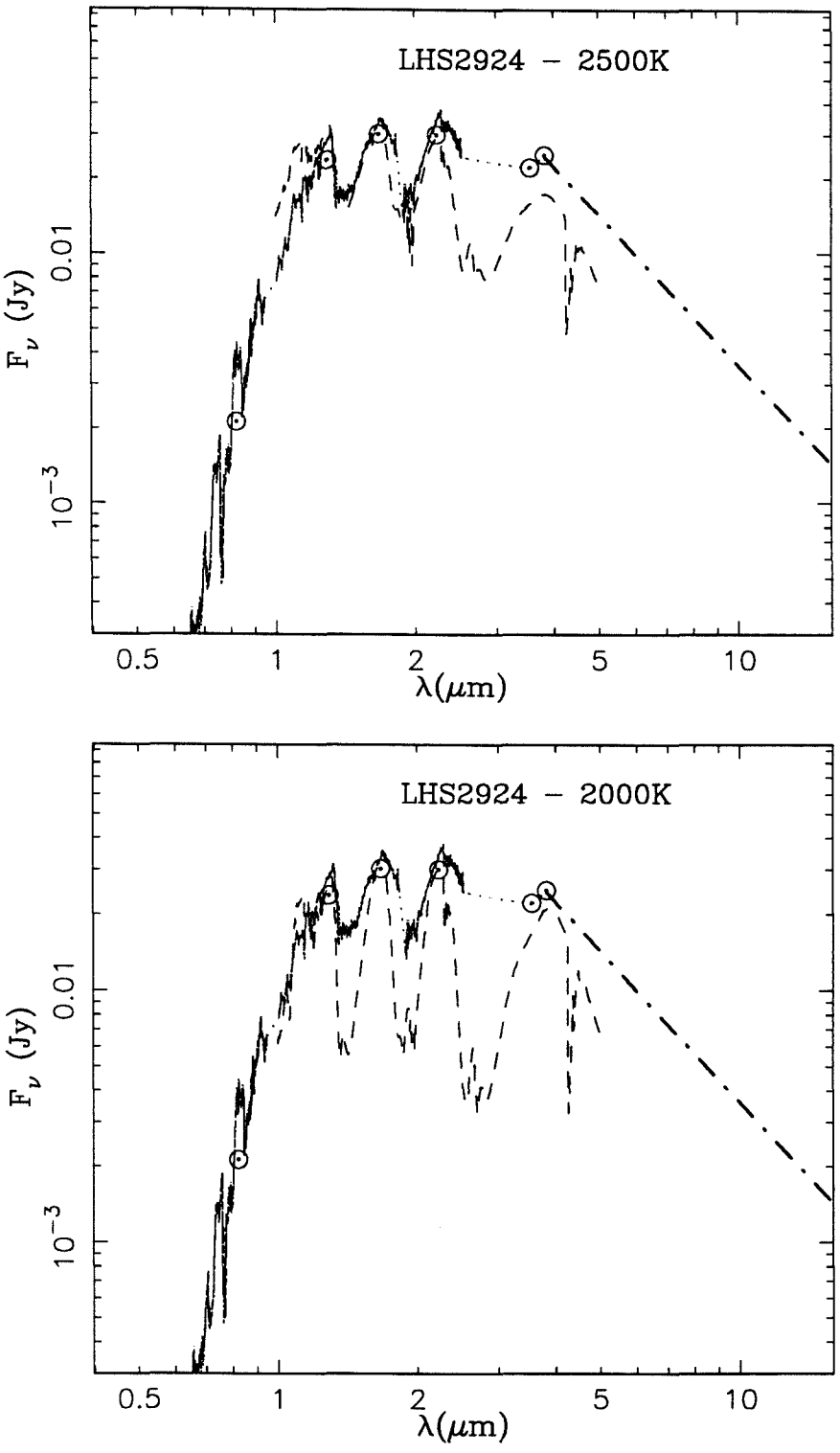
LHS2924 – 2500K
F_ν (Jy)
0.01
10^{-3}
0.5
1
2
5
10
λ(μm)
LHS2924 – 2000K
F_ν (Jy)
0.01
10^{-3}
0.5
1
2
5
10
λ(μm)

Figure 3.9

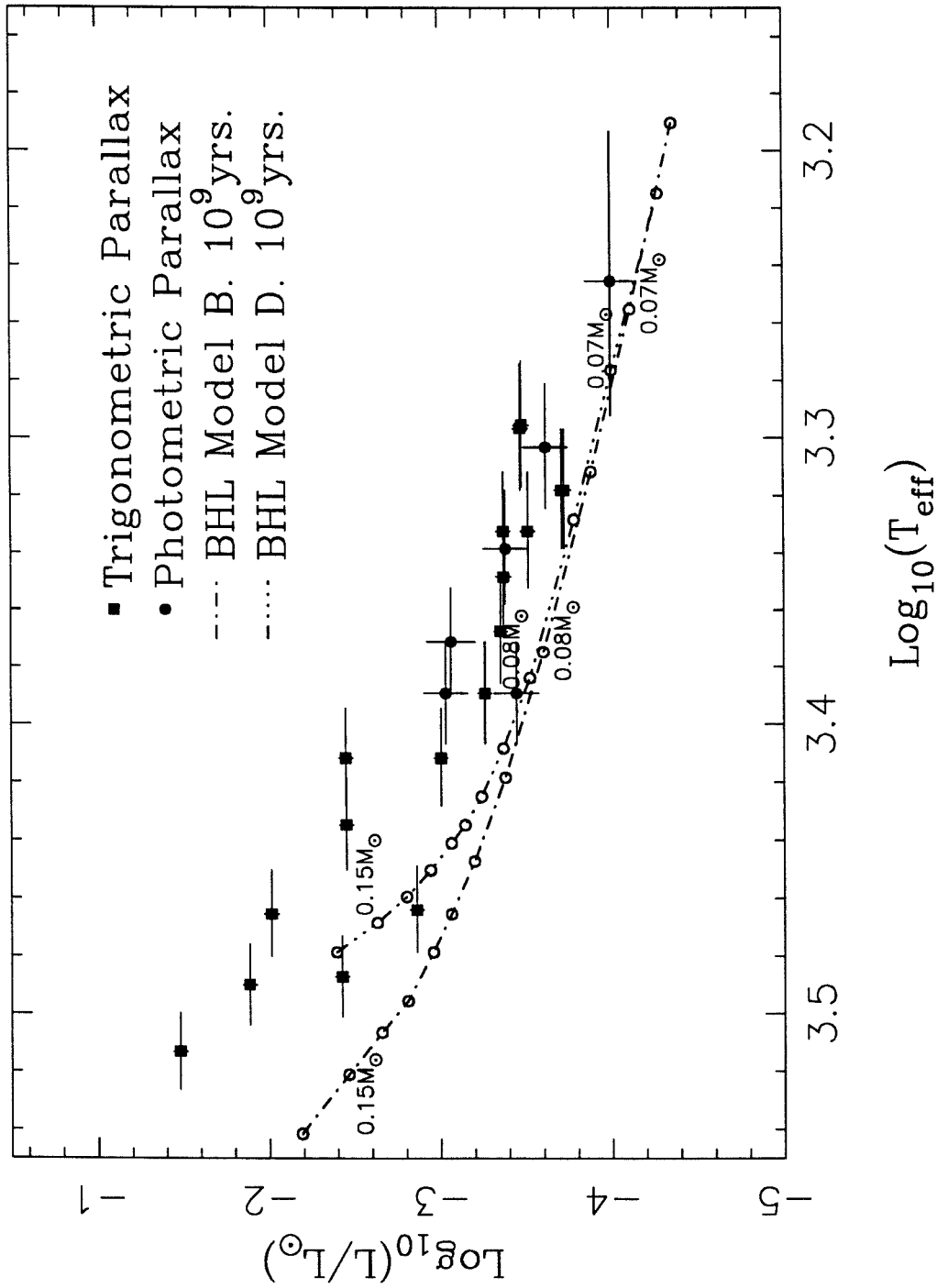
Trigonometric Parallax
Photometric Parallax
BHL Model B. 10^9yrs.
BHL Model D. 10^9yrs.
0.15M⊙
0.15M⊙
0.08M⊙
0.08M⊙
0.07M⊙
0.07M⊙
$Log_{10}(L/L_\odot)$
−1
−2
−3
−4
−5
3.5
3.4
3.3
3.2
$Log_{10}(T_{eff})$

Figure 3.10

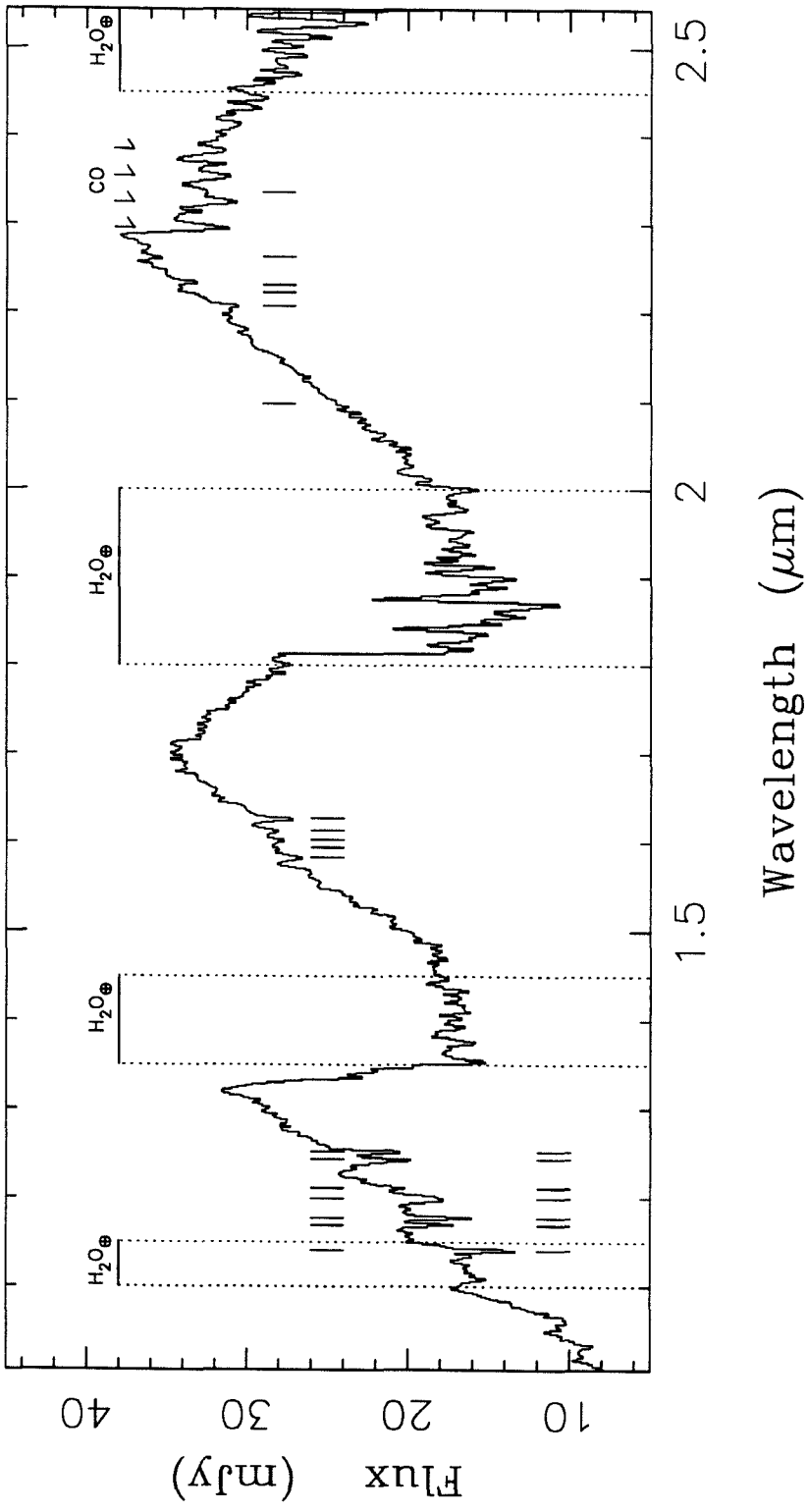

Chapter 4 - The Faintest Stars : Trigonometric CCD Parallaxes. [1]

Abstract

First results are presented from a trigonometric parallax programme being carried out with a CCD detector on the 60″ telescope at Palomar Mountain. New parallaxes for 6 extremely late M-dwarfs ($M_{bol} > 13$) are presented, more than doubling the number of such stars with directly measured distances. Structure in the main sequences constructed with this new parallax data suggest that the faintest known stars may not be stably supported by nuclear burning. It is shown that trigonometric parallaxes with accuracies of $\leq 0.004''$ can be obtained in a few years using standard CCD equipment on a common-user telescope.

Section 4.1 - Introduction

Trigonometric parallaxes are the only reliable and unbiased way measuring astronomical distances. And until recent years, parallaxes were obtainable for only the very nearest (d $\lesssim$ 30pc) objects. Moreover the measurement of parallaxes has always been considered to be the domain of a (regrettably small) contingent of dedicated astrometric observers working at a few observatories. Recent technical developments, however, have begun to change this picture. The most notable has been the introduction into common use of large format CCD detectors. CCDs make almost ideal astrometric devices and their utility for parallax work has been amply demonstrated by the excellent results now being produced at the U.S. Naval Observatory (USNO) (Monet *et al.* 1992). Moreover, the success of the USNO programme indicated the possibility of acquiring CCD astrometry at the milli-arcsecond (hereafter mas) level with a *non-dedicated* astrometric facility. It was therefore decided to institute an astrometric programme on the Palomar 60″ telescope, with a focus on measuring distances to stars at the bottom of the main sequence.

The inability of current atmospheric models to reproduce the observed spectra of Very Low Mass Stars (M $\lesssim 0.1M_{\odot}$, $M_{bol} \gtrsim 13$) has meant that interpretation of effective temperatures for these objects is, to say the least, problematic (cf. Tinney *et al.* 1992b (Paper II)). Luminosity is essentially the only parameter which can be determined unambiguously for VLM stars. In light of this, the measurement of unbiased distances for these

[1] Observations were made on the 60-inch telescope at Palomar Mountain which is jointly owned by the California Institute of Technology and the Carnegie Institution of Washington.

objects is obviously extremely important. However, prior to this publication the total number of such stars with measured parallaxes was only four (LHS2924, LHS2065, LHS2397a and VB10)! The sparsely populated colour-magnitude diagram which resulted has been a considerable source of uncertainty in the interpretation of both large-scale surveys which aim to measure the luminosity function for stars at the bottom of the main sequence (e.g., Hawkins & Bessell 1988, Leggett & Hawkins 1988 and 1989, Tinney, Mould & Reid 1992a, Tinney, Reid & Mould 1992 (Paper I), Tinney 1992 (Paper IV)), and in the study and interpretation of the individual very faint objects (variously described as VLM stars or brown dwarf candidates) currently being reported in the literature (e.g., Zuckerman & Becklin 1992, Schneider *et al.* 1991). At present $\sim$ 20 stars are included in our parallax programme. In this paper, trigonometric parallaxes for 6 new VLM stars are presented, more than doubling the number of VLM stars with measured parallaxes.

Target stars for our programme were chosen from large-scale photometric surveys of both the northern and southern skies, and from proper motion surveys (Gliese 1969, Luyten 1979). The programme was instituted primarily to measure parallaxes for new VLM stars discovered as part of a 270 square degree survey for VLM stars currently being carried out by using plates from the Second Palomar Sky Survey (and referred to as TVLM stars - Papers I and IV). During the course of this work, several very late dwarfs were discovered by the Automatic Plate-measuring Machine (APM) group as part of their scanning of the complete United Kingdom Science Research Council (UKSRC) southern sky survey (Irwin *et al.* 1991, 1992, Irwin 1992 – referred to as BRI stars) and several of these were added to our programme. The TVLM and BRI stars, therefore, represent new parallax determinations, while the Gliese and Luyten stars were included so that we could check our measurements against those of other observatories. Our observing and reduction techniques substantially follow those of the ground breaking work in this field, presented in Monet *et al.* (1992) and Monet & Dahn (1983).

Section 4.2 - Observations

The 1024×1024 Tektronix CCD used in these observations (designated CCD11 at Palomar) is a thick, front-side illuminated device with contiguous 24×24μm square pixels. At the Cassegrain $f/8.75$ focus of the 60″ telescope it has a pixel scale of 0.372″/pixel, which give a 6.35′ field of view. All observations were carried out through a Gunn i filter ($\lambda_{eff} \approx 7900$Å, $\Delta\lambda \approx 1000$Å). The CCD was mounted with its columns oriented within a few degrees of the telescope's North-South axis. Multiple exposures (with a single read)

carried out on several nights enabled us to establish the rotation of the CCD X-Y co-ordinate system with respect to the α-δ co-ordinate system on those nights to within $\pm 0.4°$. Later reductions were always transferred onto a master frame defined by observations on one of those nights, and then rotated by an appropriate angle so that the X-Y axes were always co-incident with the α-δ axes.

The TVLM survey is being carried out in eleven Second Palomar Sky Survey fields grouped around four approximate positions on the sky - 2-3^h,0°; 10^h,50°; 15^h,0°and 25°; and 22-23^h,0°. These fields were chosen specifically because they were $\sim 6^h$ apart, which allows us to optimise our use of telescope time for a parallax programme. One set of objects can be observed at high parallax factor at the beginning of the night, another near zero parallax factor in the middle of the night, and another at high parallax factor at the end of the night. This means our measurements tend to be clustered at high and low parallax factors, rather than spread over a range of factors as would be possible at a dedicated astrometric facility.

As each star was entered into our programme, a field of reference stars around it was selected. The brightest of these reference stars was used to determine the exposure time on subsequent runs (i.e., exposure times were chosen to maximise counts without saturating that star, under the prevailing seeing and transparency conditions). The observations were flat-fielded using dome-flats taken at the beginning and end of each night's observing. Like most of the Tektronix CCDs in use at Palomar, CCD11 flat-fields very easily, and images were flattened to better than 0.5% (both for pixel-to-pixel and large scale variations). The Tektronix chips also have the advantage of being thick and essentially rigid (unlike, for example, the wrinkled 800 × 800 Texas Instruments CCD used at the USNO). Accurate placement of our fields in exactly the same location from epoch to epoch is therefore not essential (reference stars were occasionally positioned hundreds of pixels away from their nominal location), though it is desirable as a consistent placement of the images in one location will tend to cancel position offsets produced by point-spread-function variations over the CCD field. The results presented here are based on observations carried out on 34 nights over the period 25 November 1990 - 6 July 1992.

Images of objects (i.e., reference stars and programme objects) were centroided using DAOPHOT (Stetson 1987). In particular, as our programme objects are almost always at high galactic latitude the stellar images were always single and the PEAK point-spread function fitting routine was used. Point spread functions were fit by hand using the PSF routine. A Moffat function analytic approximation to the observed point-spread

function was used which allows for elliptical images at an arbitrary orientation, and permits fitting to slightly trailed or (more importantly for the 60″ telescope) slightly astigmatic images. The seeing of the images actually used for astrometry varied from 0.7″ to 2.4″, with a median value of 1.2″ (see Figure 4.1).

Section 4.3 - Analysis.

4.3.1 Differential Colour Refraction.

Differential colour refraction (DCR) is now recognised as the fundamental limitation to the precision of ground based astrometry (Monet *et al.* 1992, Monet & Dahn 1983). The basic difficulty is that the colours of programme and reference stars are almost always different. This means that the mean wavelength of the flux detected for a programme star through a given filter passband, will not be the same as that for a given reference star – they will therefore be refracted by the atmosphere by different amounts. In particular the programme stars discussed here are extremely red (R–I $\approx$ 2.5), leading them to be refracted *less* than than the typically much bluer (R–I $\approx 0.4 - 1.0$) reference stars. However, the effects of DCR can substantially be corrected. In the following brief discussion, we use the formalism of Monet *et al.* (1992), which in turn follows that of Owens (1967). For further details, readers are referred to those works.

The distance a star is refracted can be decomposed into components in the X (the Right Ascension) and Y (the Declination) directions, and expressed as,

$$R_X = \alpha A Z_X \tag{4.1}$$

$$R_Y = \alpha A Z_Y, \tag{4.2}$$

where A is a function of ζ, the zenith distance for a given observation and a weak function of T, the air temperature. To a high degree of precision (better than $\pm 0.2\%$ for a conceivable range of observing conditions and observations less than 2 hours from the meridian (Monet *et al.* 1992)) A can be regarded as a constant. Z_X and Z_Y are the projected tangents of the zenith distance in the X and Y directions respectively, and are given by

$$Z_X = \cos\phi \ \sin t \ \sec\zeta \tag{4.3}$$

$$Z_Y = S(\sin\phi \ \sec\delta \ \sec\zeta - \tan\delta) \tag{4.4}$$

$$S = \left\{ \begin{matrix} +1, \text{ if } (\phi - \delta) \geq 0 \\ -1, \text{ if } (\phi - \delta) < 0 \end{matrix} \right\} \tag{4.5}$$

with ϕ being the observatory's latitude, t the observation's hour angle, and δ the object's declination.

The coefficient α in equations 4.1-2 can be regarded as the product of two terms - one purely wavelength dependent and the other determined by only the air pressure and temperature. This second term can also be treated as a constant to within a dispersion of $\pm 4\%$ for usual observing conditions at Palomar. As a result we are able to replace the coefficients in equations 4.1-2 with constants F_i,

$$R_X = F_i \; Z_X \tag{4.5}$$

$$R_Y = F_i \; Z_Y, \tag{4.6}$$

where the constant F_i is determined for each star i by its spectrum in the passband of the filter used for the observations. Monet *et al.* then adopted the further assumption that F_i could be expressed as a function of the V–I colour of star i, and corrected for differential refraction based on VI photometry of stars in each field. In contrast we have explicitly solved for these constants for each reference and programme star in our fields. When a field is observed as it rises and sets on a single night, any motion of the stars with respect to each is due to DCR alone, as stellar proper motions and parallaxes are negligible over the course of one night. It should be noted however, that the motion due to refraction observed is *with respect to the other stars used to define a reference frame* – we only determine F_i to within a zero-point determined by the mean value $\langle F \rangle$ of the F_i values of all the *reference* stars in a field. The quantities $\Delta R_X / \Delta R_Y$ are measured with respect to a reference frame,

$$\Delta R_X = \Delta F_i \; Z_X = (F_i - \langle F \rangle) \; Z_X \tag{4.7}$$

$$\Delta R_Y = \Delta F_i \; Z_Y = (F_i - \langle F \rangle) \; Z_X \tag{4.8}$$

and so a fit to the observed data can determine the constants ΔF_i.

4.3.2 - Data Reduction.

The data reduction proceeds as follows. First each frame's stars are centroided with a PSF constructed for that frame. A crude linear transformation (i.e., allowing for a shift, rotation and change in image scale) is then used to transform the centroided X-Y positions to the reference frame of single exposure on a night of good seeing with a known rotation to the α-δ co-ordinate frame (cf. §4.2). All data are then rotated to bring the

X-Y axes co-incident with the α-δ axes. A set of reference frame stars is then selected – these reference frame stars must appear in *all* the frames which will be used in the final astrometric solution. Reference frame stars with detectable proper motions are deleted. These data are then fitted for differential refraction constants ΔF_i, using observations from a single night, with the functional form given by equation 4.7. (As is shown by Monet *et al.* (1992) Z_Y varies little with hour angle, which means that a fit to the data using equation 4.8 provides little constraint on the values of ΔF_i). Once ΔF_i has been determined for each reference star i, the effects of DCR on the reference frame stars in all data frames are removed. The resulting DCR-free reference frame is used to transform all observations onto the master frame. A solution is then made for the ΔF_{prog} of the *programme* star (which is of course not included in the reference frame) using the same night's data as was used to derive the reference star ΔF_i coefficients. The effects of DCR on the programme star are then removed. It is this final position of the programme star which is used in the solution for parallax and proper motion. Reference stars are all assigned unit weight in all these reference frame transformations.

Fits are shown in Figure 4.2 for ΔF_i of a reference star with R–I = 0.79 in the field of TVLM 868-110639, and of the programme star TVLM 868-110639 with R–I = 2.38. (RI photometry has been obtained for five of the seven fields being presented here – sources are given in §4.3). This difference in R–I is typical of that seen between reference frame and programme stars, and corresponds to a difference in the measured ΔF_i values of this programme and reference star pair of 17.3 ± 4.8 mas/Z_x. The range of colours of the reference stars (in the fields for which photometry is available) is R–I = 0.40 to R–I = 1.46, and the resultant differences between ΔF_{ref} and ΔF_{prog} are $35 - 10$mas/Z_X. This is approximately 4 times smaller than the typical DCR coefficients determined by Monet *et al.*, and is because their observations were made through a considerably wider and bluer filter ($\lambda_{eff} \approx 7000$Å, $\Delta\lambda \approx 3000$Å). While such a filter with its broad bandpass decreases the exposure times required for faint stars, it considerably increases the importance of DCR effects. As a result USNO observers are limited to observations within one half hour of the meridian, while comparable observations with the Gunn i filter can be made as far as two hours from the meridian.

It is worth remembering that it is only the uncertainty of ΔF_{prog} which figures directly in the uncertainty of the final astrometric position. Because the ΔF_{ref} are differential quantities, an error in a given reference star's ΔF_i merely leads to a change in the zero-point offset $\langle F \rangle$, which we are unable to determine in any case. Errors in the determination

of ΔF_{prog}, however, figure directly in our ability to determine the 'above the atmosphere' position of the programme star. Examination of the ΔF_{prog} values and their uncertainties (see the caption to Figure 4.3) shows that ΔF_{prog} is measured with a maximum uncertainty of ± 10.0 mas/Z_X for TVLM 831-161058, and uncertainties of $\pm 2 - 4$ mas/Z_X for the rest of the objects. As the data frames used in the final astrometric solutions are limited to observations within two hours of the meridian (corresponding to $|Z_X| < 0.4$), the *maximum* errors due to residual DCR effects are < 4.0 mas (for TVLM 831-161058), though more typically $\lesssim 2$ mas.

The precision with which an astrometric position is determined varies with both observing conditions (i.e., seeing, atmospheric transparency, telescope optics) and the quality of a field's reference frame stars (i.e., their brightness and colour). To take account of this we assign an uncertainty for each *programme* star observation which is equal to the dispersion of the residuals found for the transformation of the DCR-corrected reference stars onto the selected master frame. The resulting uncertainties for a single observation of a programme star vary from 2 mas to 20 mas - largely due to variations in seeing conditions. The mean error in position for a single observation of unit weight (m.e.1), when evaluated for nights of reasonable seeing is found to lie in the range $5 - 10$ mas. Repeated observations of a single field on the same night will often show values of transformation residuals considerably smaller than this (down to the 3 mas minimum mentioned above) – presumably because exactly identical placement of the field on the CCD and close to identical seeing conditions will lead to the cancellation of most of the errors which would otherwise enter into the reference frame transformation. As such it is probably misleading to use such low values as estimates of the uncertainty for a given observation – we therefore set a minimum value of each observations uncertainty of 5 mas. The uncertainties due to possible errors in the determination of ΔF_{prog} discussed above, therefore, range from being on the order of, to considerably smaller than, the accuracy of our astrometric positions due to random variations.

Section 4.4 - Results.

Solutions for the relative parallaxes and proper motions of seven stars from our programme are shown in Table 4.1. Each entry gives – the object name; the object position (in equinox 1950.0); the object position epoch; the number of frames, the number of reference stars and the number of nights used in the astrometric solution; the relative parallax; the relative proper motion; and the position angle of the relative proper motion (measured in degrees from north through east). The last three quantities were determined by a weighted least-squares fit to the data for each object (uncertainties for each observation being assigned as described above). The formal uncertainties for these quantities quoted are derived from the weighted least-squares fit. The errors quoted for position angle of the relative proper motion include a component to account for the overall uncertainty ($\pm 0.4°$) of the CCD orientation with respect to the α-δ co-ordinate system. It should be noted that these formal uncertainties do not take account of possible residual DCR effects produced by uncertainties in our estimation of the ΔF_i coefficients. As discussed above these will typically produce an added uncertainty of only ~ 2 mas. We also show in Figure 4.3 plots of the data used and fits derived for each object. Each figure is in a three panel format. The top panel shows the motion of each object in the X (i.e., right ascension) direction as a function of Julian Date, the second panel shows the motion of each object in the Y (i.e., declination) direction also as a function of Julian Date, the bottom panel shows the actual motion of the object on the sky (north to the top, west to the right). A doted line is used to show the fitted proper motion of the star, and a solid line is used to show the fitted proper motion plus parallax. It can be seen that (except for TVLM 213-2005 which is at a declination of $+51°$) the solutions for parallax were essentially determined by motion in the right ascension direction.

The parallaxes reported for two of the objects in Table 4.1 should be considered to be preliminary – BRI0021-0214 has been constrained at only three epochs, while the fourth epoch obtained for TVLM 513-46546 consists of only a single observation. Their solutions are not as precise as those of the other stars in Table 4.1 (as is reflected by the larger uncertainties produced by the least squares fit for the parallaxes and proper motions of these stars). However, the parallaxes of both these stars are quite large, and so while the absolute uncertainties of these objects may not be as small as the other objects presented, their relative uncertainties are similar or better. A parallax and proper motion was measured for VB10 to check results of our programme against those measured by the USNO's CCD programme. All our measurements for this object ($\pi_{rel} = 167.7 \pm 2.1$, $\mu_{rel} =$

1489.9 ± 1.8, θ_{rel} = 203.2 ± 0.6) agree to within the 1-σ uncertainties with those of the USNO (π_{rel} = 169.7 ± 0.8, μ_{rel} = 1490.3 ± 0.8, θ_{rel} = 203.27 ± 0.03) (Monet *et al.* 1992). The quality of this agreement gives considerable confidence that no significant systematic error has been introduced by the reduction procedure described above. Overall the parallax estimates presented here are seen to be about 3-4 times less precise than those of Monet *et al.* – however stars in their programme have typically been observed over a time baseline $\sim 2-5$ times longer. Observations over one year (which for our programme corresponds to 3 epochs) *just* suffice to determine a position, parallax and proper motion – further observations allow over-determination of these parameters. Considerable gains in the precision of our estimates are expected as our programme continues over the next two years.

Corrections from the observed relative parallax to an absolute parallax have been derived using estimates of the distances to each fields reference stars based on photometric parallaxes. R- and I-band photometry has been acquired for five of the seven fields as part of another project under way on the Palomar 60″ telescope (Paper I). I-band magnitudes and an R–I colours (good to ±0.05 magnitudes) are listed for all available stars in Table 4.3 The stars in Table 4.3 with R–I colours in parenthesis have no R photometry – the colour shown is the mean colour of the other reference stars in that field. Photometric parallaxes have been estimated for each reference star with an M_I:R–I relation due to Leggett & Hawkins (1988), and a mean parallax for the reference frame was used to correct the programme star to an absolute parallax. As can be seen by a comparison of Tables 4.1 and 4.2, the corrections are all $\sim$ 1.5 mas – of the order of, or smaller than, the uncertainty in the relative parallax. As such the uncertainties in the correction to absolute parallax ($\sim 30-50\%$) are negligible. While there is a colour term present between the photometric system under which this photometry was acquired, and the Kron-Cousins system of the Leggett & Hawkins M_I:R–I relation, the term is small ($\lesssim$ 0.1 magnitudes) over the colour range of interest here (Paper I). Considering the cosmic scatter in the M_I:R–I relation ($\sim$ 20%) and the small size of the correction to absolute parallax, we have not attempted to apply any correction.

No R photometry was available for the BRI0021-0214 and VB10 fields. Assigning the mean R–I colour of all the other reference stars (R–I = 0.8 ± 0.4) to the stars in these fields we estimate corrections of 1.3 ± 1.0 and 4.0 ± 4.0 mas respectively. Most of the uncertainty in these two corrections comes from the range in possible distances allowed by the assumed colour. R-band photometry would remove this problem. (The correction for

VB10 is large as VB10 is itself so bright that relatively nearby stars (d $\sim$ 200pc) define the reference frame – it is the only object for which the uncertainty in correction to absolute parallax is larger than the uncertainty in the determined relative parallax. Even so the absolute parallax is consistent with that of Monet *et al.*)

Section 4.5 - Discussion.

Tangential velocities calculated using these new parallaxes are also shown in Table 4.2. As would be expected for objects drawn from a galactic disk population, none of these objects exhibit particularly large velocities. The photometry used to derive the absolute magnitudes shown in Table 4.2 is drawn from the following sources; VB10 IJK photometry – Leggett (1992); TVLM and BRI objects I photometry – Palomar 60″ telescope with CCD11 (Paper I); TVLM and BRI objects JK photometry – infrared cameras on the Palomar 200″ telescope, Du Pont 100″ telescope at Cerro Las Campanas and the NASA Infrared Telescope Facility (Papers II and IV). The IJK photometry is good to $\pm$0.05 magnitudes.

For comparison with existing absolute magnitude data, photometry and trigonometric parallaxes for all stars with I–K > 2.5 has been drawn from the recent compilation of infrared photometry by Leggett (1992). In Figure 4.4 (a)-(c) are shown the resulting M_I:I–K, M_J:I–J and M_K:I–K colour-magnitude diagrams. The solid lines in the figures are third-order polynomials which have been fit to the data. (Coefficients for these fits are given in the figure caption).

These fits give dispersions in their residuals of $\sim$ 0.5 magnitudes over the entire range shown in the figures. However, most of this dispersion is due to scatter in the bluer stars about the fitted main sequence. Over the colour range of most interest – I–K > 3.0, I–J > 2.0 – the dispersions are only $\pm$0.25 magnitudes. The dotted lines are recently published old disk main sequences due to Leggett (1992), while the dot-dashed lines are the frequently used main sequences of Bessell (1991), both of which are consistent with the data and the fitted main sequences presented here. It appears that the main-sequence has a definite 'kink' at around I–K $\sim$ 3.6 – 4.0 or I–J $\sim$ 2.6 – 3.0 – stars redder than this are not as intrinsically faint as would be estimated by a simple extrapolation of the colour-magnitude relations seen for brighter stars. This 'kink' (which is most notable in M_K:I–K, but is also present in M_J:I–J, M_I:I–K and also in M_{bol}:I–K (see Paper II)) is seen at luminosities of $M_K \sim 10$ and $M_J \sim 11$. In bolometric luminosity it occurs at $M_{bol} \sim 13 - 14$. This is precisely the luminosity range at which a change in the slope of the main sequence is expected due to the termination of the stable nuclear burning main

sequence, and the initiation of a class of non-equilibrium 'transition objects' which are only partially supported by nuclear burning . The models of Burrows, Hubbard & Lunine (1989) predict that objects with masses below M $\approx 0.08 M_{\odot}$ and above M $\approx 0.06 M_{\odot}$ will be partially supported by nuclear burning for several times 10^9 years before failing to reach an equilibrium nuclear burning state and fading to become brown dwarfs. (Objects with masses less than $0.06 M_{\odot}$ are predicted to never burn appreciable amounts of nuclear fuel.) It seems likely then that the objects in Figure 4.4 lying in the region I–K > 4 or I–J > 3 are 'transition objects' of this type – neither true brown dwarfs nor true main sequence stars.

The structure seen at the bottom of the main sequence highlights the importance of parallax programmes targeted at intrinsically very faint stars. Large surveys aimed at measuring the mass function for VLM stars and/or brown dwarves cannot attempt to determine parallaxes for all their candidate objects, and typically rely on colour-magnitude relations to estimate luminosities and masses. Good measurements of these colour-magnitude relations are therefore essential to our understanding of the space density of objects at the end of the main sequence, and beyond. The new colour-magnitude relationships presented here are clearly to be preferred over those of both Leggett and Bessell for studies which focus on the very faintest stars.

Of the new stars presented in this paper, three (TVLM 513-46546, TVLM 868-110639 and BRI 0021-0214) lie in a group with the stars LHS2924 and LHS2065 which are often canonically used to define the end of the observed main sequence. TVLM 513-46546, in particular, has the faintest absolute magnitudes ($M_I = 15.11 \pm 0.06$, $M_J = 11.98 \pm 0.04$, $M_K = 10.84 \pm 0.04$) of any object with a measured parallax – the next closest being LHS2924 ($M_I = 15.06 \pm 0.05$, $M_J = 11.69 \pm 0.04$, $M_K = 10.52 \pm 0.04$). Only GD165B (a brown dwarf candidate which is a companion to the white dwarf GD165 (Becklin & Zuckerman 1988, Zuckerman & Becklin 1992) is almost certainly fainter than these stars as it has colours (I–K=5.08, I–J=3.45) that are far redder than those of TVLM 513-46546 and LHS2924. It is interesting to note that TVLM 513-46546 lies some distance from the sequence defined by the rest of the stars in Figure 4.4. It is either significantly bluer, or significantly fainter, (or both) than the stars which appear to define the main sequence. It also demonstrates that while the colour-magnitude relations fitted in Figure 4.4 are useful in a statistical sense, they should be used with caution for estimating the luminosities of individual stars – the luminosity of TVLM 513-46546 would have been overestimated by ~ 0.8 magnitudes based on its colours alone. TVLM 831-161058 (I–K = 4.0) also lies significantly off the main sequence – though in this case it is ~ 0.8 magnitudes too *bright* for its colour. Such

a location would be explained by its being either a a young cooling brown dwarf, or (more likely) a nearly equal-mass binary. Assuming that TVLM 831-161058 is a binary system, then since it is unresolved at the level of $0.5 - 1.0''$, the component stars must be separated by $\lesssim 10 - 20$au. It should be a good target for radial velocity monitoring.

Section 4.6 - Conclusion.

New trigonometric distances have been measured for six Very Low Mass Stars, more than doubling the number of stars fainter than $M_{bol} = 13$ with measured distances. Using these new stars, and existing parallaxes and photometry for previously measured low mass stars, M_I:I–K, M_J:I–J and M_K:I–K colour-magnitude relations have been constructed and fits to the resulting main sequences are provided. Three of the new stars are as faint as the faintest stars with measured parallaxes, while one (TVLM 513-46546) has the lowest luminosity of any star with a measured parallax. A sharp change in the slope of the main sequences constructed using the available parallax data is suggestively located at the luminosity predicted by theoretical models for the termination of the stable nuclear burning main sequence. Stars like LHS2924, LHS2065 and TVLM 513-46546 (which lie below this inflection in the main sequence) are probably 'transition objects', which while currently partially supported by nuclear burning, will fade to become true brown dwarfs within a few billion years.

It has been found that the use of a redder filter with a narrower band-pass than that currently in use at the USNO allows observations significantly further from the meridian without increased DCR effects. While such a filter gives lower sensitivity it allows significantly more flexibility in planning observations – a major factor in carrying out astrometric observations on a common-user telescope. Perhaps the most significant result of this work, though, is that while extensive parallax programmes aimed at a large number of disparate targets may still be best carried out at dedicated astrometric facilities like those of the USNO, our results demonstrate that precision astrometry of a smaller, more specific sample can be carried out using standard CCD equipment on a common-user telescope. This means that parallax measurement need no longer be considered the exclusive domain of the currently small number of specialised astrometric observers. Astronomers with interesting new, nearby objects can obtain their own CCD distance estimates within a few years, without having to wait for results from the currently overtaxed USNO programme.

The author particularly wishes to thank Jeremy Mould and Neill Reid for their invaluable guidance and advice throughout this project. Both Hugh Harris and Dave Monet provided hints on the arcane field of precision astrometry, for which I am extremely grateful. Lastly I wish to thank the tireless Palomar staff without whom all the observing required for this work would never have been completed; Cindy Brewer, Mike Doyle, John Henning, Greg van Idsinga, Dave Mendenhall, Jean Mueller, Dave Tennant, and especially Will M^{c}Kinley and Skip Staples.

References

Becklin, E.E. & Zuckerman, B., 1988, Nature, 336 656

Bessell, M., 1991, AJ, 101, 662

Burrows, A., Hubbard, W.B., Lunine, J.I., 1989. ApJ 345, 939

Gliese, W., 1969, *Catalogue of Nearby Stars, Veroff. Astr. Rechen. Inst. Heidelberg No 22*

Hawkins, M.R.S, & Bessell, M.S., 1988, MNRAS, 234, 177

Irwin, M., M^{c}Mahon, R.G., Reid. N. 1991. MNRAS, 252, 61p

Irwin, M. *et al.* 1992. *in preperation*

Irwin, M. 1992. *private communication*

Leggett, S.K. 1992, ApJSuppl, *submitted*

Leggett, S.K. & Hawkins, M.R.S., 1988, MNRAS, 234, 1065

Leggett, S.K. & Hawkins, M.R.S., 1989, MNRAS, 238, 145

Luyten, W.J., 1979, *LHS Catalogue* (Minneapolis: University of Minnesota)

Monet, D.G, Dahn, C.C., 1983, AJ, 88, 1489

Monet, D.G, Dahn, C.C., Vrba, F.J., Harris, H.C., Pier, J.R, Luginbuhl, C.B., Ables, H.D., 1992, AJ, 103, 638

Owens, J.C. 1967, Appl.Opt., 6, 51

Schneider, D.P., *et al.* 1991, AJ, 102, 1180

Stetson, P.B., 1987, PASP, 99, 191

Tinney, C.G., Mould, J.R., Reid, I.N. 1992a, ApJ, 396, 173

Tinney, C.G., Mould, J.R., Reid, I.N. 1992b, AJ, *in press.* (Paper II)

Tinney, C.G., Reid, I.N., Mould, J.R., 1992a, ApJSuppl, *submitted*, (Paper I)

Tinney, C.G., 1992, ApJ, *submitted.* (Paper IV)

Table 4.1 - CCD Parallaxes.

Object	$\alpha(1950)$	$\delta(1950)$	Epoch	N_f,N_n,N_s	π_{rel} (mas)	μ_{rel} (mas/yr)	θ_{rel} (°)
TVLM 868-110639	$15^h\ 07^m\ 41.2^s$	$-02°\ 29'\ 47''$	1986.1	52,10,09	56.1	380.9	272.8
					±1.6	±2.0	±2.0
BRI 0021-0214	$00^h\ 21^m\ 51.1^s$	$-02°\ 14'\ 59''$	1992.5	38,07,04	81.2	136.8	328.1
					±3.2	±7.0	±21.7
TVLM 213-2005	$10^h\ 18^m\ 19.2^s$	$+51°\ 10'\ 11''$	1989.5	72,06,08	27.7	375.6	278.3
					±2.2	±1.1	±1.0
VB10,GL752B	$19^h\ 14^m\ 29.8^s$	$+05°\ 03'\ 45''$	1992.5	75,26,05	167.7	1489.9	203.2
					±2.1	±1.8	±0.6
TVLM 513-46546	$14^h\ 58^m\ 54.5^s$	$+23°\ 01'\ 51''$	1991.7	37,11,05	99.3	74.0	31.7
					±3.3	±6.9	±9.7
TVLM 831-161058	$02^h\ 48^m\ 38.7^s$	$+00°\ 35'\ 16''$	1981.9	42,09,05	19.4	256.5	76.9
					±2.0	±4.4	±1.9
TVLM 832-10443	$02^h\ 49^m\ 51.9^s$	$+00°\ 44'\ 09''$	1992.5	34,08,05	38.0	206.6	238.6
					±2.0	±2.7	±1.8

Table 4.2 - Absolute Magnitudes and Space Motions.

Object	π_{abs} (mas)	V_{tan} (km/s)	M_I	M_J	M_K
TVLM 868-110639	57.5 ± 1.9	31.4	14.59 ± 0.06	11.49 ± 0.06	10.14 ± 0.06
BRI 0021-0214	82.5 ± 3.4	7.9	14.65 ± 0.06	11.48 ± 0.06	10.22 ± 0.06
TVLM 213-2005	28.9 ± 2.4	61.6	13.50 ± 0.09	-	9.63 ± 0.06
VB10 (GL752B,LHS474)	171.7 ± 4.0^a	41.5	13.95 ± 0.03	11.04 ± 0.03	9.97 ± 0.03
TVLM 513-46546	100.8 ± 2.3	3.5	15.11 ± 0.06	11.92 ± 0.05	10.78 ± 0.05
TVLM 831-161058	20.5 ± 2.2	59.3	13.19 ± 0.12	10.33 ± 0.12	9.26 ± 0.12
TVLM 832-10443	39.4 ± 2.2	24.8	14.04 ± 0.09	11.11 ± 0.08	9.98 ± 0.08

a - Absolute magnitudes and tangential velocities calculated with the more precise value of $\pi_{abs} = 170.1 \pm 0.8$ due to Monet *et al.* 1992.

Table 4.3 - RI Photometry of Programme and Reference Stars.

Object Name	Object I	Object R–I	Reference Stars [a] (#;$\Delta\alpha$,$\Delta\delta$;I;R–I)
TVLM 868-110639	15.79	2.40	(1;−30.2,87.1;13.31;0.47)(3;23.7,−8.4;14.18;0.79)(6;94.2,19.5;15.40;0.50) (7;32.8,87.5;15.66;0.75)(9;−51.1,49.0;15.86;0.81)(12;100.5,62.2;16.13;0.44) (16;−80.9,110.9;16.49;(0.59))(19;19.4,79.2;16.82;0.46) (20;−99.4,28.2;16.86;0.53)(22;−86.6,−51.8;16.85;0.57)
BRI 0021-0214	15.07	-	(4;6.8,131.5;15.40)(4;154.5,34.7;15.91)(7;−109.9,−120.9;16.17)(8;−62.9,−93.4;16.28) (9;−114.5,179.8;16.41)(10;87.6,−129.3;16.48)(11;69.0,14.9;16.75)
TVLM 213-2005	16.20	2.44	(2;−196.0,17.6;13.51;0.39)(3;−10.0,90.5;15.16;0.52)(5;94.5,−158.17 : 15.34;0.52) (7;0.49,−154.8;15.89;0.44)(12;10.8,83.0;16.54;0.40)(13;−88.6,64.2;16.72;0.54)
VB10	12.80	-	(20;−43.2,158.7;13.03)(23;85.7,−3.1;13.25)(25;−5.9,132.8;13.28)(26;61.2,116.2;13.29) (27;49.4,85.1;13.29)(28;67.9,−60.8;13.33)(29;118.2,18.6;13.34)(31;18.6,135.4;13.36) (36;−107.5,78.8;12.52)(41;65.7,36.5;13.72)(43;50.0,49.4;13.74)(45;47.4,26.8;13.76) (46;−60.5,97.5;13.76)(48;103.6,−39.5;13.80)(49;−87.9,59.3;13.80) (51;−88.9,50.2;13.83)(52;71.5,119.3;13.85)(53;−57.2,98.0;13.85)(59;98.9,24.0;13.93) (63;100.2,−51.7;14.01)(64;36.8,−31.4;14.03)(73;118.4,−24.3;14.19) (75;57.9,−40.0;14.25)(76;56.9,41.9;14.26)(77;109.3,26.0;14.27) (82;6.9,−35.7;14.38)
TVLM 513-46546	15.09	2.36	(1;89.1,−228.9;14.42;(0.69))(3;93.4,−61.6;15.47;(0.69))(4;48.5,−59.5;15.76;1.46) (5;0.7,−37.8;16.26;0.36)(6;−61.8,64.8;16.28;0.38)(7;−103.7,−80.5;16.38;1.16) (9;21.0,−183.0;16.46;0.37)(11;−53.9,65.1;15.51;0.40)(12;−115.2,−187.9;16.57;(0.69)) (13;89.8,−221.8;16.57;0.96)(14;−66.4,−202.1;16.65;0.40)
TVLM 831-161058	16.63	2.58	(2;59.8,60.35;14.80;1.05)(3;184.2,31.4;14.97;(0.80))(4;53.0,−75.0;15.28;0.53) (5;−15.7,−24.9;15.90;0.41)(7;−52.5,131.5;16.32;0.78)(11;194.7,120.6;17.26;(0.80)) (12;203.7,108.2;17.27;0.79)(13;−55.0,126.5;17.31;0.62)
TVLM 832-10443	16.06	2.49	(1;−177.5,56.2;14.69;0.42)(3;−3.93,123.5;15.56;1.20)(6;−62.8,111.7;16.58;0.51) (7;64.9,31.7;16.69;0.49)(8;−146.0,82.5;16.87;0.70)(9;47.7,161.1;16.93;1.02) (10;−211.4,−166.9;17.17;1.11)(15;−56.2,−19.1;17.77;0.50) (17;−25.8,−41.4;17.86;0.42)

a - Each set of numbers gives parameters for a reference star; a number assigned during the reduction process, an offset in arcseconds from the programme object position, and I band magnitude and an R–I colour. R–I colours are not shown for BRI 0021-0214 and VB10. Sources for the photometry are given in the text.

Figure Captions

Figure 4.1 - **Histogram of Seeing Values.** A histogram of seeing for all the individual CCD frames used for astrometry of the 7 VLM stars presented in this work.

Figure 4.2 - **Differential Colour Refraction.** Data from three nights is shown for both; (a) a typical reference star (Star 3 from the field of TVLM 868-110639, R–I=0.79, I=14.83), and (b) the programme object TVLM 832-10443 (R–I=2.38, I=15.79). The fitted lines shown give $\Delta F_{ref} = -11.2 \pm 2.6$ and $\Delta F_{prog} = 6.1 \pm 4.0$.

Figure 4.3 - **Parallax and Proper Motion Solutions.** The solutions shown are for, (a) TVLM 868-110639 ($\Delta F_{prog} = 10.2 \pm 3.8$), (b) BRI 0021-0214 ($\Delta F_{prog} = 15.9 \pm 3.7$), (c) TVLM 213-2005 ($\Delta F_{prog} = 19.2 \pm 1.8$), (d) VB10 ($\Delta F_{prog} = 3.0 \pm 4.3$), (e) TVLM 513-46546 ($\Delta F_{prog} = 27.2 \pm 2.2$), (f) TVLM 831-161058 ($\Delta F_{prog} = 15.0 \pm 10.0$) and (g) TVLM 832-10443 ($\Delta F_{prog} = 8.2 \pm 2.6$). The parameters fitted by these solutions are given in Table 4.1.

Figure 4.4 - **New Colour-Magnitude Relations for VLM Stars.** (a) M_I:I–K, (b) M_J:I–J and (c) M_K:I–K. The sources of photometry are provided in the text. *Dot-dashed* lines are sequences due to Bessell (1991). *Dotted* lines are sequences due to Leggett (1992). *Solid* lines are third order fits to the data as follows;

$$\text{(a) } M_I = -35.0565 + 35.7316(\text{I–K}) - 9.03672(\text{I–K})^2 + 0.791067(\text{I–K})^3;$$

$$\text{(b) } M_J = -8.34846 + 17.9101(\text{I–J}) - 5.71739(\text{I–J})^2 + 0.643302(\text{I–J})^3;$$

$$\text{and (c) } M_K = M_I - (\text{I–K}).$$

Figure 4.1

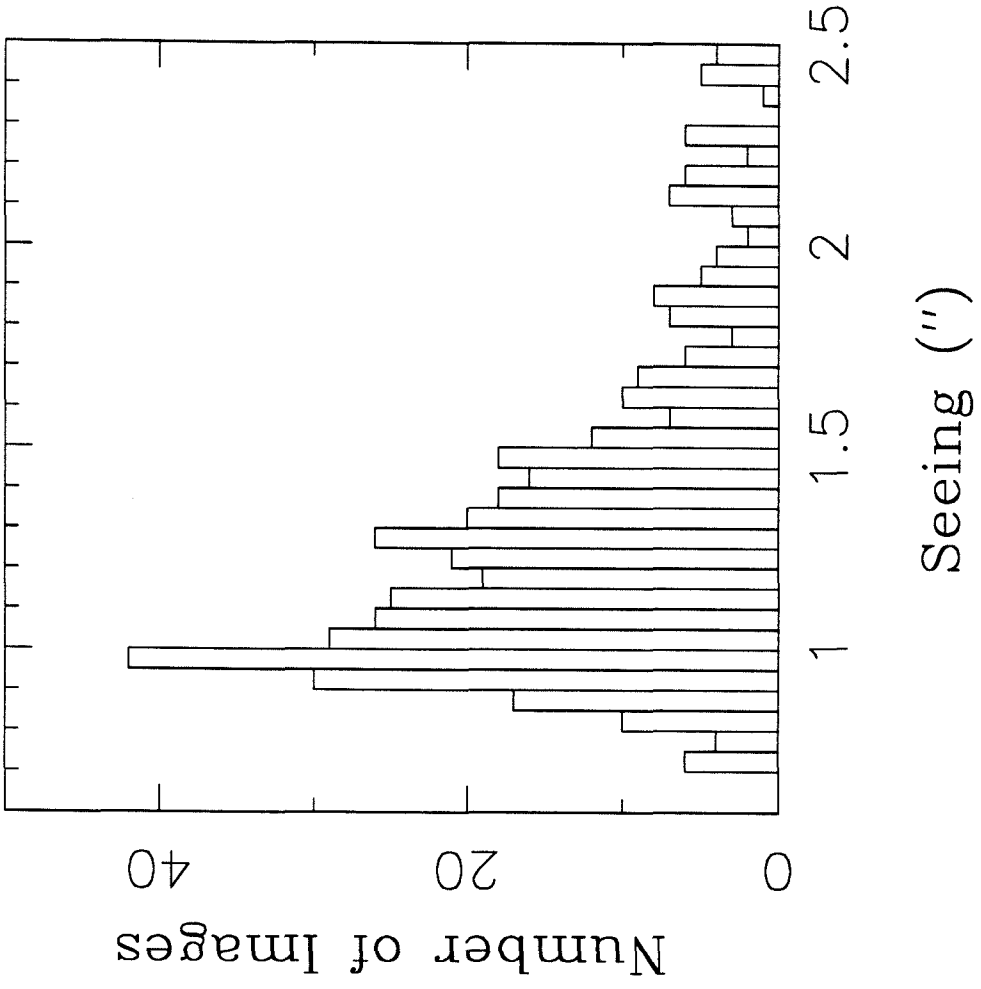

Figure 4.2(a)

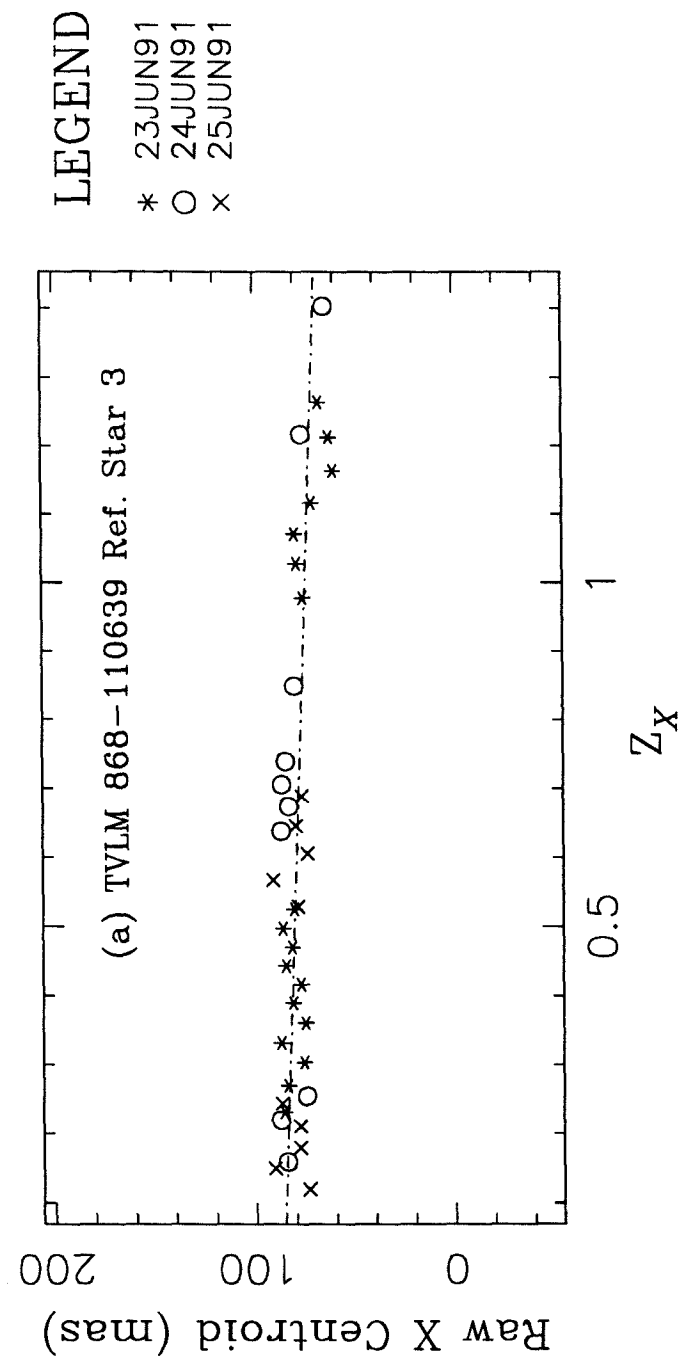
LEGEND
* 23JUN91
O 24JUN91
× 25JUN91
(a) TVLM 868–110639 Ref. Star 3
Raw X Centroid (mas)
200
100
0
0.5
1
Z_X

Figure 4.2(b)

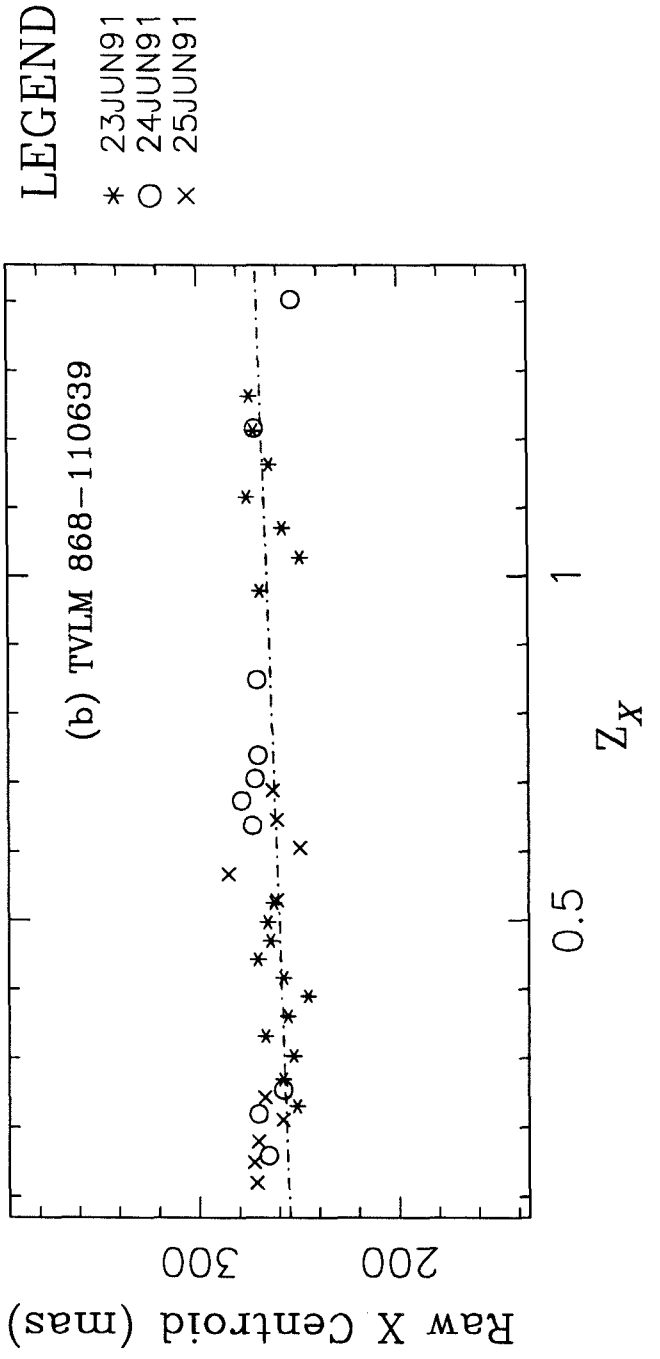
LEGEND
* 23JUN91
O 24JUN91
× 25JUN91
(b) TVLM 868−110639
Raw X Centroid (mas)
200
300
0.5
1
Z_X

Figure 4.3(a)

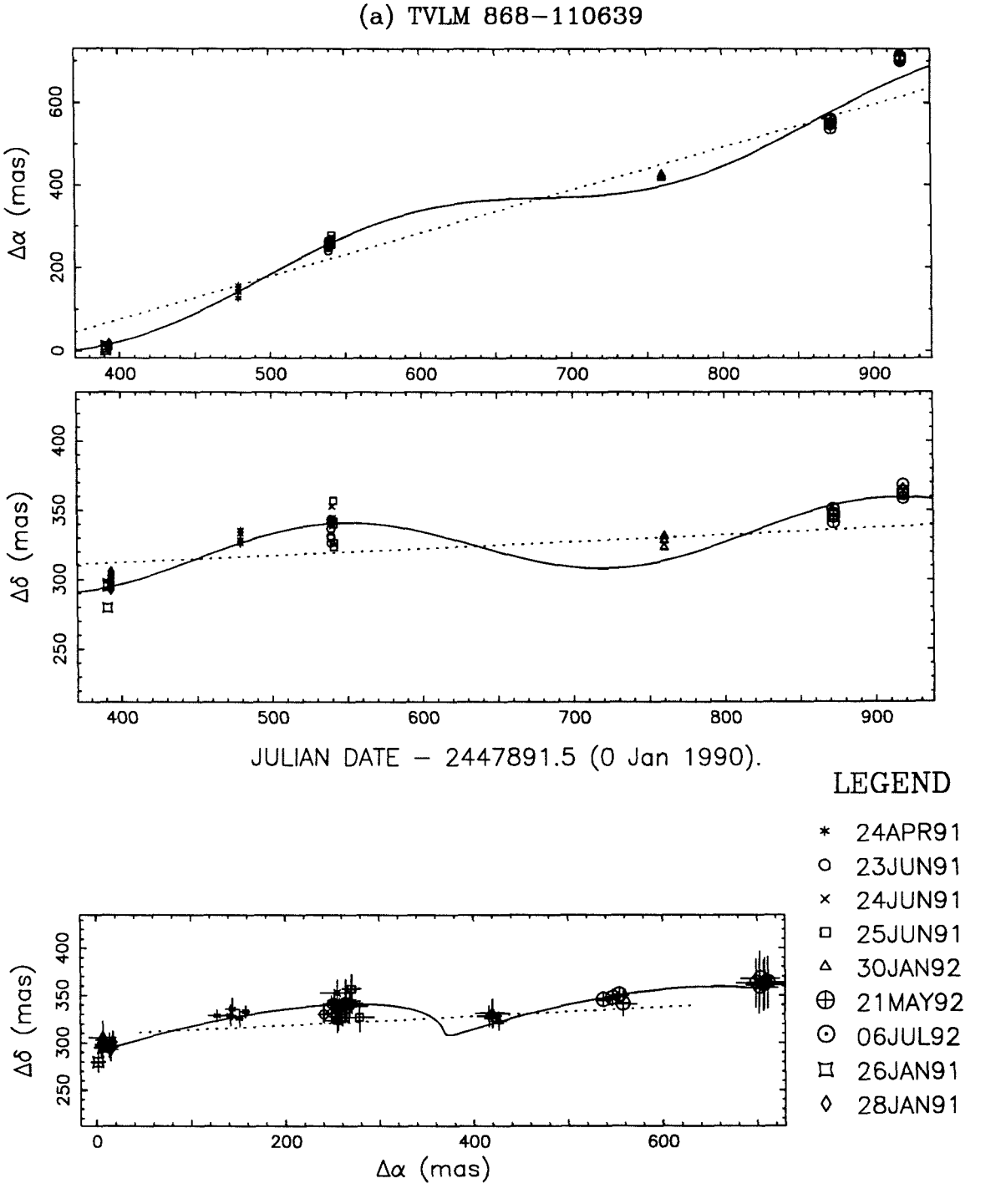
(a) TVLM 868−110639
Δα (mas)
Δδ (mas)
JULIAN DATE − 2447891.5 (0 Jan 1990).
LEGEND
24APR91
23JUN91
24JUN91
25JUN91
30JAN92
21MAY92
06JUL92
26JAN91
28JAN91
Δδ (mas)
Δα (mas)
christ 18−Aug−1992 19:43

Figure 4.3(b)

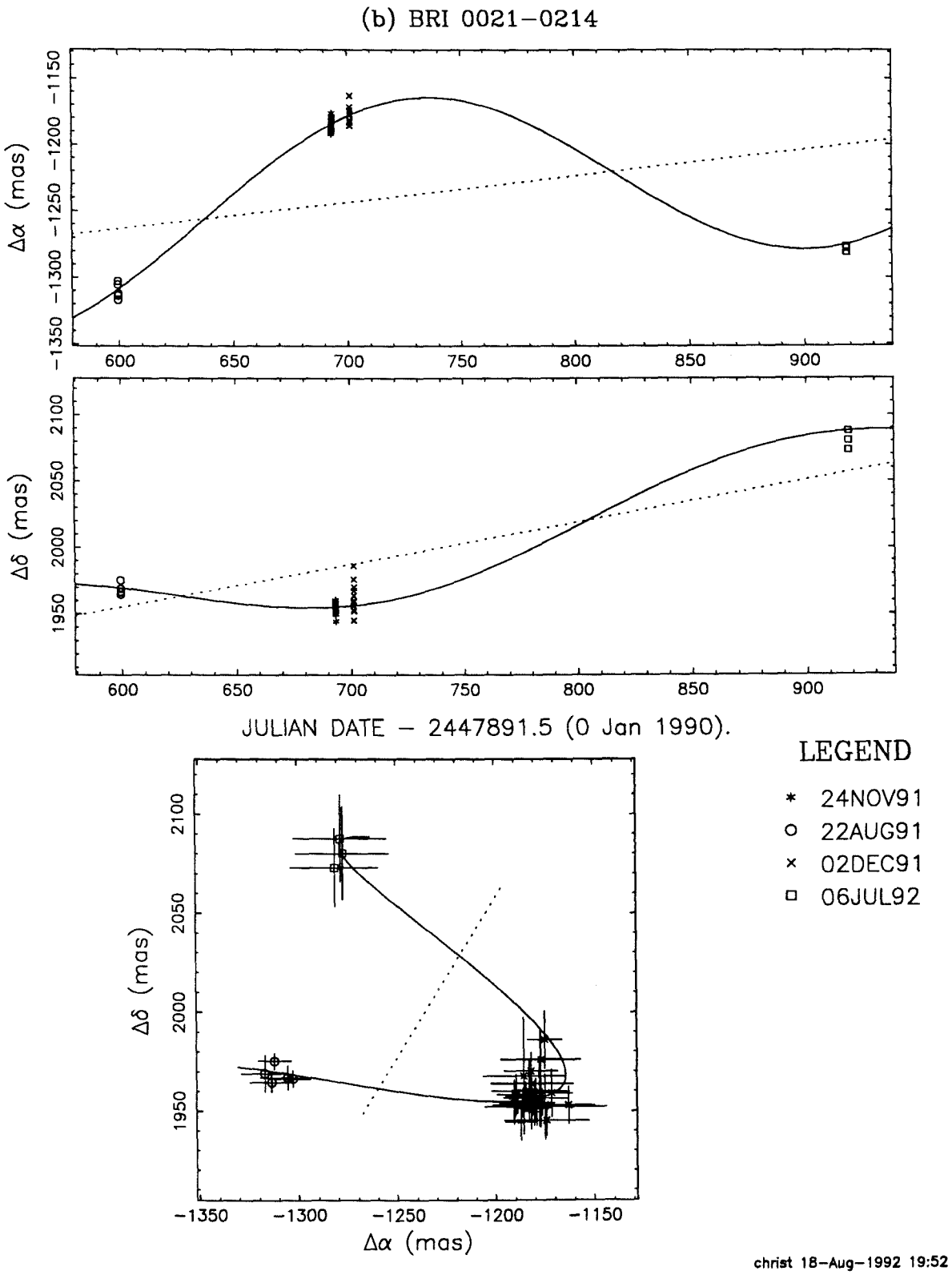
(b) BRI 0021−0214
Δα (mas)
−1350 −1300 −1250 −1200 −1150
600 650 700 750 800 850 900
Δδ (mas)
1950 2000 2050 2100
600 650 700 750 800 850 900
JULIAN DATE − 2447891.5 (0 Jan 1990).
LEGEND
* 24NOV91
o 22AUG91
× 02DEC91
□ 06JUL92
Δδ (mas)
1950 2000 2050 2100
−1350 −1300 −1250 −1200 −1150
Δα (mas)
christ 18−Aug−1992 19:52

Figure 4.3(c)

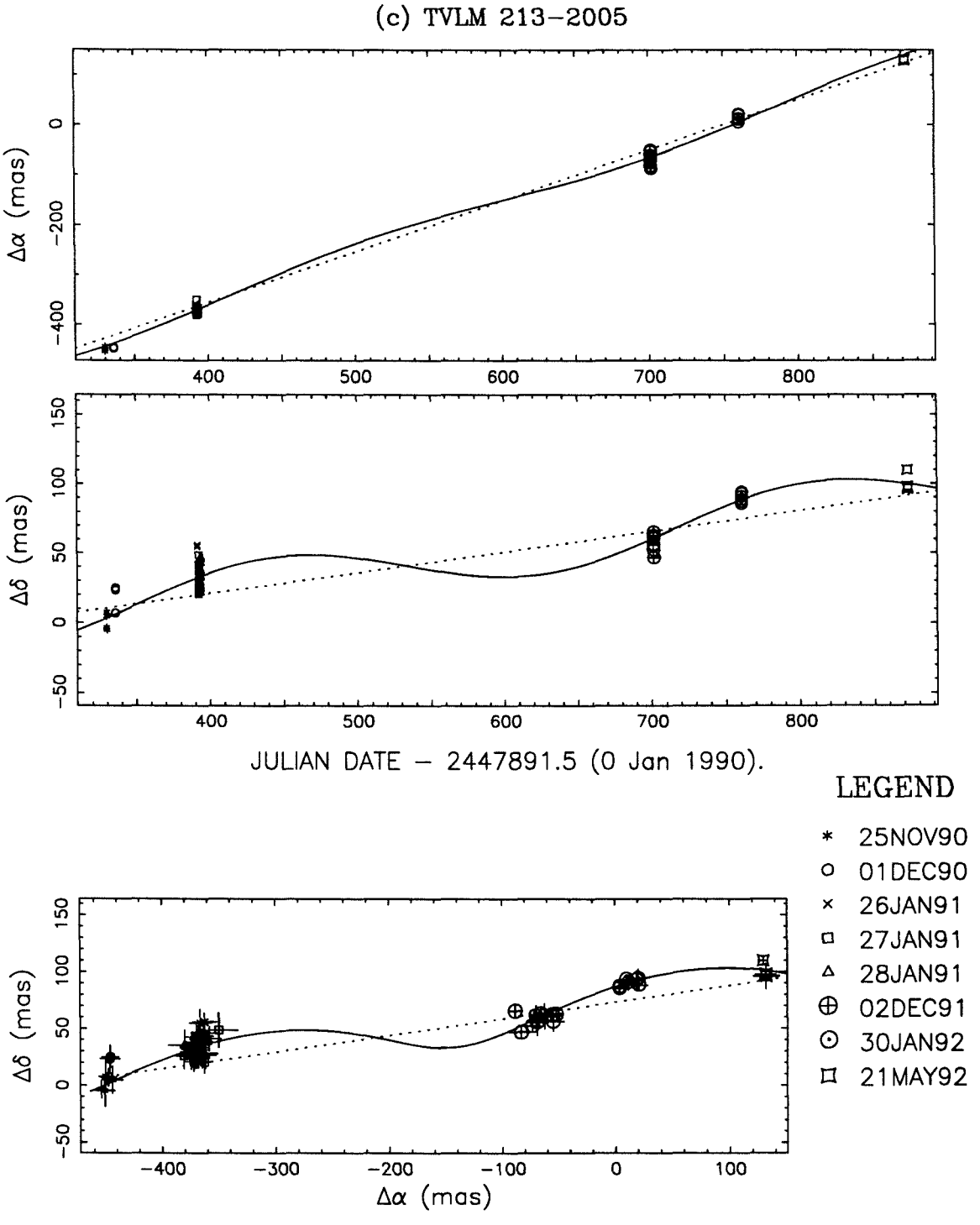
(c) TVLM 213–2005
Δα (mas)
Δδ (mas)
JULIAN DATE – 2447891.5 (0 Jan 1990).
LEGEND
* 25NOV90
o 01DEC90
× 26JAN91
□ 27JAN91
△ 28JAN91
⊕ 02DEC91
⊙ 30JAN92
⌑ 21MAY92
Δδ (mas)
Δα (mas)
christ 18–Aug–1992 19:54

Figure 4.3(d)

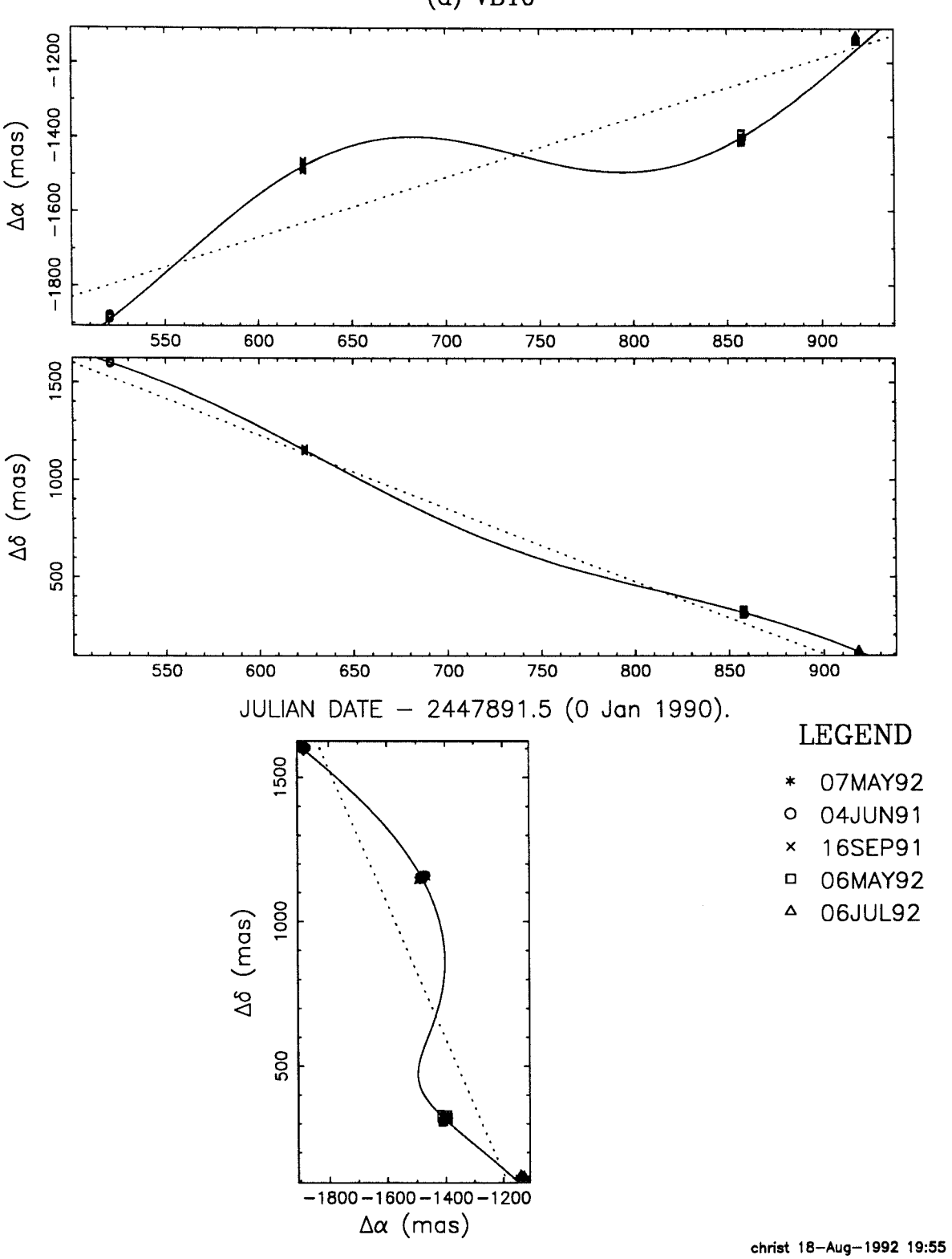
(d) VB10
Δα (mas)
−1200
−1400
−1600
−1800
550
600
650
700
750
800
850
900
Δδ (mas)
1500
1000
500
JULIAN DATE − 2447891.5 (0 Jan 1990).
LEGEND
* 07MAY92
o 04JUN91
× 16SEP91
□ 06MAY92
△ 06JUL92
Δδ (mas)
Δα (mas)
christ 18−Aug−1992 19:55

Figure 4.3(e)

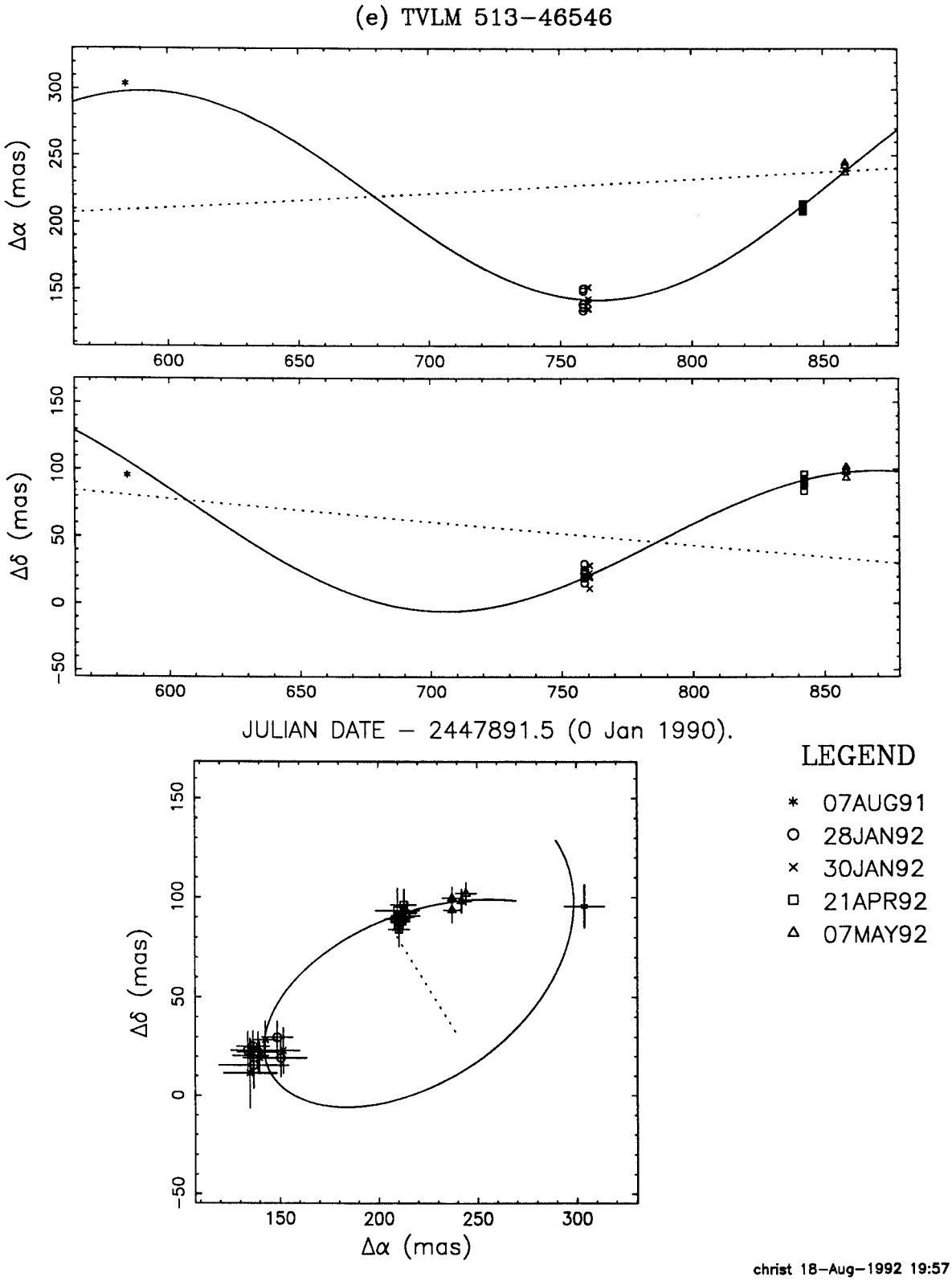
(e) TVLM 513–46546
Δα (mas)
Δδ (mas)
JULIAN DATE – 2447891.5 (0 Jan 1990).
LEGEND
* 07AUG91
o 28JAN92
× 30JAN92
□ 21APR92
△ 07MAY92
christ 18–Aug–1992 19:57

Figure 4.3(f)

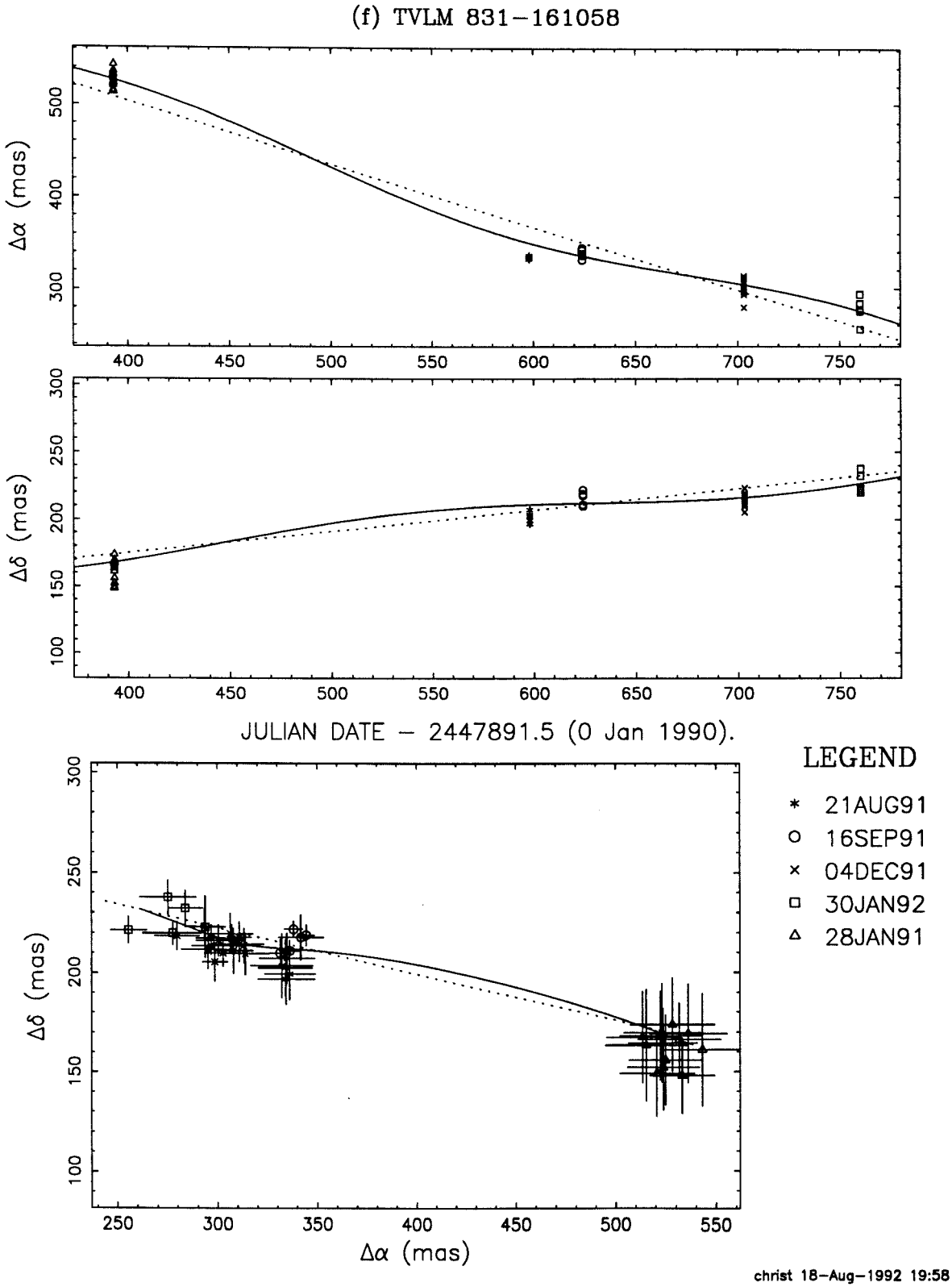
(f) TVLM 831−161058
Δα (mas)
Δδ (mas)
JULIAN DATE − 2447891.5 (0 Jan 1990).
LEGEND
* 21AUG91
o 16SEP91
× 04DEC91
□ 30JAN92
△ 28JAN91
Δδ (mas)
Δα (mas)
christ 18−Aug−1992 19:58

Figure 4.3(g)

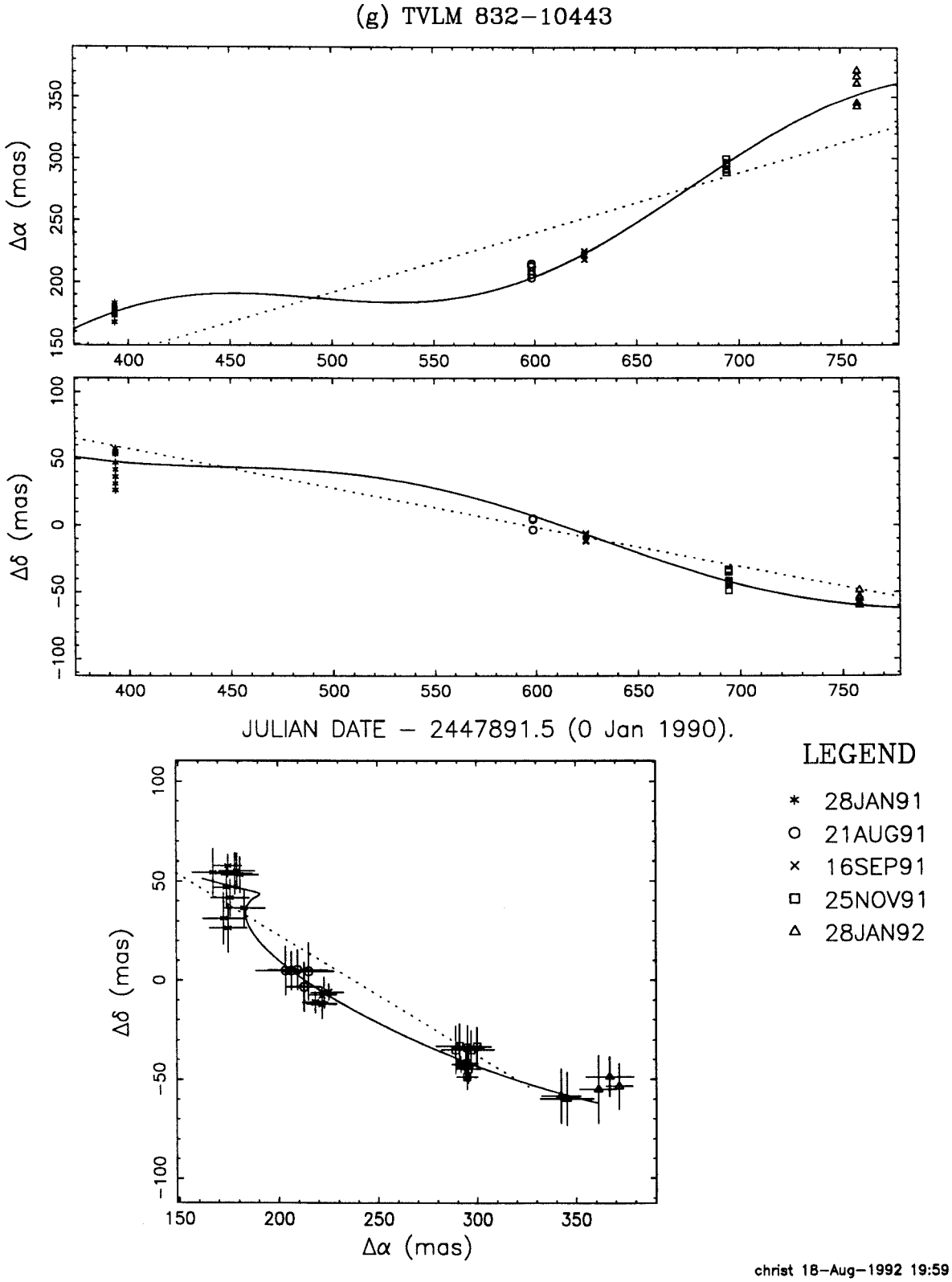
(g) TVLM 832−10443
Δα (mas)
Δδ (mas)
JULIAN DATE − 2447891.5 (0 Jan 1990).
LEGEND
28JAN91
21AUG91
16SEP91
25NOV91
28JAN92
Δδ (mas)
Δα (mas)
christ 18−Aug−1992 19:59

Figure 4.4(a) M_I:I–K

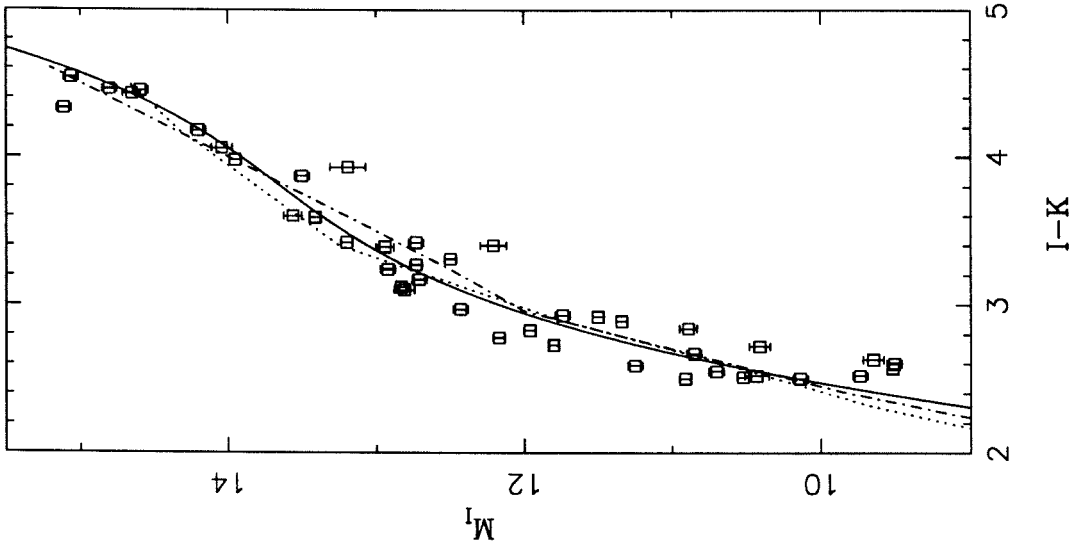

Figure 4.4(b) M_J:I–J

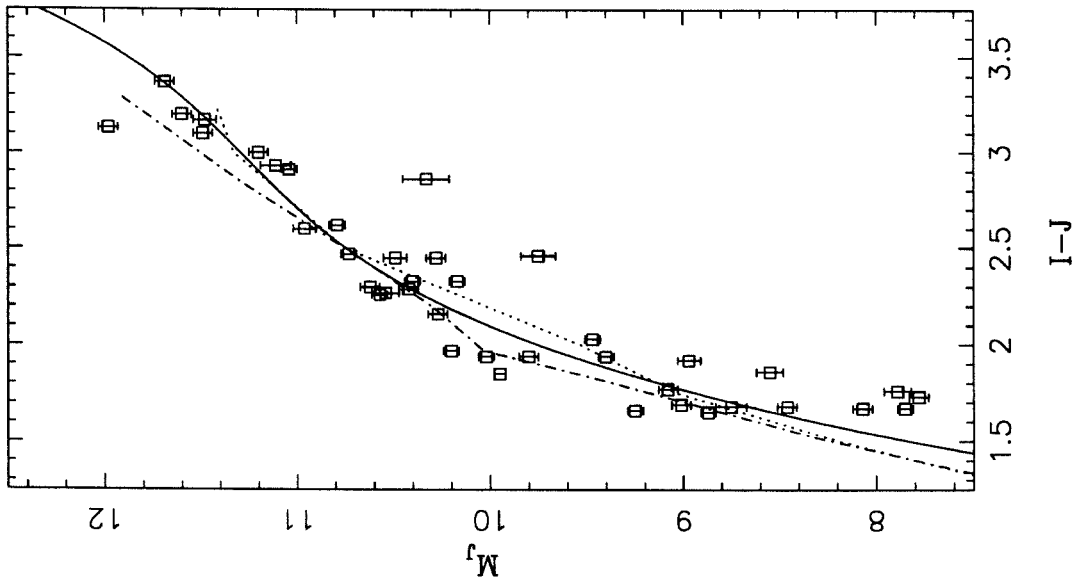

Figure 4.4(c) M_K:I–K

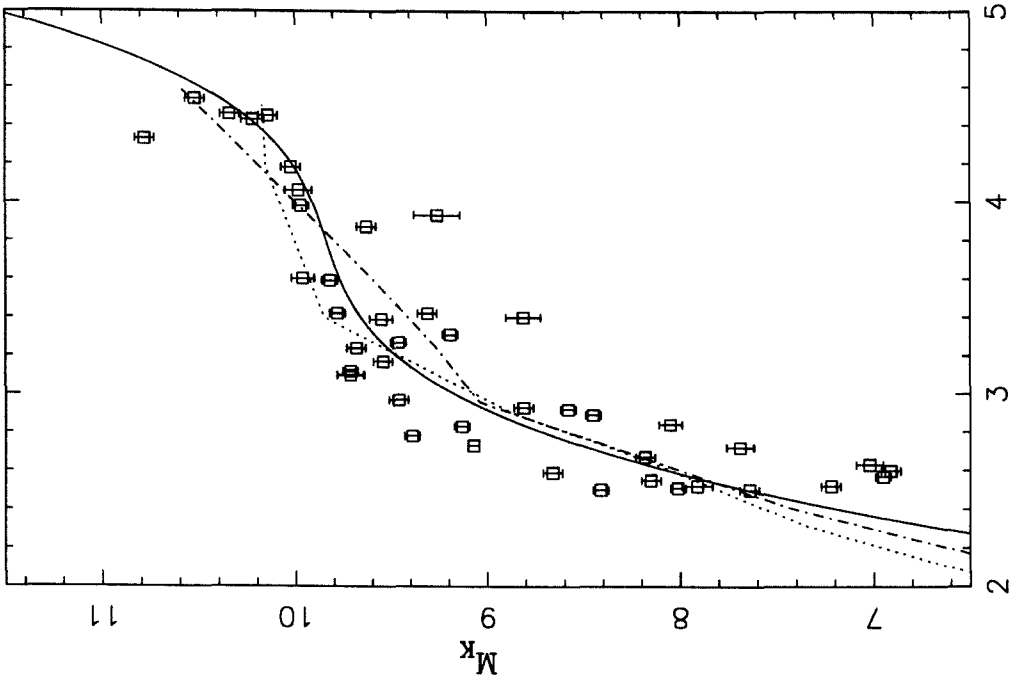

Chapter 5 - The Luminosity and Mass Functions at the Bottom of the Main Sequence. [1,2]

Abstract

We present infrared K-band photometry of complete samples of VLM candidates constructed from IIIaF and IVN plates in ten fields taken as part of the POSSII and UKSRC surveys. Using the I–K colours constructed for these stars we estimate a bolometric luminosity function which extends to $M_{Bol} = 13.75$. We find significant evidence for a luminosity function decreasing towards these luminosities. We also find that our data are consistent with the results of studies based on the Nearby Star sample, when those data are presented as a bolometric luminosity function. We convert our observed LF into the form of a mass function, which extends with reasonable statistics to $0.08M_{\odot}$ – the H-burning minimum mass. We find significant evidence for features in the mass function at these masses. Specifically, the mass function 'turns over' at $\approx 0.25M_{\odot}$, goes through a local minimum at $\approx 0.15M_{\odot}$, and seems to increase again below $0.1M_{\odot}$ – none of these features are predicted by any of the current theories of star formation. Lastly, the mass density we observe just above the H-burning minimum mass makes it difficult to envisage brown dwarfs contributing significant quantities of missing mass without invoking either a mass function in this region significantly steeper than that seen for main sequence stars, or an extremely low cut-off mass to the mass function.

---

[1] Observations were made partially on the 60-inch telescope at Palomar Mountain which is jointly owned by the California Institute of Technology and the Carnegie Institution of Washington. Observations were also made at the Las Campanas Observatory which is operated by the Carnegie Institute of Washington

[2] This work is partially based on photographic plates obtained at the Palomar Observatory 48-inch Oschin Telescope for the Second Palomar Observatory Sky Survey which was funded by the Eastman Kodak Company, the National Geographic Society, the Samuel Oschin Foundation, the Alfred Sloan Foundation, the National Science Foundation grants AST 84-08225 and AST 87-19465, and the National Aeronautics and Space Administration grants NGL 05002140 and NAGW 1710.

Section 5.1 - Introduction

The stellar mass function (MF) – as inferred from the observed stellar luminosity function (LF) – is a fundamental quantity which is intimately linked with current efforts to understand the processes of star formation, the distribution of mass within the Galaxy, and (in the form of the initial inital mass function, or IMF) is a fundamental input parameter to the modelling of other galaxies. While the MF is reasonably well described above $0.3M_{\odot}$ (Scalo 1986), its form in the important Very Low Mass (VLM, or $M < 0.3M_{\odot}$) region is far from clear, with different studies indicating both increasing *and* decreasing MFs below $\approx 0.2M_{\odot}$. The importance of accurately determining the form of the MF in this region is further emphasised by the on-going debate about whether VLM stars/brown dwarfs can contribute significantly to the so-called local Galactic 'missing mass'.

The best measurements to date of the faint end of the LF can be divided into two types; studies based on photometric surveys carried out with photographic plates from the 48″-Schmidt-class telescopes (the United Kingdom Schmidt Telescope in the south, and the Oschin Telescope at Palomar Mountain in the north); and studies based on sub-samples of stars selected from the Nearby Star Sample (Gliese 1969, Gliese & Jahreiss 1979). The former samples survey areas of several tens of square degrees to distances of $\sim 50 - 150$pc, but are forced to estimate luminosities and distances based only on optical (V–I or R–I) colours, and are unable to resolve close binary systems at the typical distances sampled (Reid & Gilmore 1982, Gilmore *et al.* 1985, Hawkins 1985, Reid 1987, Hawkins & Bessell 1988, Legget & Hawkins 1988). The latter samples cover essentially the whole sky out to distances of $\lesssim 20$pc, and are able to use distances and luminosities estimated directly from triginometric parallaxes (Weilen *et al.* 1983, Dahn *et al.* 1983, Liebert& Dahn 1986, Dahn *et al.* 1986, Henry & M^{c}Carthy 1992). However, they have the disadvantage that the volume they survey is about an order of magnitude smaller than that sampled by studies using photographic techniques, and are composed of primarily kinematically selected objects and so suffer serious completeness problems for distances $\gtrsim 10$pc. Lastly, until recent years studies conducted using both techniques have concentrated on the optical properties of the stars studied. However, because the effective temperatures of these stars are so low, they emit almost all of the flux in the near-infrared ($1 - 2.5\mu$m), making optical colours and magnitudes exceedingly poor estimatators of the fundamental quantities of most interest – i.e., bolometric luminosity and effective temperature. A few investigators have used infrared photometry in their work (most notably, Hawkins & Bessell 1988, Legget & Hawkins 1988,

Henry & M^{c}Carthy 1992), though even in these cases the detailed studies required to calibrate these properties have been neglected.

Three things, then, have limited earlier work in this field; small sampled volumes, a reliance on optical colours and insufficient calibration of fundamental properties. We seek to address these issues in this work. We have constructed samples of VLM candidates from a 270 degree^2 photographic catalogues constructed using 48″-Schmidt-class plates (Tinney, Reid & Mould 1992 – hereafter Paper I), and complete samples of these stars have been observed at the infrared K-band. We have also carried out a programme of complete infrared spectroscopy and infrared photometry in the $1-3.8\mu$m range. Using this data we have constructed new bolometric corrections which enable us to more accurately estimate apparent bolometric fluxes using the I–K colours measured for each VLM candidate (Tinney, Mould & Reid 1992b - hereafter Paper II). We have also carried out a programme of triginometric parallaxes on the Palomar 60″ telescope specifically targetted at VLM stars (Tinney 1992 - hereafter Paper III). Using this new parallax data, and the recently published results of Monet *et al.* (1992), we construct colour-magnitude relations which enable us to estimate distances and luminosities from our I–K data far more accurately than previous photometric studies have done. The resulting LF extends to (i.e., has detected objects as faint as) $M_{Bol} = 13.75$, at which level (unlike most earlier work) counting errors – not systematics – dominate. Some preliminary results of this programme have already been presented by Tinney, Mould & Reid (1992a).

Section 5.2 - Sample Selection

The procedures used to derive the lists of candidate VLM stars used as targets for infrared photometry are described in detail in Tinney, Mould & Reid (1992 - Paper I), however a summary follows. IIIaF and IVN plates from the Second Palomar Sky Survey (hereafter POSSII) and the U.K. Science Research Council Sky Survey (hereafter UKSRC) in eleven fields were digitised using the COSMOS plate scanning machine (Beard *et al.* 1990). These produce photometry over a 270 square degree area which is calibrated onto a uniform photometric system with r^C_{Pal} and i^C_{Pal} photometry acquired with a CCD camera on the Palomar 60″ telescope, to produce a catalogue of ri^P_{Pal} photometry. (The superscripts C and P are used to denote whether photometry is from CCD or photographic observations.) The ri^C_{Pal} system is defined by observations through Gunn-system r and i filters with a photometric zero-point set by Landolt (1983) standard stars in the colour range $0.5 < (R-I)_C < 1.0$. The reasons for choosing this system and the small differences between it

and the commonly used Cousins system are described in Paper I. In each POSSII/UKSRC field a catalogue was constructed by matching a single IVN plate (called the master plate) against all the other plates in that field (called slave plates). From this catalogue of r^P_{Pal} and i^P_{Pal} photometry an r^P_{Pal} -i^P_{Pal} colour is derived for each object, which is then corrected for a colour term to create a $(r-i)^P_{Pal}$ colour. Note that we differentiate between r^P_{Pal} - i^P_{Pal} and $(r-i)^P_{Pal}$ colours – the former is the simple difference of r^P_{Pal} and i^P_{Pal} photometry, while the latter has been placed on the same colour system as our $(r-i)^C_{Pal}$ photometry. VLM star candidates can then be selected on the basis of their $(r-i)^P_{Pal}$ colour.

Infrared observations of these stars are required because $(r-i)^P_{Pal}$ is a poor estimator of absolute magnitudes for very late stars. This is so for several reasons; first, the spectra of these stars are dominated in the R and, to a lesser extent, I passbands by deep molecular absorptions, which result in small differences in metallicity (for a given luminosity star) producing significant changes in R–I colour and so considerable cosmic scatter in the R–I colour/absolute-magnitude relation. (When we use the term R–I we refer to the 'generic' R and I passbands – i.e., any RI filter system; Gunn ri, ri_{Pal}, Cousins RI or Johnson RI – and we do so in order to refer to features common to all of them.) Moreover, for the very latest stars R–I colours 'saturate' (Leggett & Hawkins 1988) and provide only an upper limit to the luminosity. The $(r-i)^P_{Pal}$ colours we estimate also rely on IIIaF photographic plate data which are within a magnitude of the plate limits and consequently have typical uncertainties of ± 0.3 magnitudes, which produce uncertainties in the estimated M_{Bol} values of $\sim \pm 1$ magnitude. Lastly, the number of VLM stars detected in our survey volume is on the order of the number of contaminating spurious images and/or galaxies present in the catalogues. Together these problems mean that relying on $(r-i)^P_{Pal}$ data alone to estimate a luminosity function would necessitate using data on stars over a colour range of $1.9 \lesssim (r-i)^P_{Pal} \lesssim 2.5$, with typical uncertainties of ± 0.35 magnitudes in $(r-i)^P_{Pal}$ and producing a luminosity function with essentially only two independent luminosity bins, both which are heavily contaminated by non-stellar objects.

K-band photometry has therefore been obtained for complete samples of VLM candidates identified by our $(r-i)^P_{Pal}$ data. Using this we construct an $(i^P_{Pal} - \mathrm{K})$ colour, which (as is discussed in Paper I) is identical to an I_C–K colour (we hereafter denote both as simply I–K). As VLM stars span a much larger range in I–K than they do in $(r-i)^P_{Pal}$ ($3.0 \lesssim$ I–K $\lesssim 4.7$ as opposed to $1.8 \lesssim$ R–I $\lesssim 2.5$), I–K is a considerably more sensitive luminosity estimator. And since we do not need to rely on the IIIaF photometry our I–K colours are more precise, with typical uncertainties of less than ± 0.2 magnitudes. Of the

eleven fields for which plate material has been scanned and CCD calibration photometry obtained, K-band data has been acquired to significant limits in ten – Fields 831, 832, 213, 262, 263, 513, 868, 889, 890 and 891. For each object on the master plate in a field, a unique object number is assigned by COSMOS when the plate is scanned. We use this number together with the field number and the survey designator 'TVLM' to name each object in our survey, e.g., TVLM 868-110639.

The observing strategy followed was to observe all VLM candidate stars above certain i^P_{Pal} and $(r-i)^P_{Pal}$ limits – in each field we denote these limits as $[i^P_{Pal}]_{lim}$ and $[(r-i)^P_{Pal}]_{lim}$. Ideally, given the uncertainty of our $(r-i)^P_{Pal}$ photometry and the cosmic scatter in R–I absolute-magnitude/colour relation, these limits would be chosen such that the maximum volume available to our survey ($[i^P_{Pal}]_{lim} = 18$) is sampled with a generous colour limit ($[(r-i)^P_{Pal}]_{lim} \approx 1.6$) which would ensure $\gtrsim 99.5\%$ of VLM stars in the regions covered by our photographic plates are detected. Unfortunately such limits would require the infrared observation of ~ 1000 objects per field, more than 90% of which would be early-type M-dwarfs, which are uninteresting for our purposes. We therefore have two options, we can lower $[i^P_{Pal}]_{lim}$ which decreases our survey volume, or increase $[(r-i)^P_{Pal}]_{lim}$ which decreases our completeness for brighter stars in the final luminosity function. We chose to maintain $[i^P_{Pal}]_{lim} \sim 17.5$, and increase the colour limit to which we observed candidates to $[(r-i)^P_{Pal}]_{lim} \sim 1.9 - 2.0$. This makes our survey complete only for stars with $M_{bol} \gtrsim 12$.

In each POSSII/UKSRC field we have chosen combinations of $[i^P_{Pal}]_{lim}$ and $[(r-i)^P_{Pal}]_{lim}$ which give $\sim$ 70 candidates objects. In some fields we have selected samples with more than one limit. For example in Field 213, objects were selected for infrared observations with $i^P_{Pal} < 18.0$ and $(r-i)^P_{Pal} \geq 2.0$ (denoted sample 213-1). A further set of objects with a more stringent magnitude limit but a more generous colour limit were also observed; $i^P_{Pal} < 17.0$ and $(r-i)^P_{Pal} \geq 1.9$ (and denoted sample 213-2). In Table 5.1 we summarise the observed samples, and indicate the plate areas surveyed as well as the magnitude and colour limits adopted. In some fields, in which more than one IVN plate was available, we were able to construct lists of candidate upper limit objects (i.e., objects detected above $[i^P_{Pal}]_{lim}$, but not detected on a IIIaF plate). Those fields are so denoted in Table 5.1. Single IVN plates turn out to be almost useless for making lists of upper limits – a criterion which selects for objects detected on one IVN plate, but not on any IIIaF plates also efficiently selects for plate defects, which out-number actual VLM stars by factors of hundreds. An attempt was made in fields with only a single IVN plate to separate plate defects from actual objects using image shape parameters (as is discussed

in Paper I, plate defects have characteristic image shapes which are usually different from those of stars). However, when the candidates selected in this way from two fields (Fields 513 and 262) were observed in the infrared, none (out of 10) were found to be real stars, let alone VLM stars. Clearly image shape parameter classification is not efficient enough at removing plate defects to make such a technique an efficient way of finding VLM stars.

Section 5.3 - Infrared Observations

Infrared K-band observations of candidate VLM stars have been made on 24 nights over the period 15 October 1989 to 24 June 1992 using the following infrared camera / telescope combinations: the Cassegrain Infrared Camera on the Palomar 200″ telescope (Carico *et al.* 1990); the Las Campanas Observatory Near-infrared Camera on the duPont (2.5m) and Swope (1m) telescopes (Persson *et al.* 1991); and ProtoCAM on the NASA Infrared Telescope Facility (hereafter referred to as the IRTF). We discuss the acquisition and reduction of data from each of these cameras separately below. In general, however, the reductions follow similar general procedures : dark/bias subtraction, linearization, flat fielding, cleaning and sky- or pair-subtraction.

First a bias frame or dark frame (acquired while observing a cold load) is subtracted from each data frame, then each data frame is linearised and flattened. The arrays used showed variations from linearity of only $5 - 10\%$ at their maximum count levels. Sky observations for each frame were made by moving the telescope by a fixed offset which is smaller than the size of the array. When the sky frame is subtracted from the object frame, two images of the object are then produced – one positive and one negative – both of which are photometered. After pair subtraction each frame was cleaned of bad pixels by linear interpolation and then examined to see if the object's image had fallen on top of any bad pixels. If the central region of an object had fallen on a bad pixel, that frame was deleted, since linear interpolation cannot recover data in the image core. Standards on the smaller (Palomar and IRTF) arrays were reduced without sky subtraction. This is because the edge of the negative image often fell within the large aperture used to measure the standards – especially for data from the Palomar 200″ where standards have to be observed either out of focus or 'smeared out' by the chopping secondary. However as the standards are so bright, exposure times are always very short ($\lesssim$ 1s) and sky levels are extremely low, so no significant uncertainty is introduced by this procedure. All photometry was measured using the FOTO aperture-photometry routine of the FIGARO data reduction package. All nights were calibrated onto the CIT/CTIO system using K-band standards due to Elias *et*

al. (1982). The K-band filters used on all telescopes are sufficiently close to those used to define the CIT/CTIO system that no colour terms are present.

5.3.1 - Palomar Observations.

Observations were carried out on the Palomar 200″ telescope using the Cassegrain Infrared Camera on 11 nights over the period 15 October 1989(UT) to 15 March 1992(UT). The camera uses a 58×62 Santa Barbara Research Corporation InSb array which gives a pixel scale of 0.31″/pixel and a 18.0″×19.2″ field of view. A log of the nights on which observations were carried out is shown in Table 5.2. Raw images were dark-subtracted using frames acquired approximately every hour, with a cold (77K) load in the camera's optical path. The linearity correction used for each run was determined by using the closed mirror cover as a hot-load, which was observed at K-band with integration times ranging from 1s to 25s. The form of the linearity corrections so derived were found to be all generally the same –

$$\text{Linear Counts} = (1 - a)x + bx^2 + cx^3 \tag{5.1}$$

where x = Raw Counts, $a \approx 0.02$, $b \approx 6 \times 10^{-6}$ and $c = 0.0$. The values of the coefficients a and b varied by about ±40% from the values given above over the three years in which the observations reported here were made. In Table 5.2 we show the coefficients used to linearity-correct each night's data. The data range over which the array was used was from 0 to 11000 counts (above which the array begins to saturate). At the array's maximum range the correction for linearity is only $\sim$ 6%. A single correction (derived from counts in a region of the array free of bad pixels) was applied to the entire array. The data were flat-fielded with dome flats, which for the runs prior to March 1992 produced images which peak-to-peak variations in the sky level of $\approx$ 10%, though the variations across the regions of the array actually used to photometer images were only $\approx$ 5%. From March 1992 on, we adopted the technique described in §5.3.3 (as used at the IRTF) for constructing dome flats free of thermal emission, which improved flattening to $\sim$ 5% peak-to-peak across the array. Object images were then pair-subtracted and bad pixels cleaned by linear interpolation to produce the final images used for photometry. These images typically had sky levels flat to better than 2%. Standards were usually observed with the chopping secondary set to 'smear' the star out over 1-2″ in order to avoid saturation.

Standards were photometered through large apertures (diameters ranging from 6.8″ to 11.2″) to include more than 99.5% of the star's total flux. Objects were photometered through smaller apertures (ranging from diameters of 3.1″ to 4.3″ depending on seeing conditions) and aperture corrections were derived (using bright objects observed over the course of each night) from these observed apertures out to apertures which include more than 99% of the stars' total flux ($\approx$ 7″ diameter). The size of the apertures used to photometer objects were chosen to be large enough that the aperture corrections from measured to total flux were always small (i.e., $\lesssim$ 0.05 magnitudes). In this way we ensure that variations in the seeing and telescope focus over the course of a night produce uncertainties in the photometry of less than $\pm$0.03 magnitudes.

5.3.2 - Las Campanas Observations.

Photometry using the Las Campanas Near-Infrared Camera was obtained on 6 nights over the period 18-30 August 1992(UT) The camera contains a 128×128 Rockwell HgCdTe (NICMOS2) detector array. The camera has three available zoom settings – for our runs the camera was used in the high resolution mode. This gives a pixel scale of 0.25″/pixel and a field of view of 32″×32″ on the 2.5m duPont telescope, and a pixel scale of 0.67″/pixel and a field of view of 35.8″×85.8″ on the 1m Swope telescope. A log of nights on which observations were carried out is shown in Table 5.2. Raw images were dark-subtracted using frames acquired approximately every hour with a cold (77K) load in the camera's optical path. A standard linearity correction for the camera was applied to all images. This correction had the form given by equation 5.1 with $a = 0$, $b = 2 \times 10^{-6}$ and $c = 0$. This function linearises the counts to within 0.3% over the useful range of the array (Persson *et al.* 1992). The data were flattened using 'sky flats' constructed from observations made of the evening or morning twilight sky. Twilight observations were only used to make flats if they were taken with short exposure times (i.e., $\leq$ 5s) so that the contribution of the thermal background to the observed counts was negligible. The resultant flattened images had peak-to-peak variations in the sky across the chip of $\lesssim$ 5%. Because the camera was often subject to improper array reads, three observations were made of each object (rather than the two usually made at Palomar and the IRTF), so that even if one image was useless, at least one image pair was available for sky subtraction. Because of a residual image problem with the array (residual images of bright objects were present in the next exposure at the level of $\sim$ 2% of the original image's counts), care was taken to move the program objects through a trio of exposure positions. This meant

that for each position on the chip at which an object was acquired, there was a sky frame available which does not have a residual image present at that location.

After pair-subtraction the images were photometered in the same way as is described above for our Palomar data. Standards on the duPont telescope were usually observed with the telescope defocussed in order to avoid saturation, so these images were photometered through large apertures (10″ to 11″ diameter). Objects were photometered through a 3″ diameter aperture, which requires aperture corrections from measured to total flux of $\approx 0.15 - 0.10$ magnitudes. The uncertainty introduced into the Las Campanas photometry by seeing and focus variations over the course of a night are therefore in the range $\pm 0.05 - 0.03$ magnitudes.

5.3.3 - IRTF Observations.

Observations were carried out with the ProtoCAM infrared camera on the 3.1m NASA IRTF on 24 December 1991(UT) and 20-23 June 1992(UT). ProtoCAM uses a 58×62 Santa Barbara Research InSb detector array, configured to have variable image scales from 0.135″/pixel to 0.35″/pixel. All our observations were carried out with the camera set to 0.35″/pixel which gives the camera a field of view of 20.3″×21.7″. A log of observations made with ProtoCAM is shown in Table 5.2. Two 'features' of observing with ProtoCAM should be noted. First, the observer can vary the gate voltage applied to the array – this has the effect of trading off an increase in the number of 'hot' pixels in the array, with the amount of residual image left by a bright star on the next image taken. For our runs we chose to try and minimise the number of bad pixels. The gate voltage was set such that 2% residual images were left by the previous exposure. Since the telescope is nodded between all exposures, these residual images are only a problem if they occur in the same location as an object image in subsequent exposures. If this happens the pair subtraction process will subtract the residual image from the object and produce an artificially faint magnitude. However, if the residual image problem is known about and some care is taken when observing and reducing the data (i.e., to not subtract residual images in sky frames from object images) it can be dealt with. The second point to note is that we found when reducing data from our December 1991 run, that even after flat fielding, the camera produces photometry with systematic offsets of up to $\sim$ 10% between different parts of the array. For our June 1992 run we therefore defined two 'standard regions' of the array (i.e., two $\approx 10 \times 10$ pixel regions free of bad pixels) in which all standards and objects were photometered, enabling us to eliminate the systematic offsets from our photometry.

However, we were unable to do this for the data from our December 1992 run, meaning that all that night's photometry has uncertainties $\sim \pm 10\%$. Objects observed on 24 December with 'interesting' colours (i.e., I-K $\gtrsim 3.0$ and therefore good VLM candidates) were re-observed on later runs to obtain better photometry.

Bias frames were measured at the start of each night's observing (with a 20ms exposure taken with a cold load inserted into the camera's light path) and subtracted from all observations made on that night. A single linearity correction (derived from counts in one of the June 1992 'standard' regions) was applied to the entire array. As a test a linearity correction was derived in the other 'standard' region for the June 1992 data – no difference in the derived linearity correction was found. The linearity correction was also derived for 'hot-load' data from four different nights (three in June 1992 and one in December 1992) – again no significant difference was found. The final linearity correction adopted was of the form shown in equation 5.1, with $a = 0.0$, $b = -2.6120 \times 10^{-6}$ and $c = 1.7891 \times 10^{-10}$. Flat fields were constructed for each night's data by observing a smooth section of the dome, first illuminated by the dome's interior lights, and then with the dome's lights off. By subtracting the two images the thermal background due to the dome and the telescope is removed. The resultant image was used to flatten the data. The K-band images were flattened to within a few percent. The only feature left was a known thermal leak in the ProtoCAM system, which was removed when the images were pair subtracted. Bad pixels were then cleaned by linear interpolation. Standards (which were observed in focus) were photometered through apertures of 6.8-9.1″ diameter. Objects where photometered through apertures of 3.1-4.2″ and aperture corrected to the same aperture as was used to measure the standards for that night. The aperture corrections measured ranged from 0.027 to 0.053 magnitudes and the uncertainty introduced into the photometry by seeing and focus variations over the course of a night are $\lesssim \pm 0.02$ magnitudes.

5.3.4 - Compiled Results.

The scatter about the zero-points determined for each night's data are shown in Table 5.2. Except for a few nights of poor seeing at Palomar, the scatter about the zero points are all < 0.03 magnitudes. Also shown are the extinction coefficients determined from standard star observations. In general the extinction at Palomar is higher than that at Las Campanas or Mauna Kea, though this trend is somewhat confused by the generally higher extinction levels at all observatories seen after the Pinatuba eruption in August 1991. The compiled results for all the objects observed on the 24 nights reported here

are shown in Table 5.3. The table is divided into sub-sections (a) through (q) each of which corresponds to one of the sub-samples discussed in §5.2. For each star the following information is shown; an object name which gives the field number the object was selected from and a unique object number assigned during the COSMOS scanning of the master plate for that field, other object names for that object if it lies in regions where two fields overlap, a position in equinox B1950.0, photographic i^P_{Pal} and $(r-i)^P_{Pal}$ photometry, CCD i^C_{Pal} and $(r-i)^C_{Pal}$ photometry (where available – see Paper I for a complete discussion of the CCD photometry), K-band magnitudes as measured at Las Campanas (K_{Cam}), Palomar (K_{Pal}) and the IRTF (K_{Irtf}), a mean K-band magnitude (K_{mean}), and an I–K colour (which is calculated using i^C_{Pal} where available). Several of the stars observed in the course of this programme seemed to show much larger photometric variations than would be expected from our estimated uncertainties. We have denoted all the objects which show some evidence for photometric variations in the column labelled "V" in Table 5.3. For each of the 'raw' magnitudes (K_{Cam},K_{Pal} and K_{Irtf}) a quality flag is given; 'A' implies the photometry is good to ±0.05 magnitudes, 'B' that the photometry is good to ±0.10 magnitudes, 'C' that the photometry is only good to ±0.25 magnitudes and ':' that object was barely detected and that the photometry is only good to ±0.5 magnitudes. The mean K-band photometry (K_{mean}) is the weighted mean of all the individual observations and it also has a quality flag (with the same meanings).

During the course of this observing programme numerous stars were observed which did not fall within our final sample criteria because they were observed from lists created before it was decided to trim all objects within vignetted regions of the photographic plates (see Paper I). While these objects may not fall within our survey, numerous VLM stars were so discovered. We have included the same information as is shown in Table 5.3 for all such objects with I–K > 3.0 in Table 5.4.

In Figure 5.1(a) and (b) we show the differences (as a function of magnitude) of all the objects observed in common between (a) Palomar and Las Campanas, and (b) Palomar and the IRTF. The mean differences between the observatories ($\langle \Delta K \rangle$), the scatter about these means and the number of stars repeated are; for 8.5 < K < 13.5, $\langle \Delta K \rangle_{Pal-Las} = 0.007 \pm 0.075\,(13)$; for 8.5 < K < 13.5, $\langle \Delta K \rangle_{Pal-IRTF} = -0.060 \pm 0.08\,(12)$; for 13.5 < K < 16.0, $\langle \Delta K \rangle_{Pal-Las} = 0.00 \pm 0.13\,(17)$; for 13.5 < K < 16.0, $\langle \Delta K \rangle_{Pal-IRTF} = -0.01 \pm 0.11\,(12)$. Except for the bright end of the Palomar – IRTF diagram (which is dominated by a few extremely discrepant stars which may be variable), all these are consistent with zero offset between the three data sets. The uncertainty in a *single* observation indicated by the

residuals about the $\langle \Delta K \rangle$ values shown above can be obtained by dividing those residuals by $\sqrt{2}$, implying the observed scatter for repeated objects ($\approx \pm 0.05$ for $8.5 < \mathrm{K} < 13.5$ and $\approx \pm 0.08$ for $13.5 < \mathrm{K} < 16.0$) are consistent with the uncertainties assigned by the quality flags in Table 5.3 and 5.4. (Most objects with $\mathrm{K} < 14.0$ are assigned quality 'A', while objects with $14.0 < \mathrm{K} < 15.5$ are assigned mostly flags 'A' or 'B').

We plot in Figure 5.2 $(r-i)^P_{Pal}$ as a function of I–K for all stars (i.e., photographic colours – small symbols), and for all stars ri^C_{Pal} photometry (i.e., CCD colours – large symbols). Also shown are $(\mathrm{R–I})_C$ vs I–K sequences due to Bessell (1991) and Leggett (1992). The most obvious feature is the scatter produced by the large photometric uncertainties in the photographic $(r-i)_{Pal}$/(I–K) data. The second point to note is that the mean I–K colour of the photographic points (for a given $(r-i)_{Pal}$ colour) is significantly bluer than the mean I–K colour of the CCD data at the same $(r-i)_{Pal}$ colour. This is because the photographically selected sample is subject to a serious Malmquist-type bias. Because the number of stars present on our photographic catalogues is a steeply increasing function of decreasing colour (i.e., there are more blue stars than red ones), photometric errors, at a given colour limit, will scatter more intrinsically blue stars into our sample, than they scatter out intrinsically red stars. The effect of this bias and procedures for estimating its importance are discussed in Paper I. However, the use of I–K colours to estimate luminosities for very red stars essentially eliminates this bias from our infrared LF.

It is obvious then, that CCD photometry alone should be used to define the $(r-i)_{Pal}$/(I–K) relation – this has been done to produce the least squares fit (solid line) shown. Because of the paucity of blue stars with both K and $(r-i)^C_{Pal}$, the Bessell and Leggett sequences were used to constrain the solid line fit to the data for $(r-i)_{Pal} < 1.8$. (In the colour range $1.0 < (r-i)_{Pal} < 1.8$ the $(r-i)_{Pal}$ and $(\mathrm{R–I})_C$ systems are essentially identical (Paper I).) A further point to note is the flattening of this curve for red ($(r-i)_{Pal} \gtrsim 2.5$) stars. This bears out a point which has been made in the literature before (Leggett & Hawkins 1988) – namely that for very late stars R–I colours saturate, and provide little or no information on the star's properties. We have been able to find no dwarf stars with $(r-i)_{Pal} > 2.6$.

Section 5.4 - The Luminosity and Mass Functions.

5.4.1 - The Luminosity Function.

We estimate luminosity functions (LFs) using a generalised form of the $1/V_{max}$ technique which allows for the presence of density gradients in the Galactic disk - see Paper I for a complete discussion of the derivation of the '$1/V_a$' LF. An essential parameter to evaluate for each star in the LF sample, is the maximum distance (d_{max}) at which (given the survey limits and sample selection criteria) it could be detected. A relation is required which predicts the absolute i^P_{Pal} and r^P_{Pal} magnitudes of each star for which I–K colours have been measured, so that this maximum distance can be estimated. We use the improved colour-magnitude relations of Paper III to estimate M_I for each star in our sample. To estimate $(r-i)^P_{Pal}$ colours for each star we use the fit shown in Figure 5.2. Combining this fit with the colour term measured in Paper I between $r^P_{Pal} - i^P_{Pal}$ and $(r-i)^P_{Pal}$, the estimated M_I, and the appropriate sample and plate limits, it is a straightforward matter to estimate d_{max}. The maximum generalised volume available to each star (V_a) is then estimated as follows (Paper I),

$$V_a = \Omega \frac{h^3}{\sin^3 b}\{2 - (\xi^2 + 2\xi + 2)e^{-\xi}\}, \tag{5.2}$$

where $\xi = d_{max} \sin b/h$, h is an assumed disk scale height, b if the galactic latitude of the observation, and Ω is the solid angle covered by the observation. A 350pc scale height for the disk is assumed throughout (Scalo 1986). The sum of the inverses of these V_a values in a given luminosity bin is then an unbiased estimator of the LF, which we denote Φ_0. (We use the subscript "0" throughout to denote quantities derived from this $1/V_a$ formulation.)

A LF was constructed for *each* of the sub-samples shown in Table 5.1. Scatter in the $(r-i)^P_{Pal}$ photometry used to select these stars introduces incompleteness in the bins at the bright end of these LFs. The typical uncertainty for an $(r-i)^P_{Pal}$ measurement is ± 0.35 magnitudes (Paper I). Using the M_{Bol}:$(r-i)_{Pal}$ relation presented in Paper I, it is possible to evaluate the uncertainty in M_{Bol} that this uncertainty in $(r-i)^P_{Pal}$ corresponds to at the centre of each LF bin. Bins in which our $(r-i)^P_{Pal}$ selected sample is less than 75% complete are then ignored. For the very red colours of our sample cut-offs ($(r-i)^P_{Pal} \gtrsim 2.0$), the optical uncertainty translates into an M_{Bol} uncertainty of $\sim \pm 1.6$ - this results in most samples being $> 75\%$ complete for $M_{Bol} \gtrsim 12.5$. The bins which are more than 75% complete are scaled by their incompleteness factor, and these independent LFs are then averaged together to produce a final LF. Because the different sub-samples

sample different volumes, this final LF was calculated as a weighted mean, where bins were weighted by the volume sampled by a star with M_{Bol} equal to the luminosity of each bin centre.

We show the resulting LFs (for two binnings of the data) in Table 5.5 and Figure 5.3 (triangles and squares). Also shown in Table 5.4 are the volumes sampled by each bin, the number of objects detected in each bin and the mean correction for incompleteness applied to each bin. The uncertainties shown for each bin are Poisson counting errors. We also show in Figure 5.3 (circles and crosses), the LF derived in Paper I for more luminous stars from our $(r-i)^P_{Pal}$ catalogue data alone (again in two binnings of the data). The most obvious feature of Figure 5.3 is the excellent agreement between the space densities predicted by the photographic and infrared studies in the region where they overlap. The last two points plotted for the infrared data are bins in which no stars were found – the uncertainties plotted represent $1/V_a$ for a star at each bin centre. It should be noted, however, that these V_a estimates rely on extrapolations of the colour-magnitude relations to luminosities where they may not apply – the colour-magnitude relations used are constrained by observations only to $M_{Bol} \approx 14$. The major source of possible systematic error in the infrared LF data is the uncertainty in the estimation of the sampled volumes. The distance moduli used to determine these are good to ± 0.05 magnitudes, producing systematic uncertainties of $\approx \pm 15\%$ in the final Φ_0 values, which are similar to or smaller than the Poisson errors for most of the infrared data.

The effects of Malmquist-type biases on our photographic data are discussed in detail in Paper I. In short, it was found that a first-order correction for Malmquist-type biases led to the photographic LF becoming more 'peaked' at the apparent maximum in the LF at $M_{Bol} \approx 10$ and steepened the fall-off of the LF between $M_{Bol} \approx 10 - 12$. Malmquist-type biases should have little effect on the section of Figures 5.3 & 5.4 which are based on infrared data, for although the sample on which it was based was selected using photographic data, the subsequent infrared observations are very effective at 'weeding out' all the blue stars falsely scattered into our sample – whereas the M_{Bol} estimates based on optical colour for $M_{Bol} > 12.5$ are uncertain by up to ± 1 magnitudes, the M_{Bol} estimates based on the infrared data are good to better than ± 0.25 magnitudes (Paper III).

We compare our determination of the LF with those of several previous investigators in Figure 5.4. Figure 5.4(a) shows the same LF as Figure 5.3, with the results due to Henry & M$^{\rm c}$Carthy (1992 - hereafter HM92) and Weilen, Jahreiss & Kruger (1983 - hereafter WJK) superimposed. Both these LFs are based on volume limited subsets of the

Nearby Star Sample (Gliese 1969, Gliese & Jahreiss 1979). These are all stars near the sun with measured trigonometric parallaxes. As such they make a well defined, volume-limited sample, although the sample is small and because it is kinematically selected it suffers from questions of incompleteness. The WJK points are from a 10pc limited sample of nearby stars. They have been converted from a M_V LF to a M_{Bol} LF by Reid (1987) and it is these points which we plot. The HM92 sample consists of all stars known within 5.2pc of the sun classified as spectral type 'M' and north of $-30°$. HM92 have studied all of these stars using infrared speckle techniques, and in doing so discovered two previously unknown companions. They present absolute M_K for all the stars in their sample. We have used their M_K data (cf. their Tables 1 and 2) to estimate bolometric corrections (see Figure 5.6) and so construct from their data the M_{Bol} LF shown in Figure 5.4. Figure 5.4(b) summarise previous LF determinations based on photographic photometric surveys. In particular, we show the LF of Reid (1987) and Hawkins & Bessell (1988). Reid's LF was constructed from the WJK data for $M_{Bol} < 10$ and from an average of several 48″-Schmidt photographic studies for fainter stars. Hawkins & Bessell's LF was constructed from 48″-Schmidt data and some infrared photometry of the stars so discovered in 3 UKSRC fields. Leggett & Hawkins (1988) have also estimated LFs using photographic and IR data from 2 UKSRC fields, however as they do not present any of their results in bolometric magnitudes, comparison with their data is not straightforward. In terms of M_R however, their results are similar to those of Hawkins & Bessell. Without doubt, the most striking feature of Figure 5.5 is the agreement on the form of the LF seen from such disparate sources.

There has been considerable debate in recent years over the exact form of the LF below $M_{Bol} \sim 10$. LFs derived from the Nearby Star Sample (WJK, Dahn *et al.* 1986) showed little evidence for the pronounced minima seen in the photometric LFs constructed up till that date (Gilmore & Reid 1983, Gilmore *et al.* 1985, Hawkins 1985). Larger and deeper photometric surveys carried out since then, some incorporating infrared photometry (Hawkins & Bessell 1988, Leggett & Hawkins 1988), have only served to make the minimum seen in the photometric surveys more pronounced. On the other hand, HM92 claimed that their survey of nearby M-dwarfs produced a LF which showed no evidence for an decrease in the number density of stars fainter than $M_{Bol} \sim 10$ (or $M_K \sim 7.5$ in their LF). In fact, HM92 claimed that their LF increased all the way to $M_K \sim 10$ where it showed a pronounced dip, which they suggested may correspond to the end of the H-burning main sequence. The new LF data shown in Figure 5.4 goes some way towards resolving some of these difficulties. In particular we find strong evidence for the number density of stars being

significantly higher at $M_{Bol} \sim 10$ than at $M_{Bol} \sim 12.5$ – the minimum is *real*. Further, the effect of correcting Malmquist bias in the photographic data only makes this peak more pronounced (Stobie *et al.* 1989, Paper I). We also find that when the LF of HM92 is converted into M_{Bol} that there is almost no evidence for significant disagreement between their LF, and that derived by us. In fact it is somewhat comforting that LFs derived using such different techniques are all found to be so similar! We believe the "increasing" LF seen by HM92 to be due to their plotting their LF as M_K – there is certainly no evidence for it in a M_{Bol} LF.

A further 'bone of contention' for studies of the LF has been its form just above the H-burning limit. Early photometric studies (Reid & Gilmore 1982, Hawkins 1985) allowed the possibility that the LF went through a minimum at $M_{Bol} \sim 12.5$ and then began to steeply increase (see for example the LF of Reid in Figure 5.4(b)) – a possibility leaped upon by those in the business of searching for brown dwarfs. However, as we have discussed in Paper I, this 'increase' in the LF for very faint stars is almost certainly spurious. For these very faint stars the volumes sampled are small and the number of stars detected is small. These combine to make the end of the LF *very* sensitive to contamination by spurious, non-stellar images on the photographic plates on which these studies have been based. We found that our photographic LF produced similar upturns to those seen by earlier studies, however our examination of the levels of contamination showed that these upturns were very likely spurious. Our infrared observations bore this out, by finding far fewer ($\sim 5\%$) stars fainter than $M_{Bol} \sim 13.5$ than our photographic LFs had indicated we would. We believe this to be the strongest evidence yet presented to discount the possibility of a strongly increasing LF just above the bottom of the main sequence. Moreover, the small number of stars detected in the faintest of the bins shown in Figure 5.4 (both for the HM data and for the LFs derived by us) makes it almost impossible to make any statements about cut-offs in the LF associated with the bottom of the H-burning main sequence, which using the currently available models is predicted to occur between $M_{Bol} \sim 13 - 14.5$ (Burrows *et al.* 1989).

It should be noted at this point that the LF measured is a *system* LF. The photographic plates used to construct the LF above $M_{Bol} \approx 12.5$ are unable to resolve objects with separations less than $\approx 2.5''$. The situation is slightly better for objects observed in the IR, where objects can be resolved down to separations of $\approx 1''$. At 50pc these correspond to separations of 125au and 50au respectively, which results in a significant fraction of close binaries being merged in our sample. This has been proposed (HM92,

Dahn *et al.* 1986) as having the effect of making the LF determined in a study such as ours systematically underestimate the LF at faint magnitudes. Unfortunately correction of the *system* LF for the effects of merged binaries to derive the *stellar* LF requires knowledge of the distribution of binary masses and separations – quantities poorly determined for more massive stars, and unknown for the objects of most interest to this study. Reid (1991), however, has examined this question by using the available data to make several models of possible binary mass distributions, and then simulating the observation of several input LF using the techniques of both photometric (i.e., based on 48″-Schmidt data) and Nearby Star observations. In particular, when Reid assumes the flat LF produced by the Nearby Star sample and models its observation by a photometric survey at larger distances, he is unable to reproduce the sharply peaked LF seen in photometric studies such as this one. In fact, he finds that for reasonable assumptions about the binary mass distribution, photometric studies only underestimate the LF by 25-30%, and that only for $M_V > 16$, or $M_{Bol} > 12$. In any case, we find that when the Nearby Star sample is examined as a bolometric LF, no significant evidence for a difference between it and the photometric LF is seen.

5.4.4 - The Mass Function.

Conversion of the measured LF into a mass function (MF) requires we adopt a mass-luminosity relation. It should be kept in mind that *any* mass-luminosity relation makes the assumption that the objects we are studying lie on a main-sequence. Stars which do not lie on the main sequence will have their masses incorrectly estimated. For example, stars which are still descending the Hayashi track onto the main sequence are more luminous for a given mass than stars on the main sequence – it is necessary to know the age of these objects if we are to estimate a mass. A similar situation arises for very low mass stars, as objects with $m \lesssim 0.1 M_\odot$ (but above the H-burning minimum mass) will evolve to fainter luminosities – about 1 magnitude in M_{Bol} over the period 10^9 to 10^{10} years. Objects below the H-burning minimum mass will have luminosities which evolve faster and by larger amounts. This means that considerable care must be taken in interpreting the MF derived for these stars. In particular, it must be born in mind that a single mass-luminosity relation only applies to stars of a given age, and that our lack of knowledge about the characteristic age and age spread of the stars in our sample with $m < 0.1 M_\odot$ introduces a corresponding uncertainty in the MF. Questions of age for stars with $m > 0.1 M_\odot$ are, however, irrelevant, as stars this massive quickly ($\lesssim 10^8$ yr – Burrows *et al.* 1989) reach a stable, main sequence luminosity.

We summarise in Figure 5.5 most of the current data on mass-luminosity relations – both observational and theoretical. In particular we have shown the relations predicted by the theoretical models of D'Antona & Mazzitelli (1985 - hereafter D&M) and Burrows, Hubbard & Lunine (1989 - hereafter BHL), for objects of age 10^9 and 10^{10} years. Both D&M and BHL make use of the same opacity tables in their models (Alexander *et al.* 1983). The equations-of-state adopted are also similar, though BHL claim to carry out a more detailed treatment of hydrogen in its liquid metallic state. BHL also examined the effect of varying the convective mixing length parameter in their models. We show in Figure 5.5 their models B and D, which are calculated for convective mixing length parameters $\alpha = 1$ and $\alpha = 0.1$ respectively. Both the BHL and D&M models predict similar minimum masses for stable H-burning ($\approx 0.08 M_\odot$), and as can be seen in Figure 5.5 both predict similar behaviour for stars and sub-stellar objects, though the D'Antona & Mazzitelli models would appear to predict systematically lower luminosities for a given mass star, and predict a 'shallower' luminosity transition from main sequences stars to brown dwarfs.

Also shown in Figure 5.5 are empirical derivations of the mass-luminosity relation. These use masses determined from astrometric or spectroscopic binaries, and luminosities determined by trigonometric parallaxes. The solid line shows a relation due to Smith (1983) which is itself a fit to data of Popper (1980) which is valid for $m > 0.2 M_\odot$. The dot-dashed line is a relation due to HM92, who fit a power law to M_K and m data for stars between $0.1 M_\odot$ and $0.2 M_\odot$, which has been converted to a relation giving mass in terms of M_{Bol}. Using the bolometric correction and absolute magnitude data presented in Paper II, we derive the BC_K:M_K relation of Figure 5.6. This fit predicts M_{Bol} to be systematically 0.1-0.2 magnitudes fainter than the relation adopted by HM92 – this is because the bolometric corrections of Paper II properly take into account the effects of H_2O absorption in the infrared spectra of these stars. It is clear that the empirical power law fits shown in Figure 5.5 are unable to describe the mass-luminosity relation for $m <. 0.1 M_\odot$, where theory predicts the relationship should steepen dramatically. The empirical relations above $0.1 M_\odot$ agree very well with each other, and agree substantially with the form of the theoretical models, though the D&M models do appear to be slightly underluminous. BHL's model D can also be seen to be significantly less luminous than the available data would suggest for main sequence stars. The disagreement between the D&M and BHL model D predictions and the observations would suggest that the BHL model B be adopted as a 'canonical' mass-luminosity relation.

We define the present day mass function (PDMF) as the number density of stars in a bin of width dm centred at mass m. We derive the PDMF from the observed local LF Φ_0, and denote it as Ψ_0. That is,

$$\Psi_0(m)\,dm = \Phi_0(\mathrm{M}_{Bol})\,d\mathrm{M}_{Bol}, \tag{5.3}$$

which is evaluated using the slope of the mass-luminosity relation, $d\mathrm{M}_{Bol}/dm$,

$$\Psi_0(m) = \Phi_0(\mathrm{M}_{Bol})\,\frac{d\mathrm{M}_{Bol}}{dm}. \tag{5.4}$$

It should be noted that stars with masses $0.1\mathrm{M}_\odot < m < 0.5\mathrm{M}_\odot$ have main sequence lifetimes considerably longer than the age of the disk. The PDMF for these stars is therefore identical (to within a normalisation constant) to the initial mass function (or IMF). Below $0.1\mathrm{M}_\odot$, estimation of the IMF requires knowledge of the age of the observed stars and the star formation history of the disk. We evaluate $d\mathrm{M}_{Bol}/dm$ values for the mass-luminosity relations shown in Figure 5.5 by fitting smoothing splines (de Boor 1978) to the data points shown. For the BHL models (which only extend to $0.2\mathrm{M}_\odot$) the relations have been evaluated for higher mass using the empirical fit of Smith (1983). We plot in Figure 5.7 the PDMFs derived for each of these mass-luminosity relations, along with the adopted mass-luminosity relations. The uncertainties shown are the Poisson counting errors from the LF transformed into the MF. As with the LF, possible systematic uncertainties due to the mis-estimation of sampled volumes are present at the 10-20% level above $0.1\mathrm{M}_\odot$ where the mass-luminosity relation is fairly well constrained. Below $0.1\mathrm{M}_\odot$ the uncertainty in the 'correctness' of the theory dominates.

Also shown in Figure 5.7 is the MF of Reid (1987 - dot-dashed line) and two frequently quoted 'canonical' MFs; the Scalo MF (Scalo 1986 - dotted line) and the Salpeter IMF (Salpeter 1955 - dashed line), the latter being arbitrarily normalised to the value of the Scalo MF at $0.5\mathrm{M}_\odot$.[4] There is excellent agreement between our data and the MF of Reid. The Scalo function seems to over-predict the number of stars in the solar neighbourhood in this mass range by about a factor of two, though this difference is not significantly outside the uncertainties estimated by Scalo. The Salpeter power-law clearly looks nothing like the data in this region.

[4] Note that the Scalo function has been converted from a surface density in terms of $\log(m)$ (Scalo's $\phi_{\mathrm{ms}}(\log(m))$ to a volume density in terms of m (our $\Psi_0(m)$) using the assumed scale heights and masses of Scalo (1986, Table 4).

The most obvious feature of these plots is the pronounced turn-over of the MF at $\sim 0.25M_{\odot}$, which then seems to be followed by an upturn in the MF for $0.08M_{\odot} < m < 0.1M_{\odot}$. Suggestive evidence for a local maximum in the MF at $m \approx 0.2M_{\odot}$ can be seen in Scalo's determination. This is directly the result of his assuming a turn-over in the LF at $M_V \approx 12.5$ (as was suggested by the LF data at the time) and a power-law mass-luminosity relation. D'Antona & Mazzitelli (1986) argued that if a more realistic mass-luminosity relation (i.e., one which steepened towards lower masses) were adopted, the local maximum in the LF would not correspond to a local maximum in the MF, and that a continuously increasing MF would result. However, they used only the WJK data, which as was discussed above, extends only $M_{Bol} \sim 12$ (at which magnitude its statistics are poor) and which shows little evidence for a decreasing LF toward fainter stars. It is therefore not surprising that this LF transforms into an increasing MF. Reid (1987) used the D&M models to transform a LF constructed from photometric survey data which extended to fainter magnitudes ($M_{Bol} \sim 13$) and which did show a decreasing LF for faint stars. He found a MF with much the same features as those seen in Figure 5.4, though with poorer statistics. It was also unclear at the time the Reid LF was constructed, whether a systematic effect was making deep photometric surveys see less very faint stars than studies based on the Nearby Stars (§5.4.3).

Our new mass function resolves some of these difficulties. Since the decreasing LF seen in Figure 5.6 is almost certainly real, we have some confidence in constructing a MF in this region. And as we have used the available theoretical mass-luminosity relations (rather than the empirical power-law relations) to construct MFs, we are able to make the best possible estimate of the effect of the relations' steepening as the H-burning limit is approached. We find that a turn-over in the MF at $m \approx 0.25M_{\odot}$is seen no matter what mass-luminosity relation is assumed – it is seen in all the panels of Figure 5.7. That it is not an artifact of 'kinks' in the mass-luminosity relations is convincingly demonstrated by the fact that it reproduced even when the power-law relation of Smith (1983) is assumed (see Figure 5.7(g)). There is some systematic bias present in our photographic data due to Malmquist-type effects (§5.4.3), however the effect of this bias is to 'smear out' the observed LF – correcting for it would serve to make the MF more peaked, not less.

The form of the IMF below $0.1M_{\odot}$ is (as was mentioned above) more problematic. The luminosities of these stars evolve by as much as a magnitude over the age of the disk, making it a less precise exercise to assign masses without knowledge of the age of each object. Furthermore, the mass-luminosity relations in this region (which are completely

unconstrained by observational data) are extremely steep, meaning that small uncertainties in the theoretical data map into large uncertainties in the MF. While it is true the models of D&M and BHL both predict largely the same behaviour, it is also true that they are based on largely the same physical assumptions and identical opacity tables. The MFs presented in Figure 5.7 should therefore be approached with caution below $0.1M_{\odot}$.

Having said this we can examine the MFs produced when we assume *all* the stars observed are at ages of either 10^{10} or 10^{9} years, and so 'bracket' the most extreme cases. There appears, then, to be evidence to suggest that the MF turns up again between $0.08M_{\odot}$ and $0.1M_{\odot}$ in either case – the extent of that upturn being dependent of the model used to interpret the data. Reid (1987) found suggestive evidence for a similar upturn in the MF, though his data set included only a few stars in his final MF bins, making definitive statements about an upturn difficult – our data set now has much better statistics in this region, though the question of confidence in the models remains. 10^{10} year models place all the observed objects into masses above $0.08M_{\odot}$, as objects smaller than $0.08M_{\odot}$ cool into undetectable obscurity. 10^{9} year models spread the observed objects out toward lower masses, and place the faintest of our luminosity bins at, or below, the H-burning main sequence. As would be expected, then, the 10^{10} year models predict steeper up-turns between 0.08 and $0.1M_{\odot}$. Similarly, because the D&M models predict a less steep transition in luminosity between brown dwarfs and stars, the upturn they produce is less pronounced. It is clear that observational checks on the theoretical models in this region are desperately needed – VLM binaries need to be found and studied to determine masses and luminosities if much further progress is to be made in interpreting future survey data.

Studies of the IMF for more massive stars (Scalo 1986, Miller & Scalo 1979, Salpeter 1955) have shown the IMF to be an essentially featureless smoothly increasing function of decreasing mass. As such it is extremely attractive, and has become very common, to parameterise the IMF as a single power law. Salpeter (1955) first estimated the IMF as a power law of the form,

$$\Psi \propto m^{-k}, \text{ where } k=2.35 \tag{5.5}$$

over the mass range $0.4M_{\odot} < m < 10M_{\odot}$. Subsequent investigations (for references see Miller & Scalo (1979), Scalo (1986)), however showed that a single power law would not fit the IMF for all stars. More massive stars require a steeper power law, and less massive stars a shallower one. Miller & Scalo estimated that the Salpeter IMF was only appropriate for $2M_{\odot} < m < 10M_{\odot}$. Figure 5.7 clearly reinforces the idea that a power-law parameterisation

of the IMF represents a gross over-simplification of the observed IMF – it is *certainly* unable to describe the structure we see in the IMF at the bottom of the main sequence.

5.4.3 - The Mass Density of the Solar Neighbourhood.

From the mass function Ψ_0 we derive the differential mass density Υ_0,

$$\Upsilon_0\, dm = m\Psi_0\, dm. \tag{5.5}$$

We plot Υ_0 for the BHL model B and DM mass functions of Figure 5.7, in Figure 5.8. It is then a straightforward matter to integrate this function and determine the mass density (ρ_0) in the solar neighbourhood contributed by low mass stars. We show the results of these calculations in Table 5.6 for the BHL model B and D&M models of 10^{10} and 10^9 years. The results of integrating Υ_0 from $0.4M_\odot$ down to the lowest mass possible in each case is also shown. It can be seen that the estimates of the integrated mass density contributed by the observed stars are identical for both the 10^{10} and 10^9 year models – clearly luminosity evolution over such a small range of masses (0.08-$0.1M_\odot$) is not enough to make a difference to the total integrated mass density. The D&M models predict a smaller mass in stars over the range integrated because (as mentioned above) they systematically predict smaller masses for a given luminosity star. However, the BHL & D&M models still produce integrated mass densities different by only $\sim 10\%$; $\rho_0(m < 0.4) = 0.018M_\odot pc^{-3}$ and $0.016M_\odot pc^{-3}$ respectively. Converting these into surface densities (Σ_0) they correspond to $\Sigma_0(m < 0.4) = 12.6M_\odot pc^{-2}$ and $11.2\,M_\odot^{-1}pc^{-2}$. ($\Sigma_0$ which can be obtained by integrating through the disk for an assumed exponential density distribution, in which case $\Sigma_0 = 2h\,\rho_0$.) These ρ_0 and Σ_0 estimates are dominated by systematic uncertainties in the MF, rather than poor statistics, and are estimated to be good to $\pm 30\%$.

Integrating the Scalo PDMF for $m > 0.4M_\odot$, we find that main sequence stars contribute a further mass surface density of

$$\Sigma_0(m > 0.4) = 16.1^{+11.7}_{-6.7}\, M_\odot pc^{-2},$$

or for the 325pc scale height assumed by Scalo, a mass density of

$$\rho_0(m > 0.4) = 0.025^{+0.018}_{-0.010}\, M_\odot pc^{-3}.$$

(Uncertainties were obtained by integrating the Scalo MF using the tabulated uncertainties for each bin). This produces a total mass density in the solar neighbourhood due to main sequence stars of

$$\rho_0(ms) = 0.042 \pm 0.015\,\mathrm{M}_\odot\mathrm{pc}^{-3}$$

– the dominant source of uncertainty being the Scalo MF. The mass density contributed by white dwarfs has been estimated from the observed number density and an observed mean mass of $0.6\mathrm{M}_\odot$, to give a mass density of $0.002\text{-}0.003\,\mathrm{M}_\odot\mathrm{pc}^{-3}$ (Liebert *et al.* 1988 and references therein). Giants are estimated to add an additional $0.001\,\mathrm{M}_\odot\mathrm{pc}^{-3}$ (Weilen 1974). The only other significant observed source of mass density is the material tied up in the inter-stellar medium (ISM). Estimates for the mass density contributed by the ISM (Bahcall 1984c and references therein, Hill *et al.* 1979) are $\approx 0.04 - 0.045\,\mathrm{M}_\odot\mathrm{pc}^{-3}$.

Adding the observed components together we find the observed mass density in the solar neighbourhood (including main sequence stars down to $0.08\mathrm{M}_\odot$) to be

$$\rho_0(obs) = 0.09 \pm 0.02\,\mathrm{M}_\odot\mathrm{pc}^{-3}.$$

Comparison with the solar neighbourhood mass density predicted by dynamical studies is, unfortunately, not straightforward. On one hand the work of Bahcall and collaborators (who have examined the form of the Galactic mass distribution using F-dwarfs and K-giants as mass tracers – Bahcall *et al.* 1992, Bahcall 1984a,b,c) has consistently produced estimates for the local mass density significantly larger than the observed mass density. In their most recent work they estimate the dynamically inferred mass density to be $\rho_0(dyn) = 0.26^{+0.20}_{-0.12}\,\mathrm{M}_\odot\mathrm{pc}^{-3}$ (the quoted uncertainties are their $\pm 1\sigma$ limits), which corresponds to a surface density of $\Sigma(dyn) = 84^{+29}_{-24}\,\mathrm{M}_\odot\mathrm{pc}^{-2}$. Even for the lower limit of this dynamical mass, there would seem to be a significant amount of matter (equal in mass density to that of main sequence stars, or the ISM) which remains unaccounted for. Their best-fit estimate would require about 1.5 times the observed mass density to exist in some hidden form.

On the other hand, analyses by other authors have shown a different picture. Kuijken & Gilmore (1991, 1989a,b) have concluded from analyses of high-altitude K-dwarf survey data that the surface density lies in the range $\Sigma_0(dyn) = 39 - 57\,\mathrm{M}_\odot\mathrm{pc}^{-2}$ (again their $\pm 1\sigma$ limits), which compares with their estimate of a surface density of $\Sigma_0(obs) = 48\,\mathrm{M}_\odot\mathrm{pc}^{-2}$ for a disk without any missing matter – i.e., no missing mass is required in their models. Bienaymé, Robin & Crézé (1987) have analysed general star count data, and

conclude that the mass density in the plane of the disk is $\rho_0(obs) = 0.09 - 0.012\,M_\odot pc^{-3}$, which again implies no missing mass and is clearly in conflict with the results of Bahcall. It is, therefore, unclear whether the dynamical data are consistent with no unobserved mass, or a great deal of unobserved mass.

If there *is* mass unobserved in the solar neighbourhood, brown dwarfs are a likely form for it to take. While our survey does not extend the MF determination into the brown dwarf region, it does provide the best available data on the form of the MF just above the H-burning minimum mass. It seems reasonable to ask what mass densities are predicted in the solar neighbourhood if we extrapolate the observed MF to sub-stellar masses. However, an important 'philosophical' difficulty arises. Mass functions have traditionally been parameterised as power-laws, both because a power-law is a simple parameterisation, and because power-laws agreed reasonably well with the available data. Moreover, theories of star formation based on hierarchical fragmentation (Hoyle 1953) have naturally produced such mass functions. Extensions of the MF into the sub-stellar regime have traditionally been made by assuming a power-law MF (normalised to the observed data at some mass $>> 0.08M_\odot$), and some minimum fragmentation mass. The Salpeter IMF is commonly used for such calculations, as well as for a variety of other 'dark matter' predictions (D'Antona & Mazzitelli 1985, Staller & de Jong 1981, Nelson *et al.* 1986). However, it has become clear that a single power law is an oversimplified representation of the IMF. Because it ignores the observed turnover and flattening of the MF between $0.1M_\odot < m < 0.25M_\odot$, such a parameterisation over-predicts the mass density of the disk due to low mass stars ($m < 0.4M_\odot$) by a factor of about 3. Given that a power-law parameterisation of the MF is completely inappropriate for at least one mass range ($0.1M_\odot < m < 0.25M_\odot$), is it reasonable to assume it is appropriate in another range (i.e., $m < 0.08M_\odot$) in the absence of any data? The $0.25M_\odot$ turnover in the MF is a feature which must be produced by processes linked with star formation. However it is a feature not explained by hierarchical fragmentation models. It seems questionable, therefore, to use such a model of low mass star formation as a justification for a power law extension of the MF.

Despite this, there is some evidence in our data to indicate an increasing MF towards the H-burning minimum mass. In order to make estimates of the possible mass density 'hidden' below $0.08M_\odot$, we have to assume some parameterisation for the MF. We therefore adopt power laws of various indices, normalised to the observed mass density at $0.1M_\odot$ – *however* we emphasise that these indices are adopted purely for the purposes of estimation. There is no reason at all to assume the MF below $0.08M_\odot$ is well represented by

a power-law. The following discussion should also be tempered by recalling that the extent of the increase in the MF seen between $0.1M_{\odot} < m < 0.25M_{\odot}$ is almost wholly determined by the theoretical models. Our data indicate the LF is relatively flat in this region, with the MF increase being produced by the steeply decreasing mass-luminosity relations. Table 5.7 summarises the mass densities obtained by integrating power laws of the type given by equation 5.5 with indexes of k=0.0,1.0,2.0 and 3.0, all normalised to a value of $0.45M_{\odot}^{-1}pc^{-3}$ at $0.1M_{\odot}$. The integrated mass densities are estimated for the ranges $0.08M_{\odot}$ to $0.04M_{\odot}$, $0.02M_{\odot}$, $0.01M_{\odot}$, $0.005M_{\odot}$ and $0.001M_{\odot}$. Table 5.7 clearly shows that for a significant amount of mass ($0.05 - 0.1\,M_{\odot}pc^{-3}$) to be hidden in brown dwarfs, either an extremely steep MF (i.e., $k > 3$ which is much steeper than that seen for main sequence stars) or a mass function extending to extremely small masses is required ($\lesssim 0.001M_{\odot}$, which is much lower than that predicted by cloud fragmentation models to explain (Boss 1986)). The total absence of brown dwarf detections as a population (as opposed to the one or two current good brown dwarf candidates detected as binary companions to brighter stars) makes it impossible to place any limits on either of these possibilities.

Brown dwarfs cool so rapidly that observing them in the field (where their mean absolute magnitudes will be $M_{Bol} \gtrsim 15$) is extremely difficult. An obvious place to study a population of brown dwarfs, then, is in a young cluster. Several recent studies have attempted to do just that - most notably Stauffer *et al.* (1989), Jameson & Skillen (1989), Hambly & Jameson (1991) and Simons & Becklin (1992). All of these studies were carried out in the Pleiades. Stauffer *et al.* and Jameson & Skillen carried out CCD surveys at VI and RI (respectively) of areas on the order of a few hundred arcmins^2, while Hambly & Jameson used UKST RI plates over the entire Pleiades and Simons & Becklin have carried out a 200 arcmin^2 survey at IK. All these studies have identified Pleiades candidate members by selecting objects along a theoretical isochrone in their respective colour-magnitude diagrams. Unfortunately there are several serious problems with such a procedure. First, these studies are forced to rely on the various theoretical models discussed above which are completely unconstrained by any firm observational data. Second, as the theoretical models predict results in terms of the physical quantities T_{eff} and L, it is necessary to convert these into observables, i.e., into the respective colour magnitude diagrams. However, these conversions are not as well determined as one would like. In particular, the inability of current atmospheric models to match the observed spectra of these very late stars implies the T_{eff} scale is subject to systematic uncertainties of $\sim$ 300K (Paper II). Third, optical colours are extremely poor estimators of the properties of VLM stars and

brown dwarfs, and of the studies mentioned above only Stauffer *et al.* and Simons & Becklin have obtained infrared photometry for their Pleiades candidates. Lastly, none of the above candidate cluster members from these studies have had parallaxes or high-quality proper motions determined, making their actual cluster membership uncertain. Of these studies, the most significant results are those of Simons & Becklin who use an I:I–K colour magnitude diagram to estimate that they have detected 22 ± 10 objects in the range $0.1 - 0.04 M_{\odot}$, from which then estimate a slope for the mass function Ψ of $k = 2.8 \pm 0.5$. Such a slope in this region is not inconsistent with our MF, however it should be emphasised that their slope is based on only a few stars, is heavily model dependent, and relies on objects selected using isochrones subject to large (~ 0.6 magnitudes in I–K) systematic uncertainties. Until a significant number of the Simons & Becklin Pleiades candidates can be astrometrically identified as cluster members, and the current disparity between the theoretical and observed temperature scales can be solved, the jury must still be considered to be out on the issue of the Pleiades MF.

Section 5.5 - Conclusion.

We have presented new infrared data for a complete sample of photographically identified VLM candidates. Using the I–K colours measured for these stars and improved colour-magnitude relations and bolometric corrections we estimate the space densities of stars in the range $M_{Bol} = 12.5 - 14$. As our survey samples almost an order-of-magnitude larger volume in this luminosity range than previous work, and our M_{Bol} estimates are based on optical-infrared photometry, we believe our survey represent the best measurement of the luminosity function at the bottom of the main sequence to date. The luminosity function so constructed has been combined with the photographic luminosity function of Paper I. Our luminosity function clearly shows that the number density of stars reaches a peak at $M_{Bol} \approx 10$ and then fall away towards fainter magnitudes, contrary to the claims of HM92 and Dahn *et al.* 1986 that the luminosity function is flat, or increasing, below $M_{Bol} \approx 10$. The effects of binaries missed by our survey are not enough to artificially produce the fall-off which we see. However, when we convert the M_K LF of HM92 into an M_{Bol} luminosity function, we find no evidence for a disagreement between their data and ours. Moreover, when their data are normalised by the volume sampled, we find that the space densities they predict at $M_{Bol} \approx 12$ are significantly lower than those observed at $M_{Bol} \approx 10$ by larger and brighter Nearby Star Sample studies (WJK). We conclude that the photometric and Nearby Star luminosity functions are in good agreement.

We use this luminosity function to construct a mass function well constrained down to $0.08M_{\odot}$. We find that the resulting distribution is *extremely* poorly represented by a single power-law of the Salpeter type. The mass function shows a maximum at $m \approx 0.25M_{\odot}$, followed by a local minima or flattening between $0.1M_{\odot} < m < 0.25M_{\odot}$. There is very suggestive increase of a further increase in the mass function below $0.1M_{\odot}$, though the nature of this increase is almost completely determined by the details of the theoretical mass-luminosity relation adopted. We find that when this mass distribution is integrated, the mass density in the solar neighbourhood represented by stars with $m < 0.4M_{\odot}$ is $\rho_0(m < 0.4) = 0.017 \pm 0.01 M_{\odot} pc^{-3}$. Using a Scalo MF to estimate the mass density contributed by more massive stars we estimate the total mass density due to main sequence stars to be $\rho_0(ms) = 0.042 \pm 0.015 M_{\odot} pc^{-3}$ where most of the uncertainty is contributed by the Scalo mass function. Adding the mass density of white dwarfs, giants and the ISM brings the total observed mass density near the sun to $\rho_0(obs) = 0.09 \pm 0.02 M_{\odot} pc^{-3}$. This is consistent with previous determinations, and indicates that significant quantities of mass are not 'hidden' in the form of VLM stars. Lastly, we use our new data to provide a normalisation above the H-burning limit for estimates of the integrated mass density below the H-burning limit. We find that significant mass densities ($0.05 - 0.1\, M_{\odot} pc^{-3}$) can be hidden in the form of brown dwarfs, *only* if the mass function for these objects is much steeper than seen for main sequence stars (i.e., $\Psi \propto m^{-3.5}$ or steeper), or if the minimum mass which the processes of star formation can form is extremely small (i.e., $\lesssim 0.002M_{\odot}$ or 2 Jupiter masses). Neither possibility is ruled out by the available data, though both seem to be difficult to envisage.

It is difficult to see how our mass function could be explained by star formation dominated by hierarchical fragmentation processes, since such processes are essentially scaleless and therefore produce an essentially featureless IMF, except for at a possible single cut-off mass. If the turnover in the IMF seen at $0.25M_{\odot}$ represents a minimum mass produced by fragmentation (as is proposed by Larson (1985)), it seems difficult to see how the IMF could then increase again at lower masses.

An alternative view of the star formation process has been proposed by Shu, Adams & Lizano (1987), in which star formation is a fundamentally accretion-driven process. In this model a given star's mass is determined not by the mass of the cloud fragment, or core, from which it forms (which is usually much larger than the mass of the star which eventually forms in any case), but by some process which "turns off" the accretion of matter onto the protostar. Such a view makes it conceivable that processes internal to the star

(e.g., the turning on, or off, of a stellar dynamo, the commencement of stellar winds, or bipolar outflows, etc.) *could* have an determining effect on the final mass of the star – which would make the presence of features in the IMF far more tenable than in a hierarchical fragmentation model. Star formation theories are, however, very much in their infancy and provide only a canonical idea of the processes which determine a star's mass – the verdict is by no means in. It is clear though, that the features seen in the IMF below $0.4M_{\odot}$ must be products of the star formation process. As such they represent an outstanding challenge for proposed star formation theories, inasmuch as any theory of how stars form *must* be able to explain frequency distribution of their eventual masses, and so must be able to explain the $0.25M_{\odot}$ local maxima in that distribution.

Further study of the form of the IMF below $0.1M_{\odot}$ will be seriously hampered if fundamental properties of these objects cannot be better determined. The theoretical mass-luminosity relations are the largest source of uncertainty in interpreting the space density of VLM stars – observational determinations of the masses of these stars are essential if this uncertainty is to be resolved. This means that binary VLM and sub-stellar objects must be found and studied – both to measure their masses and their trigonometric parallaxes. Luckily as these objects can only be found close to the sun, the latter is a very straightforward task (Paper III). However, this requires that much larger samples of these objects be identified. Perhaps the best hope for this is the proposed 2 Micron All-Sky Survey, which will cover the entire sky down to K=14 (Kleinmann 1992). Based on a flat extrapolation of our MFs, such a survey can be expected to detect $\sim$ 100 objects within 15pc of the sun between $0.1M_{\odot}$ and $0.05M_{\odot}$ if these objects are brighter than $M_{Bol} \sim 16.5$. Such a sample (apart from guaranteeing the lucky discoverers a place in the record books) will enable the study of the properties of these important and elusive objects to be moved out of the sideshow, and into the laboratory.

The author particluarly wishes to acknowledge the advice, encouragement and assistance provided by Jeremy Mould and Neill Reid throughout this project. He also gratefully acknowledges the assistance of the uniformly friendly and professional staff at the Palomar, Las Campanas and the IRTF facilities used for this programme, and in particular thank Mark Shure, Tom Herbst, Miguel Roth, Angel Guerra, Herman Olivares, Fernando Peralta, Alberto Zuniga, Ernan Solis, Will McKinley, Jean Mueller, Juan Carrasco and

Skip Staples. CGT also gratefully acknowledges a grant from the Sigma Xi Foundation which supported part of the travel expenses involved in carrying out this work.

References

Alexander, D.R., Johnson, H.R. & Rypma, R.L. 1982, 272, 773

Bahcall, J.N., 1984a, ApJ, 276, 156

Bahcall, J.N., 1984b, ApJ, 276, 169

Bahcall, J.N., 1984c, ApJ, 287, 926

Bahcall, J.N., Flynn, C., Gould, A. 1992, ApJ, 389, 234

Beard, S., M^{c}Gillivray, H.T., Thanisch, P.F. 1990, MNRAS, 247, 311

Bessell, M., 1992, AJ, 101, 662

Bienaymé, O., Robin, A. & Crézé, M. 1987, AA, 180, 94

Boss, A.P., 1986, *Astrophysics of Brown Dwarfs*, ed. M.Kafatos, Cambridge University Press : Cambridge

Burrows, A., Hubbard, W.B., Lunine, J.I., 1989. ApJ 345, 939 (BHL)

Carico, D.P., Graham, J.R., Matthews, K., Wilson, T.D., Soifer, B.T., Neugebauer, G., Sanders, D.B. 1990, ApJLett, 349, L39

Dahn, C.C., Liebert, J. & Boeshar, P.C. 1983, *Nearby Stars and the Luminosity Function, IAU Colloq. No.76*, p163, eds. Davis Philip & Upgren, Davis Press:Schenectady

Dahn, C.C, Liebert, J. & Harrington, R.S. 1986, AJ, 91, 621

D'Antona, F. & Mazzitelli, I. 1985, ApJ, 296, 502 (D&M)

D'Antona, F. & Mazzitelli, I. 1986, AA, 162,80

de Boor, C. 1978, *A Practical Guide to Splines* Springer-Verlag : New York

Elias, J.H., *et al.* 1982, AJ, 87, 1029

Gilmore, G.F. & Reid, I.N., 1983, MNRAS, 202,1025

Gilmore, G.F., Reid, I.N., Hewitt, P.C. 1985, MNRAS, 213, 257

Gliese, W., 1969, *Catalogue of Nearby Stars, Veroff. Astr. Rechen. Inst. Heidelberg No 22*

Gliese, W. & Jahreiss, H., 1979. A&ASupl, 38, 423

Hawkins, M.R.S 1985, *Astrophysics of Brown Dwarfs*, ed. M.Kafatos, Cambridge University Press:Cambridge

Hawkins, M.R.S, & Bessell, M.S. 1988, MNRAS, 234, 177

Hambly, N.C. & Jameson, R.F. 1991, MNRAS,249, 137

Henry, T.J. & M^{c}Carthy, D.W., 1992, ApJ, 350, 334 (HM92)

Hill, G., Hilditch, R.W. & Barnes, J.V. 1979, MNRAS, 186, 813

Hoyle, F. 1953, ApJ, 118, 513

Jameson, R.F. & Skillen, I. 1989, MNRAS 239, 247

Kleinman, S. 1992, *Proc. Something to do with Surveys Conference*, ed:T.Soifer, PASP Conference Series No.666

Kuijken, K. & Gilmore, G. 1989a, MNRAS, 239, 571

Kuijken, K. & Gilmore, G. 1989b, MNRAS, 239, 605

Kuijken, K. & Gilmore, G. 1991, ApJLett, 267, L9

Landolt, A. 1983, Astron.J., 88, 999

Larson, R.B. 1985, MNRAS, 214, 379

Leggett, S.K. & Hawkins, M.R.S. 1988, MNRAS, 334, 1065

Leggett, S.K. 1992, ApJSupp, 82, 351

Liebert, J., Dahn, C.C. & Monet, D.G. 1988, ApJ, 332, 891

Liebert, J. & Dahn, C.C. 1986, *Astrophysics of Brown Dwarfs*, ed. M.Kafatos, Cambridge University Press : Cambridge

Miller, G.E. & Scalo, J.M. 1979, ApJSuppl, 41, 513

Nelson, L.A., Rappaport, S.A., Joss, P.C. 1986, ApJ, 311, 226

Popper, D.M. 1980, ARAA, 18, 115

Reid, I.N. 1987, MNRAS, 225, 873

Reid, I.N. 1991, AJ, 102, 1428

Reid, I.N. & Gilmore, G., 1984. MNRAS, 206, 19

Salpeter, E.E. 1955, ApJ, 121, 161

Scalo, J.M. 1986, Fund.Cosmic.Phys., 11,1

Shu, F., Adams, F. & Lizano, S. 1987, ARAA, 25, 23

Simons, D.A. & Becklin, E.E. 1992, ApJ, 390, 431

Smith, R.C. 1983, Observatory, 103, 29

Staller, R.F.A, & de Jong, T. 1981, AA, 98, 140

Stauffer, J.R. *et al.* 1989, 344, L21

Stobie, R.S., Ishida, K., Peacock, J.A., 1989, MNRAS, 238, 709

Tinney, C.G., Mould, J.R., Reid, I.N. 1992a, ApJ, 396, 173

Tinney, C.G., Mould, J.R., Reid, I.N. 1992b, AJ, *in press.* (Paper II)

Tinney, C.G., Reid, I.N., Mould, J.R., 1992a, ApJSuppl, *submitted*, (Paper I)

Tinney, C.G., 1992, AJ, *in press.* (Paper III)

Weilen, R. 1977, AA, 60, 263

Weilen, R., Jahreiss, H. & Kruger, R. 1983, *Nearby Stars and the Luminosity Function, IAU Colloq. No.76*, p163, eds. Davis Philip & Upgren, Davis Press:Schenectady (WJK)

Table 5.1 - Areas and Limits Surveyed.

Field	α (1950)	δ	Master Plate	Slave Plates	Area[a] ($\square^\circ$)	$[i^P_{Pal}]_{lim}$	$[(r-i)^P_{Pal}]_{lim}$	Limits?[b]
213-1	10^h00^m	50°	N2291	F1096, F2978.	25.13	17.0	1.90	
213-2	10^h00^m	50°	N2291	F1096, F2978.	25.13	17.5	2.00	
262-1	10^h15^m	45°	N2940	F1091, F2315.	24.96	17.5	1.90	
262-2	10^h15^m	45°	N2940	F1091, F2315.	24.96	18.0	2.00	
263-1	09^h50^m	45°	N3100	F2957.	25.05	17.0	1.90	
263-2	09^h50^m	45°	N3100	F2957.	25.05	18.0	2.06	
513	15^h00^m	25°	N1197	F1094.	23.13	17.5	2.00	
868-1	15^h00^m	00°	I11801	I9992, F1178, F2428, R5780.	22.69	17.0	1.90	y
868-2	15^h00^m	00°	I11801	I9992, F1178, F2428, R5780.	22.69	17.5	2.00	y
868-3	15^h00^m	00°	I11801	I9992, F1178, F2428, R5780.	22.69	18.0	2.20	y
831-1	02^h40^m	00°	I11526	I7377, R7376, F2889.	24.61	17.5	2.00	y
832-1	03^h00^m	00°	N3601	I11499, F1469, F3004, OR11502.	25.18	18.0	2.20	y
832-2[c]	03^h00^m	00°	I11499	F1469, F3004, OR11502.	2.50	17.5	2.10	
889-1	22^h00^m	00°	N3362	F3386, F3479, F3561.	25.10	18.0	2.00	
890-1	22^h20^m	00°	N3647	F1342, F3493, R11414.	25.22	17.5	2.00	
890-2	22^h20^m	00°	N3647	F1342, F3493, R11414.	25.22	18.0	2.10	
891-1	22^h40^m	00°	N3584	F742.	24.91	17.0	2.14	

Notes to Table

a - Areas (in square degrees) in which IIIaF and IVN plates are coincident.

b - 'y' signifies the sample is one which includes upper limits, constructed from paired IVN plates and IIIaF non-detections.

c - Area given is that of I11499 in common with IIIaF plates, but *not* in common with N3601.

TABLE 5.2 - Infrared Observations.

Notes to Table 5.2

a - P200 = Palomar 200″ telescope, C40 = 1m Swope telescope (Las Campanas), C100 = 2.5m duPont telescope (Las Campanas), IRTF = 3.2m Infrared telescope Facility, Mauna Kea.

b - The scatter in the residuals about the photometric zero-point determined from standards on that night. The number in parenthesis is the number of independent standard observations on that night (each of these usually consisted of several exposures added together).

c - Extinction coefficient at K-band (in magnitudes/airmass) determined from standard star observations. The values shown are those used for each run, which were determined by averaging determinations made on each night of observation.

d - Observations of several VLM candidates were kindly made on these nights by (respectively) D.Hamilton & I.N. Reid, and J.Mould & M.Rich. Standards were only reduced in the few hours around the observations actually used for this programme.

Date (UT)	Telescope[a]	Seeing (″)	Standard Aperture (″)	Object Aperture (″)	Aperture Correction	Linearity Correction Coefficients (cf. equation 5.1) a	b	c	σ_{stds}[b]	K_K[c]
15OCT89	P200		8.1	3.7	0.056±0.025	0.0323	8.362×10^{-6}	0.0	0.046(10)	0.10±0.02
16OCT89	P200		8.1	3.7	0.055±0.020	0.0323	8.362×10^{-6}	0.0	0.025(14)	〃
17OCT89	P200		10.5	4.3	0.065±0.030	0.0323	8.362×10^{-6}	0.0	0.040(13)	〃
01SEP90	P200		11.2	3.7	0.039±0.030	0.0258	5.506×10^{-6}	0.0	0.035(12)	0.19±0.04
02SEP90	P200		11.2	3.7	0.043±0.030	0.0258	5.506×10^{-6}	0.0	0.024(16)	〃
03SEP90	P200		11.2	3.7	0.036±0.030	0.0258	5.506×10^{-6}	0.0	0.018(17)	〃
06NOV90	P200[d]		7.4	3.7	0.086±0.031	0.0140	6.723×10^{-6}	0.0	0.027(6)	0.10±0.05
23JUL91	P200		7.4	3.1	0.074±0.024	0.0140	6.723×10^{-6}	0.0	0.027(12)	0.10±0.03
24JUL91	P200		7.4	3.1	0.056±0.020	0.0140	6.723×10^{-6}	0.0	0.027(14)	〃
18AUG91	C40		12.0	6.7	0.065±0.020	0.0	2.0×10^{-6}	0.0	0.020(20)	0.08±0.02
23AUG91	C100		10.5	3.0	0.161±0.064	0.0	2.0×10^{-6}	0.0	0.014(20)	〃
25AUG91	C100		10.0	3.0	0.187±0.057	0.0	2.0×10^{-6}	0.0	0.018(24)	〃
26AUG91	C100		11.5	3.0	0.163±0.043	0.0	2.0×10^{-6}	0.0	0.017(21)	〃
27AUG91	C100		11.0	3.0	0.102±0.030	0.0	2.0×10^{-6}	0.0	0.012(26)	〃
28AUG91	C100		11.0	3.0	0.100±0.028	0.0	2.0×10^{-6}	0.0	0.016(15)	〃
30AUG91	P200[d]		6.8	3.1	0.051±0.003	0.0	2.0×10^{-6}	0.0	0.022(8)	0.20±0.03
24DEC91	IRTF		7.0	4.2	0.038±0.030	0.0	-2.612×10^{-6}	1.7891×10^{-10}	0.031(20)	0.09±0.04
14MAR92	P200		6.8	3.1	0.046±0.023	0.0140	6.723×10^{-6}	0.0	0.036(15)	0.13±0.04
15MAR92	P200		6.8	3.1	0.049±0.040	0.0140	6.723×10^{-6}	0.0	0.024(16)	〃
12MAY92	P200	0.6-1.5	6.8	3.5	0.053±0.009	0.0140	6.723×10^{-6}	0.0	0.026(24)	0.13±0.03
20JUN92	IRTF		8.4	3.5	0.051±0.010	0.0	-2.6120×10^{-6}	1.7891×10^{-10}	0.014(22)	0.10±0.02
21JUN92	IRTF		8.4	3.5	0.051±0.010	0.0	-2.6120×10^{-6}	1.7891×10^{-10}	0.015(29)	〃
22JUN92	IRTF		9.1	3.5	0.051±0.010	0.0	-2.6120×10^{-6}	1.7891×10^{-10}	0.017(29)	〃
23JUN92	IRTF		9.1	3.5	0.052±0.014	0.0	-2.6120×10^{-6}	1.7891×10^{-10}	0.011(20)	〃

TABLE 5.3. Survey samples in each POSSII/COSMOS field selected by Photographic Colour.

Notes to Table 5.3

a - The I–K colour is calculated using i^C_{Pal} where available, and otherwise using i^P_{Pal} .

b - Objects were selected from the area of I11499 which does not overlap with N3601 (the plate used to select the Field 832-1 sample).

Object	Other Name	α(1950.0)	δ(1950.0)	i^P_{Pal}	$(r-i)^P_{Pal}$	i^C_{Pal}	$(r-i)^C_{Pal}$	K_{Cam}	K_{Pal}	K_{Irtf}	K_{mean}	I–K[a]	V
(a) Field 213-1. M=N2291. S=F1096, F2978. Limits : 12.0 < I < 17.0, R–I ≥ 1.90													
213- 13676		$10^h\ 10^m\ 43.6^s$	+49° 51′ 57″	16.06	2.19				16.03c		16.03c	0.03	
213- 43874		$09^h\ 53^m\ 01.2^s$	+49° 06′ 23″	15.54	2.19	15.73	2.18		12.60a	12.53a	12.58a	3.15	
213- 54027		$09^h\ 47^m\ 08.0^s$	+48° 32′ 13″	16.48	2.13				13.72b		13.72b	2.76	
213- 39249		$09^h\ 55^m\ 35.8^s$	+50° 46′ 32″	15.43	2.09	15.53	2.09		12.50a		12.50a	3.03	
213- 40466		$09^h\ 54^m\ 58.9^s$	+50° 20′ 55″	16.83	2.06					13.42a	13.42a	3.41	
213- 43313		$09^h\ 53^m\ 06.5^s$	+51° 56′ 29″	14.88	2.01				12.72a		12.72a	2.16	
213- 45790		$09^h\ 51^m\ 56.8^s$	+47° 50′ 26″	15.64	2.01				13.42b		13.42b	2.22	
213- 30913		$10^h\ 00^m\ 18.5^s$	+47° 47′ 11″	16.74	1.99					13.65a	13.65a	3.09	
213- 33567		$09^h\ 58^m\ 53.7^s$	+50° 12′ 15″	13.65	1.98	13.78	1.97			10.53a	10.53a	3.25	
213- 50445		$09^h\ 49^m\ 22.0^s$	+47° 40′ 06″	13.58	1.98					11.85a	11.85a	1.73	
213- 56213		$09^h\ 46^m\ 06.8^s$	+49° 52′ 38″	15.38	1.98				12.75a		12.75a	2.63	
213- 42980		$09^h\ 53^m\ 37.0^s$	+47° 32′ 09″	16.12	1.97					13.62b	13.62b	2.50	
213- 34655		$09^h\ 58^m\ 17.5^s$	+48° 24′ 20″	16.76	1.96					14.10c	14.10c	2.66	
213- 16596	263- 68812	$10^h\ 08^m\ 27.5^s$	+47° 42′ 30″	16.67	1.95				14.03b	14.27a	14.18b	2.49	
213- 31245		$10^h\ 00^m\ 30.4^s$	+52° 09′ 22″	13.65	1.94				10.78a		10.78a	2.87	
213- 32942		$09^h\ 59^m\ 10.8^s$	+47° 39′ 50″	14.94	1.93				12.42a		12.42a	2.52	
213- 47359		$09^h\ 50^m\ 59.8^s$	+48° 02′ 34″	16.74	1.93				13.80b		13.80b	2.94	
213- 48679		$09^h\ 49^m\ 53.0^s$	+50° 17′ 27″	16.59	1.91				13.82a		13.82a	2.77	
213- 43604		$09^h\ 52^m\ 53.2^s$	+50° 29′ 25″	15.69	1.90				12.97a		12.97a	2.72	
(b) Field 213-2. M=N2291. S=F1096, F2978. Limits : 17.0 < I < 17.5, R–I ≥ 2.0													
213- 9815		$10^h\ 13^m\ 14.8^s$	+51° 00′ 27″	17.33	2.43				nd.		–	–	
213- 46628		$09^h\ 51^m\ 18.4^s$	+48° 37′ 31″	17.49	2.34	17.65	2.20			14.19b	14.19b	3.46	
213- 56230		$09^h\ 46^m\ 06.1^s$	+50° 12′ 12″	17.04	2.28	17.12	2.31		13.92a	13.88c	13.91a	3.21	
213- 3503		$10^h\ 16^m\ 35.3^s$	+49° 16′ 56″	17.50	2.14				14.78b	14.56c	14.72b	2.78	
213- 19088	263- 72846	$10^h\ 06^m\ 58.3^s$	+47° 29′ 03″	17.44	2.08				14.42a	14.55b	14.47a	2.97	
213- 45695		$09^h\ 51^m\ 32.4^s$	+51° 55′ 51″	17.44	2.05	17.80	1.82			14.87c	14.87c	2.93	
213- 44143	262- 53725	$09^h\ 52^m\ 55.1^s$	+47° 31′ 05″	17.47	2.02				14.46a		14.46a	3.01	
213- 20064		$10^h\ 06^m\ 55.4^s$	+50° 24′ 41″	17.41	2.01				14.94a		14.94a	2.47	
213- 39050		$09^h\ 55^m\ 53.4^s$	+48° 12′ 37″	17.01	2.01	17.25	2.05			13.95b	13.95b	3.30	
213- 42147		$09^h\ 53^m\ 49.9^s$	+51° 38′ 49″	17.48	2.01				14.83a		14.83a	2.65	

Object	Other Name	α(1950.0)	δ(1950.0)	i^P_{Pal}	$(r-i)^P_{Pal}$	i^C_{Pal}	$(r-i)^C_{Pal}$	K_{Cam}	K_{Pal}	K_{Irtf}	K_{mean}	I–K[a]	V
(c) Field 262-1. M=N2940. S=F1091, F2315. Limits : 12.0 < I < 17.5, R–I ≥ 1.90													
262– 111511		$09^h\ 39^m\ 13.3^s$	+42° 59′ 19″	17.06	2.64	17.00	2.51		13.04a	13.05a	13.04a	3.96	
262– 21257		$10^h\ 00^m\ 01.0^s$	+44° 25′ 40″	16.48	2.29				13.11a	13.16a	13.13a	3.35	
262– 70502		$09^h\ 48^m\ 40.9^s$	+42° 47′ 57″	16.48	2.28	16.57	2.36		13.13a	1312.a	13.12a	3.45	
262– 63620		$09^h\ 50^m\ 12.7^s$	+43° 49′ 42″	17.40	2.20				14.53a		14.53a	2.87	
262– 34043		$09^h\ 57^m\ 16.9^s$	+45° 20′ 57″	16.91	2.19	16.89	2.31		13.69a	13.60a	13.65a	3.24	
262– 86514		$09^h\ 44^m\ 53.8^s$	+42° 31′ 08″	16.91	2.16				14.77c		14.77c	2.14	
262– 111559		$09^h\ 39^m\ 05.3^s$	+43° 26′ 48″	17.11	2.10				13.74a		13.74a	3.37	
262– 91736		$09^h\ 43^m\ 36.5^s$	+45° 31′ 24″	15.29	2.08				13.57c		13.57c	1.72	
262– 67182		$09^h\ 49^m\ 27.4^s$	+43° 44′ 47″	16.11	2.04				13.45a		13.45a	2.66	
262– 100107		$09^h\ 41^m\ 37.2^s$	+44° 36′ 48″	17.00	2.04				14.56a		14.56a	2.44	
262– 79742		$09^h\ 46^m\ 27.0^s$	+44° 57′ 41″	16.92	2.01				14.26b		14.26b	2.66	
262– 32311		$09^h\ 57^m\ 47.5^s$	+46° 23′ 54″	16.92	2.00				14.33b		14.33b	2.59	
262– 48276		$09^h\ 53^m\ 32.4^s$	+43° 05′ 18″	14.76	1.99				12.31a		12.31a	2.45	
262– 78665		$09^h\ 46^m\ 35.5^s$	+43° 30′ 47″	15.21	1.99				12.76a		12.76a	2.45	
262– 117366		$09^h\ 37^m\ 13.8^s$	+46° 18′ 13″	16.37	1.99				13.61b		13.61b	2.76	
262– 54157		$09^h\ 52^m\ 23.6^s$	+44° 39′ 56″	17.01	1.98				14.62b		14.62b	2.39	
262– 58084		$09^h\ 51^m\ 33.3^s$	+44° 06′ 57″	16.83	1.96				14.76b		14.76b	2.07	
262– 72232		$09^h\ 48^m\ 04.5^s$	+42° 55′ 11″	15.88	1.96				13.24a		13.24a	2.64	
262– 86827		$09^h\ 44^m\ 47.2^s$	+44° 13′ 37″	16.99	1.96								
262– 107168		$09^h\ 40^m\ 06.6^s$	+43° 37′ 03″	17.42	1.96				14.83a		14.83a	2.59	
262– 36081		$09^h\ 57^m\ 00.0^s$	+47° 12′ 04″	14.79	1.94				11.79a		11.79a	3.00	
262– 97103		$09^h\ 42^m\ 33.6^s$	+43° 13′ 25″	15.92	1.94				12.92a		12.92a	3.00	
262– 92750		$09^h\ 43^m\ 20.6^s$	+45° 29′ 14″	17.22	1.93				14.56c		14.56c	2.66	
262– 110005		$09^h\ 39^m\ 26.2^s$	+44° 19′ 29″	16.13	1.92								
262– 115303		$09^h\ 38^m\ 07.0^s$	+44° 12′ 07″	15.66	1.92				12.87a		12.87a	2.79	
262– 21526		$10^h\ 00^m\ 29.5^s$	+46° 13′ 47″	15.09	1.91				12.54a		12.54a	2.55	
262– 43652		$09^h\ 54^m\ 39.8^s$	+44° 17′ 54″	17.40	1.91				15.7 :		15.7 :	1.70	
262– 77139		$09^h\ 47^m\ 02.5^s$	+44° 47′ 00″	15.07	1.91				12.34a		12.34a	2.73	
262– 78036		$09^h\ 46^m\ 48.6^s$	+45° 05′ 52″	13.37	1.91								
262– 111177		$09^h\ 38^m\ 44.9^s$	+46° 27′ 32″	17.33	1.91				14.51b		14.51b	2.82	
262– 23215		$09^h\ 59^m\ 60.0^s$	+45° 34′ 25″	16.21	1.90				13.10a		13.10a	3.11	

Object	Other Name	α(1950.0)	δ(1950.0)	i^P_{Pal}	$(r-i)^P_{Pal}$	i^C_{Pal}	$(r-i)^C_{Pal}$	K_{Cam}	K_{Pal}	K_{Irtf}	K_{mean}	I–K[a]	V
262– 38765		$09^h\ 56^m\ 26.1^s$	$+47°\ 27'\ 04''$	17.31	1.90				14.44c		14.44c	2.87	
(d) Field 262-2. M=N2940. S=F1091, F2315. Limits : 17.5 < I < 18.0, R–I ≥ 2.00													
262– 47735		$09^h\ 53^m\ 55.6^s$	$+45°\ 14'\ 13''$	17.55	2.38	17.89	2.59		13.55a	13.53a	13.54a	4.35	
262– 14557		$10^h\ 01^m\ 24.9^s$	$+43°\ 18'\ 59''$	17.85	2.37	17.87	2.22			14.76a	14.76a	3.11	
262– 60139		$09^h\ 51^m\ 09.0^s$	$+44°\ 31'\ 33''$	17.95	2.30				15.4 :		15.4 :	2.55	
262– 59341		$09^h\ 51^m\ 17.1^s$	$+45°\ 26'\ 01''$	17.81	2.29				15.4 :		15.4 :	2.41	
262– 64856		$09^h\ 50^m\ 10.1^s$	$+45°\ 49'\ 55''$	17.51	2.29					14.97a	14.97a	2.54	
262– 97380		$09^h\ 42^m\ 17.8^s$	$+44°\ 41'\ 01''$	17.58	2.29					15.2 :	15.2 :	2.38	
262– 115214		$09^h\ 38^m\ 19.2^s$	$+43°\ 34'\ 49''$	17.80	2.29				14.71a		14.71a	3.09	
262– 118702		$09^h\ 37^m\ 16.9^s$	$+43°\ 48'\ 03''$	17.54	2.18				14.50b	14.37a	14.41a	3.13	
262– 109474		$09^h\ 39^m\ 17.0^s$	$+46°\ 38'\ 58''$	17.84	2.15				15.33c		15.33c	2.51	
262– 125171		$09^h\ 35^m\ 25.5^s$	$+45°\ 42'\ 18''$	17.86	2.13				15.43b		15.43b	2.43	
262– 49671		$09^h\ 53^m\ 37.3^s$	$+45°\ 58'\ 58''$	17.97	2.05				15.5 :		15.5 :	2.47	
262– 63212		$09^h\ 50^m\ 31.2^s$	$+46°\ 43'\ 30''$	17.82	2.05				15.66c		15.66c	2.16	
262– 68619		$09^h\ 49^m\ 06.7^s$	$+46°\ 44'\ 00''$	17.93	2.05				nd.		–	–	
262– 85430		$09^h\ 44^m\ 56.3^s$	$+46°\ 22'\ 46''$	17.51	2.05				14.74b		14.74b	2.77	
262– 76438		$09^h\ 47^m\ 12.3^s$	$+45°\ 55'\ 18''$	17.81	2.04				15.19c		15.19c	2.62	
262– 86363		$09^h\ 44^m\ 46.3^s$	$+46°\ 57'\ 43''$	17.94	2.03				14.64b		14.64b	3.30	
262– 23878		$09^h\ 59^m\ 29.7^s$	$+44°\ 12'\ 23''$	17.75	2.02				14.58a		14.58a	3.17	
262– 95905		$09^h\ 42^m\ 25.7^s$	$+46°\ 50'\ 41''$	17.93	2.02				16.1 :		16.1 :	1.83	
262– 115254		$09^h\ 38^m\ 16.1^s$	$+43°\ 51'\ 22''$	17.78	2.02				15.36b		15.36b	2.42	
262– 83208		$09^h\ 45^m\ 31.6^s$	$+44°\ 31'\ 10''$	17.85	2.01				15.55b		15.55b	2.30	
262– 114572		$09^h\ 38^m\ 08.6^s$	$+45°\ 06'\ 21''$	17.73	2.01				15.37b		15.37b	2.36	
262– 99776		$09^h\ 41^m\ 53.6^s$	$+42°\ 50'\ 59''$	17.58	2.00				14.71c		14.71c	2.87	
(e) Field 263-1. M=N3100. S=F2957. Limits : 13.0 < I < 17.0, R–I ≥ 1.90													
263– 60235		$10^h\ 11^m\ 54.5^s$	$+45°\ 36'\ 01''$	16.92	2.45				16.7 :		16.7 :	0.22	
263– 71765		$10^h\ 07^m\ 57.9^s$	$+42°\ 59'\ 52''$	15.94	2.45	16.08	2.47			12.35a	12.35a	3.73	
263– 38822		$10^h\ 19^m\ 24.3^s$	$+44°\ 25'\ 06''$	15.40	2.33	15.52	2.22		12.25a		12.25a	3.27	
263– 80574		$10^h\ 04^m\ 39.4^s$	$+42°\ 53'\ 47''$	16.90	2.30	17.04	2.03		14.31a		14.31a	2.73	
263– 54170		$10^h\ 13^m\ 58.6^s$	$+44°\ 47'\ 57''$	15.79	2.28	15.87	2.32		12.63a		12.63a	3.24	
263– 32417		$10^h\ 21^m\ 52.6^s$	$+44°\ 43'\ 54''$	16.28	2.17				13.09a		13.09a	3.19	
263– 65287		$10^h\ 10^m\ 11.3^s$	$+42°\ 33'\ 00''$	16.72	2.16				14.29a		14.29a	2.43	

Object	Other Name	α(1950.0)	δ(1950.0)	i^P_{Pal}	$(r-i)^P_{Pal}$	i^C_{Pal}	$(r-i)^C_{Pal}$	K_{Cam}	K_{Pal}	K_{Irtf}	K_{mean}	I-K[a]	V
263- 47988		$10^h\ 16^m\ 12.2^s$	+45° 29′ 35″	16.87	2.11				14.00a		14.00a	2.87	
263- 52819		$10^h\ 14^m\ 26.4^s$	+43° 44′ 37″	16.79	2.11				14.03a		14.03a	2.76	
263- 7119		$10^h\ 31^m\ 02.9^s$	+46° 20′ 32″	16.95	2.00				14.27a		14.27a	2.68	
263- 12402		$10^h\ 28^m\ 39.3^s$	+44° 19′ 03″	16.68	1.99				13.52a		13.52a	3.16	
263- 34551		$10^h\ 20^m\ 50.6^s$	+42° 49′ 29″	16.53	1.99				14.03a		14.03a	2.50	
263- 19672		$10^h\ 26^m\ 40.8^s$	+46° 51′ 58″	16.90	1.97				14.26b		14.26b	2.64	
263- 63101		$10^h\ 10^m\ 50.2^s$	+44° 16′ 31″	16.17	1.97				13.34a		13.34a	2.83	
263- 34707		$10^h\ 20^m\ 48.2^s$	+44° 14′ 19″	16.87	1.95				14.16a		14.16a	2.71	
263- 68812	213- 16596	$10^h\ 08^m\ 27.4^s$	+47° 42′ 30″	16.70	1.95				14.03b	14.27a	14.19a	2.51	
263- 76014		$10^h\ 06^m\ 13.0^s$	+44° 10′ 50″	16.13	1.95				13.45a		13.45a	2.68	
263- 53099		$10^h\ 14^m\ 20.7^s$	+46° 05′ 33″	16.90	1.94				14.08a		14.08a	2.82	
263- 63681		$10^h\ 10^m\ 37.3^s$	+43° 53′ 19″	16.95	1.94				14.23b		14.23b	2.72	
263- 84866		$10^h\ 03^m\ 00.0^s$	+44° 39′ 43″	16.93	1.94				14.46a		14.46a	2.47	
263- 46142		$10^h\ 16^m\ 55.1^s$	+45° 54′ 44″	15.67	1.93				12.63a		12.63a	3.04	
263- 48488		$10^h\ 16^m\ 05.6^s$	+44° 17′ 15″	16.24	1.93				13.80a		13.80a	2.44	
263- 54689		$10^h\ 13^m\ 55.8^s$	+44° 01′ 03″	16.27	1.93				13.38a		13.38a	2.89	
263- 27048		$10^h\ 23^m\ 54.9^s$	+45° 28′ 22″	16.90	1.92				13.99a		13.99a	2.91	
263- 7425		$10^h\ 30^m\ 08.7^s$	+43° 26′ 51″	15.73	1.91				12.80a		12.80a	2.93	
263- 51855		$10^h\ 14^m\ 47.0^s$	+46° 02′ 31″	16.49	1.91				13.52a		13.52a	2.97	
263- 16085		$10^h\ 27^m\ 18.3^s$	+43° 52′ 02″	16.94	1.90				14.11a		14.11a	2.83	
(f) Field 263-2. M=N3100. S=F2957. Limits : 17.0 < I < 18.0, R–I ≥ 2.06													
263- 57986		$10^h\ 12^m\ 36.3^s$	+46° 22′ 52″	17.29	2.43	17.44	2.01		14.24a		14.24a	3.20	
263- 39781		$10^h\ 19^m\ 24.2^s$	+47° 39′ 02″	17.40	2.32	17.50	2.04		14.19a		14.19a	3.31	
263- 47548		$10^h\ 16^m\ 23.6^s$	+47° 12′ 42″	17.52	2.27				14.36a		14.36a	3.16	
263- 27528		$10^h\ 23^m\ 30.5^s$	+44° 01′ 11″	17.60	2.26				14.54c		14.54c	3.06	
263- 72846	213- 19088	$10^h\ 06^m\ 58.2^s$	+47° 29′ 03″	17.45	2.25				14.42a	14.55b	14.47a	2.98	
263- 47967		$10^h\ 16^m\ 15.8^s$	+45° 15′ 36″	17.80	2.24				15.02c		15.02c	2.78	
263- 50996		$10^h\ 15^m\ 07.1^s$	+43° 46′ 36″	17.74	2.23				14.90b		14.90b	2.84	
263- 78482		$10^h\ 05^m\ 18.9^s$	+44° 46′ 19″	17.54	2.21								
263- 17708		$10^h\ 27^m\ 17.4^s$	+46° 44′ 29″	17.20	2.18				14.45a		14.45a	2.75	
263- 24935		$10^h\ 24^m\ 04.4^s$	+43° 06′ 17″	17.84	2.18				14.86a		14.86a	2.98	
263- 36966		$10^h\ 19^m\ 59.6^s$	+43° 40′ 37″	17.73	2.18				15.5 :		15.5 :	2.23	

Object	Other Name	α(1950.0)	δ(1950.0)	i^P_{Pal}	$(r-i)^P_{Pal}$	i^C_{Pal}	$(r-i)^C_{Pal}$	K_{Cam}	K_{Pal}	K_{Irtf}	K_{mean}	I-K[a]	V
263- 57796		$10^h\ 12^m\ 51.1^s$	+44° 32′ 40″	17.80	2.18				15.3 :		15.3 :	2.50	
263- 33082		$10^h\ 21^m\ 39.6^s$	+45° 18′ 30″	17.88	2.17				15.47b		15.47b	2.41	
263- 2394		$10^h\ 32^m\ 21.1^s$	+45° 32′ 08″	17.58	2.15				15.27b		15.27b	2.31	
263- 20113		$10^h\ 26^m\ 20.4^s$	+45° 41′ 35″	17.62	2.15				14.78b		14.78b	2.84	
263- 38438		$10^h\ 19^m\ 49.0^s$	+46° 05′ 37″	17.71	2.15				15.18b		15.18b	2.53	
263- 71738		$10^h\ 07^m\ 59.4^s$	+42° 46′ 17″	17.57	2.15				14.86a		14.86a	2.71	
263- 7595		$10^h\ 30^m\ 26.8^s$	+45° 02′ 21″	17.86	2.14				15.03a		15.03a	2.83	
263- 59016		$10^h\ 12^m\ 23.7^s$	+45° 05′ 28″	17.48	2.14				14.88b		14.88b	2.60	
263- 54323		$10^h\ 14^m\ 04.9^s$	+46° 08′ 28″	17.94	2.12				15.5 :		15.5 :	2.44	
263- 4900		$10^h\ 31^m\ 12.3^s$	+44° 12′ 54″	17.41	2.11				14.72a		14.72a	2.69	
263- 18121		$10^h\ 26^m\ 46.9^s$	+44° 50′ 16″	17.26	2.11				14.39a		14.39a	2.87	
263- 63364		$10^h\ 10^m\ 36.0^s$	+46° 19′ 53″	17.76	2.11				14.73b		14.73b	3.03	
263- 10013		$10^h\ 29^m\ 35.4^s$	+44° 48′ 49″	17.86	2.10				15.24b		15.24b	2.62	
263- 10808		$10^h\ 29^m\ 42.9^s$	+46° 33′ 11″	17.77	2.10				15.03a		15.03a	2.74	
263- 28907		$10^h\ 23^m\ 06.8^s$	+45° 48′ 04″	17.40	2.10				14.57b		14.57b	2.83	
263- 15804		$10^h\ 28^m\ 08.4^s$	+47° 01′ 10″	17.83	2.09				15.00b		15.00b	2.83	
263- 39779		$10^h\ 19^m\ 24.2^s$	+47° 38′ 29″	17.98	2.09				14.97a		14.97a	3.01	
263- 46665		$10^h\ 16^m\ 37.6^s$	+45° 09′ 52″	17.47	2.09				14.94c		14.94c	2.53	
263- 58801		$10^h\ 12^m\ 29.8^s$	+42° 41′ 31″	17.05	2.09				14.49b		14.49b	2.56	
263- 78291		$10^h\ 05^m\ 33.1^s$	+42° 55′ 58″	17.24	2.09				14.68b		14.86b	2.38	
263- 8835		$10^h\ 30^m\ 04.4^s$	+45° 10′ 15″	17.86	2.08				15.16b		15.16b	2.70	
263- 19339		$10^h\ 26^m\ 06.0^s$	+44° 02′ 21″	17.71	2.06				14.77b		14.77b	2.94	
263- 46770		$10^h\ 16^m\ 32.5^s$	+46° 06′ 46″	17.82	2.06				15.2 :		15.2 :	2.62	
263- 55140		$10^h\ 13^m\ 43.5^s$	+42° 48′ 55″	17.99	2.06				15.31b		15.31b	2.68	
263- 56085		$10^h\ 13^m\ 15.3^s$	+46° 01′ 54″	17.75	2.06				14.95b		14.95b	2.80	
263- 61161		$10^h\ 11^m\ 41.2^s$	+43° 06′ 18″	17.99	2.06				15.26c		15.26c	2.73	
(g) Field 513-1. M=N1197. S=F1094. Limits : 12.0 < I < 17.5, R–I ≥ 2.0													
513- 5656		$15^h\ 13^m\ 20.7^s$	+25° 42′ 01″	15.84	2.70	19.14	0.95		–		–	–	
513- 62073		$14^h\ 53^m\ 02.3^s$	+24° 39′ 02″	17.00	2.67				17.3 :		17.3 :	-0.30	
513- 22369		$15^h\ 07^m\ 22.8^s$	+27° 37′ 10″	15.62	2.63				16.3 :		16.3 :	-0.68	
513- 8328		$15^h\ 12^m\ 08.9^s$	+23° 52′ 12″	17.17	2.45	17.14	2.55		12.86a	13.00a	12.98a	4.16	?
513- 11762		$15^h\ 11^m\ 06.7^s$	+25° 59′ 27″	17.14	2.40					nd.	–	–	

Object	Other Name	α(1950.0)	δ(1950.0)	i^P_{Pal}	$(r-i)^P_{Pal}$	i^C_{Pal}	$(r-i)^C_{Pal}$	K_{Cam}	K_{Pal}	K_{Irtf}	K_{mean}	I-K[a]	V
513- 41966		$15^h\ 00^m\ 20.7^s$	+25° 48′ 58″	16.86	2.37	17.09	2.35		13.89a		13.89a	3.20	
513- 23614		$15^h\ 06^m\ 49.1^s$	+27° 14′ 12″	17.60	2.35	17.88	2.02		14.77a		14.77a	3.11	
513- 21916		$15^h\ 07^m\ 26.1^s$	+27° 08′ 00″	17.27	2.34	17.47	2.22		14.10a		14.10a	3.37	
513- 45780		$14^h\ 59^m\ 17.7^s$	+24° 22′ 21″	16.35	2.34				16.39c		16.39c	-0.04	
513- 6148		$15^h\ 13^m\ 13.7^s$	+26° 13′ 06″	16.66	2.29	17.29	2.05		14.25a		14.25a	3.04	
513- 6600		$15^h\ 13^m\ 02.1^s$	+25° 43′ 35″	17.47	2.29				14.71c		14.71c	2.76	
513- 58246		$14^h\ 54^m\ 15.1^s$	+27° 23′ 33″	12.91	2.29				12.46a		12.46a	0.45	
513- 64412		$14^h\ 52^m\ 08.8^s$	+25° 30′ 30″	17.46	2.28				14.46a		14.46a	3.00	
513- 51081		$14^h\ 57^m\ 08.2^s$	+27° 29′ 22″	17.47	2.23				14.48a		14.48a	2.99	
513- 59762		$14^h\ 53^m\ 43.7^s$	+23° 43′ 26″	17.32	2.21				nd.		–	–	
513- 58579		$14^h\ 54^m\ 10.4^s$	+26° 37′ 04″	17.17	2.20				14.40b		14.40b	2.77	
513- 58305		$14^h\ 54^m\ 15.0^s$	+22° 42′ 55″	17.23	2.18				nd.		–	–	
513- 42404		$15^h\ 00^m\ 10.3^s$	+25° 37′ 39″	16.53	2.15	16.59	2.28		13.38a	13.48a	13.40a	3.19	
513- 46546		$14^h\ 58^m\ 54.5^s$	+23° 01′ 50″	15.21	2.15	15.09	2.36		10.71a	10.82a	10.77b	4.32	?
513- 47181		$14^h\ 58^m\ 39.2^s$	+25° 43′ 57″	17.38	2.11				14.34b		14.34b	3.04	
513- 45005		$14^h\ 59^m\ 34.8^s$	+25° 12′ 24″	12.40	2.10				11.34a		11.34a	1.06	
513- 5151		$15^h\ 13^m\ 22.8^s$	+25° 14′ 55″	17.11	2.09				15.53b		15.53b	1.58	
513- 42555		$15^h\ 00^m\ 20.3^s$	+27° 13′ 30″	15.56	2.09				13.05a		13.05a	2.51	
513- 61725		$14^h\ 53^m\ 08.8^s$	+26° 08′ 59″	17.79	2.09				14.64a		14.64a	3.15	
513- 3005		$15^h\ 14^m\ 18.1^s$	+25° 58′ 44″	16.86	2.07				14.11b		14.11b	2.75	
513- 57961		$14^h\ 54^m\ 28.1^s$	+23° 53′ 01″	17.16	2.07				14.17a		14.17a	2.99	
513- 22351		$15^h\ 07^m\ 21.0^s$	+27° 25′ 32″	17.43	2.06				nd.		–	–	
513- 26478		$15^h\ 05^m\ 59.7^s$	+27° 42′ 07″	17.26	2.06				14.67a		14.67a	2.59	
513- 41584		$15^h\ 00^m\ 31.9^s$	+26° 15′ 06″	16.08	2.05				13.21a		13.21a	2.87	
513- 48493		$14^h\ 58^m\ 17.0^s$	+26° 39′ 30″	17.52	2.04				14.47a		14.47a	3.05	
513- 5153		$15^h\ 13^m\ 25.3^s$	+25° 15′ 22″	16.94	2.03				15.18c		15.18c	1.76	
513- 45966		$14^h\ 59^m\ 13.4^s$	+26° 38′ 11″	15.83	2.02				13.24a		13.24a	2.59	
513- 48204		$14^h\ 58^m\ 14.5^s$	+22° 49′ 51″	17.42	2.02				14.66a		14.66a	2.76	
513- 56843		$14^h\ 54^m\ 55.3^s$	+25° 06′ 04″	15.63	2.02				12.82a		12.82a	2.81	
513- 14999		$15^h\ 09^m\ 38.5^s$	+22° 58′ 12″	16.85	2.01				13.64a		13.64a	3.21	
513- 29464		$15^h\ 04^m\ 53.8^s$	+26° 43′ 26″	16.92	2.01				13.95a		13.95a	2.97	
513- 4270		$15^h\ 13^m\ 50.6^s$	+25° 27′ 48″	15.40	2.00				13.14a		13.14a	2.26	

Object	Other Name	α(1950.0)	δ(1950.0)	i^P_{Pal}	$(r-i)^P_{Pal}$	i^C_{Pal}	$(r-i)^C_{Pal}$	K_{Cam}	K_{Pal}	K_{Irtf}	K_{mean}	I–K[a]	V
513– 5045		$15^h\ 13^m\ 21.7^s$	+24° 16′ 33″	17.29	2.00				15.85b		15.85b	1.44	
513– 6601		$15^h\ 12^m\ 57.1^s$	+25° 44′ 23″	15.83	2.00				12.99a		12.99a	2.84	
(h) Field 868-1. M=I11801. S=I9992, F1178, F2428, R5780. Limits : 12.0 < I < 17.0, R–I ≥ 1.9													
868– 14665		$14^h\ 50^m\ 37.0^s$	−01° 39′ 03″	16.57	lim				15.7 :		15.7 :	0.87	
868– 84947		$15^h\ 03^m\ 26.0^s$	+00° 05′ 05″	16.28	2.20	16.28	2.32	12.92a	12.87a	12.93a	12.92a	3.36	
868– 99384		$15^h\ 05^m\ 53.7^s$	−00° 31′ 26″	15.72	2.18	15.95	2.20	12.81a			12.81a	3.14	
868– 29383		$14^h\ 53^m\ 32.6^s$	+00° 33′ 01″	16.62	2.15			13.58a			13.58a	3.04	
868– 87474		$15^h\ 03^m\ 48.4^s$	+01° 24′ 51″	16.84	2.13	17.06	2.18	13.85a		13.97a	13.91a	3.15	
868– 54745		$14^h\ 57^m\ 59.6^s$	−00° 47′ 54″	14.86	2.10			11.64a		11.73a	11.70a	3.16	
868– 72642		$15^h\ 01^m\ 16.6^s$	+00° 13′ 28″	14.47	2.09			11.64a		11.78a	11.74b	2.73	?
868– 53850		$14^h\ 57^m\ 52.2^s$	−00° 27′ 37″	13.71	2.05				10.63a		10.63a	3.08	
868– 91025		$15^h\ 04^m\ 26.8^s$	+00° 43′ 41″	16.17	2.03				13.52a		13.52a	2.65	
868– 59743		$14^h\ 58^m\ 56.0^s$	+00° 02′ 32″	16.96	2.02			14.17a	14.27a		14.22a	2.74	
868– 22962		$14^h\ 52^m\ 15.6^s$	+02° 03′ 37″	14.83	2.01				11.98a		11.98a	2.85	
868– 55586		$14^h\ 58^m\ 14.0^s$	−01° 19′ 50″	14.99	2.01				11.85a		11.85a	3.14	
868– 112182		$15^h\ 07^m\ 56.3^s$	−01° 19′ 04″	16.78	2.01			14.54a			14.54a	2.24	
868– 90975		$15^h\ 04^m\ 33.5^s$	+01° 03′ 45″	15.35	1.97				12.82a		12.82a	2.53	
868– 94168		$15^h\ 04^m\ 58.4^s$	−00° 59′ 51″	15.90	1.96				13.12a		13.12a	2.78	
868– 65430		$15^h\ 00^m\ 03.3^s$	+01° 03′ 05″	16.59	1.95				13.98a		13.98a	2.61	
868– 82602		$15^h\ 03^m\ 10.2^s$	+02° 30′ 39″	15.64	1.95				12.87a		12.87a	2.77	
868– 19224		$14^h\ 51^m\ 29.9^s$	+01° 26′ 52″	15.98	1.94				13.15a		13.15a	2.83	
868– 52652		$14^h\ 57^m\ 43.6^s$	+01° 43′ 32″	16.39	1.94				13.61a		13.61a	2.78	
868– 91955		$15^h\ 04^m\ 34.2^s$	+01° 17′ 42″	16.09	1.94				13.55a		13.55a	2.54	
868– 92555		$15^h\ 04^m\ 40.2^s$	−02° 11′ 53″	16.60	1.94				14.16a		14.16a	2.44	
868– 70042		$15^h\ 00^m\ 45.9^s$	+00° 31′ 22″	14.34	1.93				11.66a		11.66a	2.68	
868– 49360		$14^h\ 57^m\ 04.9^s$	+00° 18′ 00″	16.30	1.92				13.41a		13.41a	2.89	
868– 53830		$14^h\ 57^m\ 53.0^s$	−00° 19′ 16″	14.10	1.92				11.65a		11.65a	2.45	
868– 34306		$14^h\ 54^m\ 25.5^s$	+00° 10′ 30″	15.99	1.91				13.18a		13.18a	2.81	
868– 43076		$14^h\ 56^m\ 02.3^s$	+02° 15′ 15″	16.59	1.91				13.97a		13.97a	2.62	
868– 47907		$14^h\ 56^m\ 46.6^s$	−00° 53′ 03″	16.92	1.91				14.28a		14.28a	2.64	
868– 73194		$15^h\ 01^m\ 28.4^s$	+02° 28′ 00″	16.66	1.91				14.01a		14.01a	2.65	
868– 105127		$15^h\ 06^m\ 40.8^s$	−01° 57′ 52″	16.65	1.91				13.95b		13.95b	2.70	

Object	Other Name	α(1950.0)	δ(1950.0)	i^P_{Pal}	$(r-i)^P_{Pal}$	i^C_{Pal}	$(r-i)^C_{Pal}$	K_{Cam}	K_{Pal}	K_{Irtf}	K_{mean}	I–K[a]	V
868– 58221		$14^h\ 58^m\ 37.3^s$	$-01°\ 25'\ 55''$	16.74	1.90								
868– 100120		$15^h\ 06^m\ 00.2^s$	$+00°\ 35'\ 55''$	16.58	1.90								
868– 111050		$15^h\ 07^m\ 54.5^s$	$+00°\ 17'\ 17''$	16.54	1.90								
(i) Field 868-2. M=I11801. S=I9992, F1178, F2428, R5780. Limits : 17.0 < I < 17.5, R–I ≥ 2.0													
868– 68274		$15^h\ 00^m\ 30.5^s$	$+00°\ 05'\ 14''$	17.48	lim			14.07a		14.43a	14.25c	3.23	?
868– 62819		$14^h\ 59^m\ 21.2^s$	$-02°\ 24'\ 15''$	17.25	2.40	17.50	2.26	14.21b	14.26a	14.32a	14.28a	3.22	
868– 69080		$15^h\ 00^m\ 39.0^s$	$+00°\ 36'\ 32''$	17.46	2.40			13.67a	13.75a	13.78a	13.72a	3.74	
868– 93312		$15^h\ 04^m\ 43.9^s$	$-01°\ 18'\ 13''$	17.28	2.31			18.3 :			18.3 :	-1.02	
868– 118778		$15^h\ 09^m\ 11.4^s$	$+01°\ 51'\ 25''$	17.21	2.23			14.12a			14.12a	3.09	
868– 37835		$14^h\ 54^m\ 57.0^s$	$-01°\ 08'\ 51''$	17.41	2.18			14.75b			14.75b	2.66	
868– 80575		$15^h\ 02^m\ 41.2^s$	$-01°\ 45'\ 47''$	17.24	2.13				14.03b		14.03b	3.21	
868– 33891		$14^h\ 54^m\ 12.4^s$	$-01°\ 55'\ 49''$	17.46	2.06				15.15a		15.15a	2.31	
868– 65306		$15^h\ 00^m\ 07.2^s$	$+01°\ 51'\ 26''$	17.27	2.04				14.77c		14.77c	2.50	
868– 25587		$14^h\ 52^m\ 46.0^s$	$+00°\ 15'\ 23''$	17.42	2.02			15.41b			15.41b	2.01	
868– 97404		$15^h\ 05^m\ 31.7^s$	$+00°\ 32'\ 45''$	17.28	2.02				14.62a		14.62a	2.66	
868– 41171		$14^h\ 55^m\ 31.5^s$	$-01°\ 21'\ 07''$	17.42	2.00				14.96b		14.96b	2.46	
868– 81830		$15^h\ 02^m\ 59.7^s$	$+02°\ 04'\ 15''$	17.11	2.00				14.41c		14.41c	2.70	
(j) Field 868-2. M=I11801. S=I9992, F1178, F2428, R5780. Limits : 17.5 < I < 18.0, R–I ≥ 2.20													
868– 6302		$14^h\ 49^m\ 00.3^s$	$+00°\ 16'\ 15''$	17.96	lim				15.76b		15.76b	2.20	
868– 9488		$14^h\ 49^m\ 42.0^s$	$+01°\ 02'\ 24''$	17.64	lim			15.01b			15.01b	2.63	
868– 20073		$14^h\ 51^m\ 35.4^s$	$+01°\ 05'\ 35''$	17.85	lim				14.02a	14.12c	14.05a	3.80	
868– 38927		$14^h\ 55^m\ 18.0^s$	$+02°\ 30'\ 41''$	17.99	lim				14.87c		14.87c	3.12	
868– 44771		$14^h\ 56^m\ 16.3^s$	$-01°\ 45'\ 15''$	17.91	lim				14.97a		14.97a	2.94	
868– 50879		$14^h\ 57^m\ 29.1^s$	$+01°\ 57'\ 44''$	17.87	lim			14.56c			14.56c	3.31	
868– 93436		$15^h\ 04^m\ 43.9^s$	$-02°\ 08'\ 21''$	17.86	lim				15.29b		15.29b	2.57	
868– 60337		$14^h\ 59^m\ 09.4^s$	$+01°\ 48'\ 37''$	17.66	2.29			14.55b			14.55b	3.11	
868– 115952		$15^h\ 08^m\ 42.8^s$	$+02°\ 02'\ 07''$	17.60	2.26			14.74b			14.74b	2.86	
868– 21152		$14^h\ 51^m\ 47.3^s$	$-01°\ 06'\ 06''$	17.76	2.25			16.00c			16.00c	1.76	
868– 46997		$14^h\ 56^m\ 39.5^s$	$-00°\ 16'\ 13''$	17.77	2.24								
(k) Field 831-1. M=I11526. S=I7377, R7376, F2889. Limits : 12.0 < I < 17.5, R–I ≥ 2.0													
831– 127499		$02^h\ 44^m\ 15.0^s$	$+01°\ 48'\ 19''$	17.28	lim	17.44	2.13	14.50b			14.50b	2.94	
831– 82373		$02^h\ 38^m\ 21.6^s$	$-00°\ 03'\ 13''$	17.45	lim	17.57	2.06	14.60b			14.60b	2.97	

Object	Other Name	α(1950.0)	δ(1950.0)	i^P_{Pal}	$(r-i)^P_{Pal}$	i^C_{Pal}	$(r-i)^C_{Pal}$	K_{Cam}	K_{Pal}	K_{Irtf}	K_{mean}	I–K[a]	V
831- 69820		$02^h\ 36^m\ 48.5^s$	$-00°\ 45'\ 22''$	17.50	lim	17.73	2.19	14.20b			14.20b	3.53	
831- 161058	832- 3494	$02^h\ 48^m\ 38.7^s$	$+00°\ 35'\ 16''$	16.51	2.50	16.63	2.58		12.67a		12.67a	3.96	
831- 123282		$02^h\ 43^m\ 35.4^s$	$-01°\ 15'\ 40''$	17.37	2.44	17.50			14.73a		14.73a	2.77	
831- 40282		$02^h\ 33^m\ 05.1^s$	$-00°\ 05'\ 33''$	17.04	2.28	17.32	2.23		14.20b		14.20b	3.12	
831- 37956		$02^h\ 32^m\ 47.1^s$	$+00°\ 11'\ 46''$	17.50	2.26			14.86b			14.86b	2.64	
831- 70880		$02^h\ 36^m\ 59.1^s$	$+00°\ 32'\ 13''$	17.00	2.25	17.11			13.87a		13.87a	3.24	
831- 95119		$02^h\ 40^m\ 05.2^s$	$+00°\ 14'\ 36''$	17.26	2.20				14.71a		14.71a	2.55	
831- 104386		$02^h\ 41^m\ 11.4^s$	$-00°\ 58'\ 20''$	17.43	2.20				14.75a		14.75a	2.68	
831- 153675		$02^h\ 47^m\ 34.1^s$	$-02°\ 14'\ 06''$	16.47	2.17				13.12a		13.12a	3.35	
831- 165166	832- 7464	$02^h\ 49^m\ 09.4^s$	$-01°\ 14'\ 25''$	16.37	2.17	16.47	2.37		13.29a		13.29a	3.18	
831- 78881		$02^h\ 37^m\ 54.2^s$	$-01°\ 20'\ 45''$	17.35	2.16	17.50	2.16		14.24a		14.24a	3.26	
831- 154910		$02^h\ 47^m\ 39.4^s$	$-02°\ 03'\ 49''$	15.21	2.16	15.23	2.26	11.91a	11.94a		11.94a	3.29	
831- 27194		$02^h\ 31^m\ 17.7^s$	$+01°\ 55'\ 28''$	17.25	2.14			14.80b	15.01b		14.88b	2.37	
831- 73383		$02^h\ 37^m\ 20.3^s$	$+00°\ 51'\ 22''$	17.44	2.14			14.85a			14.85a	2.59	
831- 58459		$02^h\ 35^m\ 18.2^s$	$-02°\ 25'\ 48''$	16.92	2.11	17.00			13.72a		13.72a	3.28	
831- 81946		$02^h\ 38^m\ 25.7^s$	$+02°\ 02'\ 15''$	17.45	2.11			14.89a			14.89a	2.56	
831- 86303		$02^h\ 38^m\ 53.6^s$	$-01°\ 59'\ 47''$	16.01	2.09				13.17a		13.17a	2.84	
831- 133619		$02^h\ 44^m\ 52.6^s$	$+00°\ 42'\ 23''$	17.42	2.08			14.76a			14.76a	2.66	
831- 62316		$02^h\ 35^m\ 54.0^s$	$+01°\ 08'\ 45''$	17.38	2.07			13.96a			13.96a	3.42	
831- 132423		$02^h\ 44^m\ 51.7^s$	$+00°\ 17'\ 37''$	17.25	2.06				14.79b		14.79b	2.46	
831- 73274		$02^h\ 37^m\ 23.1^s$	$+01°\ 28'\ 11''$	17.06	2.05			14.03a			14.03a	3.03	
831- 141368		$02^h\ 45^m\ 57.6^s$	$+01°\ 51'\ 22''$	17.22	2.05			14.45a			14.45a	2.77	
831- 83487		$02^h\ 38^m\ 32.3^s$	$-00°\ 29'\ 34''$	17.29	2.03			14.72a			14.72a	2.57	
831- 125999		$02^h\ 44^m\ 02.8^s$	$+02°\ 27'\ 05''$	16.66	2.02			13.70a	13.76a		13.76a	2.90	
831- 148159		$02^h\ 46^m\ 59.9^s$	$+01°\ 30'\ 44''$	17.16	2.02				14.28a		14.28a	2.88	
831- 118286		$02^h\ 42^m\ 58.1^s$	$+00°\ 58'\ 23''$	17.15	2.00			15.29b			15.29b	1.86	
(l) Field 832-1. M=N3601. S=I11499, F1469, F3004, OR11502. Limits : 12.0 < I < 18.0, R–I ≥ 2.20													
832- 11330		$03^h\ 09^m\ 05.6^s$	$+01°\ 23'\ 36''$	17.00	lim			13.43b		13.44b	13.44a	3.56	
832- 15398		$03^h\ 07^m\ 51.2^s$	$-00°\ 43'\ 11''$	17.79	lim			14.85a			14.85a	2.94	
832- 17708		$03^h\ 07^m\ 13.7^s$	$+02°\ 02'\ 03''$	17.94	lim			14.36a			14.36a	3.58	
832- 42500		$03^h\ 00^m\ 01.9^s$	$-01°\ 28'\ 13''$	15.57	2.40	15.76	2.42	12.77a	12.73a		12.75a	3.01	
832- 18440		$03^h\ 06^m\ 57.4^s$	$-01°\ 43'\ 28''$	16.69	2.35								

Object	Other Name	α(1950.0)	δ(1950.0)	i^P_{Pal}	$(r-i)^P_{Pal}$	i^C_{Pal}	$(r-i)^C_{Pal}$	K_{Cam}	K_{Pal}	K_{Irtf}	K_{mean}	I–K[a]	V
832– 58985		$02^h\ 55^m\ 12.1^s$	$-00°\ 47'\ 20''$	17.18	2.33			13.83a			13.83a	3.35	
832– 58583		$02^h\ 55^m\ 19.4^s$	$+00°\ 22'\ 12''$	16.10	2.29			13.21a			13.21a	2.89	
832– 66362		$02^h\ 52^m\ 58.7^s$	$+01°\ 00'\ 57''$	17.87	2.29	18.00			14.68b		14.68b	3.32	
832– 16533		$03^h\ 07^m\ 28.7^s$	$+00°\ 36'\ 21''$	17.92	2.24								
832– 71123		$02^h\ 51^m\ 38.5^s$	$+01°\ 52'\ 59''$	17.21	2.23			14.18a			14.18a	3.03	
832– 62805		$02^h\ 54^m\ 02.9^s$	$+02°\ 02'\ 53''$	17.64	2.23			14.91b			14.91b	2.73	
832– 43178		$02^h\ 59^m\ 56.3^s$	$+00°\ 16'\ 55''$	16.82	2.23				13.88a	13.92c	13.90a	2.92	
(m) Field 832-2. M=I11499[b]. S=F1469, F3004, OR11502. Limits : 12.0 < I < 17.5, R–I > 2.1													
832– 10443		$02^h\ 49^m\ 52.0^s$	$+00°\ 44'\ 08''$	15.91	2.61	16.06	2.49		12.00a	11.99a	11.99a	4.07	
832– 3494	831-161058	$02^h\ 48^m\ 38.7^s$	$+00°\ 35'\ 17''$	16.54	2.55	16.63	2.58		13.67a		13.67a	2.96	
832– 7464	831-165166	$02^h\ 49^m\ 09.4^s$	$-01°\ 14'\ 26''$	16.31	2.48	16.47	2.37		13.29a		13.29a	3.18	
832– 79766		$03^h\ 02^m\ 38.4^s$	$-01°\ 04'\ 08''$	17.48	2.34			nd.			–	–	
832– 76662		$03^h\ 02^m\ 07.4^s$	$-02°\ 33'\ 15''$	15.87	2.31			13.01b		12.92a	12.96a	2.91	
832– 14960		$02^h\ 50^m\ 32.2^s$	$-01°\ 51'\ 00''$	16.69	2.31				13.59a		13.59a	3.10	
832– 82584		$03^h\ 03^m\ 12.4^s$	$+01°\ 32'\ 20''$	17.48	2.13			16.5 :			16.5 :	0.98	
(n) Field 889-1. M=N3362. S=F3386, F3479, F3561. Limits : 12.0 < I < 18.0, R–I ≥ 2.0													
889– 67105		$22^h\ 03^m\ 35.5^s$	$-00°\ 52'\ 03''$	16.80	2.38	16.88	2.35	13.62a	13.56a	13.61a	13.63a	3.25	
889– 142724		$21^h\ 54^m\ 41.9^s$	$-02°\ 27'\ 23''$	16.98	2.34	17.21	2.12		14.10a		14.10a	3.11	
889– 90604		$22^h\ 00^m\ 50.4^s$	$+00°\ 09'\ 34''$	17.30	2.25	17.29	2.28		14.04b	14.16a	14.12a	3.17	
889– 58026		$22^h\ 04^m\ 36.9^s$	$-02°\ 10'\ 09''$	16.78	2.22				13.84a		13.84a	2.94	
889– 28166		$22^h\ 08^m\ 25.5^s$	$+00°\ 22'\ 46''$	16.98	2.21	17.03	2.15		13.72b		13.72b	3.31	
889– 165454		$21^h\ 52^m\ 19.0^s$	$+02°\ 20'\ 39''$	17.53	2.19					16.3 :	16.3 :	1.23	
889– 12612		$22^h\ 10^m\ 27.2^s$	$+00°\ 47'\ 32''$	17.79	2.17					15.02b	15.02b	2.77	
889– 47948		$22^h\ 06^m\ 05.6^s$	$+01°\ 23'\ 54''$	17.08	2.15	17.02	2.25		13.82a		13.82a	3.20	
889– 29122		$22^h\ 08^m\ 15.8^s$	$-00°\ 39'\ 53''$	17.45	2.14				14.90c		14.90c	2.55	
889– 23794		$22^h\ 09^m\ 10.1^s$	$+01°\ 57'\ 02''$	16.48	2.13				13.49a		13.49a	2.99	
889– 69513		$22^h\ 03^m\ 20.0^s$	$-01°\ 48'\ 49''$	17.29	2.10				14.24a	14.38b	14.30a	2.99	
889– 124071		$21^h\ 56^m\ 55.3^s$	$-02°\ 06'\ 59''$	16.62	2.09				13.72a		13.72a	2.90	
889– 143310		$21^h\ 54^m\ 42.1^s$	$+00°\ 06'\ 29''$	17.39	2.09	17.62	2.01		14.59a		14.59a	3.03	
889– 73238		$22^h\ 03^m\ 02.8^s$	$+02°\ 30'\ 30''$	17.33	2.08				14.45b		14.45b	2.88	
889– 130840		$21^h\ 56^m\ 09.1^s$	$-01°\ 11'\ 42''$	17.36	2.08				14.29a		14.29a	3.07	
889– 146544		$21^h\ 54^m\ 27.9^s$	$+02°\ 04'\ 59''$	17.19	2.08				14.51b		14.51b	2.68	

Object	Other Name	α(1950.0)	δ(1950.0)	i^P_{Pal}	$(r-i)^P_{Pal}$	i^C_{Pal}	$(r-i)^C_{Pal}$	K_{Cam}	K_{Pal}	K_{Irtf}	K_{mean}	I–K[a]	V
889– 148063		$21^h\ 54^m\ 09.3^s$	$-02°\ 25'\ 11''$	17.65	2.08			14.64c			14.64c	3.01	
889– 139901		$21^h\ 55^m\ 14.3^s$	$+02°\ 31'\ 53''$	17.71	2.07				14.65a		14.65a	3.06	
889– 30215		$22^h\ 08^m\ 14.3^s$	$-01°\ 06'\ 05''$	17.50	2.06				14.48b		14.48b	3.02	
889– 37974		$22^h\ 07^m\ 16.8^s$	$+01°\ 34'\ 37''$	17.86	2.06			14.95b	14.96a		14.96a	2.90	
889– 49006		$22^h\ 05^m\ 50.4^s$	$+01°\ 03'\ 58''$	15.14	2.06				13.50a		13.50a	1.64	
889– 24940		$22^h\ 09^m\ 00.4^s$	$+01°\ 50'\ 15''$	17.11	2.05			14.47a			14.47a	2.64	
889– 39819		$22^h\ 06^m\ 57.7^s$	$-01°\ 37'\ 00''$	17.26	2.05				14.39a		14.39a	2.87	
889– 71784		$22^h\ 03^m\ 08.5^s$	$+02°\ 11'\ 31''$	17.54	2.05				14.67c		14.67c	2.87	
889– 88351		$22^h\ 01^m\ 06.9^s$	$+01°\ 45'\ 47''$	16.41	2.05				13.40b		13.40b	3.01	
889– 115453		$21^h\ 57^m\ 52.6^s$	$+00°\ 42'\ 08''$	17.69	2.05			14.47b	14.40b		14.44a	3.25	
889– 29102		$22^h\ 08^m\ 22.2^s$	$-00°\ 45'\ 29''$	17.99	2.04								
889– 85958		$22^h\ 01^m\ 30.5^s$	$+02°\ 17'\ 10''$	17.64	2.04			14.45a	14.38b		14.43a	3.21	
889– 35238		$22^h\ 07^m\ 34.6^s$	$+00°\ 40'\ 13''$	17.72	2.03				14.88c		14.88c	2.84	
889– 66147		$22^h\ 03^m\ 45.2^s$	$+00°\ 20'\ 04''$	17.71	2.03				14.70a		14.70a	3.01	
889– 91652		$22^h\ 00^m\ 42.0^s$	$-01°\ 01'\ 27''$	17.84	2.03				14.97b		14.97b	2.87	
889– 161837		$21^h\ 52^m\ 30.6^s$	$-00°\ 55'\ 52''$	16.82	2.03					13.79b	13.79b	3.03	
889– 15077		$22^h\ 10^m\ 11.6^s$	$+01°\ 24'\ 21''$	16.27	2.02					13.77a	13.77a	2.50	
889– 44702		$22^h\ 06^m\ 17.8^s$	$-02°\ 09'\ 22''$	17.56	2.02				14.57b		14.57b	2.99	
889– 57744		$22^h\ 04^m\ 49.2^s$	$+02°\ 02'\ 20''$	17.36	2.02					14.51b	14.51b	2.85	
889– 28246		$22^h\ 08^m\ 32.2^s$	$+00°\ 47'\ 08''$	17.91	2.01								
889– 106720		$21^h\ 59^m\ 00.4^s$	$+02°\ 15'\ 22''$	17.11	2.01					14.49c	14.49c	2.62	
889– 143541		$21^h\ 54^m\ 42.2^s$	$+01°\ 00'\ 02''$	17.86	2.01				14.82b		14.82b	3.04	
889– 169996		$21^h\ 51^m\ 36.6^s$	$-01°\ 51'\ 13''$	15.99	2.01					14.48c	14.48c	1.51	
889– 25557		$22^h\ 08^m\ 43.3^s$	$-00°\ 28'\ 29''$	17.09	2.00			14.31c			14.31c	2.78	
889– 30750		$22^h\ 08^m\ 15.4^s$	$+01°\ 28'\ 15''$	16.84	2.00					14.64b	14.64b	2.20	
889– 95696		$22^h\ 00^m\ 12.5^s$	$+00°\ 02'\ 22''$	17.49	2.00			14.77a		14.75a	14.75a	2.74	
889– 152307		$21^h\ 53^m\ 42.5^s$	$-01°\ 36'\ 59''$	14.55	2.00					11.66a	11.66a	2.89	
	(o) Field 890-1. M=N3647. S=F1342, F3493, R11414. Limits : 12.0 < I < 17.5, R–I ≥ 2.0												
890– 98528		$22^h\ 13^m\ 35.3^s$	$-01°\ 42'\ 02''$	16.51	2.84				14.82b		14.82b	1.69	
890– 36996		$22^h\ 24^m\ 53.0^s$	$+02°\ 11'\ 07''$	16.73	2.60				17.4 :		17.4 :	-0.67	
890– 58410		$22^h\ 20^m\ 52.6^s$	$-00°\ 39'\ 54''$	17.11	2.43				nd.		–	–	
890– 93715		$22^h\ 14^m\ 34.7^s$	$+01°\ 50'\ 24''$	16.73	2.37			13.36a	13.39a		13.37a	3.36	

Object	Other Name	α(1950.0)	δ(1950.0)	i^P_{Pal}	$(r-i)^P_{Pal}$	i^C_{Pal}	$(r-i)^C_{Pal}$	K_{Cam}	K_{Pal}	K_{Irtf}	K_{mean}	I–K[a]	V
890– 4633	891-137643	$22^h\ 31^m\ 05.0^s$	$-00°\ 31'\ 51''$	16.68	2.36			13.50a	13.54a		13.52a	3.16	
890– 60235		$22^h\ 20^m\ 32.0^s$	$+00°\ 14'\ 59''$	16.65	2.36	16.65	2.35	13.03a	13.05a	13.22b	13.10a	3.55	?
890– 85686		$22^h\ 16^m\ 01.3^s$	$-00°\ 31'\ 07''$	16.28	2.36				17.0 :		17.0 :	-0.72	
890– 85972		$22^h\ 15^m\ 55.7^s$	$+01°\ 22'\ 43''$	17.31	2.33				14.47a	14.52a	14.50a	2.81	
890– 49148		$22^h\ 22^m\ 33.3^s$	$+00°\ 18'\ 01''$	17.43	2.32			13.64b		13.73b	13.67a	3.76	
890– 8443		$22^h\ 30^m\ 17.2^s$	$-00°\ 14'\ 20''$	17.32	2.26				16.4 :		16.4 :	0.92	
890– 65370		$22^h\ 19^m\ 36.7^s$	$+00°\ 38'\ 43''$	17.05	2.24			13.89a	14.10b		14.00b	3.05	
890– 85785		$22^h\ 15^m\ 55.4^s$	$+00°\ 13'\ 21''$	16.78	2.23			13.22b	13.35a		13.30a	3.48	
890– 44486		$22^h\ 23^m\ 30.4^s$	$+02°\ 39'\ 42''$	16.48	2.22			13.33a	13.43a		13.38a	3.10	
890– 81856		$22^h\ 16^m\ 40.2^s$	$+01°\ 50'\ 47''$	17.23	2.20				14.55b		14.55b	2.68	
890– 42708		$22^h\ 23^m\ 43.0^s$	$+01°\ 38'\ 22''$	15.18	2.16			12.20a	12.07a		12.13a	3.05	
890– 16345		$22^h\ 28^m\ 43.7^s$	$-00°\ 17'\ 03''$	17.17	2.15				14.22a		14.22a	2.95	
890– 16591		$22^h\ 28^m\ 50.7^s$	$+01°\ 22'\ 10''$	16.59	2.15				13.71a		13.71a	2.88	
890– 33755		$22^h\ 25^m\ 22.8^s$	$+01°\ 54'\ 58''$	16.91	2.15			14.36a			14.36a	2.55	
890– 8477		$22^h\ 30^m\ 17.0^s$	$+00°\ 02'\ 53''$	17.40	2.14				14.78b		14.78b	2.62	
890– 68883		$22^h\ 18^m\ 57.5^s$	$-00°\ 32'\ 19''$	16.41	2.13			13.40a			13.40a	3.01	
890– 63029		$22^h\ 20^m\ 06.5^s$	$+02°\ 00'\ 10''$	17.43	2.12			14.80a			14.80a	2.63	
890– 18103		$22^h\ 28^m\ 33.2^s$	$+01°\ 24'\ 22''$	16.63	2.10			13.94a			13.94a	2.69	
890– 26475		$22^h\ 26^m\ 46.2^s$	$+00°\ 24'\ 44''$	17.21	2.10			14.30b		14.53b	14.42b	2.79	
890– 34884		$22^h\ 25^m\ 09.0^s$	$-01°\ 03'\ 20''$	16.33	2.10	16.71	2.17	13.11a			13.11a	3.60	
890– 86893		$22^h\ 15^m\ 50.2^s$	$+01°\ 57'\ 37''$	16.58	2.10					13.66a	13.66a	2.92	
890– 106100		$22^h\ 12^m\ 26.1^s$	$+00°\ 37'\ 39''$	16.17	2.10					13.20b	13.20b	2.97	
890– 27207		$22^h\ 26^m\ 40.0^s$	$+00°\ 17'\ 50''$	17.36	2.09								
890– 42256		$22^h\ 23^m\ 44.2^s$	$-01°\ 21'\ 26''$	16.36	2.07					13.53a	13.53a	2.83	
890– 78174		$22^h\ 17^m\ 21.9^s$	$-00°\ 02'\ 50''$	17.46	2.07					14.48b	14.48b	2.98	
890– 78993		$22^h\ 17^m\ 12.7^s$	$-00°\ 19'\ 29''$	17.43	2.07					14.65a	14.65a	2.78	
890– 30621		$22^h\ 25^m\ 59.9^s$	$+02°\ 01'\ 24''$	16.36	2.06					13.49a	13.49a	2.87	
890– 41743		$22^h\ 23^m\ 56.1^s$	$+00°\ 40'\ 18''$	14.35	2.05					11.78a	11.78a	2.57	
890– 48834		$22^h\ 22^m\ 30.2^s$	$-01°\ 33'\ 37''$	16.66	2.05					14.10a	14.10a	2.56	
890– 71063		$22^h\ 18^m\ 41.2^s$	$+02°\ 13'\ 28''$	17.19	2.05					14.78b	14.78b	2.41	
890– 71748		$22^h\ 18^m\ 30.1^s$	$+01°\ 31'\ 40''$	16.70	2.05					13.75a	13.75a	2.95	
890– 30561		$22^h\ 26^m\ 00.4^s$	$+01°\ 31'\ 49''$	17.43	2.04					15.27c	15.27c	2.16	

Object	Other Name	α(1950.0)	δ(1950.0)	i^P_{Pal}	$(r-i)^P_{Pal}$	i^C_{Pal}	$(r-i)^C_{Pal}$	K_{Cam}	K_{Pal}	K_{Irtf}	K_{mean}	I–K[a]	V
890- 32112		$22^h\ 25^m\ 46.2^s$	$+01°\ 29'\ 05''$	17.02	2.03					14.44c	14.44c	2.58	
890- 50904		$22^h\ 22^m\ 11.3^s$	$+00°\ 44'\ 22''$	17.27	2.03					14.93b	14.93b	2.34	
890- 64905		$22^h\ 19^m\ 35.5^s$	$-02°\ 12'\ 22''$	16.84	2.03					nd.	–	–	
890- 102488		$22^h\ 13^m\ 06.0^s$	$+00°\ 45'\ 37''$	17.44	2.03					14.35b	14.35b	3.09	
890- 20278		$22^h\ 27^m\ 59.1^s$	$+00°\ 20'\ 43''$	16.71	2.02					14.16a	14.16a	2.55	
890- 41624		$22^h\ 23^m\ 53.0^s$	$+00°\ 05'\ 57''$	16.50	2.02					14.82b	14.82b	1.68	
890- 104767		$22^h\ 12^m\ 30.8^s$	$-01°\ 43'\ 35''$	16.95	2.02					14.27b	14.27b	2.68	
890- 49208		$22^h\ 22^m\ 31.8^s$	$+00°\ 36'\ 43''$	17.29	2.01					14.34b	14.34b	2.95	
890- 90478		$22^h\ 15^m\ 15.6^s$	$+02°\ 31'\ 06''$	17.42	2.01					14.81b	14.81b	2.61	
890- 17129		$22^h\ 28^m\ 39.2^s$	$-00°\ 10'\ 55''$	16.26	2.00					13.88a	13.88a	2.38	
890- 19502		$22^h\ 28^m\ 08.7^s$	$+00°\ 19'\ 17''$	17.26	2.00					14.90a	14.90a	2.36	
890- 82747		$22^h\ 16^m\ 30.0^s$	$+02°\ 05'\ 15''$	15.32	2.00					13.01a	13.01a	2.31	
	(p) Field 890-2. M=N3647. S=F1342, F3493, R11414. Limits : 17.5 < I < 18.0, R–I ≥ 2.10												
890- 33719		$22^h\ 25^m\ 22.3^s$	$+01°\ 43'\ 35''$	17.50	2.30			14.43a	14.49a		14.46a	3.04	
890- 70603		$22^h\ 18^m\ 42.7^s$	$-00°\ 37'\ 24''$	17.56	2.30			13.78b	13.74a	13.96a	13.83b	3.73	?
890- 98588		$22^h\ 13^m\ 37.1^s$	$-01°\ 19'\ 45''$	17.67	2.29	17.73	2.16		14.82b		14.82b	2.91	
890- 17985		$22^h\ 28^m\ 25.0^s$	$+00°\ 39'\ 49''$	17.55	2.20				nd.		–	–	
890- 100189		$22^h\ 13^m\ 16.2^s$	$-02°\ 24'\ 15''$	17.82	2.20				15.12b		15.12b	2.70	
890- 39507		$22^h\ 24^m\ 18.8^s$	$+02°\ 23'\ 58''$	17.73	2.19				nd.		–	–	
890- 82895		$22^h\ 16^m\ 22.4^s$	$-02°\ 15'\ 45''$	17.76	2.19				14.77a		14.77a	2.99	
890- 98229		$22^h\ 13^m\ 52.3^s$	$+01°\ 49'\ 34''$	17.82	2.17				nd.		–	–	
890- 32436		$22^h\ 25^m\ 35.9^s$	$-01°\ 36'\ 05''$	17.66	2.15				15.00c		15.00c	2.66	
890- 33009		$22^h\ 25^m\ 31.9^s$	$+02°\ 23'\ 06''$	17.59	2.15				16.3 :		16.3 :	1.29	
890- 81745		$22^h\ 16^m\ 41.1^s$	$+01°\ 17'\ 31''$	17.57	2.15			14.73a			14.73a	2.84	
890- 48868		$22^h\ 22^m\ 31.4^s$	$-01°\ 23'\ 13''$	17.87	2.14			14.77a			14.77a	3.10	
890- 24370		$22^h\ 27^m\ 18.5^s$	$+01°\ 36'\ 45''$	17.57	2.13			15.06b			15.06b	2.51	
890- 56599		$22^h\ 21^m\ 09.3^s$	$-01°\ 26'\ 21''$	17.72	2.13			14.80c			14.80c	2.92	
890- 30496		$22^h\ 26^m\ 03.9^s$	$+01°\ 06'\ 21''$	17.84	2.11			14.96a			14.96a	2.88	
890- 115722		$22^h\ 10^m\ 55.9^s$	$+01°\ 38'\ 13''$	17.83	2.11								
890- 16291		$22^h\ 28^m\ 47.6^s$	$-00°\ 38'\ 55''$	17.82	2.10								
890- 26301		$22^h\ 26^m\ 49.4^s$	$-00°\ 54'\ 31''$	17.71	2.10			14.93a			14.93a	2.78	
890- 94576		$22^h\ 14^m\ 30.6^s$	$+02°\ 05'\ 57''$	17.51	2.10								

Object	Other Name	α(1950.0)	δ(1950.0)	i^P_{Pal}	$(r-i)^P_{Pal}$	i^C_{Pal}	$(r-i)^C_{Pal}$	K_{Cam}	K_{Pal}	K_{Irtf}	K_{mean}	I–K[a]	V
890– 99209		$22^h\ 13^m\ 44.7^s$	$+02°\ 24'\ 38''$	17.86	2.10								
(q) Field 891-1. M=N3584. S=F742. Limits : 12.0 < I < 17.0, R–I ≥ 2.14													
891– 94040		$22^h\ 37^m\ 27.2^s$	$-01°\ 45'\ 08''$	16.11	2.30					nd.	–	–	
891– 15871		$22^h\ 49^m\ 28.2^s$	$-00°\ 45'\ 19''$	16.55	2.24					13.73a	13.73a	2.82	
891– 102678		$22^h\ 36^m\ 17.9^s$	$+01°\ 56'\ 48''$	16.78	2.24					13.66a	13.66a	3.12	
891– 137643	890- 4633	$22^h\ 31^m\ 05.0^s$	$-00°\ 31'\ 52''$	16.69	2.22			13.50a	13.54a		13.52a	3.17	
891– 31483		$22^h\ 47^m\ 01.5^s$	$+00°\ 10'\ 05''$	16.54	2.20					13.51b	13.51b	3.03	
891– 109182		$22^h\ 35^m\ 05.7^s$	$-00°\ 55'\ 25''$	16.45	2.19					12.98b	12.98b	3.47	
891– 84585		$22^h\ 39^m\ 00.6^s$	$+00°\ 23'\ 34''$	13.58	2.15								
891– 1689		$22^h\ 51^m\ 48.2^s$	$+00°\ 24'\ 52''$	15.53	2.14					13.55a	13.55a	1.98	
891– 5542		$22^h\ 51^m\ 07.3^s$	$-00°\ 15'\ 33''$	16.53	2.14					14.11a	14.11a	2.42	
891– 33798		$22^h\ 46^m\ 49.7^s$	$+02°\ 09'\ 37''$	16.54	2.14					13.71b	13.71b	2.83	

TABLE 5.4. Miscellaneous interesting objects (I–K > 3.0) not part of Survey Sample.

Notes to Table 5.4

a - The I–K colour is calculated using i^C_{Pal} where available, and otherwise using i^P_{Pal} .

b - Discovered as an infrared companion to the star TVLM 513-42404.

Object	Other Name	α(1950.0)	δ(1950.0)	i^P_{Pal}	$(r-i)^P_{Pal}$	i^C_{Pal}	$(r-i)^C_{Pal}$	K_{Cam}	K_{Pal}	K_{Irtf}	K_{mean}	I–K[a]	V
213– 2005		$10^h\ 18^m\ 19.2^s$	+51° 10′ 11″	15.88	2.93	16.20	2.44		12.35a	12.31a	12.33a	3.87	
213– 8240		$10^h\ 14^m\ 12.3^s$	+50° 43′ 15″	17.16	1.98	17.20	2.38		13.72a	13.63a	13.68a	3.52	
262– 14557		$10^h\ 01^m\ 24.9^s$	+43° 19′ 00″	17.80	2.33	17.87	2.22			14.76c	14.76c	3.11	
262– 584		$10^h\ 05^m\ 15.0^s$	+45° 53′ 19″	17.71	2.29	17.76	2.10			14.31a	14.31a	3.45	
263– 78128	262- 3688	$10^h\ 04^m\ 54.5^s$	+47° 03′ 09″	17.23	2.04				13.80a		13.80a	3.43	
513– 42404B		$15^h\ 00^m\ 10.3^s$	+25° 37′ 49″			18.52	2.43		14.16b		14.16b	4.36	
829– 24380		$01^h\ 52^m\ 08.9^s$	−02° 31′ 21″	16.93	2.46			13.60a			13.60a	3.33	
829– 20237		$01^h\ 51^m\ 19.1^s$	−02° 47′ 34″	17.02	2.53			13.71a			13.71a	3.31	
831– 99002		$02^h\ 40^m\ 35.4^s$	+00° 00′ 42″	17.74	lim	17.88	2.08	14.89b	14.73b		14.80b	3.08	
831– 30214		$02^h\ 31^m\ 37.0^s$	−02° 09′ 53″	16.64	2.26	16.69			13.55a		13.55a	3.14	
831– 68968		$02^h\ 36^m\ 46.2^s$	−02° 20′ 02″	17.85	2.21			14.85a			14.85a	3.00	
831– 71037		$02^h\ 37^m\ 04.1^s$	+00° 00′ 35″	17.82	2.01			14.8 b			14.80b	3.02	
831– 56633		$02^h\ 35^m\ 08.2^s$	+00° 49′ 33″	17.60	1.98	17.60			14.44c		14.44c	3.16	
831– 150173		$02^h\ 47^m\ 07.3^s$	−01° 36′ 00″	17.36	1.90				14.19a		14.19a	3.17	
832– 65814		$02^h\ 53^m\ 10.4^s$	+00° 35′ 45″	17.17	2.17			13.99a			13.99a	3.18	
832– 65280		$02^h\ 53^m\ 21.5^s$	+00° 38′ 53″	17.56	2.17					14.42b	14.42b	3.14	
832– 44064		$02^h\ 59^m\ 39.3^s$	−00° 55′ 24″	17.94	2.16			14.77b			14.77b	3.17	
832– 44554		$02^h\ 59^m\ 25.2^s$	−01° 02′ 46″	17.41	2.15					14.21b	14.21b	3.20	
832– 47250		$02^h\ 58^m\ 40.6^s$	−00° 31′ 03″	17.79	2.14			14.54a			14.54a	3.25	
832– 59849		$02^h\ 54^m\ 56.8^s$	−01° 54′ 40″	17.50	2.11			14.33a			14.33a	3.17	
832– 38078		$03^h\ 01^m\ 27.5^s$	+00° 34′ 10″	13.90	2.09					10.83a	10.83a	3.07	
832– 68722		$02^h\ 52^m\ 17.9^s$	−02° 12′ 29″	17.91	2.09			14.68a			14.68a	3.23	
832– 44203		$02^h\ 59^m\ 39.2^s$	+00° 56′ 22″	17.99	2.07					14.93a	14.93a	3.06	
O832– 68408		$03^h\ 00^m\ 38.6^s$	+00° 42′ 37″	13.74	2.77			10.15a		10.47a	10.21c	3.53	?
868– 110639		$15^h\ 07^m\ 41.2^s$	−02° 29′ 47″	15.60	2.75	15.79	2.40	11.33a	11.30a	11.44a	11.37a	4.42	?
868– 3405		$14^h\ 48^m\ 25.9^s$	−02° 17′ 44″	17.52	2.76	17.92	1.91	14.88a			14.88a	3.04	
868– 5585		$14^h\ 48^m\ 57.2^s$	−00° 07′ 17″	16.82	2.67	17.04	2.32		13.95a		13.95a	3.09	
868– 93316		$15^h\ 04^m\ 41.7^s$	−01° 20′ 13″	17.75	2.49			14.40a			14.40a	3.35	
868– 105679		$15^h\ 06^m\ 56.8^s$	−00° 10′ 35″	17.86	2.05			14.79a			14.79a	3.07	
889– 7319		$22^h\ 11^m\ 03.9^s$	−01° 09′ 18″	17.84	2.07				14.82a		14.82a	3.02	
889– 88099		$22^h\ 01^m\ 09.2^s$	+00° 41′ 04″	17.35	2.04			14.21a	14.15a		14.18a	3.17	
890– 20645		$22^h\ 28^m\ 03.8^s$	+02° 33′ 09″	16.64	2.17			13.20a	13.32a		13.26a	3.38	
890– 2923		$22^h\ 31^m\ 20.4^s$	−02° 20′ 06″	15.33	2.10	15.58	2.14	12.48a	12.48a		12.48a	3.10	
890– 36265		$22^h\ 25^m\ 03.2^s$	+02° 46′ 24″	17.04	2.06			14.03a			14.03a	3.01	

Table 5.5 - The Stellar Luminosity Function.

Binning 1						Binning 2					
M_{Bol}[a]	Φ_0^b ($pc^{-3}mag.^{-1}$)	$\sigma(\Phi_0)$[b]	#	Volume[c] (10^3pc^3)	Compl[d].	M_{Bol}	Φ_0 ($pc^{-3}mag.^{-1}$)	$\sigma(\Phi_0)$	#	Volume (10^3pc^3)	Compl.
8.75	22.197	1.783	155	12.01	-	9.00	27.007	1.431	356	30.58	-
9.25	25.946	1.118	539	43.64	-	9.50	27.622	1.043	702	52.72	-
9.75	32.074	1.052	930	58.97	-	10.00	30.879	0.997	960	63.25	-
10.25	24.944	0.871	820	66.15	-	10.50	21.554	0.798	730	68.11	-
10.75	16.190	0.684	560	69.42	-	11.00	13.123	0.619	449	70.29	-
11.25	11.419	0.629	330	57.75	-	11.50	10.567	0.736	206	38.64	-
11.75	8.779	0.801	120	25.70	-	12.00	7.658	0.943	66	16.99	-
12.25	9.561	1.313	53	11.18	-	12.50	1.335	0.217	38	8.47	70.6%
12.75	8.100	1.909	18	5.22	75.8%	13.00	6.018	2.006	9	3.69	79.5%
13.25	8.890	2.963	9	2.28	82.7%	13.50	7.612	3.108	6	1.57	82.3%
13.75	3.589	2.538	2	0.71	85.7%	14.00	0.000	6.956	0	0.29	88.7%
14.25	0.000	8.057	0	0.111	91.3%	14.50	0.000	7.967	0	0.042	93.3%
14.75	0.000	8.803	0	0.0155	95.0%						

Notes to Table

[a] - Bolometric magnitude of bin centre. All bins have width 0.5 magnitudes.

[b] - Values of Φ_0 and $\sigma(\Phi_0)$ are $\times 10^3$.

[c] - Volume sampled by survey (in 10^3 cubic parsecs) for a star with M_{Bol} equal to the bin centre value.

[d] - *Blank entries* - indicate the data are from the photographic LF of Paper I, and are better than 90% complete. *Numbered entries* - indicate infrared LF data, which have been corrected for incompleteness as described in the text. Each entry gives the mean correction for incompleteness applied to that bin.

Table 5.6 - Mass Densities in the Solar Neighbourhood.

10^{10} years.				10^{9} years.			
m^a ($M_\odot$)	dm ($M_\odot$)	Ψ_o ($M_\odot{}^{-1}pc^{-3}$)	Υ_0 (pc^{-3})	m ($M_\odot$)	dm ($M_\odot$)	Ψ_o ($M_\odot{}^{-1}pc^{-3}$)	Υ_0 (pc^{-3})
Burrows, Hubbard & Lunine (1989 - BHL) Model B.							
0.3696	0.0700	0.157	0.0579	0.3696	0.0700	0.157	0.0579
0.3018	0.0630	0.206	0.0621	0.3018	0.0630	0.206	0.0621
0.2440	0.0531	0.303	0.0738	0.2440	0.0531	0.303	0.0738
0.1955	0.0435	0.287	0.0561	0.1955	0.0435	0.287	0.0561
0.1573	0.0330	0.246	0.0386	0.1573	0.0330	0.245	0.0386
0.1292	0.0237	0.242	0.0313	0.1292	0.0237	0.241	0.0312
0.1097	0.0157	0.281	0.0308	0.1095	0.0159	0.278	0.0304
0.0973	0.0095	0.510	0.0496	0.0969	0.0099	0.488	0.0473
0.0902	0.0053	0.781	0.0705	0.0891	0.0064	0.644	0.0574
0.0864	0.0028	1.621	0.1400	0.0838	0.0046	0.966	0.0810
0.0842	0.0018	0.990	0.0834	0.0796	0.0038	0.470	0.0374
		$\int_{min}^{0.4} \Upsilon_0 dm = 0.0179$				$\int_{min}^{0.4} \Upsilon_0 dm = 0.0179$	
D'Antona & Mazzitelli (1985 - D&M) Model.							
0.4309	0.0770	0.144	0.0621	0.4309	0.0770	0.144	0.0621
0.3532	0.0769	0.168	0.0592	0.3532	0.0769	0.168	0.0593
0.2796	0.0681	0.235	0.0657	0.2796	0.0681	0.235	0.0657
0.2184	0.0531	0.234	0.0511	0.2184	0.0531	0.234	0.0511
0.1739	0.0366	0.222	0.0387	0.1739	0.0366	0.222	0.0387
0.1440	0.0243	0.236	0.0341	0.1440	0.0243	0.237	0.0342
0.1241	0.0166	0.267	0.0331	0.1243	0.0164	0.270	0.0336
0.1101	0.0118	0.406	0.0446	0.1105	0.0116	0.413	0.0456
0.1001	0.0085	0.481	0.0482	0.1008	0.0086	0.477	0.0480
0.0929	0.0060	0.747	0.0694	0.0930	0.0070	0.640	0.0595
0.0880	0.0040	0.456	0.0401	0.0862	0.0068	0.264	0.0228
		$\int_{min}^{0.4} \Upsilon_0 dm = 0.0161$				$\int_{min}^{0.4} \Upsilon_0 dm = 0.0161$	

Notes to Table

a - These bins correspond to the eleven LF entries of 'Binning 1' in Table 5.5. That is they correspond to bins from $M_{Bol} = 8.75$ to 13.75 of width 0.5 magnitudes.

Table 5.7 - Mass Densities for Arbitrary Mass Functions below $0.08M_\odot$.

k	Mass Densities ($M_\odot pc^{-3}$)				
	$\int_{0.04}^{0.08}$	$\int_{0.02}^{0.08}$	$\int_{0.01}^{0.08}$	$\int_{0.005}^{0.08}$	$\int_{0.001}^{0.08}$
0	0.0011	0.0014	0.0014	0.0014	0.0014
1	0.0018	0.0027	0.0032	0.0034	0.0036
2	0.0031	0.0062	0.0094	0.0125	0.020
2	0.0042	0.010	0.018	0.030	0.080
3	0.0056	0.017	0.039	0.084	0.44
4	0.011	0.053	0.221	0.90	22.5

Figure Captions

Figure 5.1 - The panels show measured magnitude differences for stars observed in common between (a) Palomar and Las Campanas, and (b) Palomar and the IRTF.

Figure 5.2 - Plot of $(r-i)_{Pal}$ versus I–K colour. The large solid squares are CCD $(r-i)^C_{Pal}$ photometry, the small circles are photographic $(r-i)^C_{Pal}$. The dotted line is a main sequence for old disk stars due to Leggett (1992), the dot-dashed line is a main sequence due to Bessell (1992). The solid line is a fit to the CCD data, with the Leggett and Bessell sequences being used to constrain the fit for blue stars where no CCD photometry is available. The fit gives;

$$(r-i)_{Pal} = -3.46255+3.47941(r-i)_{Pal}-0.669576(r-i)_{Pal}{}^2 0.0423648(r-i)_{Pal}{}^3$$

Figure 5.3 - The Stellar Luminosity Function. The triangles and squares are two binnings of our infrared luminosity function. The circles and crosses are two binnings of our photographic luminosity function.

Figure 5.4 - Comparison of our Luminosity Function with Previous Work. (a) The filled squares are the LF due to WJK, the filled circles the LF of HM92 converted to M_{Bol} as described in the text. We show only one binning of our data. (b) The filled squares are the LF of Hawkine & Bessell (1988). The Filled circles are the LF of Reid (1987).

Figure 5.5 - Mass-Luminosity Relations. The symbols show the results of the models listed. The solid line is the empirical relation of Smith (1983). The dot-dashed line is the empirical relation of HM92 converted to M_{Bol} as described in the text.

Figure 5.6 - BC_K as a function of M_K. The upper line is our fit to the BC_K data of Paper II, the lower line is the relation assumed by HM92. The fit gives

$$BC_K = 2.06980 + 0.105137\,M_K \quad \text{with} \sigma(BC_K) = 0.11$$

Figure 5.7 - The Stellar Mass Function. Each pair of panels shows the MF estimated for a given adopted mass-luminosity relation – one panel showing the adopted relation (dotted line), the other the resulting MF. The Scalo (1986) MF is shown

as a dotted line, the Reid (1987) MF as a dot-dashed line, and a Salpeter MF (normalised to the Scalo function at $0.5M_{\odot}$) as a dashed line.

Figure 5.8 - Differential Mass Densities. Plot of the differential mass densities are shown for the D&M model and BHL model B.

Figure 5.1(a)

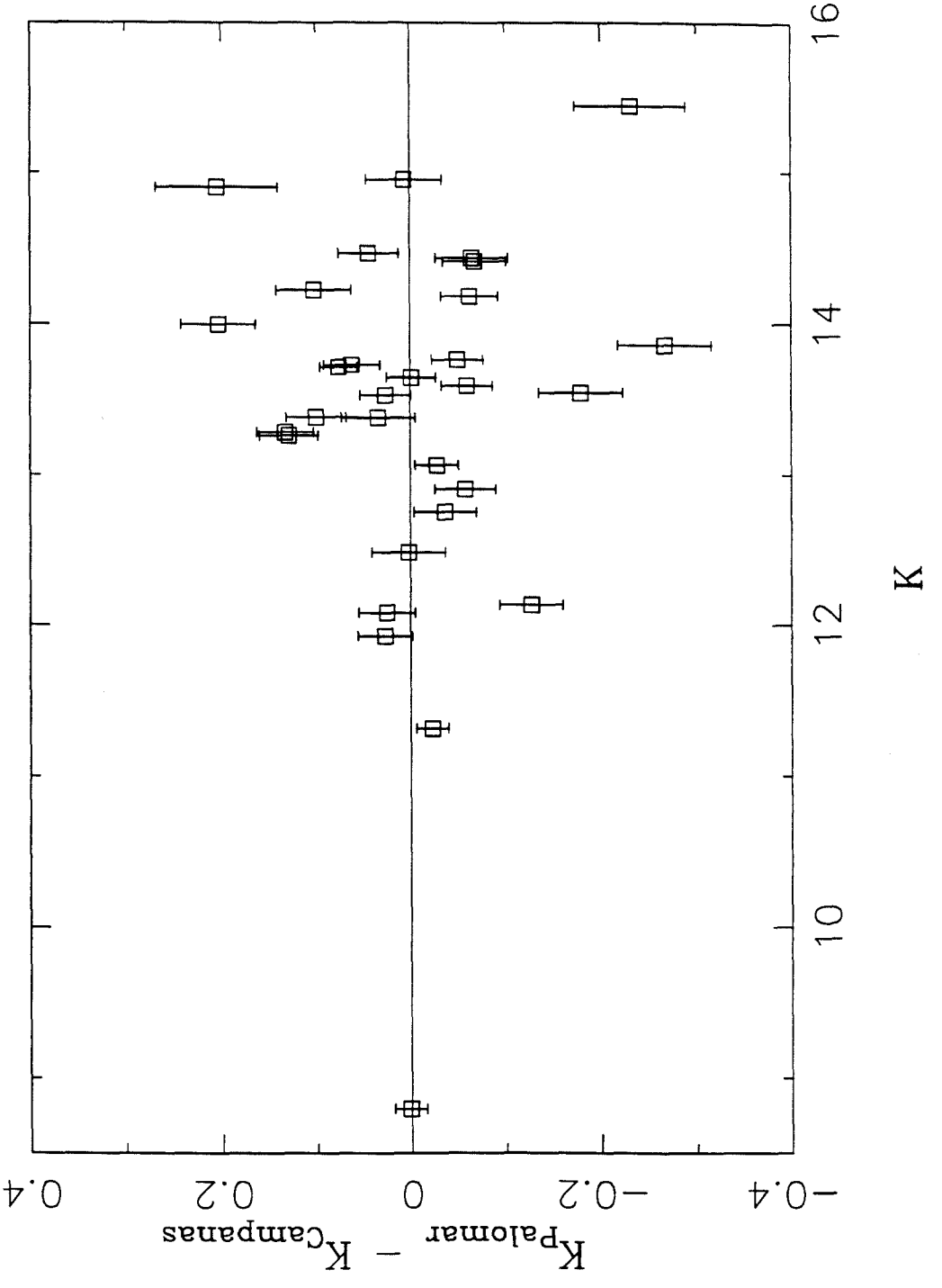

Figure 5.1(b)

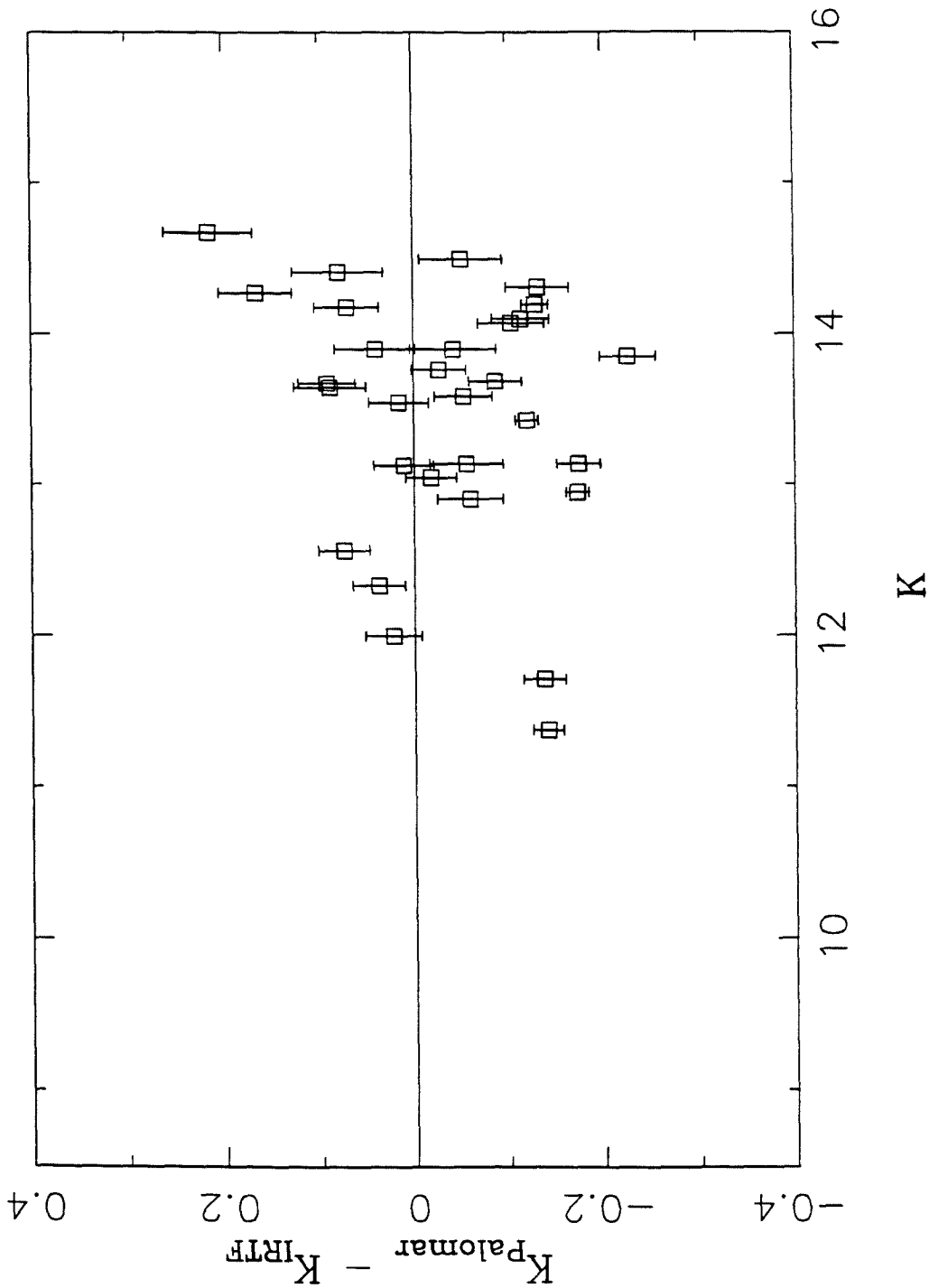

Figure 5.2

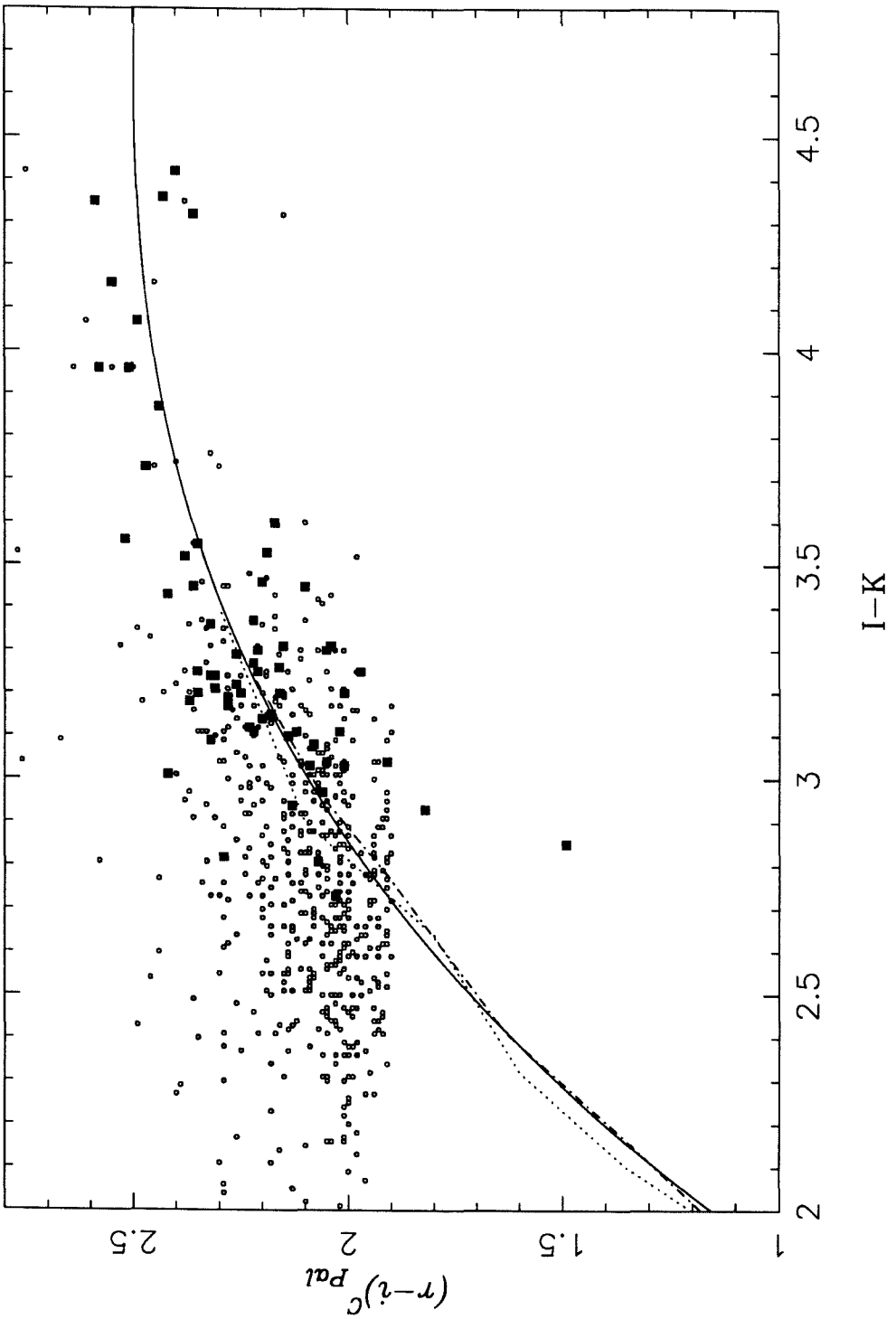

Figure 5.3

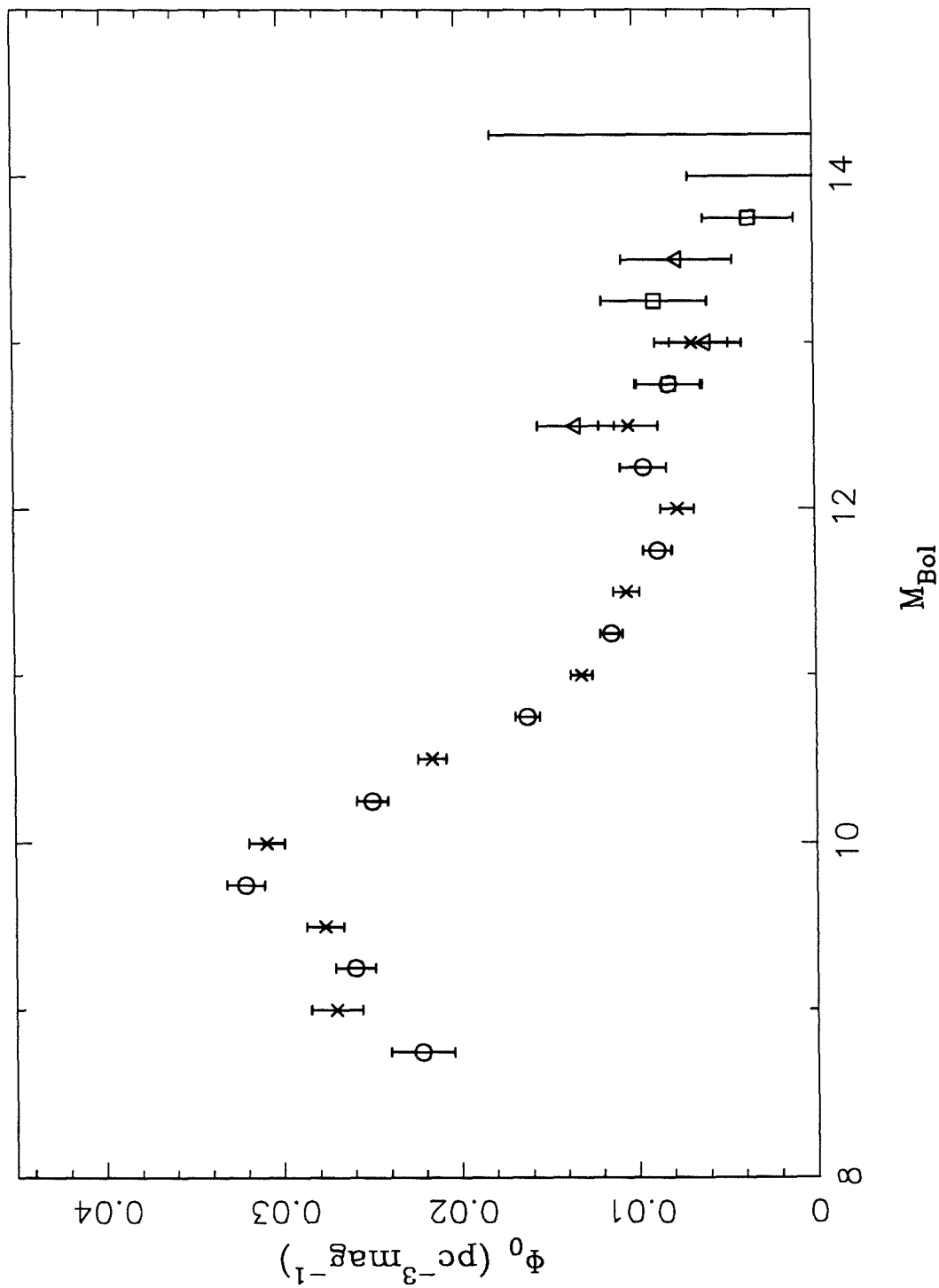

Figure 5.4(a)

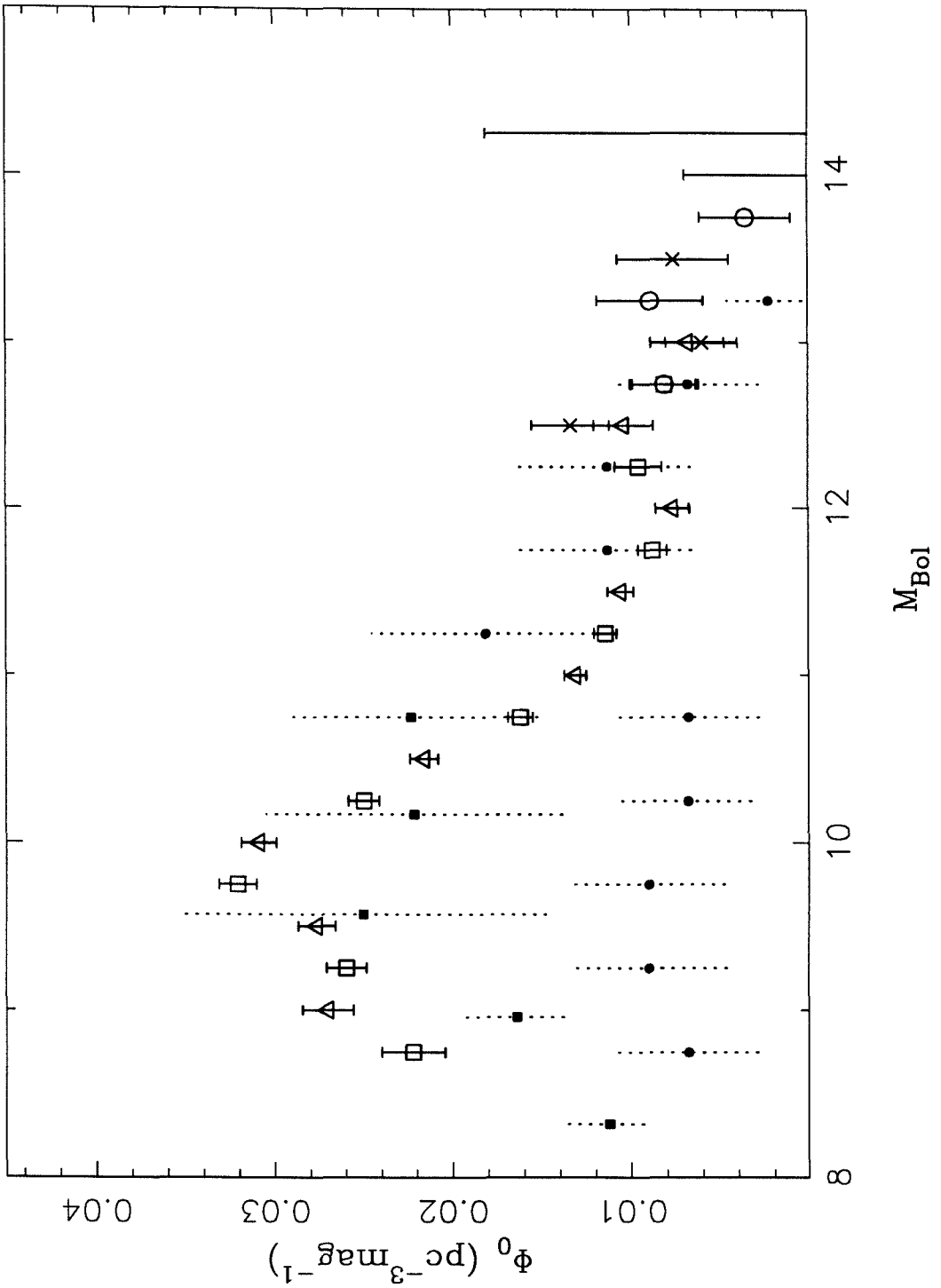

Figure 5.4(b)

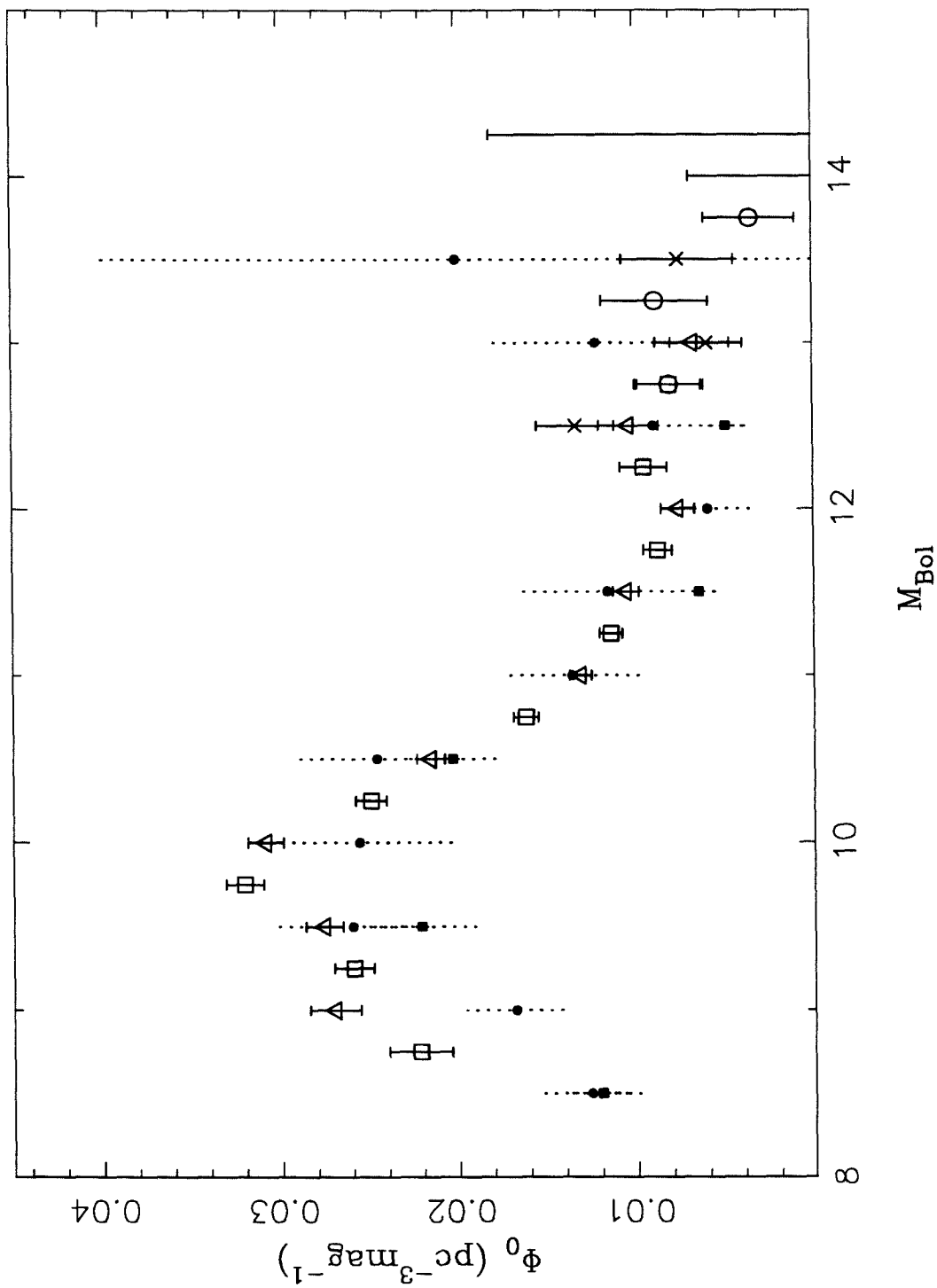

Figure 5.5

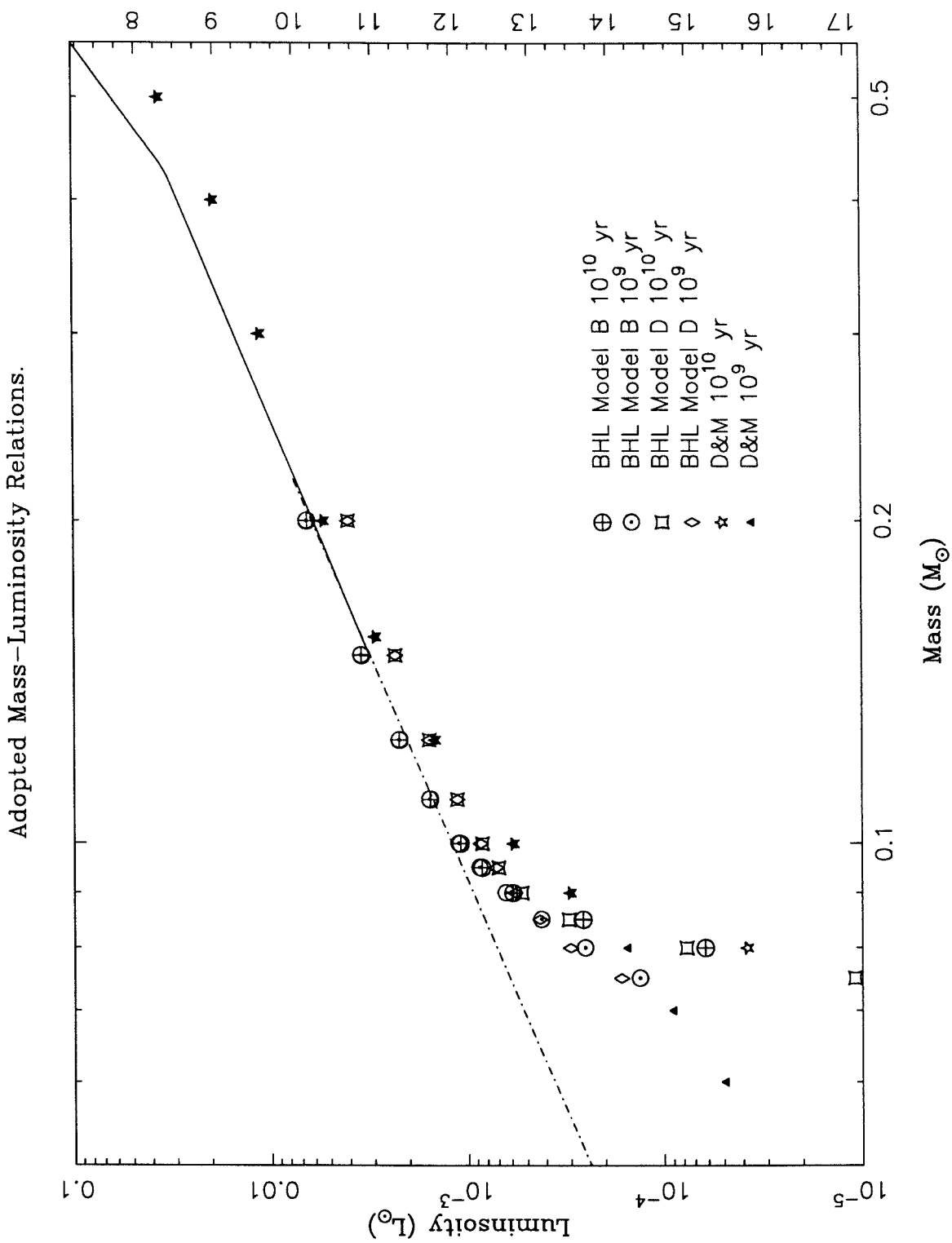
Adopted Mass–Luminosity Relations.
M_{Bol}
8
9
10
11
12
13
14
15
16
17
Luminosity ($L_\odot$)
10^{-5}
10^{-4}
10^{-3}
0.01
0.1
Mass ($M_\odot$)
0.1
0.2
0.5
BHL Model B 10^{10} yr
BHL Model B 10^{9} yr
BHL Model D 10^{10} yr
BHL Model D 10^{9} yr
D&M 10^{10} yr
D&M 10^{9} yr

Figure 5.6

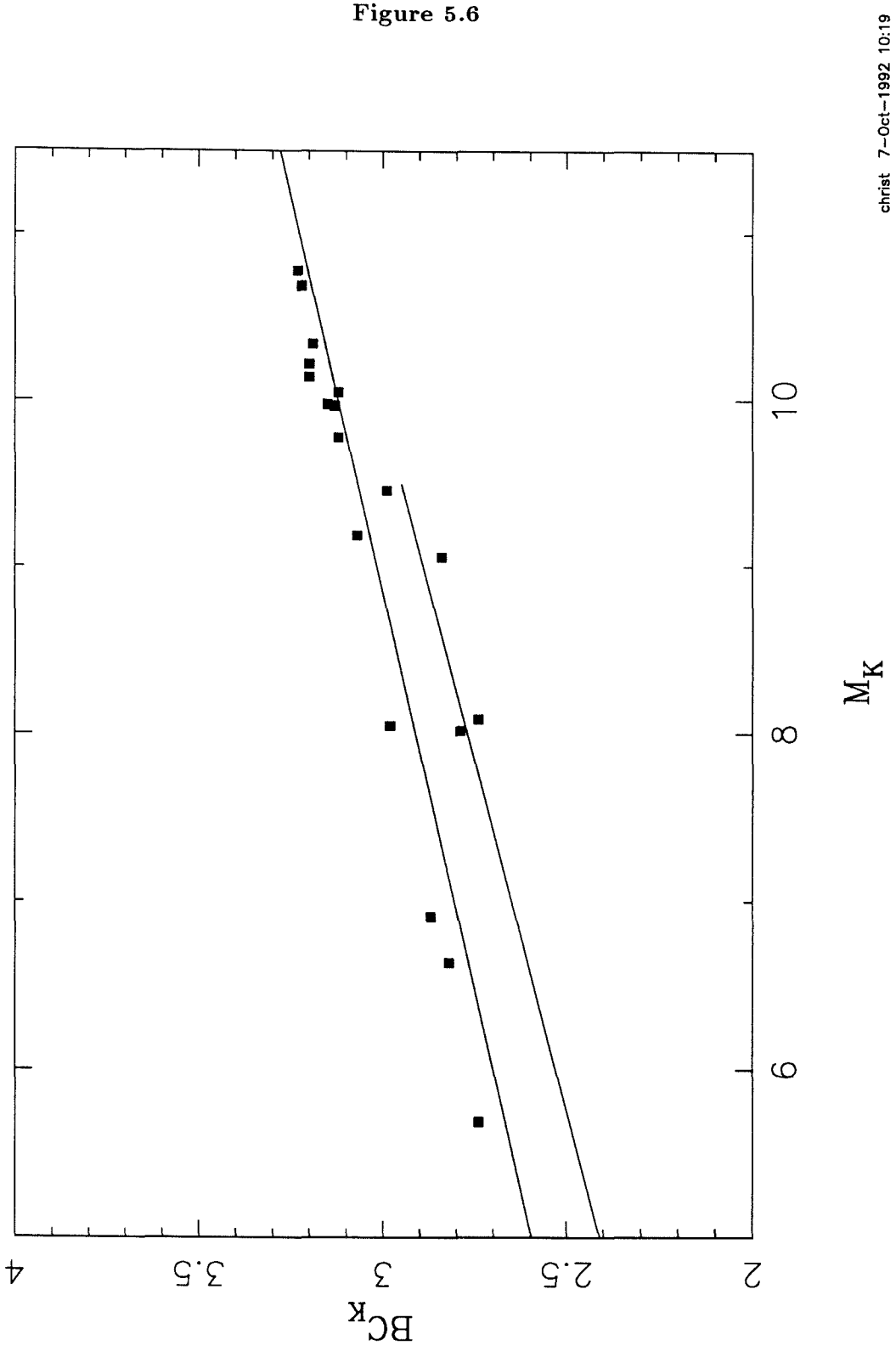

Figure 5.7(a)-(c)

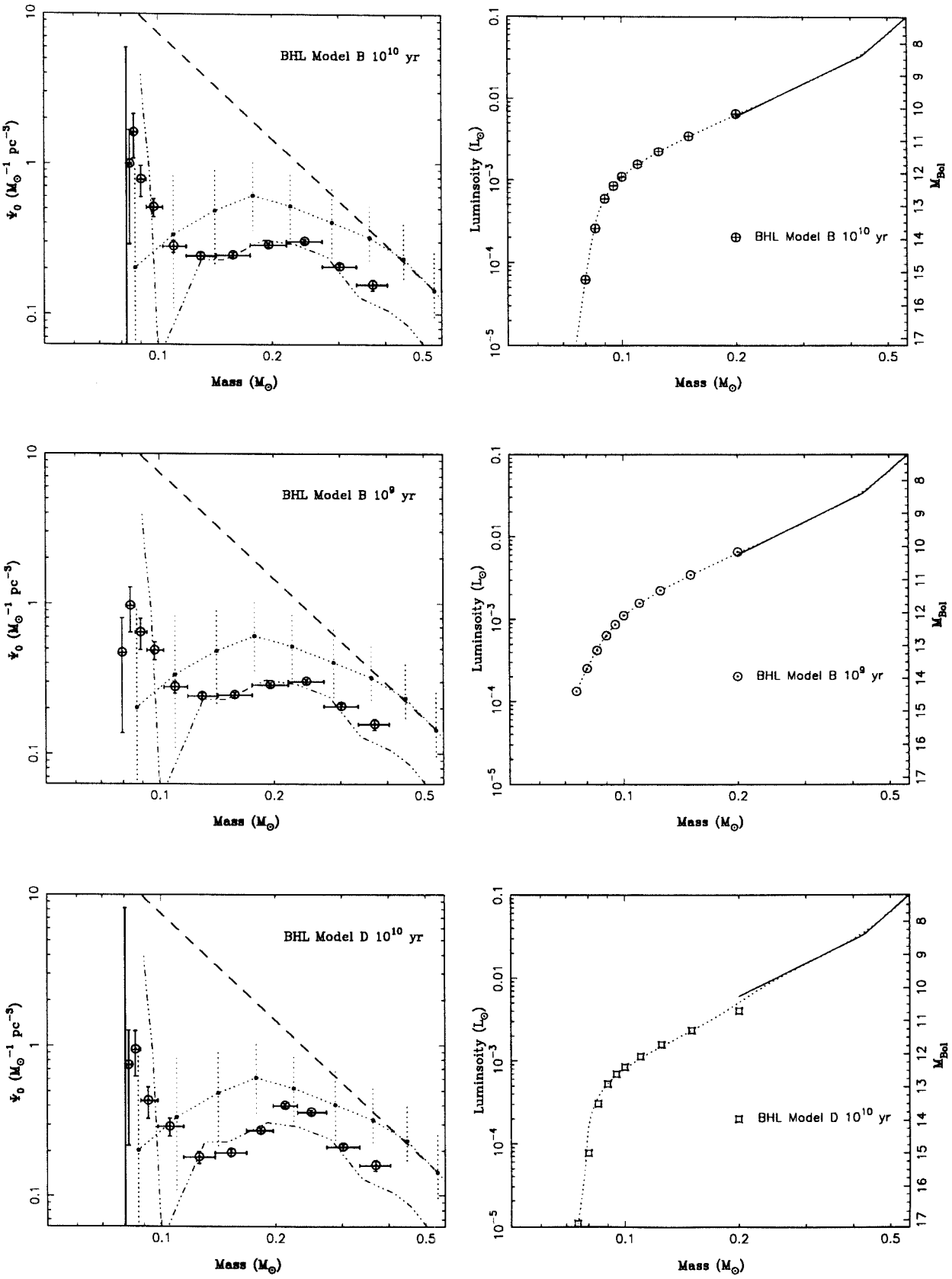
BHL Model B 10^10 yr
Ψ0 (M⊙^-1 pc^-3)
Mass (M⊙)
Luminsoity (L⊙)
MBol
BHL Model B 10^9 yr
BHL Model D 10^10 yr

Figure 5.7(d)-(f)

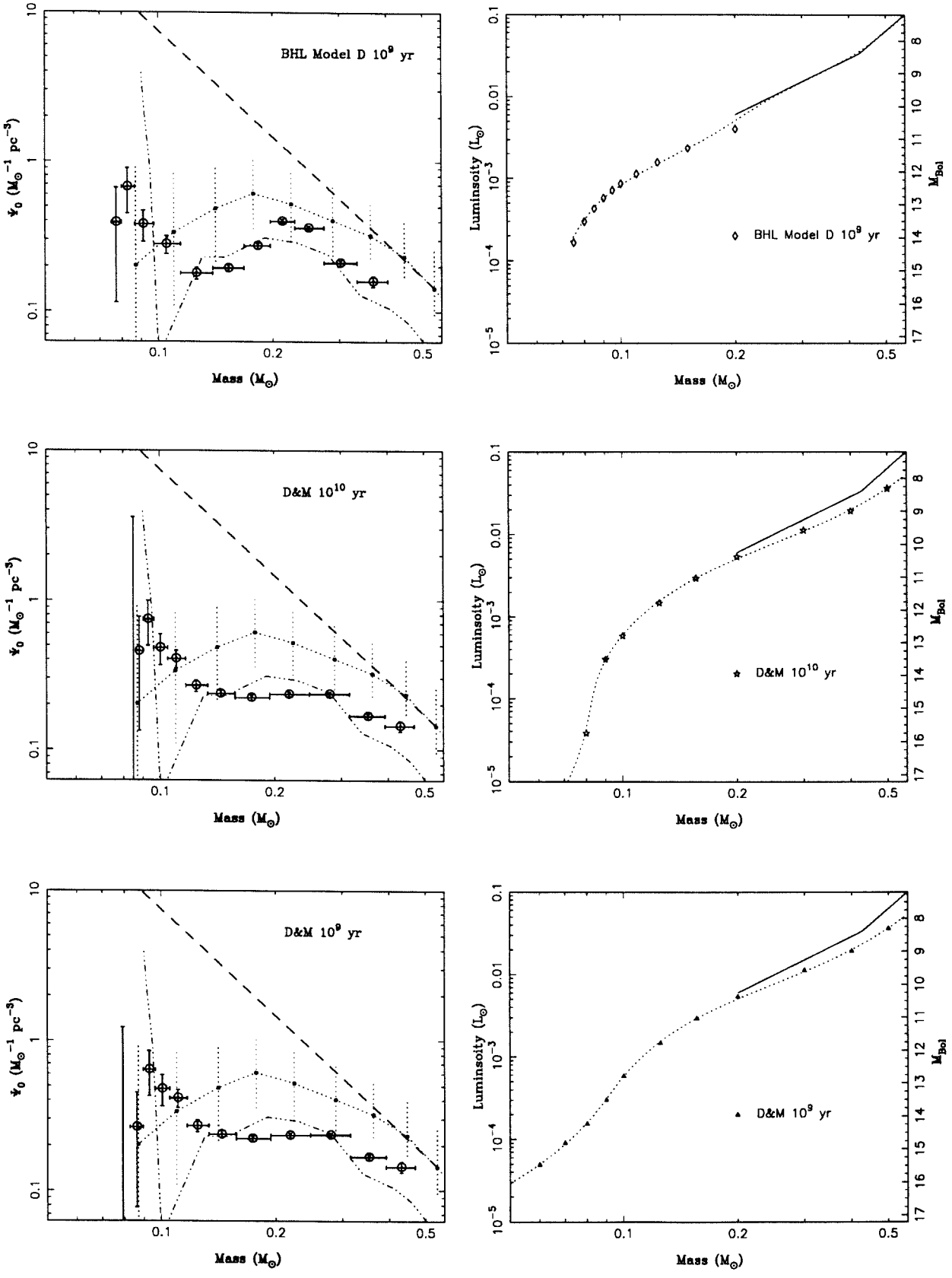
BHL Model D 10^9 yr
D&M 10^10 yr
D&M 10^9 yr
Ψ0 (M⊙^-1 pc^-3)
Mass (M⊙)
Luminsoity (L⊙)
M_Bol

Figure 5.7(g)

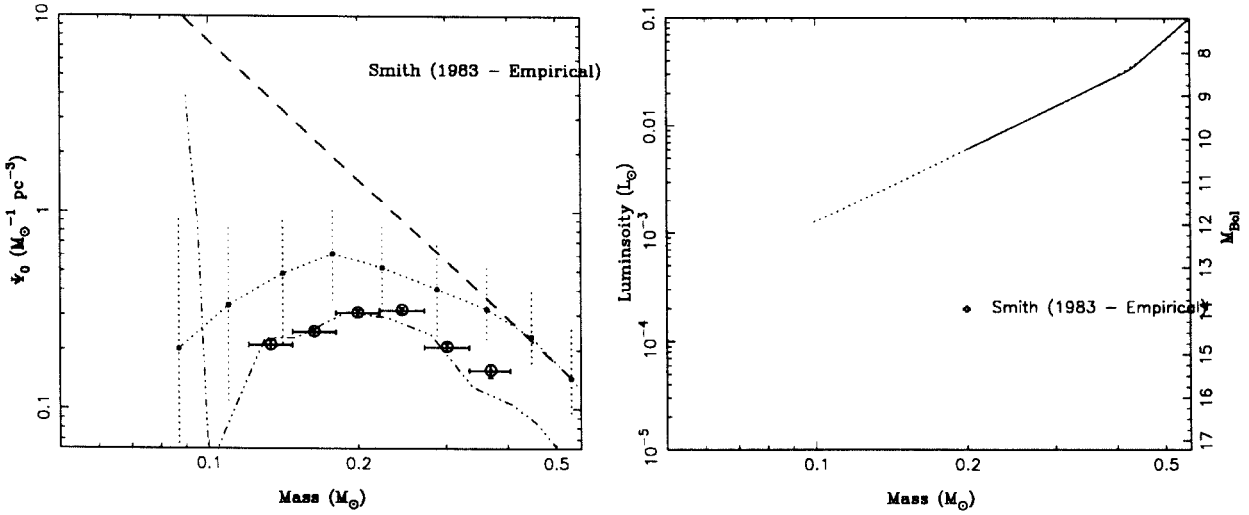
Smith (1983 – Empirical)
Ψ_0 ($M_\odot^{-1}$ pc^{-3})
Mass ($M_\odot$)
Luminosity ($L_\odot$)
M_{Bol}
Smith (1983 – Empirical)
Mass ($M_\odot$)

Figure 5.8(a)-(d)

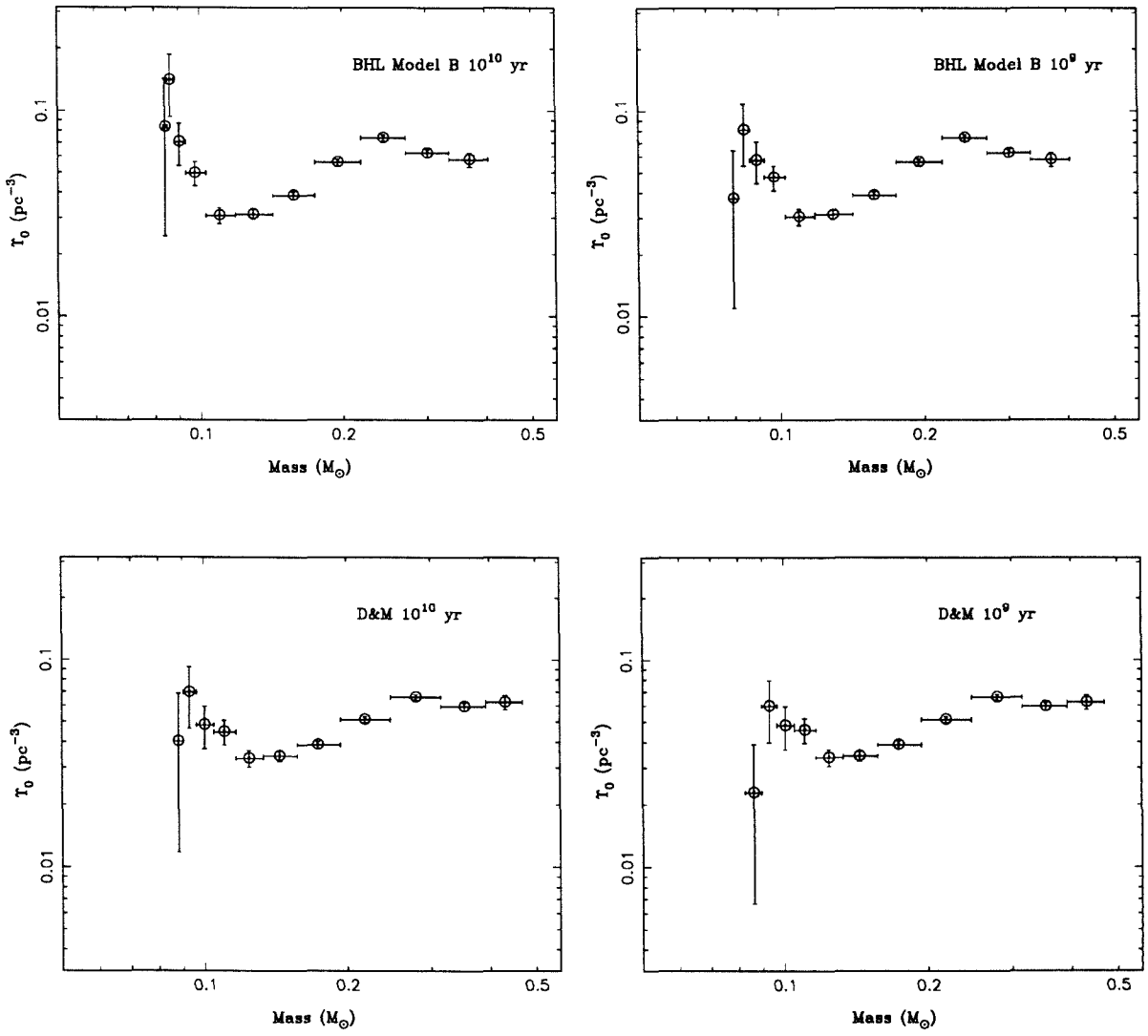
BHL Model B 10^{10} yr
BHL Model B 10^{9} yr
D&M 10^{10} yr
D&M 10^{9} yr
Υ_0 (pc^{-3})
Mass ($M_\odot$)
0.1
0.01
0.1
0.2
0.5

Chapter 6 - Backword.

If you've actually ploughed through all 200-odd pages of the thesis so far, (as opposed to just skipping to the back to see how it ends, in which case I have no sympathy for you), you'll probably be glad to read that I do not intend to provide a detailed summary of all the aims and results of the preceding chapters. Full discussions of the results of each of the papers included are given in their respective 'Conclusion' sections – while more terse descriptions are contained in the 'Abstract' sections. However, I would like to recap what, to me, seem to be the important results, and what future they point out in this field.

The results of Chapters 2 and 5 clearly show that luminosity functions for VLM stars obtained with photographic plates *without* follow-up infrared photometry are almost completely useless. The fact that the steeply increasing luminosity functions for $M_{Bol} \gtrsim 12.5$ of previous studies were reproduced by our photographic work, and were subsequently shown to be wrong by infrared photometry, is very telling. Future work on the number density and properties of VLM stars *must* be carried out in the infrared. While photographic (and even optical CCD) surveys may have a role to play in identifying VLM candidates, it should now be clearly realised that VLM stars and/or brown dwarfs can only be characterised in the infrared.

The many advantages (and possible pitfalls) of photometry from photographic plates are described in detail in Chapter 2. It is widely held that the forthcoming digital scans of the POSSII plate material (presumably accompanied by scans of the southern UKSRC plate material) will revolutionise optical astronomy – for the first time the general astronomical community will be able use the POSS plates for more than just making finding charts. Studies using the entire optical sky as a data base will be feasible. However, it should be pointed out that scans of photographic plates do *not* produce images just like an enormous CCD. There will be serious problems to be dealt with in the calibration of images. CCD photometry will have to be acquired in every field – and not just at the field centre – if a uniform catalogue of optical objects is to be produced. I found that a significant fraction of plates (especially the IVN plates) were almost unusable for a survey because of their pronounced field-effects, and that those field-effects were not correlated with the plate grades assigned by Palomar or the UKST. Astronomical photography is an

amzingly powerful resource – but we do it a disservice by assuming that it will solve all the problems of optical astronomers in one fell swoop.

I believe that *the* exciting result of this work was that described in the very shortest chapter. It has been shown in Chapter 4 that triginometric parallaxes of astronomically significant accuracies can be obtained in just a few years on a common-user telescope. Of course there are a few *caveats* – the observer has to be careful, and a sympathetic time-allocation committee is required if observations are to be made at optimal times. But even so, it is clear that direct measurements of astronomical distances need *not* be considered to be the exclusive domain of a small group of 'fuddy-duddy' astrometrists.

In Chapter 3 it was shown that the best available atmospheric models for VLM stars are still unable to reproduce the observed infrared spectra of these objects. Until such models can reproduce an observed spectrum it should be emphasised that *no useful effective temperature scale for these objects exists.* This means that comparisons between observed HR diagrams and theoretical predictions should be regarded as extremely suspect and that $\sim$ 300K systematic errors are likely to be present when an observed T_{eff} is constructed. As a result, surveys of clusters which identify cluster-members using theoretical isochrones are somewhat dodgy, and will remain so unless cluster-membership can be established using other techniques. On the other hand, observations of the main sequence in nearby clusters, based on an objective criteria for cluster membership, may represent one of the best hopes for resolving the current theoretical-observational HR diagram disagreement.

Lastly, I hope that the results of Chapter 5 will see the end of the IMF being characterised by a single power-law, whether it is Salpeter or not. There clearly exists structure in the IMF near the bottom of the main sequence. This structure must be telling us something about the nature of the process by which these stars formed. As theories of low mass star formation are currently a 'hot' topic in Galactic astronomy it is to be hoped that the observations can be interpreted soon.

The nature of the 'missing mass' continues to remain almost as elusive as agreement on whether or not it even exists. The new data presented, which enables a more precise normalisation of the mass function above the H-burning limit, would seem to indicate that an extremely steep mass function for brown dwarfs is required in order to hide significant quantities of mass in this form. Of course, a mass function with a characteristic power-law index greater than 2 can be made to hide an infinite amount of mass, if you assume it extends to small enough objects. But current theories and numerical simulation

of collapsing molecular cloud cores, would seem to indicate that the minimum masses for forming self-gravitating objects are $\sim 0.05 - 0.01 M_{\odot}$. The only way to hide a significant amount of mass in objects between 0.08 and $0.01 M_{\odot}$ is for there to be *a lot* of them – orders of magnitudes more than the number of $0.08 M_{\odot}$ objects observed.

Where does this field go from here? I think a few obvious areas need to be concentrated on. The most urgent theoretical requirement is a set of atmospheric models which match the observed spectra of these stars. It cannot be emphasised how detrimental the lack of such models is to the study of VLM stars and brown dwarfs. Observationally, we need to see just how many brown dwarfs there are out there, and what their properties are. The first task can be best tackled by observations in clusters, where the age of the objects is known and brown dwarfs are brighter than they are in the field. Progress in the area will require much deeper and wider angle work than has been done to date. In the Pleiades, for example, areas of tens of square degrees need to be covered down to $M_{Bol} \sim 14 - 15$. At a distance of 125pc, this means getting to K-magnitudes of ~ 17, or I-magnitudes of ~ 22 over significant areas of the cluster. Such a programme would represent a major undertaking given current array sizes, but would also almost certainly provide significant results if the work of Simons & Becklin can be taken as a guide. An important feature of such a programme would have to be follow-up CCD astrometry in order to unambiguously assign cluster membership. The results would not only give us a luminosity function for the cluster, but also a robust empirical VLM/brown-dwarf colour-magnitude diagram to compare with theory.

Even if we ignore effective temperatures as an imprecise way in which to estimate masses, significant uncertainties remain about the luminosities predicted by current interiors models, and how those luminosities evolve. The current models are completely unconstrained by observations. It will be necessary for VLM and brown dwarf masses to be measured directly in multiple systems before we can completely trust the models. This means that we need to find such objects close enough to the sun that: parallaxes are easily measurable; infrared speckle can resolve components; and so that radial velocities can be measured. Perhaps the best hope of establishing such a sample lies with the 2 Micron All-Sky Survey. Covering the entire sky in three pass bands down to K = 14, the 2MASS should include in its catalogue almost 100 VLM stars and brown dwarfs above $0.05 M_{\odot}$. A large programme of follow-up photometry will be required to select only the very low luminosity stars of interest, but such a programme is, in principle, very straightforward. Around a

quarter to a third of the VLMs/brown dwarfs found as a result should be multiple (assuming the binary fractions for more massive stars hold), and would make an excellent sample for radial velocity and infrared-speckle studies on the new generation of 8-m telescopes.

Clearly then, the study of dim stars, has a bright future!